DOE Final Report on Grant DE-FG02-03ER46063
"The Controlled Synthesis of Metastable Oxides Utilizing Epitaxy and Epitaxial Stabilization"
August 2003 - February 2007

Principal Investigator: Darrell G. Schlom
Period Covered by this Final Report: August 2003 - February 2007
DOE Award Number: DE-FG02-03ER46063
Amount of Unexpended Funds: $0

The research enabled by this DOE grant led to 13 publications in leading refereed journals including *Physical Review Letters* and *Applied Physics Letters* as well as feature articles in the *Journal of the American Ceramic Society* and *Physik Journal* (the German equivalent of *Physics Today* distributed to all members of the German Physical Society) on the controlled synthesis of metastable oxides utilizing epitaxy and epitaxial stabilization. In total our results fill over 100 pages of archived journals and are attached.

Much of our work has been performed in collaboration with other DOE researchers. Specifically, we have active collaborations with (please see publications on the next page) with the following DOE groups.

DOE COLLABORATORS ON THE WORK SUPPORTED BY THIS DOE GRANT

DOE Laboratory	Collaborators
Argonne National Laboratory	Stephen K. Streiffer, Mark A. Zurbuchen, and Dillon D. Fong
Pacific Northwest National Laboratory	Scott A. Chambers
Los Alamos National Laboratory	Marilyn E. Hawley

PERSONNEL SUPPORTED BY THIS DOE GRANT

Name	Position
Darrell G. Schlom	Principal Investigator
Wei Tian	Postdoctoral Researcher

PUBLICATIONS AND PRESENTATIONS

The support from this DOE program has led to the publications listed below and attached to the end of this document.

Publications

1. M.A. Zurbuchen, Y. Jia, S. Knapp, A.H. Carim, D.G. Schlom, and X.Q. Pan, "Defect Generation by Preferred Nucleation in Epitaxial Sr_2RuO_4 / $LaAlO_3$," *Applied Physics Letters* **83** (2003) 3891-3893.

2. A.V. Pogrebnyakov, J.M. Redwing, S. Raghavan, V. Vaithyanathan, D.G. Schlom, S.Y. Xu, Q. Li, D.A. Tenne, A. Soukiassian, X.X. Xi, M.D. Johannes, D. Kasinathan, W.E. Pickett, J.S. Wu, and J.C.H. Spence, "Enhancement of Superconducting Transition Temperature of MgB_2 by a Strain-Induced Bond-Stretching Mode Softening," *Physical Review Letters* **93** (2004) 147006-1 - 147006-4.
3. A.V. Pogrebnyakov, X.X. Xi, J.M. Redwing, V. Vaithyanathan, D.G. Schlom, A. Soukiassian, S.B. Mi, C.L. Jia, J.E. Giencke, C.B. Eom, J. Chen, Y.F. Hu, Y. Cui, and Q. Li, "Properties of MgB_2 Thin Films with Carbon Doping," *Applied Physics Letters* **85** (2004) 2017-2019.
4. D.A. Tenne, X.X. Xi, Y.L. Li, L.Q. Chen, A. Soukiassian, M.H. Zhu, A.R. James, J. Lettieri, D.G. Schlom, W. Tian, and X.Q. Pan, "Absence of Low-Temperature Phase Transitions in Epitaxial $BaTiO_3$ Thin Films," *Physical Review B* **69** (2004) 174101-1 - 174101-5.
5. X.X. Xi, A.V. Pogrebnyakov, X.H. Zeng, J.M. Redwing, S.Y. Xu, Q. Li, Z.K. Liu, J. Lettieri, V. Vaithyanathan, D.G. Schlom, H.M. Christen, H.Y. Zhai, and A. Goyal, "Progress in the Deposition of MgB_2 Thin Films," *Superconductor Science and Technology* **17** (2004) S196-S201 and in: *Applied Superconductivity 2003: Proceedings of the Sixth European Conference on Applied Superconductivity*, IOP Vol. 181 (Institute of Physics, Bristol, 2004), pp. 37-44.
6. J. Mannhart and D.G. Schlom, "Oxide—Tausendsassa für die Elektronik," *Physik Journal* **4** (2005) 45-51.
7. A. Venimadhav, A. Soukiassian, D.A. Tenne, Q. Li, X.X. Xi, D.G. Schlom, R. Arroyave, Z.K. Liu, H.P. Sun, X.Q. Pan, M.Y. Lee, and N.P. Ong, "Structural and Transport Properties of Epitaxial Na_xCoO_2 Thin Films," *Applied Physics Letters* **87** (2005) 172104-1 – 172104-3.
8. P. Orgiani, Y. Cui, A.V. Pogrebnyakov, J.M. Redwing, V. Vaithyanathan, D.G. Schlom, and X.X. Xi, "Investigations of MgB_2 / MgO and MgB_2 / AlN Heterostructures for Josephson Devices," *IEEE Transactions on Applied Superconductivity* **15** (2005) 228-231.
9. B.T. Liu, X.X. Xi, V. Vaithyanathan, and D.G. Schlom, "MgB_2 Thin Films Grown at Different Temperatures by Hybrid Physical-Chemical Vapor Deposition," *IEEE Transactions on Applied Superconductivity* **15** (2005) 3249-3252.
10. M.A. Zurbuchen, J. Lettieri, Y. Jia, A.H. Carim, S.K. Streiffer, and D.G. Schlom, "Out-of-phase Boundary (OPB) Nucleation in Layered Oxides," in: *Ferroelectric Thin Films XIII* edited by R. Ramesh, J.-P. Maria, M. Alexe, and V. Joshi, Vol. 902E (Materials Research Society, Warrendale, 2006), pp. T10-55.1 – T10-55.6.
11. W. Tian, J.H. Haeni, D.G. Schlom, E. Hutchinson, B.L. Sheu, M.M. Rosario, P. Schiffer, Y. Liu, M.A. Zurbuchen, and X.Q. Pan, "Epitaxial Growth and Magnetic Properties of the First Five Members of the Layered $Sr_{n+1}Ru_nO_{3n+1}$ Oxide Series," *Applied Physics Letters* **90** (2007) 022507-1 – 022507-3.
12. M.A. Zurbuchen, W. Tian, X.Q. Pan, D. Fong, S.K. Streiffer, M.E. Hawley, J. Lettieri, Y. Jia, G. Asayama, S.J. Fulk, D.J. Comstock, S. Knapp, A.H. Carim, and D.G. Schlom, "Morphology, Structure, and Nucleation of Out-of-Phase Boundaries (OPBs) in Epitaxial Films of Layered Oxides," *Journal of Materials Research* **22** (2007) 1439-1471.
13. M.A. Zurbuchen, R.S. Freitas, M.J. Wilson, P. Schiffer, M. Roeckerath, J. Schubert, M.D. Biegalski, G.H. Mehta, D.J. Comstock, J.H. Lee, Y. Jia, and D.G. Schlom, "Synthesis and Characterization of an $n = 6$ Aurivillius Phase Incorporating Magnetically Active Manganese, $Bi_7(Mn,Ti)_6O_{21}$," *Applied Physics Letters* **91** (2007) 033113-1 – 033113-3.
14. D.G. Schlom, L.Q. Chen, X.Q. Pan, A. Schmehl, and M.A. Zurbuchen, "A Thin Film Approach to Engineering Functionality into Oxides," *Journal of the American Ceramic Society* **91** (2008) 2429-2454. (**Feature Article with Journal Cover**)

Defect generation by preferred nucleation in epitaxial $Sr_2RuO_4/LaAlO_3$

Mark A. Zurbuchen,[a] Yunfa Jia, Stacy Knapp, Altaf H. Carim,[b] and Darrell G. Schlom
Department of Materials Science and Engineering, The Pennsylvania State University, University Park, Pennsylvania 16803-6602

X. Q. Pan
Department of Materials Science and Engineering, University of Michigan, Ann Arbor, Michigan 48109-2136

(Received 27 May 2003; accepted 12 September 2003)

The atomic structure of the film–substrate interface of a (001) $Sr_2RuO_4/(100)_c$ $LaAlO_3$ film, determined by high-resolution transmission electron microscopy and simulation, is reported. The structure of superconductivity-quenching $\Delta c \approx 0.25$ nm out-of-phase boundaries (OPBs) in the film is also reported. Growth in one region on the La-terminated surface is observed to nucleate with a SrO layer. Because two structurally equivalent SrO layers exist within the unit cell, two neighboring nuclei with differing growth order ($SrO\text{-}RuO_2\text{-}SrO$ or $RuO_2\text{-}SrO\text{-}SrO$) will nucleate an OPB where their misaligned growth fronts meet. Strategies to avoid OPB generation by this mechanism are suggested, which it is hoped may ultimately lead to superconducting Sr_2RuO_4 films. © *2003 American Institute of Physics.*
[DOI: 10.1063/1.1624631]

Sr_2RuO_4 is the only known copper-free layered perovskite superconductor,[1] and is believed to have an unconventional spin-triplet (p-wave) symmetry of the superconducting order parameter.[2] Electrical transport studies of Sr_2RuO_4 are expected to further the understanding of the superconducting state.[3] Sr_2RuO_4 is well lattice-matched to $YBa_2Cu_3O_{7-\delta}$ and other cuprate superconductors. Epitaxial heterostructures would be useful for probing the interaction between d-wave and p-wave superconductors. Although the epitaxial growth of Sr_2RuO_4 films[4,5] and epitaxial $YBa_2Cu_3O_{7-\delta}/Sr_2RuO_4$ heterostructures[6] have been demonstrated, no superconducting Sr_2RuO_4 films have been reported.[4,5] As we show in this letter, greater attention to nucleation and growth is important to reducing defects and to possibly achieving superconductivity in Sr_2RuO_4 films.

Both impurities and crystallographic defects can quench superconductivity in Sr_2RuO_4. As little as 300 ppm of aluminum is sufficient to destroy superconductivity.[7] Crystallographic defects that quench superconductivity include out-of-phase boundaries (OPBs).[8] These are translation boundaries consisting of a fractional misalignment in the long axis (c-axis) direction between two neighboring regions of the same crystal. Because any interruption of the structure can act as a pair-breaker, a linear density of OPBs on the order of $1/\xi_{ab}(0)$, where $\xi_{ab}(0)$ is the superconducting coherence length in the (001) plane, $\xi_{ab}(0) \approx 66$ nm,[9] renders a high-purity film nonsuperconducting.[9] A correlation between T_c and the residual resistivity (ρ_0), a measure of disorder in equivalent-purity crystals, has also been reported.[10] Although OPBs are common defects in complex oxides, little is known about their nucleation mechanisms or impact upon properties.[11–13]

In the heteroepitaxial growth of layered structures, substrate surface quality has a great effect on final film quality.[14] Advances in substrate engineering have enabled the preparation of substrates with known atomic terminations.[14,15] Some disagreement currently exists regarding the atomic termination of (001) $LaAlO_3$.[16–19]

It would be useful experimentally to determine which atomic layers are energetically preferred for the nucleation of Sr_2RuO_4 on a given substrate, so that high-quality films can be grown by sequential deposition techniques [e.g., molecular-beam epitaxy (MBE)]. Few studies of the preferred nucleation layer of epitaxial thin films of complex oxides on substrates with known termination have been reported.[20–22] Understanding defect nucleation mechanisms and microstructural development in the growth of complex oxide films will allow greater control over their growth. Substrate surface features have been demonstrated to result in micron-scale crystallographic defects in some similarly structured layered perovskites ($n=2$ Aurivillius phases).[23,24] In this letter, the structure of the film–substrate interface of an epitaxial (001) $Sr_2RuO_4/(001)_c$ $LaAlO_3$[16] film is reported, and the mechanism whereby the preferred nucleation layer can lead to the generation of superconductivity-quenching OPBs is described.

$(001)_c$ Sr_2RuO_4 epitaxial films were grown on (001) $LaAlO_3$[16] substrates by pulsed-laser deposition (PLD) at 1000 °C in a radiatively heated sample chamber. Specifics of the film growth are described in detail elsewhere.[8] The film described here was a high-quality film, judged by the full width at half-maximum of the 006 Sr_2RuO_4 peak of approximately 0.23° in 2θ, and 0.33° in ω (instrumental resolution ≈0.20°) in x-ray diffraction measurements. Samples for cross-sectional transmission electron microscopy (TEM) examination were prepared by standard sandwiching, slicing, dimpling, and argon ion milling on a liquid nitrogen-cooled stage at 4 kV and 8° to 11°.

[a]Presently at: Argonne National Laboratory, Argonne, IL; electronic mail: mark_z@mac.com
[b]Presently at: the U.S. Department of Energy, Germantown, MD.

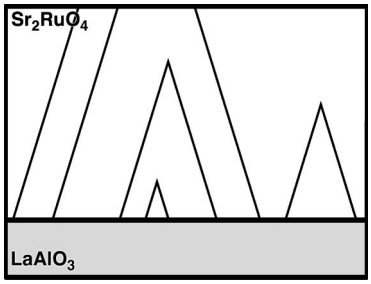

FIG. 1. Schematic of the planar defect morphology of OPBs in $SrRu_2O_4/LaAlO_3$ films; diagonal lines represent OPBs. Two OPBs with opposing inclination, on the far right, have annihilated where they met. On the far left, two OPBs with parallel inclination penetrate through the full thickness of the film.

High-resolution TEM (HRTEM) imaging was performed using JEOL 4000-EX and Hitachi HF-2000 microscopes. Regions of appropriate and consistent thickness of the film–substrate phase boundary and an individual OPB were located, and through-focus image series were acquired. Appropriate multislice simulation parameters were determined by matching of images to simulated images of the individual phases, and supercells based on possible interfacial and defect structures were constructed. HRTEM image simulations used sufficiently large supercells to remove cell-edge distortions, caused by their nonrepeating nature, from the region of interest. Bulk values for a and b of Sr_2RuO_4 and $LaAlO_3$ were used in constructing the interfacial models, with cells aligned in the center. The 2.1% lattice mismatch between $(001)_c$ $LaAlO_3$[16] and (001) Sr_2RuO_4 at room temperature resulted in negligible variation in alignment (0.12 Å) over the length scale of the supercell. As a check, simulations of a coherent interface were also performed, with identical results. Only the 2.1% lattice-mismatched supercell simulations are presented here.

Figure 1 shows a schematic of the generalized defect morphology we have observed in (001) $Sr_2RuO_4/(001)_c$ $LaAlO_3$[16] epitaxial films.[8,23] Films contain a number of $\Delta c \approx 0.25$ nm ($\sim c/5$) OPBs, inclined 17° from the c direction. These features either penetrate the full film thickness, or else annihilate where pairs of opposite inclination meet. Similar features in other $n=1$ Ruddlesden-Popper (RP)[25] phases have been reported,[11,12] although no detailed information on their structure or nucleation is available.

A [100] HRTEM image of a single OPB, showing a (011) habit, is shown in Fig. 2. A model and HRTEM simulation are inset, showing a very good match with the image. Both chemical and physical interruptions of the structure exist at the OPB. A distorted rocksalt SrO layer is incorporated along the OPB. This lattice interruption not only will scatter phonons,[8] but also interrupts the continuity of the $a-b$ plane RuO_2 layers, believed to be responsible for superconductivity in the material.

Figure 3(a) shows a [100] HRTEM image of the film–substrate interface, with a Fourier-filtered region of the image on the right. Bright spots correspond to atomic columns. Models and HRTEM simulations for each of the possible termination-nucleation layer pairs are shown in Figs. 3(b)–3(f), with the exception of growth beginning with RuO_2 on an AlO_2-terminated surface, which was ruled out because no known phases with the corresponding structure could be found. Close examination of the images reveals that only the model in Fig. 3(d), with a charge-neutral SrO layer nucleating on a LaO-terminated surface, matches the HRTEM image. This result is consistent with the previous determination of a LaO surface termination of $LaAlO_3$ above ≈300 °C in vacuum or near vacuum.[17,19] Growth proceeds with a SrO-RuO_2-SrO layer ordering. The Sr_2RuO_4 unit cell contains two structurally equivalent SrO layers, and only one RuO_2 layer, and the OPB offset is equivalent to one SrO layer. There are, then, two possibilities for the nucleation mechanism. (i) If SrO is strongly energetically preferred as the starting layers, then a LaO-SrO-SrO-RuO_2 growth order, as shown in Fig. 3(c), might also be possible. However, this layer order contains three AO (rocksalt)-type layers in a row, which has never been observed in these RP nor in substoichiometric perovskite type phases,[26] so that it is considered to be unlikely. (ii) If the energy difference of a SrO versus a RuO_2 nucleation layer is small, then a LaO-RuO_2-SrO-SrO

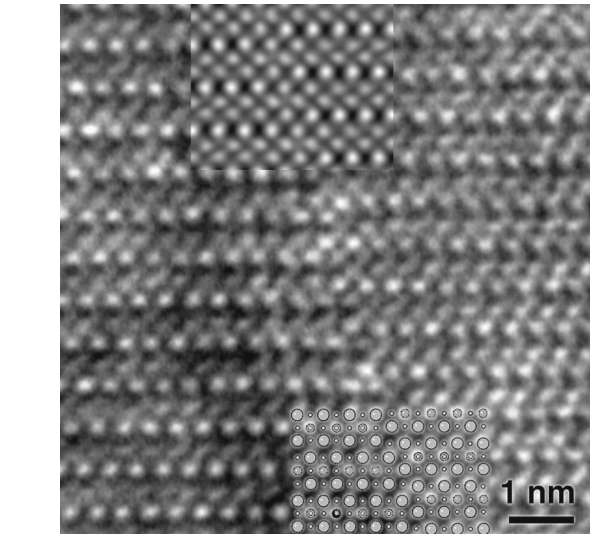

FIG. 2. HRTEM image of a single OPB in a (001) $SrRu_2O_4/(001)_c$ $LaAlO_3$ film, with a model and simulation of the defect inset. Large circles represent strontium, small circles ruthenium. An extra SrO layer is incorporated along the OPB. The c-direction misregistry across the OPB is 0.25 nm, equal to the c-direction dimension of a single layer of SrO.

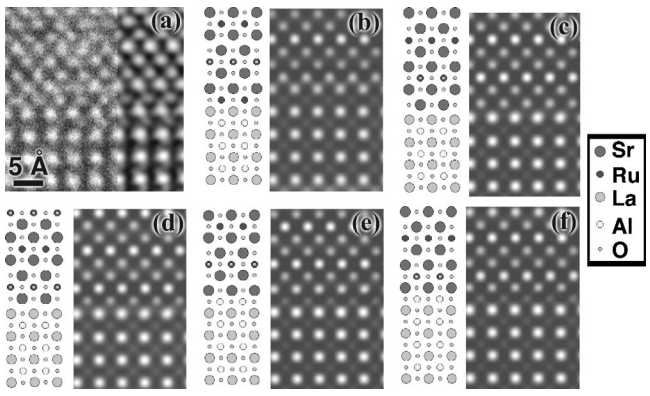

FIG. 3. (a) HRTEM image of the (001) $Sr_2RuO_4/(001)_c$ $LaAlO_3$ (see Ref. 16) film–substrate interface, taken at Scherzer defocus. A Fourier-filtered region of the image is overlaid on the right. (b)–(f) Models of the possible termination-nucleation layer pairs for the film, shown with HRTEM simulations ($\Delta f = -58$ nm, $t = 4.5$ nm). The model in (d) shows the only reasonable match with the image. The film nucleated with a SrO-RuO_2-SrO layer sequence on a LaO-terminated substrate.

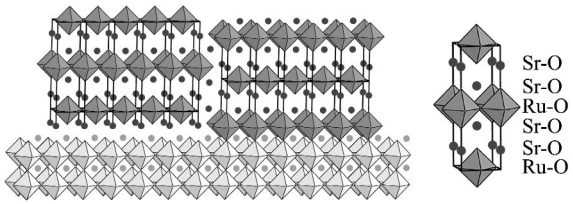

FIG. 4. Nucleation-layer growth-order OPB nucleation mechanism in the (001) Sr_2RuO_4 /(001)$_c$ $LaAlO_3$ (see Ref. 16) film. Because two structurally equivalent SrO layers exist in the Sr_2RuO_4 unit cell, adjacent nuclei growing with either SrO-RuO_2-SrO or RuO_2-SrO-SrO ordering, will form an OPB where they meet. The coordination octahedra of the ruthenium and aluminum are shown, with circles representing strontium and lanthanum, in shades of gray equivalent to those in Fig. 3. A unit cell of Sr_2RuO_4 is shown to the right for reference.

growth order, as shown in Fig. 3(b), might also be possible. A schematic of this OPB nucleation mechanism, considered most likely to be correct, is shown in Fig. 4.

Growth proceeding in either of these scenarios would result in the generation of OPBs through the preferred nucleation mechanism. The energetics of continuing growth after the first layer would be expected to be quite similar, considering the close lattice match and the fact that each layer is charge neutral, so electrostatic effects do not affect growth ordering, as they undoubtedly do in other layered perovskites such as the Aurivillius phases. The *c*-direction misregistry of the OPBs is equal to the *c* dimension of a single SrO layer (i.e., an extra one or a missing one) within the unit cell. This implies that OPBs nucleated at the film–substrate interface (almost all of the OPBs observed) by the meeting of two nuclei with differing growth order.

Bearing this model in mind, we reconsider the general OPB morphology depicted in Fig. 1. Because neighboring out-of-phase nuclei have only one possible offset, OPB interaction is uncomplicated. Two OPBs with opposing inclinations, like those shown on the right in Fig. 1, will annihilate when the film growth front proceeds past the point where they meet. Two nuclei with parallel inclinations, like those shown on the left, will not interact and will penetrate the full film thickness.

Additional mechanisms that may also lead to the generation of OPBs in $n=1$ RP phases on perovskite substrates are surface steps,[23] and perhaps in the case of films on $LaAlO_3$ substrates, twinning of the substrate upon transformation during cooling from the growth temperature.[16] The slight tilt between domains could conceivably be accommodated by a defect having a similar appearance to the OPBs described here, although the linear OPB density in the samples we have examined ($\geqslant$1 of every 17 perovskite cells)[8] is much greater than the linear density of domain boundaries in $LaAlO_3$ is likely to be.

Several strategies that might suppress the nucleation-layer OPB generation mechanism in Sr_2RuO_4 films are possible, and could lead to lower OPB densities and possibly to the first superconducting Sr_2RuO_4 films. An atomic layer-by-layer growth technique such as MBE[27] could be used to engineer the growth order, for example, beginning growth with either the preferred SrO layer, or perhaps a RuO_2 layer, on a LaO-terminated substrate, and continuing with either sequence. Perhaps the best strategy would be to use a (001) $LaSrAlO_4$ substrate instead of (001)$_c$ $LaAlO_3$,[16] as $LaSrAlO_4$ is isostructural to Sr_2RuO_4. Lastly, extra kinetic activation (e.g., higher temperature, higher laser fluence) during growth of the first few atomic layers could increase surface diffusivities, increasing the average nuclei diameter,[28] thereby reducing the density of OPBs.

The authors gratefully acknowledge the financial support of the Department of Energy through contract DE-FG-02-03ER46063. Microscopy was performed in the University of Michigan's EMAL, and Penn State's MCL.

[1] Y. Maeno, H. Hashimoto, K. Yoshida, S. Nishizaki, T. Fujita, J. J. Bednorz, and F. Lichtenberg, Nature (London) **372**, 532 (1994).
[2] T. M. Rice and M. Sigrist, J. Phys. C **7**, L643 (1995).
[3] Y. Maeno, T. M. Rice, and M. Sigrist, Phys. Today **54**, 42 (2001).
[4] D. G. Schlom, Y. Jia, L.-N. Zou, J. H. Haeni, S. Briczinski, M. A. Zurbuchen, C. W. Leitz, S. Madhavan, S. Wozniak, Y. Liu, M. E. Hawley, G. W. Brown, A. Dabkowski, H. A. Dabkowska, R. Uecker, and P. Reiche, Proc. SPIE **3481**, 226 (1998).
[5] S. Ohashi, M. Lippmaa, N. Nakagawa, H. Nagasawa, H. Koinuma, and M. Kawasaki, Rev. Sci. Instrum. **70**, 178 (1999).
[6] F. Lichtenberg, A. Catana, J. Mannhart, and D. G. Schlom, Appl. Phys. Lett. **60**, 1138 (1992).
[7] A. P. Mackenzie, R. K. W. Haselwimmer, A. W. Tyler, G. G. Lonzarich, Y. Mori, S. Nishizaki, and Y. Maeno, Phys. Rev. Lett. **80**, 161 (1998).
[8] M. A. Zurbuchen, Y. Jia, S. K. Knapp, A. H. Carim, D. G. Schlom, L.-N. Zou, and Y. Liu, Appl. Phys. Lett. **78**, 2351 (2001).
[9] T. Akima, S. Nishizaki, and Y. Maeno, J. Phys. Soc. Jpn. **68**, 694 (1999).
[10] Z. Q. Mao, Y. Mori, and Y. Maeno, Phys. Rev. B **60**, 610 (1999).
[11] J. G. Wen, C. Traeholt, and H. W. Zandbergen, Physica C **205**, 354 (1993).
[12] G. Kong, M. O. Jones, J. S. Abell, P. P. Edwards, S. T. Lees, K. E. Gibbons, I. Gameson, and M. Aindow, J. Mater. Res. **16**, 3309 (2001).
[13] M. A. Zurbuchen, J. Lettieri, Y. Jia, D. G. Schlom, S. K. Streiffer, and M. E. Hawley, J. Mater. Res. **16**, 489 (2001).
[14] M. Kawasaki, K. Takahashi, T. Maeda, R. Tsuchiya, M. Shinohara, O. Ishiyama, T. Yonezawa, M. Yoshimoto, and H. Koinuma, Science **266**, 1540 (1994).
[15] T. Ohnishi, K. Takahashi, M. Nakamura, M. Kawasaki, M. Yoshimoto, and H. Koinuma, Appl. Phys. Lett. **74**, 2531 (1999).
[16] Cubic indices; $LaAlO_3$ is cubic at the film growth temperature, and transforms to rhombohedral on cooling.
[17] J.-P. Jacobs, M. A. San Miguel, and L. J. Alvarez, J. Mol. Struct.: THEOCHEM **390**, 193 (1997).
[18] D.-W. Kim, D.-H. Kim, B.-S. Kang, T. W. Noh, D. R. Lee, and K.-B. Lee, Appl. Phys. Lett. **74**, 2176 (1999).
[19] P. A. W. van der Heide and J. W. Rabalais, Chem. Phys. Lett. **297**, 350 (1998).
[20] S. Bals, G. Rijnders, D. H. A. Blank, and G. Van Tendeloo, Physica C **355**, 225 (2001).
[21] J. C. Jiang and X. Q. Pan, J. Appl. Phys. **89**, 6365 (2001).
[22] M. Salluzzo, C. Aruta, I. Maggio-Aprile, Ø. Fischer, S. Gals, and J. Zegenhagen, Phys. Status Solidi A **186**, 339 (2001).
[23] M. A. Zurbuchen, J. Lettieri, G. Asayama, Y. Jia, A. H. Carim, D. G. Schlom, and S. K. Streiffer (unpublished).
[24] B. Aurivillius, Ark. Kemi **1**, 463 (1950); **1**, 499 (1950); **2**, 519 (1951); **5**, 39 (1953).
[25] S. N. Ruddlesden and P. Popper, Acta Crystallogr. **10**, 538 (1957); **11**, 54 (1958).
[26] C. N. R. Rao and B. Raveau, *Transition Metal Oxides: Structure, Properties, and Synthesis of Ceramic Oxides*, 2nd ed. (Wiley, New York, 1998), p. 61.
[27] D. G. Schlom, J. H. Haeni, J. Lettieri, C. D. Theis, W. Tian, J. C. Jiang, and X. Q. Pan, Mater. Sci. Eng., B **87**, 282 (2001).
[28] B. Dam and B. Stäuble-Pümpin, J. Mater. Sci.: Mater. Electron. **9**, 217 (1998).

Enhancement of the Superconducting Transition Temperature of MgB_2 by a Strain-Induced Bond-Stretching Mode Softening

A. V. Pogrebnyakov,[1,2,3] J. M. Redwing,[2,3] S. Raghavan,[2,3] V. Vaithyanathan,[2,3] D. G. Schlom,[2,3] S. Y. Xu,[1,3] Qi Li,[1,3] D. A. Tenne,[1,3] A. Soukiassian,[2,3] X. X. Xi,[1,2,3] M. D. Johannes,[4] D. Kasinathan,[4] W. E. Pickett,[4] J. S. Wu,[5] and J. C. H. Spence[5]

[1]*Department of Physics, The Pennsylvania State University, University Park, Pennsylvania 16802, USA*
[2]*Department of Materials Science and Engineering, The Pennsylvania State University, University Park, Pennsylvania 16802, USA*
[3]*Materials Research Institute, The Pennsylvania State University, University Park, Pennsylvania 16802, USA*
[4]*Department of Physics, University of California, Davis, California 95616, USA*
[5]*Department of Physics and Astronomy, Arizona State University, Tempe, Arizona 85287, USA*

(Received 5 June 2004; published 30 September 2004)

We report a systematic increase of the superconducting transition temperature T_c with a biaxial tensile strain in MgB_2 films to well beyond the bulk value. The tensile strain increases with the MgB_2 film thickness, caused primarily by the coalescence of initially nucleated discrete islands (the Volmer-Weber growth mode.) The T_c increase was observed in epitaxial films on SiC and sapphire substrates, although the T_c values were different for the two substrates due to different lattice parameters and thermal expansion coefficients. We identified, by first-principles calculations, the underlying mechanism for the T_c increase to be the softening of the bond-stretching E_{2g} phonon mode, and we confirmed this conclusion by Raman scattering measurements. The result suggests that the E_{2g} phonon softening is a possible avenue to achieve even higher T_c in MgB_2-related material systems.

DOI: 10.1103/PhysRevLett.93.147006 PACS numbers: 74.62.–c, 74.70.–b, 74.78.–w

Since the discovery of superconductivity in MgB_2 by Nagamatsu *et al.* [1], many techniques, including substitution, disorder, and pressure, have been used in an attempt to further increase the transition temperature T_c. However, the highest T_c in MgB_2 has remained at about 40 K. Doping and chemical substitution in MgB_2 are difficult [2]. The successful cases such as substitution of Mg by Al [3] and B with C [4] have so far always suppressed T_c. Although atomic disorder induced by proton irradiation enhances the pinning of vortices, it reduces T_c [5]. Subjecting MgB_2 to pressure also causes T_c to decrease [6]. The only higher T_c values reported are from the ^{10}B isotope effect ($T_c = 40.2$ K) [7] and by Hur *et al.* when they exposed B crystals to Mg vapor (zero resistance $T_{c0} = 39.8$ K) [8]. Recently, we have shown that T_c of MgB_2 films on (0001) SiC increases with film thickness [9]. There have been speculations that a tensile strain may be the cause of enhanced T_c in the films [8,9]. In this Letter, we show unambiguously a systematic increase of T_c with epitaxial tensile strain in MgB_2 films on both SiC and sapphire substrates to well beyond the bulk value (the highest $T_{c0} = 41.8$ K). Moreover, we identify the underlying mechanism, among several materials' characteristics that determine T_c, to be the softening of the E_{2g} phonon.

MgB_2 is a clear and rather extreme example of a "two gap" superconductor [10–12], arising due to two qualitatively different Fermi surfaces (called σ and π) and their different pairing strengths (extremely strong and weak, respectively). The σ contribution is dominant, however, and specifically the contribution from the B-B stretch modes (of E_{2g} symmetry) in the B_2 graphene layer [13,14]. Therefore, it suffices to consider only the σ contribution to T_c. According to the McMillan-Allen-Dynes analysis,

$$T_c \propto \omega e^{-f(\lambda,\hat{\mu})}, \tag{1}$$

where ω is the phonon frequency, $f(\lambda, \hat{\mu}) = (1 + \lambda)/(\lambda - \hat{\mu})$, and $\hat{\mu}$ is similar to the Coulomb repulsion μ^*. The electron-phonon coupling due to the σ band and the bond-stretching mode becomes [14]

$$\lambda_{E_{2g}}^{\sigma\sigma} \propto \frac{m^*|\mathcal{D}|^2}{M\omega^2}, \tag{2}$$

where the σ band effective mass m^* is proportional to the density of states of holes in the σ band at the Fermi level, $\mathcal{D}$ is the σ-band deformation potential, and M is the B mass. A change in T_c can arise from any combination of changes in ω, $\mathcal{D}$, m^*, or $\hat{\mu}$.

The epitaxial MgB_2 films in this work were deposited by hybrid physical-chemical vapor deposition (HPCVD) [15]. Pure magnesium chips were heated simultaneously with the substrate to 720 °C to generate a high Mg pressure, and 1000 ppm diborane (B_2H_6) in H_2 was used as the B precursor. The carrier gas was a H_2 flow of 450 sccm at a pressure of 100 Torr. The films were deposited on both (0001) 4H-SiC and (0001) sapphire substrates. Films on (0001) SiC are *c*-axis oriented and epitaxial with an in-plane alignment of the *a* axis of MgB_2 with that of SiC [16]. Films on (0001) sapphire are also *c*-axis oriented and epitaxial, but the *a* axis of MgB_2 is rotated by 30° in plane from the *a* axis of sapphire [15].

We have reported previously that the properties of MgB_2 films on (0001) SiC depend on film thickness [9].

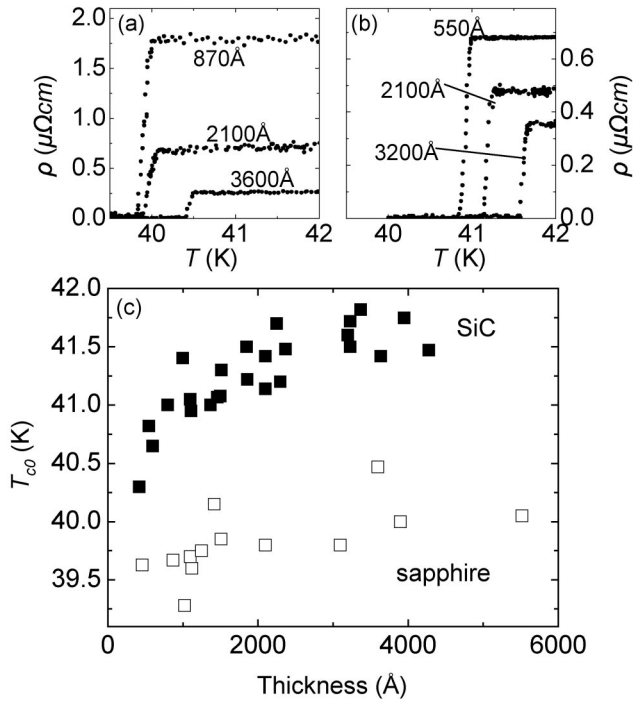

FIG. 1. Superconducting transition in MgB_2 films of different thicknesses on (a) (0001) sapphire and (b) (0001) SiC substrates. (c) Zero-resistance T_{c0} as a function of film thickness on both sapphire and SiC substrates.

We found a similar trend of thickness dependence on (0001) sapphire substrates. Figure 1 shows resistivity versus temperature curves for MgB_2 films with different thicknesses grown on sapphire [Fig. 1(a)] and SiC [Fig. 1(b)] substrates. Both figures clearly show that T_c becomes higher as the film thickness increases. The thickness dependence of the zero-resistance T_{c0} for both substrates is plotted in Fig. 1(c). A clear trend of increasing T_{c0} with film thickness is seen for both substrates with T_{c0} consistently 1–1.5 K higher in films on SiC than on sapphire. The highest T_{c0} observed (41.8 K) is 2 K higher than the bulk value.

X-ray diffraction analysis, from both $\theta - 2\theta$ and ϕ scans, shows a direct correlation between the film strain and T_{c0}. Figure 2(a) shows the a-axis and c-axis lattice constants of several MgB_2 films, of different thicknesses and on sapphire (open symbols) and SiC (solid symbols) substrates, versus their T_{c0} values. Clearly, a higher T_{c0} corresponds to a larger a-axis and smaller c-axis lattice constants. Consequently, as T_{c0} increases, the c/a ratio decreases [see Fig. 2(b)] and the unit cell volume increases [see Fig. 2(c)]. Most strikingly, although the results on SiC and sapphire follow two different T_{c0} versus thickness curves in Fig. 1(c), they fall on the same curves in Fig. 2. Compared to the bulk values indicated by the dashed lines in Fig. 2 ($a = 3.086$ Å, $c = 3.524$ Å [1], $c/a = 1.142$, and cell volume of 29.06 Å^3), it is evident that the tensile strain in the films causes T_{c0} to increase

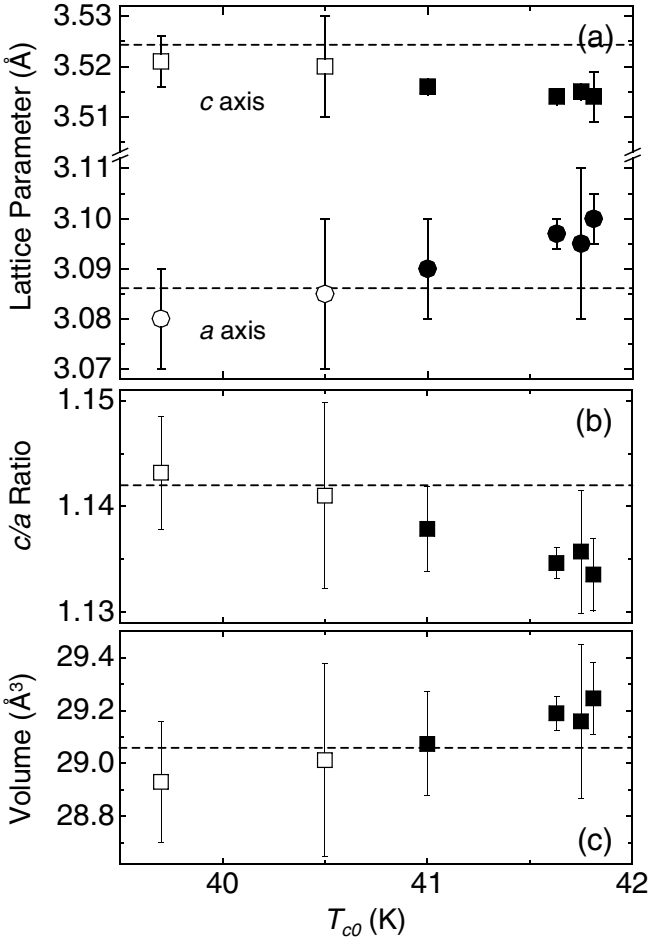

FIG. 2. (a) T_{c0} versus a-axis and c-axis lattice constants. (b) T_{c0} versus the c/a ratio. (c) T_{c0} versus the MgB_2 unit cell volume. The open symbols are for sapphire, and the solid symbols are for the SiC substrate. The error bars indicate the accuracy of the measurement. The dashed lines are the bulk values.

beyond the bulk value, and the thicker the films the larger the tensile strain.

An increase of tensile strain with film thickness has been observed in films grown in the Volmer-Weber mode: film growth by initial nucleation of discrete islands which later coalesce [17,18]. When the islands coalesce, they "zip up" because the surface energy of the islands is larger than the free energy of the grain boundaries, thus creating a tensile strain which increases with film thickness [19]. In the so-called "low-mobility" films, the height of the zipped boundary is less than the film thickness when the islands coalesce, and the "zipping up" continues at the surface terrace level long afterwards [20]. Therefore, the tensile strain continues to increase with film thickness toward the upper bound value predicted by the Nix-Clemens model [19].

Atomic force microscopy (AFM) images confirm that MgB_2 films grow in the Volmer-Weber mode. AFM images of two MgB_2 films on SiC are shown in Figs. 3(a)

(thickness 75 Å) and 3(b) (thickness 900 Å). Hexagonal-shaped MgB_2 crystallites are seen in the thinner film, which coalesce into a continuous film at larger film thickness. The continued increase of the tensile strain beyond coalescence and the surface terraces that are readily observable in thicker films indicate that MgB_2 behaves like a low-mobility system at 720 °C. This is consistent with the high melting temperature of B (2075 °C) or MgB_2 (it melts congruently at 2430 °C with pressure higher than 6.5 MPa [21]). The grain growth as the film becomes thicker may also contribute to the tensile strain [22]. This is supported by the cross-section transmission electron microscopy (TEM) images of a 2100 Å thick MgB_2 film on (0001) SiC in Fig. 3(c) (low magnification) and Fig. 3(d) (high resolution), which show that the defect density is high near the film/substrate interface and decreases as the film thickness increases.

The lattice mismatch could result in 11% compressive strain (with a 30° in-plane rotation) in MgB_2 films on sapphire ($a = 3.07$ Å) and 0.1% compressive strain on SiC ($a = 4.765$ Å). The coefficient of thermal expansion in the (0001) plane at room temperature is 5.5×10^{-6} K^{-1} for MgB_2 [23], 3.0×10^{-6} K^{-1} for SiC [24], and 6.7×10^{-6} K^{-1} for sapphire [25]. Therefore, the thermal expansion mismatch will lead to a tensile strain in films on SiC, and a compressive strain on sapphire. The combined effect of all the sources of strain results in larger tensile strain in MgB_2 films on SiC than on sapphire. It is difficult to accurately predict the maximum tensile strain attainable in MgB_2 films. A rough estimate from Eq. (1) in Ref. [19] [taking the following parameters: grain boundary energy = 0 J/cm^2, solid/vapor surface energy = 1 J/m^2, biaxial modulus of MgB_2 = 421 GPa [26], and grain size at coalescence = 1300 Å from Fig. 3(a)] indicates an upper bound value of ~0.8%, which is larger than the maximum tensile strain reported here (~ 0.55%). However, this stress estimation may be oversimplified and the films may partially relax as the thickness increases.

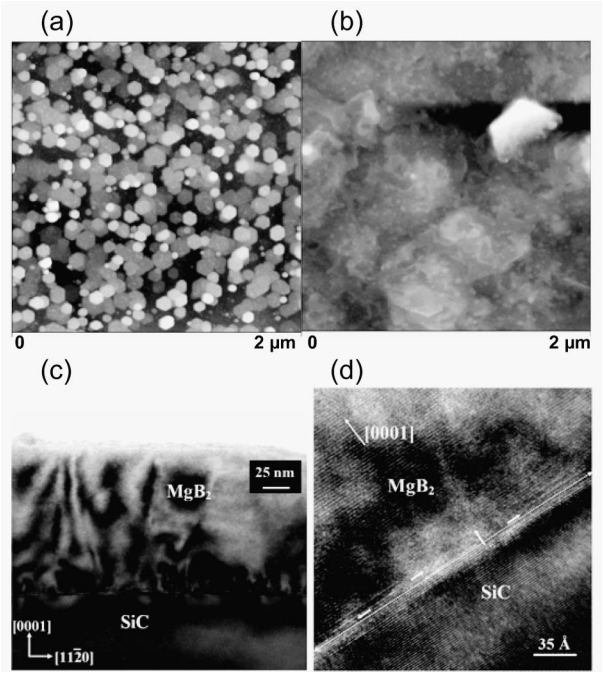

FIG. 3. AFM images of (a) a 75 Å and (b) a 900 Å thick MgB_2 films grown on (0001) SiC substrates at 720 °C. (c) Low-magnification and (d) high-resolution cross-section TEM images of a 2100 Å thick MgB_2 film on (0001) SiC taken along the [1$\bar{1}$00] direction. The dotted line in (d) indicates the MgB_2/SiC interface, and the small arrows show the lattice deformation due to dislocations.

The systematic increase of T_c with tensile strain shown in Fig. 2 has led us to search for the mechanism responsible for the rise in T_c of MgB_2 by first-principles calculations. For the highest T_c sample in Fig. 2, $\Delta a/a = +0.55\%$ and $\Delta c/c = -0.25\%$, which leads to changes $\Delta m^*/m^* = -1.2\%$ and $2\Delta|\mathcal{D}|/|\mathcal{D}| = -2.6\%$. The calculated change in the E_{2g} phonon frequency, $\Delta\omega/\omega = -5.5\%$, is in agreement with the experimentally extrapolated value [27]. From these values and using Eq. (2), we obtain

$$\frac{\Delta\lambda^{\sigma\sigma}_{E_{2g}}}{\lambda^{\sigma\sigma}_{E_{2g}}} = \frac{\Delta m^*}{m^*} + 2\frac{\Delta|\mathcal{D}|}{|\mathcal{D}|} - 2\frac{\Delta\omega}{\omega} \approx +7\%. \quad (3)$$

From Eq. (1) and using representative numbers, $\lambda = \lambda_\sigma + \lambda_\pi = 0.9 + 0.2 = 1.1$, and $\hat{\mu} = 0.2$,

$$\frac{\Delta T_c}{T_c} = \frac{\Delta\omega}{\omega} - \Delta f = -5.5\% + 10.4\% \approx +5\%. \quad (4)$$

This value is quite close to the experimental enhancement of T_c. This analysis identifies the underlying mechanism of the tensile-strain-induced increase in T_c as the decrease in the E_{2g} phonon frequency. It leads to the large (7%) increase in the σ band coupling strength, which, being leveraged in $f(\lambda, \hat{\mu})$, more than compensates the 5% lowering of the temperature/energy scale governed by ω. The result is consistent with that of Yildirim and Gülseren on the pressure effects in MgB_2 [28], although this previous work did not address biaxial strain.

The E_{2g} phonon frequencies of MgB_2 films of different thicknesses were measured by Raman scattering using a SPEX Triplemate spectrometer in backscattering geometry with the 514.5 nm Ar^+ laser excitation. Figure 4 shows the spectra of two films: a 3400 Å thick film on SiC and a 800 Å thick film on sapphire. The thicker film on SiC has larger tensile strain than the thinner film on sapphire and consequently has a higher T_{c0} as compared to the film on sapphire. The broad peak around 600 cm^{-1} has been assigned to the E_{2g} mode [27]. A clear difference between the peak energies for the two films is seen. The higher T_c film on SiC has a softer E_{2g} mode than the lower T_c film on sapphire by about 20 cm^{-1}, i.e., 3.3%.

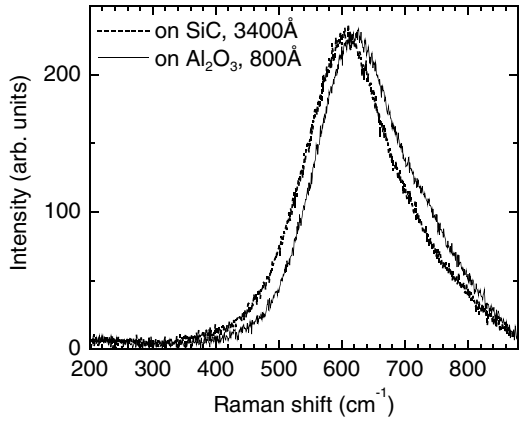

FIG. 4. Raman spectra of two MgB_2 films: 3400 Å thick on SiC and 800 Å thick on sapphire. The former shows a lower E_{2g} phonon frequency.

In conclusion, we have shown unambiguously that T_{c0} in MgB_2 films deposited by HPCVD increases with biaxial tensile strain. The highest T_{c0} obtained in the MgB_2 films, 41.8 K, is well above the bulk value. First-principles calculations show that the T_c increase is due to the softening of the bond-stretching E_{2g} phonon mode, which is confirmed by Raman scattering measurements. There have been reports that a reduced T_c in MgB_2 corresponds to a higher E_{2g} phonon frequency [27,29]. Our result is the first example that lowering the E_{2g} phonon frequency can increase T_c to above the bulk value. In this work, the T_c enhancement seems to saturate at large film thicknesses. If one could reduce the E_{2g} phonon frequency further using other techniques, the T_c of MgB_2 should be even higher than what we have shown here.

We thank Bill Nix for useful discussions on the coalescence tensile strain and E. Wertz for his help with the temperature calibration. The work is supported in part by ONR under Grants No. N00014-00-1-0294 (X. X. X.) and No. N0014-01-1-0006 (J. M. R.), by NSF under Grants No. DMR-0306746 (X. X. X. and J. M. R.), No. DMR-9876266 and No. DMR-9972973 (Q. L.), No. DMR-0103354 (G. S. and X. X. X.), No. DMR-0114818 (W. E. P.), and No. DMR-0245702 (J. C. H. S.), and by DOE under Grants No. DE-FG02-03ER46063 (G. S.) and No. DE-FG02-01ER45907 (X. X. X.).

[1] J. Nagamatsu *et al.*, Nature (London) **410**, 63 (2001).
[2] R. J. Cava, H.W. Zandbergen, and K. Inumaru, Physica (Amsterdam) **385C**, 8 (2003).
[3] J. S. Slusky *et al.*, Nature (London) **410**, 343 (2001).
[4] S. Lee *et al.*, Physica (Amsterdam) **397C**, 7 (2003).
[5] Y. Bugoslavsky *et al.*, Nature (London) **410**, 563 (2001).
[6] M. Monteverde *et al.*, Science **292**, 75 (2001).
[7] D. G. Hinks, H. Claus, and J. D. Jorgensen, Nature (London) **411**, 457 (2001).
[8] N. Hur *et al.*, Appl. Phys. Lett. **79**, 4180 (2001).
[9] A. V. Pogrebnyakov *et al.*, Appl. Phys. Lett. **82**, 4319 (2003).
[10] H. J. Choi *et al.*, Nature (London) **418**, 758 (2002).
[11] W. Pickett, Nature (London) **418**, 733 (2002).
[12] S. Souma *et al.*, Nature (London) **423**, 65 (2003).
[13] A. Y. Liu, I. I. Mazin, and J. Kortus, Phys. Rev. Lett. **87**, 087005 (2001).
[14] J. M. An and W. E. Pickett, Phys. Rev. Lett. **86**, 4366 (2001).
[15] X. H. Zeng *et al.*, Nat. Mater. **1**, 35 (2002).
[16] X. H. Zeng *et al.*, Appl. Phys. Lett. **82**, 2097 (2003).
[17] J. A. Floro *et al.*, MRS Bull. **27**, No. 1, 19 (2002).
[18] R. Koch, J. Phys. Condens. Matter **6**, 9519 (1994).
[19] W. D. Nix and B. M. Clemens, J. Mater. Res. **14**, 3467 (1999).
[20] B.W. Sheldon, K. H. A. Lau, and A. Rajamani, J. Appl. Phys. **90**, 5097 (2001).
[21] Z. K. Liu, D. G. Schlom, Q. Li, and X. X. Xi, Appl. Phys. Lett. **78**, 3678 (2001b).
[22] P. Chaudhari, J. Vac. Sci. Technol. **9**, 520 (1972).
[23] C. Buzea and T. Yamashita, Supercond. Sci. Technol. **14**, R115 (2001).
[24] Z. Li and R. Brandt, J. Am. Chem. Soc. **69**, 863 (1986).
[25] Y. S. Touloukian *et al.*, *Thermophysical Properties of Matter* (Plenum, New York, 1977), Vol. 13.
[26] V. Milman and M. C. Warren, J. Phys. Condens. Matter **13**, 5585 (2001).
[27] A. F. Goncharov and V.V. Struzhkin, Physica (Amsterdam) **385C**, 117 (2003).
[28] T. Yildirim and O. Gülseren, J. Phys. Chem. Solids **63**, 2201 (2002).
[29] T. Masui, S. Lee, and S. Tajima, Phys. Rev. B **70**, 024504 (2004).

Properties of MgB_2 thin films with carbon doping

A. V. Pogrebnyakov[a] and X. X. Xi
Department of Physics, Department of Materials Science and Engineering and Materials Research Institute, The Pennsylvania State University, University Park, Pennsylvania 16802

J. M. Redwing, V. Vaithyanathan, D. G. Schlom, and A. Soukiassian
Department of Materials Science and Engineering and Materials Research Institute, The Pennsylvania State University, University Park, Pennsylvania 16802

S. B. Mi and C. L. Jia
Institut für Festkörperforschung, Forschungszentrum Jülich GmbH, D-52425 Jülich, Germany

J. E. Giencke and C. B. Eom
Department of Materials Science and Engineering and Applied Superconductivity Center, University of Wisconsin, Madison, Wisconsin 53706

J. Chen, Y. F. Hu, Y. Cui, and Qi Li
Department of Physics and Materials Research Institute, The Pennsylvania State University, University Park, Pennsylvania 16802

(Received 29 March 2004; accepted 15 June 2004)

We have studied structural and superconducting properties of MgB_2 thin films doped with carbon during the hybrid physical-chemical vapor deposition process. A carbon-containing precursor metalorganic bis(methylcyclopentadienyl)magnesium was added to the carrier gas to achieve carbon doping. As the amount of carbon in the film increases, the resistivity increases, T_c decreases, and the upper critical field increases dramatically as compared to clean films. The self-field J_c in the carbon doped film is lower than that in the clean film, but J_c remains relatively high to much higher magnetic fields, indicating stronger pinning. Structurally, the doped films are textured with columnar nano-grains and highly resistive amorphous areas at the grain boundaries. The carbon doping approach can be used to produce MgB_2 materials for high magnetic-field applications. © *2004 American Institute of Physics*. [DOI: 10.1063/1.1782258]

The 39 K superconductor MgB_2[1] has attracted tremendous interest for its potential in high magnetic-field applications. In particular, high critical current density J_c near the depairing limit has been observed in MgB_2,[2] and unlike high temperature superconductors grain boundaries in MgB_2 do not behave like weak links.[3] Although clean MgB_2 shows low upper critical field H_{c2},[4] in high resistivity MgB_2 films H_{c2} is substantially higher;[5] the critical current density J_c in clean MgB_2 is suppressed quickly by magnetic field,[6] but defects and impurities have been shown to enhance pinning.[7,8] Recently, we have developed a hybrid physical-chemical vapor deposition (HPCVD) technique which produces *in situ* epitaxial MgB_2 films with T_c above 40 K.[10] Because of the highly reducing H_2 ambient and the high purity B_2H_6 source used in the HPCVD process, the technique produces very clean MgB_2 thin films. In this letter, we describe the properties of HPCVD MgB_2 films doped with carbon. The H_{c2} values in these "dirtier" films are significantly higher and the vortex pinning is significantly stronger than those in the clean films.

In situ epitaxial growth of MgB_2 films by HPCVD has been described in detail previously.[9] For carbon doping, we added bis(methylcyclopentadienyl)magnesium [$(MeCp)_2Mg$], a metalorganic magnesium precursor, to the carrier gas of 300 sccm hydrogen at 100 Torr. The flow of the boron precursor gas, 1000 ppm diborane (B_2H_6) in H_2, was kept at 150 sccm. A secondary hydrogen flow was passed through the $(MeCp)_2Mg$ bubbler which was held at 760 Torr and 21.6 °C to transport $(MeCp)_2Mg$ to the reactor. The amount of carbon doping depends on the secondary hydrogen flow rate through the $(MeCp)_2Mg$ bubbler, which was varied between 25 and 200 sccm to vary the flow rate of $(MeCp)_2Mg$ into the reactor from 0.0065 to 0.052 sccm. The chemical compositions of a series of films were determined by wavelength dispersive x-ray spectroscopy to establish a correlation between the carbon concentrations in the films and the hydrogen flow rates through the $(MeCp)_2Mg$ bubbler. The nominal atomic concentrations determined by this approach are used as the carbon concentrations presented in this letter. The films were deposited on (001) 4H–SiC substrates at 720 °C. The thickness of the films was around 2000 Å.

The resistivity (in log scale) versus temperature curves for MgB_2 films with different carbon doping levels are shown in Fig. 1(a). The carbon doping causes a dramatic increase in the resistivity, whereas the T_c of the film is suppressed much more slowly. For example, with a carbon concentration of 24 at. %, the residual resistivity increases from the undoped value of less than 1 $\mu\Omega$ cm to $\sim$200 $\mu\Omega$ cm, but T_c only decreases from over 41 to 35 K. The dependencies of residual resistivity and T_c on the carbon concentration in the doped MgB_2 films are plotted in Fig. 1(b). T_c is suppressed to below 4.2 K at a nominal carbon concentration of 42 at. % when the residual resistivity is 440 mΩ cm. This is very different from those in carbon-doped single crystals, where T_c is suppressed to 2.5 K at a residual resistivity of 50 $\mu\Omega$ cm when 12.5 at. % of carbon is doped into MgB_2.[11] This discrepancy indicates that only a small portion of the carbon in the films is doped into the MgB_2 structure and the

[a]Electronic mail: avp11@psu.edu

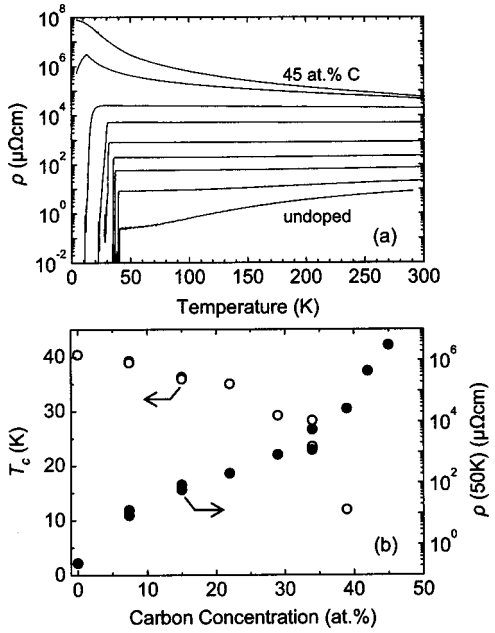

FIG. 1. (a) Resistivity vs temperature curves for MgB_2 films of different carbon doping. (b) Residual resistivity (closed circles) and T_c (open circles) as a function of carbon concentration for films plotted in (a). In (a), from bottom to top, the nominal carbon concentrations of the curves are 0, 7.4, 15, 22, 29, 34, 39, 42, and 45 at. %.

rest most likely forms high resistance grain boundaries giving rise to poor connectivity of the $Mg(B_{1-x}C_x)_2$ grains.[12]

The granular structure of the carbon-doped MgB_2 films is confirmed by TEM. Figure 2(a) is a cross-sectional TEM image of a film with 22 at. % nominal carbon concentration taken along the $[\bar{1}10]$ direction of the substrate. It shows that the film consists of columnar nano-grains (the contrast changes laterally, but not vertically) of $Mg(B_{1-x}C_x)_2$ with a preferential *c*-axis orientation. The selected area electron diffraction pattern taken from the MgB_2/SiC interface area in Fig. 2(b) shows two types of features, diffraction spots and arcs. The spots belong to the single crystal SiC substrate (SC) and the arcs to the MgB_2 film (MB). The arcs consist of many fine spots originating from individual columnar grains which show a deviation of their *c* axis from the film normal.

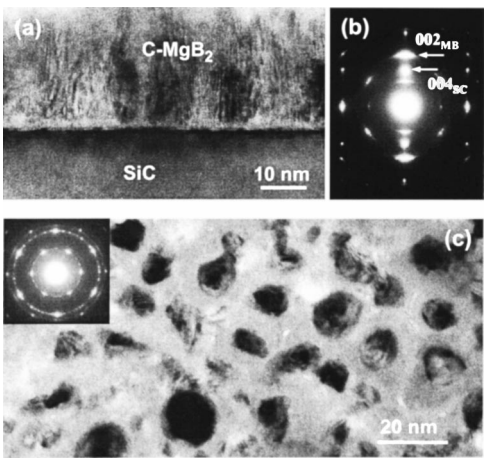

FIG. 2. TEM results of a film with 22 at. % nominal carbon concentration. (a) Cross-sectional image taken along the $[\bar{1}10]$ direction of the substrate. (b) Selected area electron diffraction taken from the MgB_2/SiC interface area. (c) Planar-view image showing nano-grains of carbon doped MgB_2 and an amorphous phase between the grains. The insert is the select area electron diffraction pattern taken along the film normal.

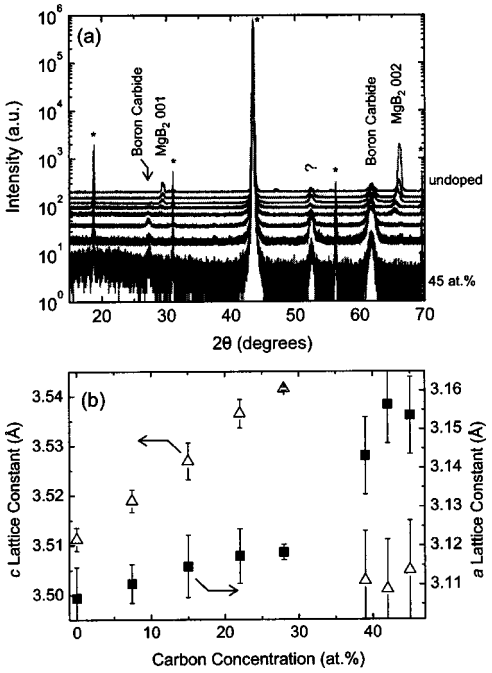

FIG. 3. (a) X-ray diffraction θ–2θ scans for MgB_2 films with carbon doping. From top to bottom, the nominal carbon concentrations are 0, 7.4, 15, 22, 28, 39, 42, and 45 at. %. The spectra are shifted vertically for clarity. The peaks labeled with an asterisk are due to the SiC substrate peaks. (c) The *c*-axis lattice constant (open triangles) and *a*-axis lattice constant (closed squares) of the carbon doped MgB_2 films as a function of nominal carbon concentration.

In the planar-view image in Fig. 2(c), the change of contrast indicates an equiaxial in-plane morphology of the columnar grains, and an amorphous phase is also observed between the grains. We were not able to determine the composition of the amorphous areas, but it is most likely that the large portion of carbon that is not doped into MgB_2 is contained in these areas. The insert in Fig. 2(c) is a typical diffraction pattern taken along the film normal. The strong hexagonal-distributed spots show that the hexagonal-on-hexagonal in-plane relationship between the columnar grains and SiC dominates, while the diffraction rings reveal grains that are randomly in-plane oriented.

Figure 3(a) shows θ–2θ scans of an undoped MgB_2 film and films doped with different amounts of carbon. Compared to the undoped films, the MgB_2 00*l* peaks are suppressed as carbon concentration increases, and dramatically when the carbon concentration is above ~30 at. %. Meanwhile, as shown in Fig. 3(b), both the *c* and *a* axes expand until about 30 at. %, above which the *c* lattice constant decreases and the *a* lattice constant increases dramatically. This behavior is different from that in carbon-doped single crystals, where the *a* axis lattice constant decreases but that of *c* axis remains almost constant for all the carbon concentration.[11] The peak marked by "?" is likely 101 MgB_2, the most intense diffraction peak of MgB_2. It becomes stronger as the carbon concentration increases, indicating an increased presence of randomly oriented MgB_2. The peaks marked by "boron carbide," according to extensive pole figure analysis, are most likely due to B_4C, B_8C, or $B_{13}C_2$. Their intensities also increase with carbon concentration. From the TEM and x-ray diffraction results, we conclude that below about 30 at. %, a small portion of carbon is doped into the $Mg(B_{1-x}C_x)_2$ columnar, *c*-axis-oriented nano-grains, and the rest goes into the grain boundaries consisting of highly resistive amor-

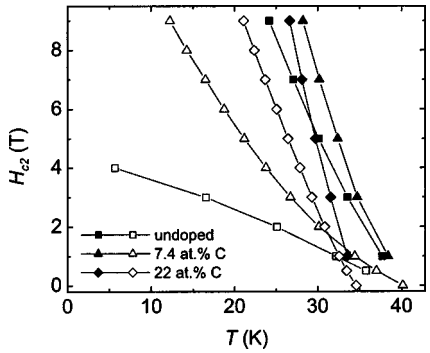

FIG. 4. Upper critical field as a function of temperature for an undoped film and two doped films with 7.4 at. % and 22 at. % nominal carbon concentrations, respectively. The closed symbols are for parallel field ($H_{c2}^{\parallel}$) and the open symbols are for perpendicular field ($H_{c2}^{\perp}$).

phous phases or boron carbides. Above about 30 at. %, the $Mg(B_{1-x}C_x)_2$ nano-grains are completely separated from each other by highly resistive phases, become more randomly oriented, and their lattice constants relax. This is consistent with the result in Fig. 1(b).

The upper critical field H_{c2} was measured using a Quantum Design PPMS system with a 9 T superconducting magnet. Figure 4 shows the results for an undoped, 7.4 at. %, and 22 at. % carbon doped films. The value of H_{c2} is defined by 50% of the normal-state resistance $R(H_{c2})=0.5R(T_c)$. It can be clearly seen that carbon doping changes the downward curvature in $H_{c2}^{\perp}(T)$ for the undoped film to an upward curvature in the carbon doped films. Both the slope, dH_{c2}/dT, near T_c and the low temperature H_{c2} increase with carbon concentration. In high magnetic field measurements, Braccini *et al.* have shown that carbon-doped MgB_2 films as described here have extraordinary $H_{c2}(0)$ values as high as 70 T.[13] The transport $J_c(H)$ at different temperatures, determined by a 1 μV criterion from 20–50 μm bridges, for an undoped and a carbon doped MgB_2 film are shown in Fig. 5.

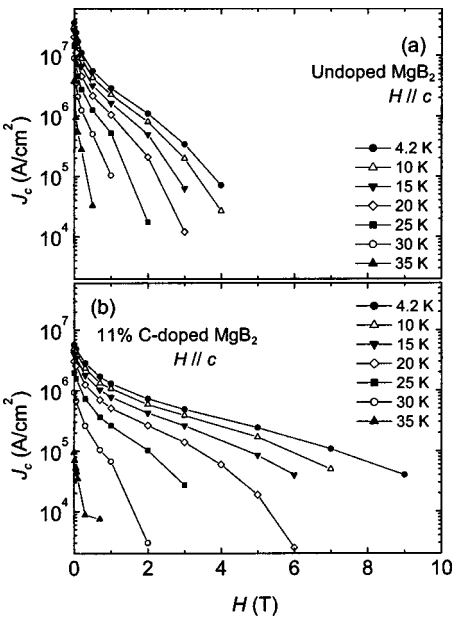

FIG. 5. Critical current density as a function of magnetic field ($\mathbf{H} \| c$) and temperature for (a) an undoped film and (b) a film doped with with 11 at. % nominal carbon concentration.

While the undoped film has high self-field critical current densities, they are suppressed quickly by magnetic field due to the weak pinning. For the film doped with 11 at. % nominal carbon concentration, J_c values are relatively high in much higher magnetic fields. This indicates a significantly enhanced vortex pinning in carbon doped MgB_2 films.

In conclusion, MgB_2 thin films were doped with carbon by adding bis(cyclopentadienyl)magnesium to the carrier gas during the HPCVD process. The residual resistivity increases rapidly while T_c decreases much more slowly with carbon doping. Structural analyses show that only part of the carbon is doped into the MgB_2 lattice and the rest forms highly resistive foreign phases in the grain boundaries. $H_{c2}(T)$ and its slope near T_c increase dramatically as compared to the clean films, which is consistent with the multiband superconductor model of Gurevich and indicates a dirtier π band upon carbon doping.[14] The critical current density in magnetic field increases markedly from that in the clean film due to stronger vortex pinning.

The work is supported in part by ONR under grant Nos. N00014-00-1-0294 (X.X.X.) and N0014-01-1-0006 (J.M.R.), by NSF under grant Nos. DMR-0306746 (X.X.X. and J.M.R.), DMR-9876266 and DMR-9972973 (Q.L.), and through the MRSEC for Nanostructure Materials (C.B.E.), and by DOE under grant No. DE-FG02-03ER46063 (D.G.S.).

[1] J. Nagamatsu, N. Nakagawa, T. Muranaka, Y. Zenitani, and J. Akimitsu, Nature (London) **410**, 63 (2001).
[2] S. Y. Xu, Q. Li, E. Wertz, Y. F. Hu, A. V. Pogrebnyakov, X. H. Zeng, X. X. Xi, and J. M. Redwing, Phys. Rev. B **68**, 224501 (2003).
[3] D. C. Larbalestier, L. D. Cooley, M. O. Rikel, A. A. Polyanskii, J. Jiang, S. Patnaik, X. Y. Cai, D. M. Feldmann, A. Gurevich, A. A. Squitieri, M. T. Naus, C. B. Eom, E. E. Hellstrom, R. J. Cava, K. A. Regan, N. Rogado, M. A. Hayward, T. He, J. S. Slusky, P. Khalifah, K. Inumaru, and M. Haas, Nature (London) **410**, 186 (2001).
[4] P. C. Canfield and G. Crabtree, Phys. Today **56**, 34 (2003).
[5] A. Gurevich, S. Patnaik, V. Braccini, K. H. Kim, C. Mielke, X. Song, L. D. Cooley, S. D. Bu, D. M. Kim, J. H. Choi, L. J. Belenky, J. Giencke, M. K. Lee, W. Tian, X. Pan, A. Siri, E. E. Hellstrom, C. B. Eom, and D. Larbalestier, Supercond. Sci. Technol. **17**, 278 (2004).
[6] X. H. Zeng, A. V. Pogrebnyakov, M. H. Zhu, J. E. Jones, X. X. Xi, S. Y. Xu, E. Wertz, Q. Li, J. M. Redwing, J. Lettieri, V. Vaithyanathan, D. G. Schlom, Z. K. Liu, O. Trithaveesak, and J. Schubert, Appl. Phys. Lett. **82**, 2097 (2003).
[7] Y. Bugoslavsky, G. K. Perkins, X. Qi, L. F. Cohen, and A. D. Caplin, Nature (London) **410**, 563 (2001).
[8] C. B. Eom, M. K. Lee, J. H. Choi, L. Belenky, X. Song, L. D. Cooley, M. T. Naus, S. Patnaik, J. Jiang, M. O. Rikel, A. A. Polyanskii, A. Gurevich, X. Y. Cai, S. D. Bu, S. E. Babcock, E. E. Héllstrom, D. C. Larbalestier, N. Rogado, K. A. Regan, M. A. Hayward, T. He, J. S. Slusky, K. Inumaru, M. Haas, and R. J. Cava, Nature (London) **411**, 558 (2001).
[9] X. H. Zeng, A. V. Pogrebnyakov, A. Kotcharov, J. E. Jones, X. X. Xi, E. M. Lysczek, J. M. Redwing, S. Y. Xu, Q. Li, J. Lettieri, D. G. Schlom, W. Tian, X. Q. Pan, and Z. K. Liu, Nat. Mater. **1**, 35 (2002).
[10] A. V. Pogrebnyakov, J. M. Redwing, J. E. Jones, X. X. Xi, S. Y. Xu, Q. Li, V. Vaithyanathan, and D. G. Schlom, Appl. Phys. Lett. **82**, 4319 (2003).
[11] S. Lee, T. Masui, A. Yamamoto, H. Uchiyama, and S. Tajima, Physica C **397**, 7 (2003).
[12] J. Rowell, Supercond. Sci. Technol. **16**, R17 (2003).
[13] V. Braccini, A. Gurevich, J. Giencke, M. Jewell, C. Eom, D. Larbalestier, A. Pogrebnyakov, Y. Cui, B. T. Liu, Y. F. Hu, J. M. Redwing, Q. Li, X. X. Xi, R. Singh, R. Gandikota, J. Kim, B. Wilkens, N. Newmann, J. Rowell, B. Moeckly, V. Ferrando, C. Tarantini, D. Marr, M. Putti, C. Ferdeghini, R. Vaglio, and E. Haanappel (unpublished).
[14] A. Gurevich, Phys. Rev. B **67**, 184515 (2003).

Absence of low-temperature phase transitions in epitaxial $BaTiO_3$ thin films

D. A. Tenne,[1,*] X. X. Xi,[1,2,3] Y. L. Li,[2] L. Q. Chen,[2,3] A. Soukiassian,[2] M. H. Zhu,[1,†] A. R. James,[1,‡] J. Lettieri,[2] D. G. Schlom,[2,3] W. Tian,[4] and X. Q. Pan[4]

[1]*Department of Physics, the Pennsylvania State University, University Park, Pennsylvania 16802, USA*

[2]*Department of Materials Science and Engineering, the Pennsylvania State University, University Park, Pennsylvania 16802, USA*

[3]*Materials Research Institute, the Pennsylvania State University, University Park, Pennsylvania 16802, USA*

[4]*Department of Materials Science and Engineering, the University of Michigan, Ann Arbor, Michigan 48109, USA*

(Received 14 January 2004; published 3 May 2004)

We have studied phase transitions in epitaxial $BaTiO_3$ thin films by Raman spectroscopy. The films are found to remain in a single ferroelectric phase over the temperature range from 5 to 325 K. The low-temperature phase transitions characteristic of bulk $BaTiO_3$ (tetragonal-orthorhombic-rhombohedral) are absent in the films. X-ray diffraction shows that the $BaTiO_3$ films are under tensile strain due to the thermal expansion mismatch with the buffer layer. A phase-field calculation of the phase diagram and domain structures in $BaTiO_3$ thin films predicts, without any *priori* assumption, that an orthorhombic phase with in-plane polarization is the thermodynamically stable phase for such values of tensile strain and temperature, consistent with the experimental Raman results.

DOI: 10.1103/PhysRevB.69.174101 PACS number(s): 77.84.Dy, 77.55.+f, 78.30.Hv, 63.70.+h

I. INTRODUCTION

Phase transitions in thin film ferroelectrics, which differ substantially from those in corresponding bulk materials, are of significant scientific and technological interest.[1,2] Much effort has been devoted in recent years to the thermodynamics of domain structures and phase diagrams in ferroelectric thin films.[3–6] Different approaches have been employed by various groups. For example, Pertsev *et al.*[5] predicted a number of domain stability maps for $BaTiO_3$ and $PbTiO_3$ using thermodynamic calculations whereas Li *et al.*[6] proposed a phase-field model to predict the dependence of domain structures on temperature and strain. Experimentally, enhancement of the paraelectric-ferroelectric phase transition temperature, T_c, by strain has been reported in epitaxial ferroelectric films.[7–10] Recently, Streiffer *et al.* observed nanoscale 180° stripe domains in ferroelectric $PbTiO_3$ thin films.[11] Strain-induced ferroelectricity in $SrTiO_3$ thin films has been reported by Fuchs *et al.*[12] and Tikhomirov *et al.*[13] In this paper, we present a Raman scattering study of $BaTiO_3$ films in the temperature range 5–320 K, which shows that the tetragonal-orthorhombic and orthorhombic-rhombohedral phase transitions characteristic for the bulk $BaTiO_3$ disappear completely in the thin films. Detailed structural characterizations of the films suggest that a tensile strain locks the films in a single ferroelectric phase. A comparison with the phase-field model calculation confirms that the orthorhombic phase with in-plane polarization is the stable phase in this strain and temperature range.

In bulk $BaTiO_3$, the crystal structure changes from cubic to tetragonal at 403 K, then to orthorhombic at 278 K, and to rhombohedral at 183 K.[14] The cubic phase is paraelectric and the other phases are ferroelectric. Raman spectroscopy is a powerful tool to study phase transitions as the structural changes alter the vibrational spectra. Lattice dynamics and Raman spectra of single crystal and polycrystalline $BaTiO_3$ have been studied in detail.[15–22] Raman studies of thin $BaTiO_3$ films[23] have mostly focused on the ferroelectric phase transition from cubic to tetragonal phase above room temperature. In the present paper we focus on the temperature range 5–325 K.

II. EXPERIMENTAL RESULTS

The $BaTiO_3$ films studied in this work were grown by pulsed laser deposition on $(001)SrTiO_3$ and $(001)LaAlO_3$ substrates. Between the substrate and $BaTiO_3$ film a 0.3 μm thick conducting layer of $SrRuO_3$ was deposited to screen Raman signal from the substrate.[24] The thickness of the $BaTiO_3$ films was 1 μm. The deposition conditions of the $BaTiO_3$ and $SrRuO_3$ layers were the same as those described previously.[25] Both layers were deposited at the substrate temperature of 750 °C. The structural properties of the $BaTiO_3/SrRuO_3$ samples were characterized by x-ray diffraction and transmission electron microscopy (TEM). $BaTiO_3$ single crystal was obtained from MTI Corp. (Richmond, CA). Raman spectra were recorded using a SPEX Triplemate spectrometer equipped with a liquid-nitrogen-cooled multichannel coupled-charge-device detector. The 514.5 nm line of an Ar^+ laser was used for excitation, and the laser power density was kept at a low level ($\lesssim$30 W/cm^2) to avoid heating of the sample. Raman spectra from the films were measured in backscattering geometry both in parallel $z(x,x)\bar{z}$ and perpendicular $z(x,y)\bar{z}$ polarization configurations (z direction is normal to the film plane). The measurements in the crystal were in backscattering geometries both along the c axis of the initial tetragonal phase [$z(x,x)\bar{z}$ and $z(x,y)\bar{z}$ geometries] and perpendicular to it [$x(z,z)\bar{x}$ and $x(z,y)\bar{x}$ geometries].

Figure 1 shows Raman spectra of (a) a $BaTiO_3$ single crystal and (b) a $BaTiO_3$ film grown on a $SrTiO_3$ substrate, both measured in the parallel polarization configuration, as a function of temperature. The spectra of the single crystal show clear changes attributed to the phase transitions. At low temperatures, in the rhombohedral phase, the most intensive

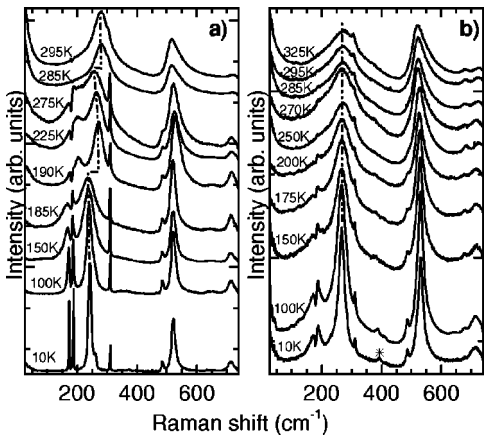

FIG. 1. Temperature evolution of Raman spectra of (a) a $BaTiO_3$ single crystal and (b) a $BaTiO_3$ film grown on $SrTiO_3$ substrate with a $SrRuO_3$ buffer layer, measured in parallel polarization geometry $z(x,x)\bar{z}$. Dashed-dotted lines are guides to eye. Star in the spectra of the film indicates features due to $SrRuO_3$ layer

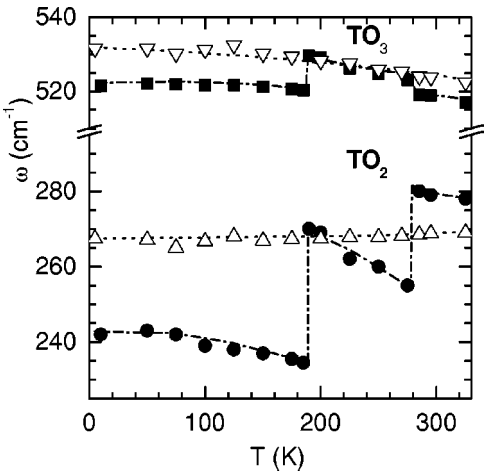

FIG. 2. Temperature dependence of the A_1 (TO_2) and A_1 (TO_3) phonon frequencies for $BaTiO_3$ single crystal (solid symbols) and film grown on $SrTiO_3$ substrate with $SrRuO_3$ buffer layer (open symbols).

lines observed in the polarized Raman spectrum are at 173, 187, 242, 485, 522, and 714 cm^{-1}, and are attributed to TO_1, LO_1, TO_2, LO_2, TO_3, LO_3 modes of A_1 symmetry, respectively.[20] The peak at 310 cm^{-1} is due to mixed LO_2–TO_3 phonon of E symmetry.[20] The shoulder at 261 cm^{-1} was shown by micro-Raman experiments to be due to the near-domain-wall regions of $BaTiO_3$ crystal.[22] When the $BaTiO_3$ crystal was warmed to ~185 K, the Raman spectra went through large changes, most noticeable in the frequency range 150–300 cm^{-1}. Sudden jumps to a higher frequency, as large as 35 cm^{-1} took place for the A_1 (TO_2) phonon line. A less dramatic, but still well pronounced jump (~10 cm^{-1}) occurred for the A_1 (TO_3) line. These changes are indicative of the rhombohedral-orthorhombic phase transition. When the crystal was heated further to ~280 K, another sudden jumps of the A_1 TO_2 and TO_3 phonon frequencies (25 and 4 cm^{-1}, respectively) and changes in the Raman spectra occurred, which indicates the orthorhombic-tetragonal phase transition. The observed frequency shifts are well detectable in Raman spectra despite large linewidths TO_2 and TO_3 phonons, and are in agreement with the reported results for $BaTiO_3$ crystals.[15,21,22]

The temperature dependence of the Raman spectra of the $BaTiO_3$ film, shown in Fig. 1(b), is markedly different from that of the single crystal. It does not show sharp changes in the temperature range of 5–300 K. When temperature increases, the phonon lines broaden, but their frequencies are either almost constant (TO_2) or change only very slightly and gradually (TO_3). The two intensive sharp lines observed at 173 and 187 cm^{-1} at low temperatures (rhombohedral phase) in the $BaTiO_3$ crystal are broader and their relative intensity is much smaller in the films at all temperatures measured. In fact, the positions, relative intensities and line shapes of phonon modes in the spectra of the films are similar to those of the orthorhombic phase of the single crystal.

The low-frequency range of Raman spectra (below 100 cm^{-1}) both in the crystals and thin films contains a feature of overdamped soft mode characteristic for $BaTiO_3$.[16–18] The heavy overdamping of the soft mode in $BaTiO_3$ has been attributed to the order-disorder character of the phase transitions.[26] In the crystal overdamping is observed in the orthorhombic and tetragonal phases and increases with temperature, in agreement with earlier reported results.[17,18] In thin films overdamping has also been observed to increase with temperature. However, no qualitative difference has been observed in the low-frequency Raman spectra of the films, as well as the crystals in the orthorhombic and tetragonal phases; there are no sharp changes in the overdamping behavior which would indicate the O-T phase transitions. Therefore, the behavior of the overdamped soft mode cannot be used to determine the phase transition temperature. So we focus on two hard phonon modes, TO_2 and TO_3, which exhibit most noticeable changes upon the rhombohedral-orthorhombic and orthorhombic-tetragonal phase transitions in $BaTiO_3$ crystals.

The temperature dependence of the frequencies of the A_1 (TO_2) and A_1 (TO_3) phonon modes for both the crystal and film shown in Fig. 2 clearly demonstrates the difference between the crystal and film behavior. Large jumps in the A_1 (TO_2) phonon frequency are clearly seen in the crystal, but it is constant in the film. The A_1 (TO_3) phonon frequency shows smaller jumps in the crystal, whereas no such jumps are visible in the film. This behavior indicates that the $BaTiO_3$ film does not undergo any phase transition in the temperature range 5–325 K. The same behavior was observed for films grown both on $SrTiO_3$ and $LaAlO_3$ substrates. The tetragonal-orthorhombic and orthorhombic-rhombohedral phase transitions of the bulk $BaTiO_3$ are completely absent in the thin films.

A quantitative determination of film strain is critical for the understanding of the complete disappearance of the low-temperature phase transitions. Figure 3 shows the x-ray diffraction results for a $BaTiO_3/SrRuO_3$ film on $LaAlO_3$ substrate. The θ-2θ scan [Fig. 3(a)] shows that both the $BaTiO_3$ and $SrRuO_3$ layers grow with c axis normal to the substrate. The full width at half maximum (FWHM) values in 2θ are

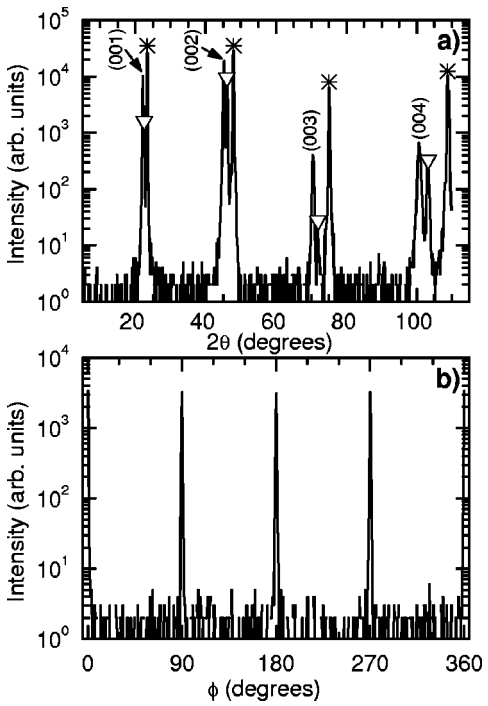

FIG. 3. X-ray diffraction patterns of $BaTiO_3/SrRuO_3$ film on $LaAlO_3$ substrate: (a) θ–2θ scan; $LaAlO_3$ and $SrRuO_3$ peaks are marked by stars and down triangles, respectively. (b) ϕ scan of the $BaTiO_3$ 202 peak; $\phi=0°$ is aligned to be parallel to the [100] in-plane direction of the $LaAlO_3$ substrate.

small (0.48° for the 003 peak). The ϕ scan of the $BaTiO_3$ 202 peak [Fig. 3(b)] shows that the layers are also in-plane aligned with the substrate lattice with [100] $BaTiO_3$‖[100] $SrRuO_3$‖[100] $LaAlO_3$. The FWHM value for the 202 peak is 0.8°. From these scans, the lattice parameters of $SrRuO_3$ buffer layers are determined to be $a=3.93$ Å for the pseudocubic lattice, equal to the bulk values. For $BaTiO_3$ films the measured lattice constants are $a=b=4.01\pm0.01$ Å (in plane), and $c=4.004\pm0.001$ Å. Similar x-ray diffraction data were obtained for films grown on $SrTiO_3$ substrates, with the same epitaxial orientation, the same $SrRuO_3$ and $BaTiO_3$ lattice constants, and even smaller FWHM values (0.38° for 003 and 0.7° for 202 peaks).

TEM studies showed that the films consist of columnar grains with in-plane grain size of ~100 nm. Electron diffraction results indicated the $BaTiO_3$ grains are oriented in same direction and confirmed the epitaxial relationship between the substrate, $SrRuO_3$ and $BaTiO_3$ layers described above. High crystalline quality of the films allows to presume the structural defects are unlikely to cause so drastic changes in the phase transition behavior. Although we cannot completely exclude other factors which can affect the film properties, such as composition fluctuations or grain size effect, we believe the strain in the thin films is the most probable cause of suppressing the low-temperature phase transitions characteristic for bulk $BaTiO_3$.

From the material parameters of $BaTiO_3$, the same as used by Koukhar *et al.* in Ref. 5, we calculated the lattice constants of the unstrained $BaTiO_3$ film to be $a_0=3.987$ Å and $c_0=4.031$ Å, slightly different from those in the bulk $BaTiO_3$. Then from the measured lattice constants of our $BaTiO_3$ films the strain in the thin film $(a-a_0)/a_0$ is calculated to be a tensile strain of 0.58%. Although the lattice constants of both $LaAlO_3$ and $SrTiO_3$ substrates and of $SrRuO_3$ buffer layer are smaller than that of $BaTiO_3$, the misfit strain in our $BaTiO_3$ film is fully relaxed at the growth temperatures because the film thickness far exceeds the critical thickness for strain relaxation. The tensile strain arises from the mismatch between the thermal expansions of $SrRuO_3$ and $BaTiO_3$. The thermal expansion coefficient of $SrRuO_3$ (Ref. 27) is smaller than that of $BaTiO_3$.[28] Consequently, when a $BaTiO_3$ film is cooled to room temperature after the deposition, it contracts more than the $SrRuO_3$ buffer layer and a tensile stress is imposed on it. It is difficult to calculate the strain between 5–300 K because the thermal expansion coefficients of $SrRuO_3$ and $BaTiO_3$ are temperature dependent. It is, however, expected to increase when the temperature is lowered, which is schematically indicated by the dotted line in Fig. 4. The end point at 5 K (0.78%) was estimated by assuming the average thermal mismatch between $SrRuO_3$ and $BaTiO_3$ to be temperature independent.

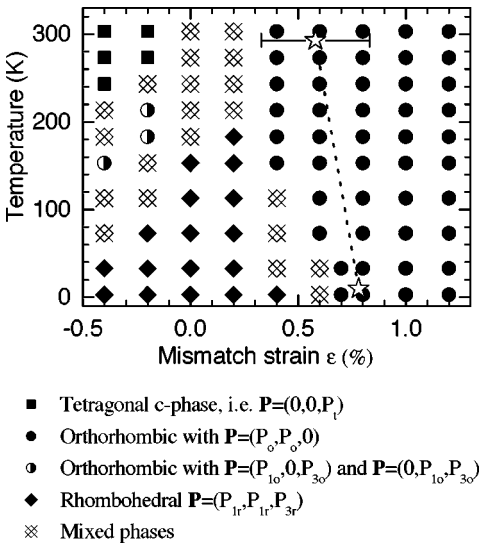

FIG. 4. Domain stability map for $BaTiO_3$ films under biaxial strain. The stars indicate the strain at room temperature, determined from x-ray data, and estimated strain at 5 K.

III. PHASE-FIELD MODELING AND DOMAIN STABILITY MAP

We compare the film strain with the calculated phase diagram of $BaTiO_3$ films under biaxial substrate constraint and over the temperature range from room temperature to 0 K. The widely quoted phase diagram of Pertsev *et al.*[5] assumes a simple domain structure with a particular domain wall orientation as *a priori* for the thermodynamic calculations. As a matter of fact, for $BaTiO_3$ films, three different domain stability maps have been presented, which depend on the assumptions of possible domain states and domain-wall orientations.[5] In this work, we used a phase-field approach in which no *priori* assumption on the occurrence of certain

phases and domain structures is made.[6] A brief description of the technique is as follows.

A ferroelectric domain structure is represented by the spatial distribution of the polarization field $\mathbf{P}=(P_1,P_2,P_3)$, and its temporal evolution is described by the time dependent Ginzburg-Landau (TDGL) equations,

$$\frac{\partial P_i(\mathbf{x},t)}{\partial t}=-L\frac{\delta F}{\delta P_i(\mathbf{x},t)} \quad (i=1,2,3), \tag{1}$$

where L is the kinetic coefficient related to the domain-wall mobility, and F is the total free energy of the system. $\mathbf{x}=(x_1,x_2,x_3)$ is a rectangular coordinate system and x_3 is normal to the film-substrate interface. The total free energy of the system includes the bulk free energy, the domain wall energy, and the elastic energy. The TDGL equation (1) was solved numerically using the semi-implicit Fourier-spectral method[29] for the time-stepping and spatial discretization. The macroscopic constraint of the substrate to the film is measured by the average strain $\bar{\epsilon}_{11}=\bar{\epsilon}_{22}=\epsilon$ and $\bar{\epsilon}_{12}=0$. The continuities of the deformation and stresses on film-substrate interface provide the local/microscopic constraint. By evolving Eq. (1) from an initial paraelectric state with small random perturbation, the thermodynamically stable domain structure and phase at given temperature and substrate constraint strain were obtained at the end of a simulation.

The results of the phase-field calculation for $BaTiO_3$ films are plotted in a phase diagram (domain stability map) shown in Fig. 4. The phases represented by various symbols are: solid squares—the tetragonal phases with polarization normal to the film/substrate interface, i.e., $\mathbf{P}=(0,0,\pm P_t)$; solid diamonds—the distorted rhombohedral phase with $\mathbf{P}=(\pm P_{1r},\pm P_{1r},\pm P_{3r})$; solid circles—the orthorhombic phase with polarization parallel to the film/substrate interface, i.e., $\mathbf{P}=(\pm P_o,\pm P_o,0)$; and half-solid circles—the distorted orthorhombic phase with $\mathbf{P}=(\pm P_{1o},0,\pm P_{3o})$ or $\mathbf{P}=(0,\pm P_{1o},\pm P_{3o})$. There are small regions, represented by crossed diamonds, within which more than one ferroelectric phases coexist. From this domain map, it is seen that a tensile strain of 0.58% places a $BaTiO_3$ film in the orthorhombic phase at room temperature. It should be noted that the uncertainty in the in-plane lattice parameter determined prom x-ray data (0.01 Å) produces rather large uncertainty in the value of strain (shown by error bars on Fig. 4). Therefore, we cannot absolutely rule out the possibility of existing mixed phases in the films at room temperature, if the lower uncertainty limit is taken into account. In the case of mixed orthorhombic-tetragonal phases there would be 90° domain walls at the boundaries between the orthorhombic phase with in-plane polarization and tetragonal phase polarized along *c* axis. However, the TEM images of our films showed the existence of many antiphase boundaries, but no 90° domains were found. Therefore, the films are most likely to be in the orthorhombic phase with in-plane polarization. This is confirmed by the Raman spectroscopy results (Figs. 1 and 2) as the form of the spectra, the phonon line positions and relative intensities in the $BaTiO_3$ film are close to those of the orthorhombic phase of $BaTiO_3$ single crystal. Because the tensile strain in the film increases when the temperature decreases from room temperature to 5 K, as schematically shown by the dotted line in Fig. 4, the film remains in the orthorhombic phase without undergoing any phase transitions.

IV. CONCLUSION

In summary, Raman spectroscopy in $BaTiO_3$ films grown by pulsed laser deposition on $SrTiO_3$ and $LaAlO_3$ substrates covered by $SrRuO_3$ buffer layers in the temperature range 5–325 K shows that the phase transitions between the different ferroelectric phases (tetragonal-orthorhombic-rhombohedral), characteristic of bulk $BaTiO_3$, are completely absent in the films. This behavior is explained by the presence of tensile strain in the $BaTiO_3$ film caused by thermal mismatch with the underlying $SrRuO_3$ layer. This is confirmed by a thin film phase diagram obtained from a phase-field calculation, which predicts, without any *priori* assumption, that the thermodynamically stable phase between 5–325 K for the experimentally determined value of tensile strain in the $BaTiO_3$ film is an orthorhombic phase with in-plane polarization.

ACKNOWLEDGMENTS

This work was partially supported by DOE under Grant Nos. DFFG02-84ER45095 (Xi) and DE-FG02-97ER45638 (Schlom), by DARPA under Grant No. MDA972-01-1-0023 (Xi) and by NSF under Grant Nos. DMR-01-22638 (Chen), DMR-9875405 and DMR-9871177 (Pan), and DMR-0103354 (Schlom, Chen, Xi).

*Electronic address: dat10@psu.edu; On leave from the Institute of Semiconductor Physics, Novosibirsk, Russia.

†Currently at Tsinghua University, Beijing, China.

‡Current address: Solid State Physics Laboratory, Lucknow Rd., Timarpur, Delhi-110 054, India.

[1] S.K. Streiffer, C. Basceri, C.B. Parker, S.E. Lash, and A.I. Kingon, J. Appl. Phys. **86**, 4565 (1999).

[2] D. Damjanovic, Rep. Prog. Phys. **61**, 1267 (1998).

[3] J.S. Speck and W. Pompe, J. Appl. Phys. **76**, 466 (1994)

[4] A.L. Roytburd, J. Appl. Phys. **83**, 228 (1998); S.P. Alpay and A.L. Roytburd, *ibid.* **83**, 4714 (1998).

[5] N.A. Pertsev, A.G. Zembilgotov, and A.K. Tagantsev, Phys. Rev. Lett. **80**, 1988 (1998); N.A. Pertsev and V.G. Koukhar, *ibid.* **84**, 3722 (2000); V.G. Koukhar, N.A. Pertsev, and R. Waser, Phys. Rev. B **64**, 214103 (2001).

[6] Y.L. Li, S.Y. Hu, Z.K. Liu, and L.Q. Chen, Appl. Phys. Lett. **78**, 3878 (2001); Y.L. Li, S.Y. Hu, Z.K. Liu, and L.Q. Chen, Acta Mater. **50**, 395 (2002); L.Q. Chen, Annu. Rev. Mater. Research **32**, 113 (2002).

[7] Y. Yoneda, T. Okabe, K. Sakaue, H. Terauchi, H. Kasatani, and K. Deguchi, J. Appl. Phys. **83**, 2458 (1998).

[8] C.L. Li, Z.H. Chen, D.F. Cui, Y.L. Zhou, H.B. Lu, C. Dong, F. Wu, and H. Chen, J. Appl. Phys. **86**, 4555 (1999).

[9] K. Iijima, T. Terashima, K. Yamamoto, K. Hirata, and Y. Bando, Appl. Phys. Lett. **56**, 527 (1990).

[10] Yu. I. Yuzyuk, P. Simon, I.N. Zakharchenko, V.A. Alyoshin, and

E.V. Sviridov, Phys. Rev. B **66**, 052103 (2002); Yu.I. Yuzyuk, J.L. Sauvajol, P. Simon, V.L. Lorman, V.A. Alyoshin, I.N. Zakharchenko, and E.V. Sviridov, J. Appl. Phys. **93**, 9930 (2003).
[11] S.K. Streiffer, J.A. Eastman, D.D. Fong, C. Thompson, A. Munkholm, M.V. Ramana Murty, O. Auciello, G.R. Bai, and G.B. Stephenson, Phys. Rev. Lett. **89**, 067601 (2002).
[12] D. Fuchs, C.W. Schneider, R. Schneider, and H. Rietschel, J. Appl. Phys. **85**, 7362 (1999).
[13] O. Tikhomirov, H. Jiang, and J. Levy, Phys. Rev. Lett. **89**, 147601 (2002).
[14] *Landolt-Börnstein Numerical Data and Functional Relationships in Science and Technology, New Series, Group III* (Springer, Berlin, 1981), p. 67 , Vol. 16.
[15] C.H. Perry and D.B. Hall, Phys. Rev. Lett. **15**, 700 (1965).
[16] M. DiDomenico, Jr., S.P.S. Porto, and S.H. Wemple, Phys. Rev. Lett. **19**, 855 (1967); M. DiDomenico, Jr., S.H. Wemple, S.P.S. Porto, and R.P. Bauman, Phys. Rev. **174**, 522 (1968).
[17] A. Scalabrin, A.S. Chaves, D.S. Shim, and S.P.S. Porto, Phys. Status Solidi B **79**, 731 (1977).
[18] G. Burns and F.H. Dacol, Phys. Rev. B **18**, 5750 (1978).
[19] H. Vogt, J.A. Sanjurjo, and G. Rossbroich, Phys. Rev. B **26**, 5904 (1982); H. Presting, J.A. Sanjurjo, and H. Vogt, *ibid.* **28**, 6097 (1983).
[20] J.D. Freire and R.S. Katiyar, Phys. Rev. B **37**, 2074 (1988).
[21] U.D. Venkateswaran, V.M. Naik, and R. Naik, Phys. Rev. B **58**, 14 256 (1998).
[22] M. Osada, M. Kakihana, S. Wada, T. Noma, and W.-S. Cho, Appl. Phys. Lett. **75**, 3393 (1999).
[23] L.H. Robins, D.L. Kaiser, L.D. Rotter, P.K. Schenck, G.T. Stauf, and D. Rytz, J. Appl. Phys. **76**, 7487 (1994).
[24] V.I. Merkulov, J.R. Fox, H.-C. Li, W. Si, A.A. Sirenko, and X.X. Xi, Appl. Phys. Lett. **72**, 3291 (1998).
[25] D.A. Tenne, A.M. Clark, A.R. James, K. Chen, and X.X. Xi, Appl. Phys. Lett. **79**, 3836 (2001).
[26] R.E. Cohen and H. Krakauer, Phys. Rev. B **42**, 6416 (1990).
[27] J.J. Neumeier, A.L. Cornelius, and K. Andres, Phys. Rev. B **64**, 172406 (2001).
[28] Y.S. Touloukian, R.K. Kirby, R.E. Taylor, and T.Y.R. Lee, *Thermal Expansion, Nonmetallic Solids, Thermophysical Properties of Matter* (Plenum, New York, 1977), Vol. 13.
[29] L.Q. Chen and J. Shen, Comput. Phys. Commun. **108**, 147 (1998).

Festkörperphysik

Oxide – Tausendsassas für die Elektronik

Oxide bieten eine spektakuläre Vielfalt an funktionalen Eigenschaften

Jochen Mannhart und Darrell G. Schlom

Dank gewaltiger Fortschritte der Dünnschichttechnik ist es seit einem Jahrzehnt möglich, aus einer Vielzahl von Materialien hochwertige Schichten und Multilagenstrukturen zu wachsen. Die für elektronische Bauelemente zur Verfügung stehende Materialpalette hat sich dadurch wesentlich verbreitert und ist inzwischen außerordentlich reichhaltig. Die mit Oxiden erzielbaren Funktionalitäten sind sehr vielfältig und umfassen mit Piezoelektrizität, Sensoreigenschaften und elektrooptischem Verhalten sogar die Übergangsbereiche zur Mechanik, Optik, Chemie und Biologie. Die Halbleiterindustrie nutzt schon jetzt funktionale Oxide, beispielsweise Ferroelektrika für nichtflüchtige Speicher, und im Jahr 2007 sollen in den Transistoren der Laptops Hafnium-basierte Oxide als Gate-Dielektrika eingesetzt werden.

Ultraschall-Bild eines Babies im Mutterleib, aufgenommen mithilfe von Ultraschallsendern und -empfängern aus dem Oxid $Pb(Zr,Ti)O_3$. Die Aufnahme wurde digital bearbeitet (Quelle: GE Healthcare Technologies.)

Ein aktuelles, großes Problem der Halbleiterindustrie ist die begrenzte Leistungsfähigkeit von SiO_2, das als Gate-Isolator in den Si-MOSFETs (Metall-Oxide-Semiconductor Field-Effect Transistors) verwendet wird, den „Arbeitspferden" der meisten Computerchips. Falls bis 2007 keine alternativen Materialien für die Gate-Isolatoren zur Verfügung stehen, verlangsamt sich die gegenwärtig phänomenale Entwicklung der Computer-Leistung massiv, da die Integrationsdichte der Transistoren dann nicht mehr dem berühmten Mooreschen „Gesetz" folgen könnte [1].

Ein Blick auf einen MOSFET eines aktuellen Pentium-4-Prozessors verdeutlicht die Physik, die diesem Problem zugrunde liegt (Abb. 1). In diesen MOSFETs ist die nitrierte SiO_2-Schicht, welche die Gate-Kontakte von den darunterliegenden Drain-Source-Kanälen isoliert, nur 1,2 nm dick. Um die FETs mit möglichst geringer Arbeitsspannung betreiben zu können und dennoch im Drain-Source-(DS)-Kanal die für den Betrieb notwendige Ladungsträgerdichte zu erhalten, muss das Verhältnis von Dielektrizitätskonstante und Dicke der Gate-Barriere t möglichst groß, t also möglichst klein sein. Andererseits funktionieren die heutigen Gate-Barrieren-Stapel aus SiO_2 and Oxinitrid (Si-O-N) aber nicht mehr, falls t etwa 1 nm unterschreitet, da dann der durch die SiO_2-Barriere tunnelnde Strom eine Dichte von über 1000 A/cm^2 aufweist. Die Tunnelstromdichte steigt für jedes Zehntel Nanometer, um das die Barrierendicke verringert wird, um eine Größenordnung an und führt zu unakzeptablem Energieverbrauch, zu Kühlproblemen sowie zu einer unerwünschten Rückwirkung des DS-Kanals auf das Gate. Dieses Problem lässt sich nur mit Materialien als Gate-Isolatoren lösen, welche schon bei großen Barrierendicken die vorteilhaften dielektrischen Eigenschaften ultradünner SiO_2-Schichten aufweisen. Wie unten beschrieben, sollen deswegen in den kommenden Jahren in den hochintegrierten Schaltungen Hafnium-basierte Oxide als Gate-Isolatoren mit hohen Dielektrizitätskonstanten eingesetzt werden.

Kompakt

- Oxide sind als gute Isolatoren unersetzlich für die Mikroelektronik, weisen aber auch zahlreiche andere interessante Eigenschaften auf.
- Für Bauelemente stehen heute oxidische Schichtsysteme aus u. a. magnetischen, ferroelektrischen, piezoelektrischen und sog. multiferroischen Materialien sowie Hochtemperatur-Supraleitern zur Verfügung.
- Die vielfältigen Anwendungen reichen von Gate-Barrieren für die Mikroelektronik über supraleitende Filter für den Mobilfunk, FRAM-Speicher, Infrarotdetektoren bis hin zu selbstreinigenden Fliesen.

Dieser Einsatz komplexer Oxide in der Elektronik ist kein Einzelfall. Für Anwendungen in der Elektronik sind die Oxide sogar ausgesprochen beliebt. Woran liegt dies? Zum großen Teil lässt sich das auf die große Elektronegativität des Sauerstoffs, den im Vergleich zu anderen Anionen kleinen Radius des O^{2-}-Ions und seine doppelte Ladung zurück-

Prof. Dr. Jochen Mannhart, Bereich Elektronische Korrelationen und Magnetismus (EKM), Institut für Physik, Universität Augsburg, 86135 Augsburg; Prof. Darrell G. Schlom, PhD, Materials Science and Engineering, Penn State University, 108 Materials Research Institute Building, University Park, PA 16802-5005, USA

 1617-9439/05/0606-45

führen. Aufgrund dieser besonderen Eigenschaften lassen sich viele Oxide, selbst solche mit mehreren Kationensorten, unter praktikablen Synthesebedingungen in thermodynamisch stabilen Phasen herstellen. Da diese, auch wegen der hohen Polarisierbarkeit des Sauerstoffs, zudem eine außerordentliche Vielfalt elektronischer Eigenschaften aufweisen, sind sie besonders attraktiv für Bauelemente.

Aufgrund der Größe und der Bindungseigenschaften der Sauerstoffionen sowie des breiten Spektrums der zur Verfügung stehenden Metallionen kristallisieren die Oxide in einer Fülle von Strukturen (s. Infokasten „Kristallstrukturen"). Sie bilden unter anderem Rutile (z. B. CrO_2) und Spinelle (z. B. Fe_3O_4), häufig auch Perowskite (z. B. $BaTiO_3$) oder perowskitverwandte Gitter (z. B. $YBa_2Cu_3O_7$). Die Mannigfaltigkeit der Kristallstrukturen, die Tendenz des Sauerstoffs, um Metallionen mit d-Valenzelektronen Oktaeder oder Tetraeder auszubilden, sowie die Variationsmöglichkeiten der Sauerstoffbesetzung und der Dotierung bilden sich in vielförmigen elektronischen Eigenschaften ab. Dieser Vielfalt übergeordnet ist das charakteristische Auftreten von Energielücken im Elektronenvolt-Bereich. Diese werden durch den Einfluss der elektrostatischen Energie (Madelung-Energie) und der Energien der chemischen Bindung auf die elektronischen Energien der freien Metall- und Sauerstoff-Ionen erzeugt. Bestimmt durch die Energielücken sind eine größere Zahl der Oxide Bandisolatoren. Die elektronischen und magnetischen Eigenschaften vieler Oxide sind auch durch starke elektronische Korrelationen geprägt (s. Infokasten „Elektronische Korrelationen"). Diese Korrelationen können in den komplexen Kristallstrukturen Ladungsordnungen und sogar Ordnungen des Spinsystems oder der Orbitale im Kristallgitter generieren, wobei auch Quasiteilchenzustände angeregt werden können. Aufgrund der Spin-Ordnung sind die Oxide wichtige Kandidaten für die Spintronik [2, 3], deren Bauelemente, z. B. Leseköpfe von Festplattenlaufwerken, den Spin der Elektronen nutzen. Ob sich sogar, wie im Konzept der „Orbitronic" vorgeschlagen [3], Anregungen der Orbital-Anordnung im Kristallgitter für Bauelemente nutzen lassen, wird die Zukunft zeigen.

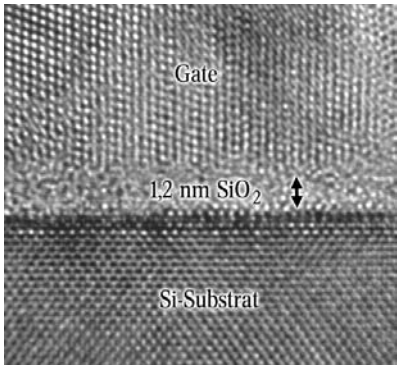

Abb. 1:
Transmissions-Elektronenmikroskopische (TEM) Aufnahme des Querschnitts eines CMOS-Transistors in einem Pentium-4-Prozessor (Quelle: Intel Corporation).

Oxide haben aufgrund ihrer großen Energielücken das Zeug zu hervorragenden Isolatoren. Lange Zeit begnügte man sich damit, sie als solche in elektrischen Komponenten einzusetzen. Die elektronischen Eigenschaften der Oxide lassen sich jedoch durch Dotieren dramatisch verändern, wobei sehr hohe Dotierkonzentrationen von mehreren $10^{21}/cm^3$ gebräuchlich sind [4]. Dotierte Oxide können ausgesprochen gute Leiter sein. Einen ganz besonderen Fall bilden hierbei die Kuprat-Supraleiter, die bei Temperaturen bis zu 135 K, unter Druck sogar bis 153 K, supraleitend sind. Die hohen Dotierungen bringen, im Gegensatz zu Halbleitern, nicht nur Ladungsträger in Bänder ein, sondern ändern zugleich auch die spektrale Dichte der Elektronen, die Korrelationsparameter und die Suszeptibilitäten. Dadurch können Phasenübergänge, zum Beispiel Metall-Isolator-Übergänge, induziert werden. Somit lassen sich die Eigenschaften solcher Oxide in extrem weiten Bereichen durch Ändern ihrer Ladungsträgerdichte variieren, was nicht nur durch Dotierung, sondern beispielsweise auch durch elektrische Felder oder durch Bestrahlung mit Licht möglich ist (s. u.).

Da Sauerstoff-Defekte die Oxide in der Regel dotieren und Sauerstoff zudem leicht diffundiert, wird in der Oxidelektronik der Kontrolle der Sauerstoffkonzentration viel Aufmerksamkeit gewidmet. Die einzelnen Oxide verhalten sich hierbei sehr unterschiedlich. In manchen Manganat-Schichten lässt sich der Sauerstoffgehalt beispielsweise oft nur mit Aufwand präzise einstellen. Die Hoch-T_c-Supraleiter sind hier robuster und zudem langzeitstabil; epitaktische Schichten, wie sie zum Beispiel in Hochfrequenzfiltern eingesetzt werden, erfüllen sogar die hohen Anforderungen der Raumfahrttechnik.

Wenngleich von den ionischen Materialien bisher bevorzugt Oxide für elektronische Anwendungen ge-

Kristallstrukturen

▶ (a) $BaTiO_3$, ein klassischer Perowskit, ist ein Ferroelektrikum, mit einer Raumtemperatur-Polarisation von 26 $\mu C/cm^2$, das sich durch Gitterverspannungen auf ca. 70 $\mu C/cm^2$ erhöhen lässt;
▶ (b) $YBa_2Cu_3O_7$, das Arbeitspferd der Hochtemperatur-Supraleiter, hat ein T_c von 93 K. Auf metallischen Trägerbändern aufgebracht, kann $YBa_2Cu_3O_7$ bei 77 K Ströme mit Dichten von mehreren 10^6 A/cm^2 verlustfrei transportieren;
▶ (c) Mit Anatase, einer Modifikation von TiO_2, beschichtete Oberflächen sind unter Lichteinfall selbstreinigend (s. Abb. 5);
▶ (d) Das von den Audiokassetten bekannten CrO_2 besitzt die Struktur des Rutils. Die Elektronen des CrO_2 sind bei tiefen Temperaturen hochgradig spinpolarisiert (s. Infokasten „Elektronische Korrelationen").
▶ (e) Die Elektronen des ferrimagnetischen Spinells Fe_3O_4 (Magnetit) sind sogar bei Raumtemperatur spinpolarisiert.

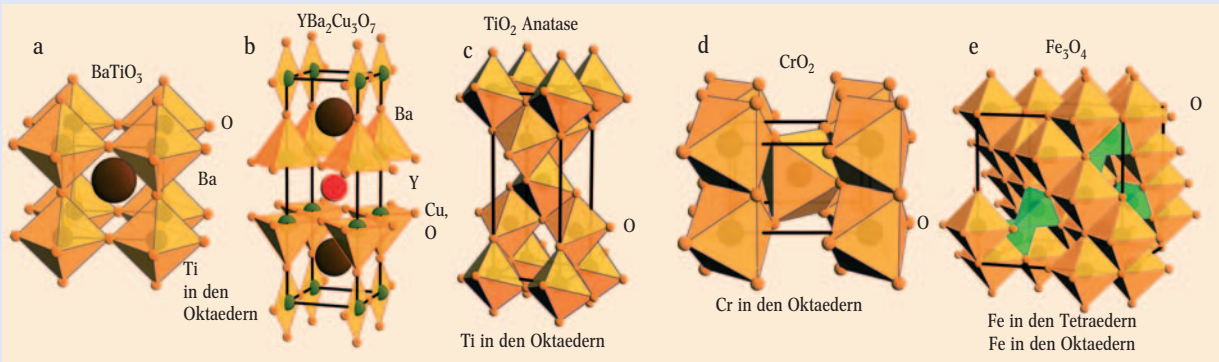

nutzt werden, lassen zum Beispiel auch Nitride und Oxinitride, Halogenide und Sulfide vielfältige und nützliche elektronische Eigenschaften erwarten; diese Materialien wurden aber bislang in weit geringerem Umfang untersucht, da sie oft nur schwer einphasig und stabil zu synthetisieren sind.

Wachstum oxidischer Schichten und Heterostrukturen

Für zahlreiche Anwendungen werden dünne Oxidfilme benötigt, je nach Anforderung als amorphe, polykristalline oder einkristalline (epitaktische) Schichten. Amorphe und polykristalline Schichten lassen sich auf vielen Substraten und in einem weiten Bereich von Wachstumsbedingungen deponieren, meist durch Sputtern und CVD (Chemical Vapor Deposition). Diese Verfahren sind kostengünstig und gestatten die Beschichtung großer Flächen. Manche Anwendungen erfordern jedoch den Einsatz epitaktischer Schichten, da diese in aller Regel die besten elektronischen Eigenschaften aufweisen.

Verglichen mit der Epitaxie von Halbleitern wie Si oder GaAs stellt das epitaktische Wachstum von Oxiden ganz besondere Anforderungen. Diese resultieren aus der Komplexität der Komponenten, der häufig großen Zahl möglicher Phasen und den erforderlichen Wachstumsbedingungen, die in der Regel Temperaturen zwischen 600–800 °C in oxidierender Atmosphäre involvieren [5]. Zudem ist bei nichtbinären Verbindungen eine präzise Kontrolle der Kationen-Stöchiometrie erforderlich. Dies gelingt, indem entweder ein genauer Stöchiometrieübertrag von einem Target auf das Substrat gewährleistet wird – dies ist bei der Laser-Ablation der Fall – oder indem die Depositionsraten der individuellen Atomsorten, z. B. mittels Absorption von Licht, gemessen und aktiv kontrolliert werden. Hierbei lässt sich die Bildung einzelner Ebenen von Einheitszellen mittels RHEED (Reflection High-Energy Electron Diffraction) *in situ* beobachten. Da dies in Echtzeit geschieht, bietet sich mit den RHEED-Informationen die Möglichkeit, das Schichtwachstum auf Sub-Einheitszellenniveau zu steuern. Dank dieser Fortschritte ist die Qualität oxidischer Schichten und Heterostrukturen mittlerweile mit der Güte von Halbleiterschichten vergleichbar, die mit Molekularstrahlepitaxie gewachsen wurden (Abb. 2).

Neben der Laser-Ablation und optimierten Sputterprozessen werden heute mit großem Erfolg die Molekularstrahlepitaxie (MBE) und reaktives Verdampfen zur Herstellung oxidischer Schichten eingesetzt. Thermisches Verdampfen hat sich als kostengünstig erwiesen und gestattet mit Substratdurchmessern von gegenwärtig bis zu 8 Zoll einen hohen Durchsatz. Initiiert durch die Hoch-T_c-Supraleitung, hat sich hier die deutsche Firma Theva, ein Spin-Off der TU München, zum erfolgreichen weltweiten Marktführer entwickelt. Hochwertige Oxidschichten werden mittlerweile auch mit Nicht-Vakuum-Verfahren hergestellt, z. B. mittels Dip- oder Spray-Coating, und bilden beispielsweise das Kernstück der Bandsupraleiter für preiswerte und leistungsfähige Hoch-T_c-Kabel [6].

Epitaktisch gewachsene Schichten tendieren dazu, sich den Gitterkonstanten des Substrats anzupassen; unterscheiden sich die Gitterkonstanten von Substrat und Film, entstehen Druck- oder Zugspannungen. Diese epitaktischen Verspannungen werden in der Halbleitertechnik genutzt, um die Beweglichkeit der Ladungsträger und damit die Schaltgeschwindigkeit von Transistoren zu optimieren. Da die Substrate auch eine mögliche Rissbildung hemmen, sind Verspannungen im Prozent-Bereich möglich. Zudem sind die Oxide, insbesondere die piezoelektrischen und damit auch alle ferroelektrischen, außergewöhnlich verspannungsempfindlich. Jüngste Arbeiten zeigen, dass es mit Zugspannungen sogar möglich ist, Oxide, die

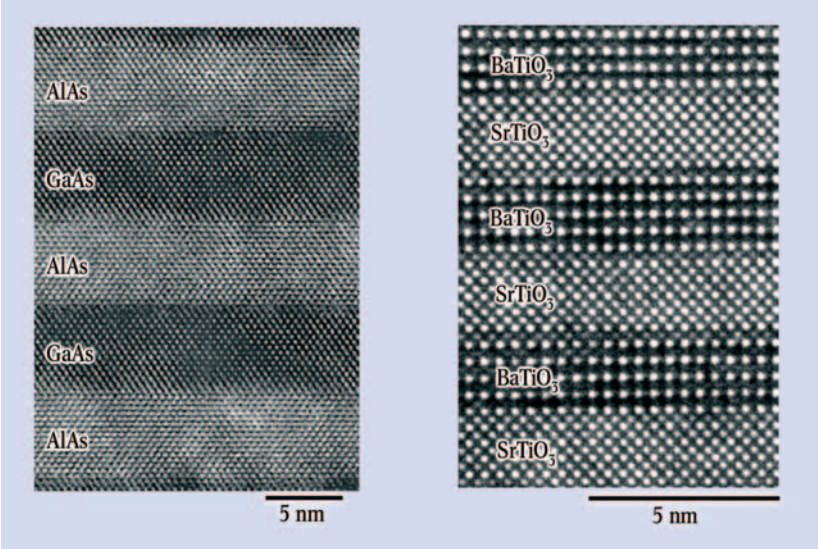

Abb. 2:
Wie diese TEM-Aufnahmen zeigen, ist die Qualität eines $BaTiO_3/SrTiO_3$-Übergitters (rechts, [22]) mittlerweile vergleichbar mit derjenigen eines MBE-gewachsenen GaAs/AlAs-Übergitters (links, [21]).

normalerweise selbst bei tiefen Temperaturen nicht ferroelektrisch sind, in Ferroelektrika bei Zimmertemperatur umzuwandeln [7]. Die Eigenschaften von Oxiden, die schon von sich aus ferroelektrisch sind, lassen sich mit Verspannungen dramatisch verbessern. Beispielsweise gelang es, die spontane Polarisation des ferroelektrischen $BaTiO_3$ zu verdreifachen und seine kritische Temperatur um etwa 500 °C zu erhöhen [7]. Mit verspanntem $BaTiO_3$ steht erstmals für nichtflüchtige Speicher und elektrooptische Bauelemente ein Ferroelektrikum zur Verfügung, das kein Blei enthält – eine wünschenswerte Eigenschaft für die Integration in Halbleiter-Bauelementen.

Funktionale Eigenschaften der Oxide

Die Vielfalt der funktionalen Eigenschaften der Oxide ist spektakulär; hier sollen kurz die wichtigsten zusammen mit ihren Anwendungsbereichen aufgeführt werden.

Elektronische Eigenschaften

In der Einleitung haben wir geschildert, dass in den hochintegrierten Schaltungen die Dicke der, zum Teil nitrierten, SiO_2-Gate-Isolatoren von Feldeffekttransistoren kontinuierlich reduziert wird, und mittlerweile den kritischen Wert von 1,2 nm erreicht hat. Doch warum sind immer dünnere Gate-Barrieren notwendig? Höhere Integrationsdichten lassen sich zunächst einmal dadurch erreichen, dass die Transistoren bei konstanter Barrierendicke nur lateral verkleinert werden. Leider läuft bei einer solchen Skalierung die Verlustleistung schnell aus dem Ruder. Die pro Flächeneinheit dissipierte Leistung steigt mit $\alpha^3 f$, wobei α der Skalierungsfaktor der linearen Verkleinerung und f die Schaltfrequenz des Chips bezeichnet. Werden hingegen alle Komponenten der Transistoren, also auch die Gate-Isolatoren und damit die Arbeitsspannung

verkleinert, ist der Leistungsverbrauch unabhängig von α [8]. Diese Skalierung mit konstanter Feldstärke wird seit 35 Jahren mit großem Erfolg bei der MOSFET-Integration eingesetzt.

In den MOSFETs ist die spezifische Kapazität eine entscheidende Größe, da sie die Ladungsträgerdichte bestimmt, die im DS-Kanal von einer gegebenen Gatespannung induziert wird. Das Mooresche Gesetz könnte zumindest einige Jahre weiter eingehalten werden, wenn das SiO_2 durch ein Material mit einer Dielektrizitätskonstanten (K) ersetzt würde, die diejenige des amorphen SiO_2 ($K = 3{,}9$) deutlich übersteigt [1]. Hätte der neue Gate-Isolator zum Beispiel ein fünffach erhöhtes K, ließe sich bei gleichbleibender Kapazität die Barrierendicke verfünffachen. Bei Gate-Barrieren dieser Dicke wäre der Tunnel-Leckstrom drastisch reduziert, und die Transistoren könnten höher integriert werden.

SiO_2 durch eine hoch-K-Alternative zu ersetzen, ist keine triviale Aufgabe, denn es waren seine wunderbaren Eigenschaften und die überragende Qualität der Si/SiO_2-Grenzfläche, die zur atemberaubenden Entwicklung der Si-MOSFETs geführt haben. Ein alternatives Material muss u. a. folgende Eigenschaften aufweisen: (1) bei Tempertemperaturen von ca. 900 °C im Kontakt mit Si stabil sein, (2) eine mindestens 4–5 eV große Bandlücke aufweisen, um Leckströme zu minimieren, und (3) an der Grenzfläche zum Si eine geringe Dichte elektrisch aktiver Defekte besitzen.

Diesen Ansprüchen gerecht zu werden ist eine ausgesprochen knifflige Aufgabe. Dies ist ein heißes Feld der Forschung und Prozessentwicklung. Große Fortschritte wurden schon erzielt, und Intel, NEC und Toshiba haben angekündigt, im Jahr 2007 hoch-K-Gate-Isolatoren in die Produktion einzuführen. Mit den amorphen Hf-Si-O-N-Verbindungen ($K \approx 11$–22) [9], die zunächst verwendet werden sollen, ist vermutlich noch nicht das letzte Wort gesprochen, da das Wachstum der Hafniumoxide an der Grenzfläche zum Si zur Bildung von SiO_2 führt. Durch Verwendung von Oxiden wie $LaAlO_3$ ($K \approx 25$) [10] hofft die Industrie, dem Mooreschen Gesetz für weitere zehn, fünfzehn Jahre folgen zu können.

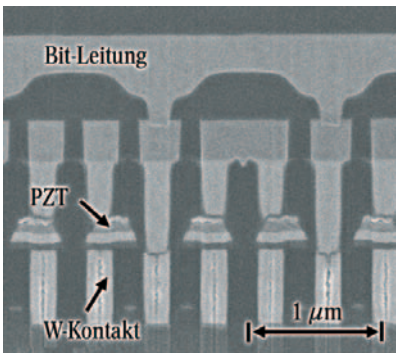

Abb. 3: **In einem nichtflüchtigen FRAM-Speicher (hier eine TEM-Aufnahme) werden die Daten mithilfe ferroelektrischer Materialien wie PZT gespeichert (Quelle: Texas Instruments und Agilent).**

Oxide sind auch für nichtflüchtige Speicherbauelemente hochinteressante Systeme. Die Polung ferroelektrischer Materialien wie $PbZr_{0,3}Ti_{0,7}O_3$ (PZT) oder $SrBi_2Ta_2O_9$ bildet die Funktionsgrundlage der FRAMs (Ferroelectric Random Access Memory) [11]. In FRAMs werden ferroelektrische Schichten über Gate-Elektroden polarisiert. Da diese Polarisationen stabil sind und mittels der Gate-Elektroden auch wieder ausgelesen werden können, lassen sich auf einfache Art nichtflüchtige Speicherzellen realisieren (Abb. 3). Die FRAMs entsprechen in ihrer Funktion den Flash-RAMs, die in den heutigen Memory-Sticks eingesetzt werden, bieten aber deutlich kürzere Schreibzeiten: wenige 10 Nanosekunden im Vergleich zu Mikrosekunden. Die Integrationsdichte der FRAMS reicht leider noch nicht an die Dichte der Flash-Speicher heran. Siemens und Toshiba haben jedoch Chips mit 32 Mb vorgestellt und Fujitsu verkauft 1-Mb-FRAM-Chips. Aktuelle Untersuchungen haben ergeben, dass in Materialien wie PZT selbst Volumina von $(20\ \text{nm})^3$ ferroelektrisch sind, das Integrationspotenzial der Technik ist offensichtlich enorm. In Laborexperimenten, in denen die Domänen mit Rastersondenmikroskopen gepolt wurden, wurden Speicherdichten bis zu 1,5 Tb/inch^2 erzielt [12]. Auch einen Monat nach dem Schreibvorgang sind keine wesentlichen Änderungen der Domänenstruktur zu erkennen (Abb. 4).

Verschiedene Oxide, die im Grunde isolierend sind, beispielsweise $Pr_{0,7}Ca_{0,3}MnO_3$ oder Cr-dotiertes $SrTiO_3$, können durch einen kurzen Strompuls in einen leitfähigen Zustand geschaltet werden. Dieser lässt sich durch einen Puls umgekehrter Polarität auch wieder löschen. Auch hier liegt die Anwendung in nichtflüchtigen, hochintegrierten Speichern auf der Hand, das Gebiet wird derzeit intensiv erforscht [13].

Ein ganz besonderes Phänomen der Oxide ist die Hochtemperatur-Supraleitung. Für Hochfrequenz-Bauelemente sind hierbei der niedere Oberflächenwiderstand und die kleine Intermodulation supraleitender Schichten von großem Interesse. Limitiert durch die zur Verfügung stehenden Frequenzbereiche führt insbesondere in den USA und Japan die wachsende Mobiltelefon-Dichte zu Kapazitätsengpässen. Der Einsatz extrem scharfbandiger und rauscharmer, supraleitender Filter und kryogekühlter Halbleiter-Verstärker in den Basis-Stationen mildert diese Engpässe, da die supraleitenden Filter die Kapazität und auch die Flächendeckung der Netzwerke verbessern.

Elektronische Korrelationen

In den Oxiden ist die elektrostatische Abstoßungsenergie U der Ladungsträger, die sich auf den gleichen Gitterplätzen befinden, im Vergleich zu den Bandbreiten oft nicht vernachlässigbar. Dieser Effekt unterstützt die Lokalisierung der Ladungsträger. Die Elektronen, die somit in solchen Materialien stark miteinander wechselwirken, lassen sich nicht mehr in der Hartree-Fock-Näherung beschreiben; man bezeichnet diese Systeme als korreliert.

Ist die Abstoßungsenergie U groß im Vergleich zu den Bandbreiten, können sich in halbgefüllten Bändern die Elektronen (dargestellt durch blaue Kugeln) selbst dann nicht mehr bewegen, wenn das Oxid kein Bandisolator ist, da die Besetzung eines Gitterplatzes mit zwei Elektronen (mit entgegengesetzter Spinrichtung, durch rote Pfeile symbolisiert) die elektrostatische Abstoßungsenergie U der Elektronen kosten würde (Abb. links); es bildet einen Mott-Isolator.

Elektronische Korrelationen verursachen in viele Oxiden auch bemerkenswerte magnetische Phänomene. Wie in der Abb. rechts anhand des Halbmetalls CrO_2 dargestellt, kann die Austauschwechselwirkung dazu führen, dass die Bänder der Elektronen mit Spin-up- und Spin-down-Elektronen derart (links bzw. rechts) gegeneinander verschoben sind, dass sich das Fermi-Niveau für eine Spinrichtung in einer Bandlücke befindet. Im gezeigten Beispiel ist dies für die Spin-up-Elektronen der rechte Bildhälfte der Fall. Das Oxid ist in dann ein Halbmetall, die beweglichen Ladungsträger an der Fermi-Energie E_F sind spinpolarisiert (nach [23]).

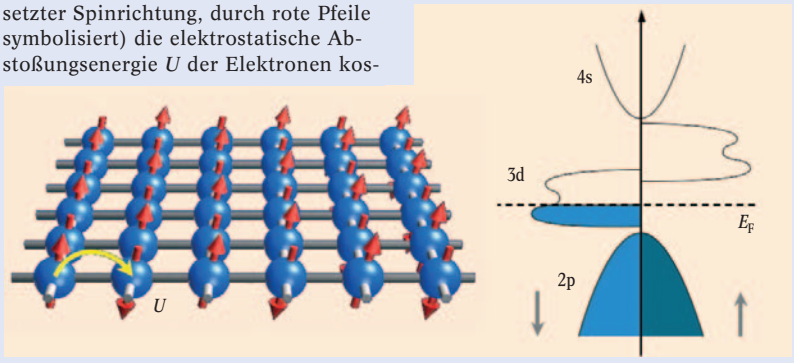

Amerikanische Feldtests zeigten, dass durch die Einführung dieser Filter das Signal-Rausch-Verhältnis der Basisstation-Empfänger mehr als verdoppelt wird. In den USA sind mehr als 4000 supraleitende Systeme in Betrieb [6].

Hoch-T_c-Schichten werden auch in Bauelementen mit Josephson-Kontakten verwendet. Josephson-Kontakte an Hochtemperatur-Supraleitern lassen sich heute mit verschiedenen Techniken in sehr guter Qualität herstellen, insbesondere durch die sog. Bikristall- und die Rampenkontakt-Technologien, bei denen Korngrenzen bzw. nichtsupraleitende Zwischenschichten als Barrieren genutzt werden. Leider streuen die Parameter der Kontakte bis jetzt um etwa 5–10 %. Von wenigen Ausnahmen abgesehen, verhindert diese Streuung die Realisierung hochintegrierter Schaltungen. Indes werden heute routinemäßig leistungsfähige SQUIDs (Superconducting Quantum Interference Devices) und die mit ihnen verwandten SQUIFs (Superconducting Quantum Interference Filter) hergestellt, die wenige Kontakte erfordern. Die Rauschwerte von Hoch-T_c-SQUIDs übersteigen bei 77 K nur unwesentlich die Werte kommerzieller, bei 4,2 K betriebener SQUIDs. Eingesetzt werden Hoch-T_c-SQUIDs beispielsweise zur Erzsuche, um Magnetfeld- oder Leitfähigkeitsanomalien von Lagerstätten während des Überfluges zu detektieren. Auf der Mikro-Skala machen sich Hoch-T_c-SQUIDs in der Halbleiterproduktion in Raster-SQUID-Mikroskopen nützlich, um elektrische Ströme über ihre Magnetfelder hochaufgelöst abzubilden. Weitere Einsatzgebiete sind die zerstörungsfreie Materialprüfung oder die Medizin, z. B. in der Kardiographie [6].

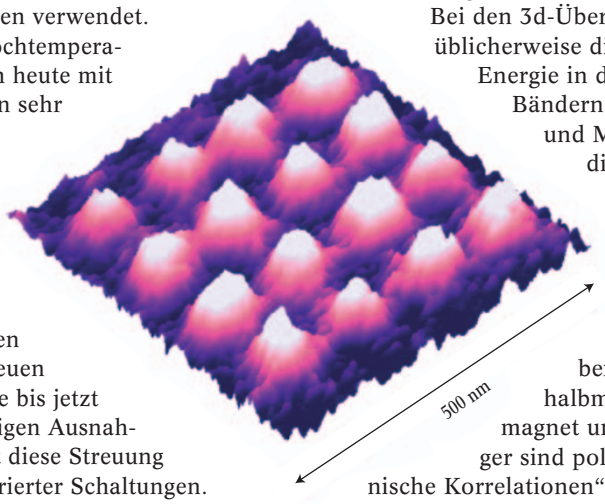

Abb. 4: Diese Domänen eines ferroelektrischen PZT-Films wurden mit 500 ns langen und 12 V hohen Spannungspulsen zwischen Spitze und Probe in einem Rastertunnelmikroskop geschrieben und einen Monat später abgebildet (Quelle: P. Paruch und J.-M. Triscone, Universität Genf).

Die Einsatzbreite funktionaler Oxide ist erstaunlich und reicht bis zur Herstellung aktiver Oberflächen. Wird Anatase (TiO_2, s. Infokasten „Kristallstrukturen“) oder ein vergleichbares Material mit UV-Licht bestrahlt, erzeugt dieses über Bandübergänge Elektronen-Loch-Paare. Die Löcher wirken extrem oxidierend, sodass Verunreinigungen, die sich auf der Oberfläche befinden, zerstört und letztendlich beseitigt werden. Die Oberfläche reinigt sich daher selbst [14]. Dieser Selbstreinigungseffekt wird durch ein zweites Phänomen unterstützt: Die Beleuchtung erzeugt Sauerstoff-Fehlstellen an der Oberfläche, die dadurch extrem hydrophil wird. Dadurch können Wasserfilme unter organische Verunreinigungen kriechen und die Verschmutzung abspülen. Um den Selbstreinigungseffekt zu nutzen, wurden in den vergangenen Jahren Hochhausfassaden mit TiO_2 beschichtet, ebenso Lampengalerien in Straßentunnels oder Wand- und Bodenfliesen in Operationssälen (Abb. 5). Erwartungsgemäß desinfizieren sich die beschichteten Fliesen zu einem erheblichen Grad selbst. Im Jahr 2003 wurden mit selbstreinigenden Oberflächen etwa 500 Mio. US-Dollar umgesetzt.

Magnetische Eigenschaften

Unter den Oxiden gibt es Systeme mit außergewöhnlichen magnetischen Eigenschaften. So sind beispielsweise die beweglichen Elektronen in CrO_2, in Fe_3O_4 und in speziellen Manganaten hochgradig spinpolarisiert. Der elektrische Widerstand mancher Manganate verringert sich in Magnetfeldern dramatisch. Weltweit sind Arbeitsgruppen bestrebt, diese Eigenschaften der Oxide in der Spintronik [2, 3] zu nutzen. Hier soll ein kurzer Überblick über die magnetischen Eigenschaften der Oxide und möglicher Anwendungen gegeben werden.

Bei den 3d-Übergangsmetalloxiden liegen üblicherweise die 3d-Bänder und die Fermi-Energie in der Energielücke zwischen den Bändern der hybridisierten Sauerstoff-2p und Metall-4s-Niveaus. Verschiebt die Austauschwechselwirkung 3d-Zustände mit Spin-up gegenüber denjenigen mit Spin-down, kann es geschehen, dass sich in einer Spinrichtung am Fermi-Niveau E_F keine beweglichen Zustände befinden. Dann ist das Oxid ein halbmetallischer Ferro- oder Ferrimagnet und die beweglichen Ladungsträger sind polarisiert (s. Infokasten „Elektronische Korrelationen“). Bei tiefen Temperaturen kann der Polarisationsgrad ausgesprochen hoch sein: für $La_{0,7}Sr_{0,3}MnO_3$ und CrO_2 beispielsweise fast 100 % bei 5 K. Leider nimmt die Polarisation P mit zunehmender Temperatur in der Regel rapide ab. Mit $P = -80$ % bei Zimmertemperatur bildet das im Infokasten vorgestellte Fe_3O_4 hierbei einen Sonderfall. Das negative Vorzeichen kennzeichnet die Polarisationsrichtung der beweglichen Ladungsträger, die im Fe_3O_4 dem angelegten Feld entgegengerichtet ist [15]. Die Kombination von Fe_3O_4-Schichten mit positiv polarisierten Materialien eröffnet vielleicht sogar die Möglichkeit, in Bauelementen Elektronen beider Spinpolaritäten einzusetzen.

Der hohe Spinpolarisationsgrad macht die Oxide, neben Legierungen aus Fe, Co oder Ni, als Quellen oder als Detektoren von Spins attraktiv. Um die hohe Spinpolarisation zu nutzen, wird zum einen an rein oxidischen Bauelementen gearbeitet, zum anderen an Bauelementen, in denen spinpolarisierte Elektronen in Oxiden erzeugt und dann in Halbleiter oder in Metalle injiziert werden. Hierbei reduzieren Probleme der Widerstandsanpassung und Streuprozesse bislang leider die Polarisation bei Zimmertemperatur auf unakzeptable Werte.

Abb. 5: Die mit TiO_2 beschichteten Wand- und Bodenfliesen dieses Operationssaals reinigen und desinfizieren sich unter Lichtbestrahlung von selbst (Quelle: K. Hashimoto, University of Tokyo).

Für aktive Bauelemente wie Spin-Transistoren wären ferromagnetische Halbleiter hervorragende Materialien, falls sie bei Zimmertemperatur eine hohe Spin-Polarisation der Bandelektronen aufweisen. Vielversprechende Kandidaten sind verdünnte magnetischen Halbleiter („Diluted Magnetic Semiconductors"). Für Co-dotiertes TiO_2 wurden beispielsweise Curie-Temperaturen von $T_c = 700$ K gemessen. Aufgrund des potenziell hohen Spinpolarisationsgrades sind Oxide zudem verlockende Anwärter zum Einsatz in magnetischen Tunnelkontakten, die zur Verwendung in nichtflüchtigen magnetischen Speichern (MRAMs) entwickelt werden.

Abb. 6:
Diese nächtliche Infrarotaufnahme wurde mit einem ungekühlten Detektor aufgenommen. Seine aktiven Elemente sind Pixel aus einer ferroelektrischen (Pb,La)(Zr,Ti)O_3-Schicht, die im pyroelektrischen Modus ausgelesen werden (Quelle: L-3 Communications Infrared Products).

Oxide werden natürlich schon jetzt als Barrieren in den Tunnelkontakten eingesetzt. Zur Erhöhung des Ausgangssignals wäre es von Vorteil, wenn es gelänge, die Tunnelelektroden aus voll-polarisierten Oxiden zu wachsen. Wie bei den ferromagnetischen Halbleitern existieren hier vielversprechende Ansätze, von der Realisierung einsetzbarer Bauelemente ist man allerdings auch hier noch weit entfernt.

Zum Einsatz in Magnetfeldsensoren sind die sog. CMR-Manganate (Colossal Magneto Resistance) vielbeachtete Systeme. In einer Zusammenarbeit zwischen Siemens und der Universität Augsburg wurde 1993 entdeckt, dass Schichten dieser Manganate einen „kolossalen" Magnetwiderstand zeigen [16]. $La_{0,7}Ca_{0,3}MnO_3$, beispielsweise, weist bei 240 K einen Metall-Isolator-Übergang auf, der mit einer Widerstandsänderung von mehreren Größenordnungen verbunden ist. Da sich die Übergangstemperatur durch ein äußeres Magnetfeld erhöhen lässt, ändert sich der Widerstand im Magnetfeld gewaltig. Der Widerstand von $La_{0,7}Ca_{0,3}MnO_3$ wird bei 77 K durch Felder von mehreren Tesla um mehr als einen Faktor 1000 reduziert. Um diesen kolossalen Magnetowiderstand beispielsweise in Sensoren nutzen zu können, gilt es, die Materialien so zu optimieren, dass sie bei den gewünschten Arbeitstemperaturen auf kleine Magnetfelder empfindlich reagieren und zudem Variationen der Sauerstoffdotierung tolerieren.

Phasenübergänge und multiferroische Eigenschaften

Die Komplexität der Elektronensysteme führt bei den Oxiden häufig zu Phasenübergängen zwischen Phasen mit überaus unterschiedlichen elektronischen Eigenschaften. Lichteinstrahlung, magnetische und elektrische Felder, Temperatur, Druck und Ladungsträgerdichte sind Kontrollparameter, mit denen Phasenübergänge induziert werden können. Da die Phasenübergänge häufig solch dramatische Änderungen der elektronischen Eigenschaften der Materialien verursachen und sich somit leicht auslesen lassen, eignen sie sich für empfindliche Sensoren. Natürlich besteht auch die Möglichkeit, Transistoren und andere Dreitorbauelemente zu verwirklichen, in denen der Phasenübergang durch ein elektromagnetisches Eingangssignal gesteuert wird. Besonders spannend für Anwendungen sind hierbei Feldeffekttransistoren (FETs), bei denen die Drain-Source-Kanäle aus Oxiden bestehen, in denen Phasenübergänge durch eine Gate-induzierte Änderung der Ladungsträgerdichte hervorgerufen werden. Das große Hindernis auf dem Weg zu solchen Phasenübergangs-FETs ist die genannte hohe Ladungsträgerdichte, die sehr große Gate-Polarisationen ($> 10\ \mu C/cm^2$) erfordert, um die Phasenübergänge zu induzieren [4]. Verschiedenen Gruppen gelang es schon, erste ermutigende Bauelemente zu realisieren, indem sie oxidische Gate-Isolatoren mit extremen Polarisationen nutzten, um beispielsweise Hoch-T_c-Kuprate von der isolierenden in die supraleitende Phase zu schalten.

Ein anderes Beispiel für Materialien mit mehrfachen Phasenübergängen sind Verbindungen, die magnetisch und ferroelektrisch zugleich sind. Sie sind sowohl durch die kritischen Temperaturen der magnetischen Phasenübergänge – z. B. in ferromagnetische, ferrimagnetische oder antiferromagnetische Phasen – als auch durch die Übergangstemperaturen der paraelektrisch-ferroelektrischen Phasenübergänge charakterisiert. Solche multiferroischen Materialien sind selten – aus Symmetriegründen können sie nur in 13 der 90 magnetischen Punktgruppen auftreten. Ein einfaches Beispiel für ein multiferroisches Material ist der Perowskit $BiMnO_3$, der unterhalb von ca. 105 K gleichzeitig ferromagnetisch und ferroelektrisch ist.

Magnetische Ferroika weisen alle funktionellen Eigenschaften von magnetischen und ferroelektrischen Materialien auf, aber auch Funktionalitäten, die in den einzelnen Klassen allein gar nicht zu finden sind. So lässt sich, wie vor über einem Jahrhundert von Pierre Curie vorhergesagt [17], die elektrische Polarisation mancher Multiferroika mittels Magnetfelder orientieren, die Magnetisierungsrichtung durch elektrische Felder drehen. Solch funktionellen Eigenschaften sind für Bauelementanwendungen von offensichtlichem Interesse. Da sich elektrische Felder von integrierten Schaltungen leichter erzeugen lassen als Magnetfelder, ist man beispielsweise bestrebt, magnetische Multiferroik-Bits über elektrische Felder zu schalten. Zum Auslesen ist hingegen die Magnetisierung praktisch, da elektrische Felder leicht über freie Ladungen abgeschirmt werden und damit schwerer zu detektieren sind.

Aufgrund ihrer außergewöhnlichen multifunktionellen Eigenschaften werden multiferroische Materialien intensiv erforscht. Die mögliche Kopplung zwischen den ferromagnetischen und ferroelektrischen Domänen ist hierbei von besonderem Interesse. Diese Kopplung wird mittlerweile nicht mehr nur in einphasigen Materialien erreicht, sondern auch in multiferroischen Nanostrukturen, die aus magnetischen und ferroelektrischen Verbindungen bestehen [18]. Allerdings gelang es bisher noch nicht, bei Zimmertemperatur Ferro- oder Ferrimagnetismus mit Ferroelektrizität zu kombinieren.

Weitere funktionelle Eigenschaften

Die Vielfalt der elektronischen Eigenschaften der Oxide umfasst auch die Schnittstellen zur Mechanik und zur Optik. So lassen sich aus den Oxiden hervorragende Strahlungsdetektoren bauen, wofür Abb. 6 ein Beispiel zeigt. Die abgebildete Szene wurde im Infraroten mit einem Nachtsichtgerät aufgenommen, dessen Detektor aus ferroelektrischen (Pb,La)(Zr,Ti)O_3-Pixeln bestehen, die eine beleuchtungsabhängige Ausgangsspannung erzeugen. Diese Detektoren arbeiten nicht nur ungekühlt, sie sind auch tolerant gegen Temperaturschwankungen und bieten dennoch ein extrem geringes Rauschen. Pb(Zr,Ti)O_3 ist auch piezoelektrisch und eignet sich hervorragend, um Ultraschall-Sender und Empfänger zu bauen. Die Leistungsfähigkeit dieser Wandler, die ebenso wie die Infrarotdetektoren auf Pixelfeldern basieren, ist beeindruckend und ermöglicht qualitativ hervorragende Ultraschallbilder (s. Abb. auf S. 45). Da diese Bilder in Echtzeit aufgezeichnet werden können, lassen sich in dieser Qualität sogar Filme aufnehmen.

Das Feld der Oxidelektronik ist so breit, dass wir aus Platzgründen auf wichtige Materialien, etwa ZnO, das heute intensiv zur Herstellung blauer Leuchtdioden und Laser entwickelt wird [19], oder auch auf wichtige Bauelemente, etwa auf durchstimmbare Hochfrequenzfilter [20], nicht eingehen konnten.

Ausblick

Der Einsatz funktionaler Oxide eröffnet neue Perspektiven, die Leistungsfähigkeit und Integration der halbleitenden Elektronik voranzutreiben. Hierbei ist zu erwarten, dass langfristig neben den Oxiden auch Oxinitride, Halogenide und Chalkogenide eingesetzt werden, auch die Verwendung organischer Substanzen liegt auf der Hand. Da die Oxidelektronik durch viele offene Fragen geprägt ist und auch die Entdeckungen zahlreicher neuer Phänomene vorhergesagt werden kann, sind die Möglichkeiten der Oxidelektronik noch gar nicht abschätzbar. Auf der ganzen Breite, von der Grundlagenforschung bis zu Anwendungen, entwickelt sie sich rasant und im großen Maßstab.

*

Die Autoren bedanken sich bei S. Aggarwal, H. R. Beratan, S. Chambers, C.-B. Eom, H. Eschrig, V. Eyert, F. Gießibl, A. Gupta, A. Herrnberger, T. Kopp, C. Laschinger, F. Lichtenberg, P. Paruch, P. Reiche, A. Reller, E. Saladie, A. Schmehl, C. W. Schneider, J. Schubert, J.-M. Triscone, R. Uecker, M. Vara und K. Wiedenmann für hilfreiche Diskussionen, Informationen und Unterstützung beim Abfassen des Manuskripts, sowie beim BMBF und beim VDI (Projekt EKM 13N6918), der DFG (SFB 484), der ESF (THIOX), der Alexander von Humboldt-Stiftung, dem DOE (Projekt DE-FG02-03ER46063), der SEMATECH und der SRC für die Unterstützung ihrer Forschungsarbeiten auf dem Gebiet der Oxidelektronik.

Literatur

[1] International Technology Roadmap for Semiconductors, 2003 Edition, Front End Processes, (Semiconductor Industry Association, San Jose, 2003) S. 2, 23–33. Erhältlich unter http://public.itrs.net/Files/2003ITRS/Home2003.htm; *G. E. Moore*, Electronics **38**, 114 (1965)
[2] *R. Winkler* und *M. Oestreich*, Physik Journal, November 2004, S. 39; *I. Žutić, J. Fabian* und *S. Das Sarma*, Rev. Mod. Phys. **76**, 323 (2004); *M. Ziese* und *M. J. Thornton* (Hrsg.), Spin Electronics, Springer Verlag, Berlin, Heidelberg, New York (2001)
[3] *Y. Tokura*, Physics Today, Juli 2003, S. 50
[4] *C. H. Ahn, J.-M. Triscone* und *J. Mannhart*, Nature **424**, 1015 (2003)
[5] *D. G. Schlom* und *J. Mannhart*, High Temperature Superconductors: Thin Films and Multilayers, in: Encyclopedia of Materials: Science and Technology, Elsevier, S. 3806 (2001)
[6] *A. Malozemoff, J. Mannhart* und *D. Scalapino*, Physics Today, April 2005, S. 41.
[7] *J. F. Haeni* et al., Nature **430**, 758 (2004); *K. J. Choi* et al., Science **306**, 1005 (2004)
[8] *R. H. Dennard* et al., IEEE J. Solid-State Circuits **SC-9**, 256 (1974)
[9] *G. D. Wilk* und *R. M. Wallace*, Appl. Phys. Lett. **74**, 2854 (1999); *D. G. Schlom* und *J. H. Haeni*, MRS Bull. **27**, 198 (2002)
[10] *B.-E. Park* und *H. Ishiwara*, Appl. Phys. Lett. **82**, 1197 (2003)
[11] *O. Auciello, J. F. Scott* und *R. Ramesh*, Physics Today, Juli 1998, S. 22
[12] *Y. Cho* et al., Nanotechnology **14,** 637 (2003); *P. Paruch* et al., cond-mat/0411178
[13] *Y. Watanabe* et al., Appl. Phys. Lett. **79**, 3738 (2001)
[14] *M. Kaneko* und *I. Okura* (Hrsg.), Photocatalysis Science and Technology, Kodansha, Tokyo, Springer, Berlin, Heidelberg, New York (2002)
[15] *Yu. S. Dedkov, U. Rüdiger* und *G. Güntherodt*, Phys. Rev. B **65**, 064417 (2002)
[16] *R. von Helmolt* et al., Phys. Rev. Lett. **71**, 2331 (1993)
[17] *P. Curie*, J. Physique 3e Série III, 393 (1894)
[18] *H. Zheng* et al., Science **303**, 661 (2004)
[19] *A. Tsukazaki* et al., Nature Materials **4,** 42 (2004)
[20] *N. K. Pervez, P. J. Hansen* und *R. A. York*, Appl. Phys. Lett. **85**, 4451 (2004)
[21] *A. K. Gutakovskii* et al., Phys. Stat. Sol. A **150**, 127 (1995)
[22] *D. G. Schlom* et al., Mat. Sci. & Eng. B **87**, 282 (2001)
[23] *J. M. D. Coey* und *C. L. Chien*, MRS Bull. **28**, 720 (2003)

Die Autoren

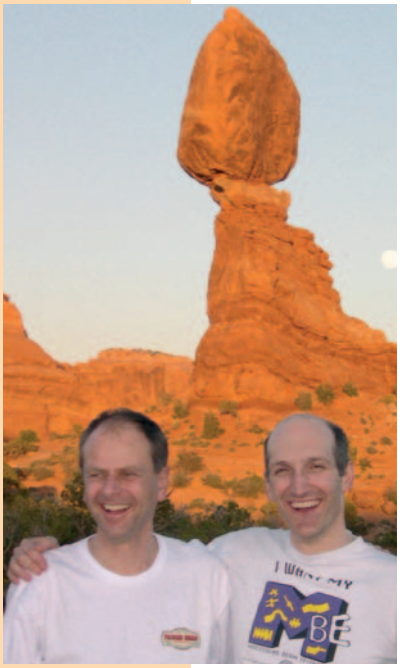

Jochen Mannhart (links) promovierte in Tübingen mit einer Arbeit zur elektronenmikroskopischen Abbildung magnetischer Flussquanten in supraleitenden Tunnelkontakten. Nach einem Post-Doc-Aufenthalt am IBM T. J. Watson Research Center in Yorktown Heights (USA) wurde er Research Staff Member am IBM-Forschungslabor in Rüschlikon (Schweiz). Seit 1996 leitet er den Lehrstuhl Experimentalphysik VI an der Universität Augsburg. Zu seinen Arbeitsgebieten gehören die Oxidelektronik, die Supraleitung und die Rastersondenmikroskopie.
Darrell G. Schlom (rechts) studierte am Caltech (USA) und an der Stanford University (USA), wo er in Materials Science auch promovierte. Anschließend arbeitete er als Post-Doc am IBM-Forschungslabor in Rüschlikon (Schweiz) und wechselte dann zur Penn State University (USA), wo er 2002 zum Professor ernannt wurde. Seine Forschungsgruppe befasst sich mit der Entwicklung alternativer Gate-Oxide und, unter Verwendung der Molekularstrahl-Epitaxie (MBE), mit der Präparation von neuen, für die Oxidelektronik relevanten, Materialien und Heterostrukturen.

INSTITUTE OF PHYSICS PUBLISHING SUPERCONDUCTOR SCIENCE AND TECHNOLOGY

Supercond. Sci. Technol. **17** (2004) S196–S201 PII: S0953-2048(04)71770-4

Progress in the deposition of MgB_2 thin films

X X Xi[1,2,3], A V Pogrebnyakov[1,2], X H Zeng[1], J M Redwing[1,2], S Y Xu[1], Qi Li[1,3], Zi-Kui Liu[2,3], J Lettieri[2,3], V Vaithyanathan[2,3], D G Schlom[2,3], H M Christen[4], H Y Zhai[4] and A Goyal[5]

[1] Department of Physics, The Pennsylvania State University, University Park, PA 16802, USA
[2] Department of Materials Science and Engineering, The Pennsylvania State University, University Park, PA 16802, USA
[3] Materials Research Institute, The Pennsylvania State University, University Park, PA 16802, USA
[4] Condensed Matter Science Division, Oak Ridge National Laboratory, Oak Ridge, TN 37831, USA
[5] Metals and Ceramics Division, Oak Ridge National Laboratory, Oak Ridge, TN 37831, USA

Received 11 November 2003
Published 2 March 2004
Online at stacks.iop.org/SUST/17/S196 (DOI: 10.1088/0953-2048/17/5/021)

Abstract
An MgB_2 thin film deposition technology is the first critical step in the development of superconducting electronics utilizing the 39 K superconductor. It turned out to be a challenging task due to the volatility of Mg and phase stability of MgB_2, the low sticking coefficients of Mg at elevated temperatures, and the reactivity of Mg with oxygen. A brief overview of current deposition techniques is provided here from a thermodynamic perspective, with an emphasis on a very successful technique for high quality *in situ* epitaxial MgB_2 films, the hybrid physical–chemical vapour deposition. Examples of heterostructures of MgB_2 with other materials are also presented.

1. Introduction

Two years after the discovery of superconductivity in MgB_2 at 39 K [1], great progress has been made in the deposition of MgB_2 thin films. This has been driven mostly by the potential of MgB_2 for Josephson junctions and integrated circuits that would be operating at above 20 K [2]. Josephson junctions of MgB_2 should be easier to fabricate than high-T_c superconductors since it is a phonon-mediated BCS superconductor [3] and its coherence length is longer [4]. Its two energy gaps (at 1.8 and 6.8 meV [5, 6]) are larger than Nb (1.5 meV), which could potentially lead to higher speeds than Nb integrated circuits [7].

There are serious difficulties in depositing MgB_2 films, including the volatility of Mg and phase stability of MgB_2 [8, 9], the low sticking coefficients of Mg at elevated temperatures [10], and the reactivity of Mg with oxygen [11, 12]. These challenges have been overcome, and epitaxial MgB_2 films with superior superconducting properties have been produced. In the meantime, MgB_2 Josephson junctions [13–18], SQUIDs [19–21], microwave surface resistance [22, 23, 26, 24, 25], and bolometers [27] have been actively pursued. The current focus of research is on the fabrication of MgB_2/barrier/MgB_2 trilayers for Josephson junctions and circuits that can operate above 20 K.

2. Issues in the deposition of MgB_2 thin films

2.1. Phase stability of MgB_2

Mg is a highly volatile material and the phase stability of MgB_2 is a serious issue for MgB_2 film deposition. For materials containing a volatile constituent (for example As in GaAs [28] and O in $YBa_2Cu_3O_{7-x}$ [29]), thermodynamics can help identify appropriate growth conditions for thin films. The pressure–temperature phase diagram of the Mg–B system, obtained by a CALPHAD calculation [8], is shown in figure 1 for $x_{Mg}/x_B \geqslant 1{:}2$. For the MgB_2 phase to be thermodynamically stable, and for there to be no extra Mg mixed with MgB_2, the film processing conditions need to fall within the growth window marked by 'gas + MgB_2'. Note that the Mg pressure for the growth window is very high.

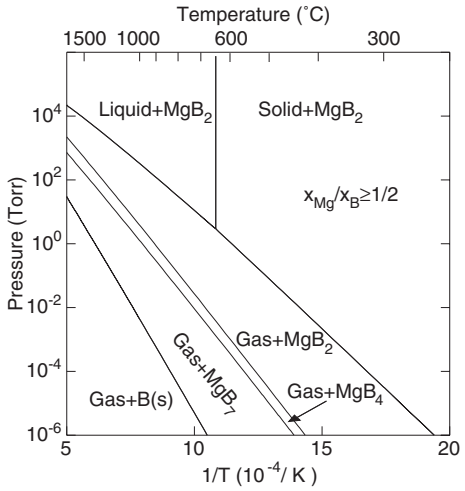

Figure 1. The pressure–temperature phase diagram for the Mg:B atomic ratio $x_{Mg}/x_B \geqslant 1/2$. The region of 'gas + MgB_2' represents the growth window for MgB_2 films (from [8]).

For example, at 750 °C a Mg pressure greater than 44 mTorr is necessary to keep MgB_2 thermodynamically stable. This pressure may be overestimated as Fan *et al* [10, 30] has shown that a significant kinetic barrier to the thermal decomposition of MgB_2 exists. However, the mass spectrometry-Knudsen effusion experiment seems to support the thermodynamic predictions [31].

The pressure–temperature phase diagram is the same for all Mg:B ratios above 1:2. As long as the Mg vapour pressure is within the 'gas + MgB_2' growth window, the Mg:B ratio can be above the stoichiometric 1:2 and does not have to be very carefully controlled. Extra Mg is in the gas phase and will be evacuated. This is the automatic composition control that accompanies the adsorption-controlled growth of films containing volatile species.

2.2. Sticking coefficient of Mg at elevated temperatures

Kim *et al* [10] showed that the sticking coefficient of Mg onto the substrate and onto the deposited B film drops to near zero above 250 °C, whereas that of B does not change. Therefore, at elevated temperatures there is only a small probability that Mg reacts with B to form MgB_2. Similar results have been shown by Ueda and Naito [32, 33] in MgB_2 films prepared by molecular beam epitaxy. This is another reason that an extremely high Mg pressure, thus a large Mg flux, is desirable for the deposition of MgB_2 films at elevated temperatures.

2.3. Reactivity of Mg with oxygen

Mg reacts strongly with oxygen to form MgO: the Gibbs energy for the reaction $2Mg + O_2 = 2MgO$ is about -1.14×10^6 J mol^{-1} of O_2 at 298 K and 1 atm, more negative than those for oxidation of Si and Fe, which are -8.56×10^5 and -5.08×10^5 J mol^{-1}, respectively. For the deposition of MgO films, an oxygen pressure of 10^{-6} Torr is sufficient to form the MgO phase at 300 °C [34]. For *in situ* deposition of MgB_2 at 250–300 °C, a background pressure of 3×10^{-8} Torr leads to insulating films [12, 32, 33]. The oxidation of Mg is extremely detrimental for the deposition of MgB_2 because it effectively reduces the Mg pressure from what is generated from the Mg source, thus pushing the system to the thermodynamically unstable region even when the nominal Mg pressure generated is high. Further, it leads to insulating grain boundaries and prevents grain growth of MgB_2, resulting in nanocrystalline structure [11, 35], poor connectivity [36], and poor superconducting properties. On the other hand, Eom *et al* [11] have suggested that some level of oxygen contamination may help to enhance the flux pinning in MgB_2 films.

3. Deposition techniques for MgB_2

From a thermodynamic standpoint, the MgB_2 deposition techniques can be categorized according to the highest temperatures employed during the film processing. In this paper, the term 'high temperature' refers to those around and above 850 °C, 'intermediate temperature' around 600 °C, and 'low temperature' around 300 °C and below.

3.1. High-temperature processes

Typically, a growth temperature about one half of the melting temperature (in kelvin) is optimal for epitaxy and high crystallinity in thin films. For MgB_2, that temperature is around ∼1080 °C. This requires a Mg pressure of at least 11 Torr according to thermodynamic stability conditions [8]. It is possible to generate such high Mg pressures by heating Mg bulk in an enclosure, which then allows processing of MgB_2 thin films at high temperatures. The technique to growth MgB_2 thin films with *ex situ* annealing in Mg vapour above 850 °C corresponds to the high temperature–high Mg pressure region of the phase diagram.

In the report by Kang *et al* [37], amorphous B thin films were deposited at room temperature, sealed into a Ta tube in an Ar atmosphere together with a high-purity Mg metal, and annealed at 900 °C for 10–30 min. The B film may be deposited by pulsed laser deposition [37–40], magnetron sputtering [41, 43, 42, 44], electron-beam evaporation [45, 46], thermal evaporation [47, 48], or chemical vapour deposition [49–51]. The annealing temperatures used are mostly above 850 °C [40]. The precursor films may also be deposited from a MgB_2 target [11]. A somewhat different approach sealed the precursor film and Mg in a Nb box *in situ* in the vacuum chamber before annealing at 830 °C [42].

The high temperature ensures that the MgB_2 thin films grown by the high-temperature processes are epitaxial [40, 41]. The superconducting properties are also excellent, showing $T_c \sim 39$ K [37, 38, 45] and very high J_c exceeding 10^7 A cm^{-2} at zero field [46, 52].

3.2. Intermediate-temperature processes

The two-step *in situ* annealing techniques employ intermediate temperatures. Precursor films or multilayers of MgB_2, Mg + MgB_2, or Mg + B, are deposited at room temperature to 300 °C, and then annealed *in situ* in the growth chamber at temperatures and duration such that severe Mg loss or MgB_2 decomposition does not occur. The precursor films may be deposited by pulsed laser deposition [10, 35, 38, 53, 54, 57, 55, 56], sputtering [58–60], or thermal evaporation [47], or e-beam evaporation [61–63].

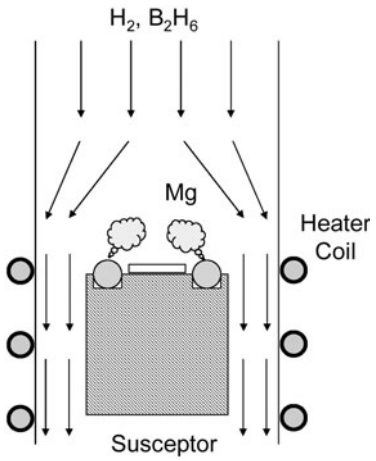

Figure 2. Schematic of the HPCVD reactor. (From [69].)

During the annealing, Mg sublimes or evaporates, MgB_2 phase forms, nucleation and growth of crystallites takes place, and MgB_2 decomposes. Kim *et al* [10] studied in detail the interplay between the annealing temperature and duration. They found that one may either anneal at 550 °C for 30 min or at 800 °C for a very short period. Because the Mg pressure is provided locally by the evaporation of excess Mg in the films and eventually drops with time, careful balancing between MgB_2 formation and decomposition is critical.

Because of the lower temperature used, films produced by the intermediate-temperature processes do not have as good crystallinity as in the high-temperature processes. They are often nanocrystalline [35]. The T_c ranges from the early reports of around or below 25 K [38, 53, 54, 57] to about 34 K [10, 35].

3.3. Low-temperature processes

If the MgB_2 phase can form at lower temperatures, the Mg pressure required for phase stability can be greatly reduced, for example to 10^{-8} Torr at 300 °C [8], easily achievable by vacuum deposition techniques. This is indeed the case as demonstrated by the low-temperature *in situ* growth of MgB_2 thin films reported by several groups [10, 12, 32, 33, 64–67]. A key to their success is the reduced oxidation of Mg, partly due to the UHV background and partly due to the use of pure metal sources. The low sticking coefficient of Mg at elevated temperatures [10, 32, 33], however, has limited the deposition below about 300 °C.

Superconducting MgB_2 films were obtained for substrate temperatures between 150 and 320 °C, but higher temperature corresponds to better T_c: $T_c \sim 36$ K for 320 °C [32, 33]. The films show clear MgB_2 peaks in x-ray diffraction [32, 33, 64, 68] and the grains are as large as 400 Å [64, 68].

4. Hybrid physical–chemical vapour deposition (HPCVD)

4.1. Setup and process

Guided by the thermodynamic understanding that a high Mg vapour pressure is necessary for *in situ* deposition of MgB_2 films, we have developed the HPCVD technique. It combines physical vapour deposition (heated bulk Mg is used as the Mg source) with chemical vapour deposition (diborane, B_2H_6, is used as the boron precursor gas). The schematic of the system is shown in figure 2 and the details have been described elsewhere [69, 70]. When the substrate along with the bulk Mg pieces are heated to 700–760 °C in the 400 sccm, 100 Torr H_2 carrier gas, a high Mg vapour pressure is generated in the vicinity of the substrate. As the Mg sticking coefficient is extremely low at this temperature, no deposition of Mg occurs. The 1000 ppm B_2H_6 in H_2 mixture is then introduced into the reactor to initiate growth. The deposition rate depends on the B_2H_6 flow rate, and can be controlled from 3 to 18 Å s^{-1} [71]. After deposition, the B_2H_6 gas is switched off and the film is cooled in H_2 to room temperature.

The HPCVD technique solves all the three problems discussed in section 2. The high Mg vapour pressure satisfies the thermodynamic phase stability condition at the temperature used for the deposition. At the same time, it provides an abundance of Mg to react with B originated from the breaking up of B_2H_6. The reducing hydrogen ambient in the deposition process suppresses the oxidation of Mg. No MgO formation has been observed in HPCVD MgB_2 films on SiC substrates, although local MgO regions are seen on Al_2O_3 substrate near the film/substrate interface, likely caused by oxygen diffusion out of the substrate [69].

The processing temperature used in HPCVD, around 700 °C, is between the high and intermediate temperatures

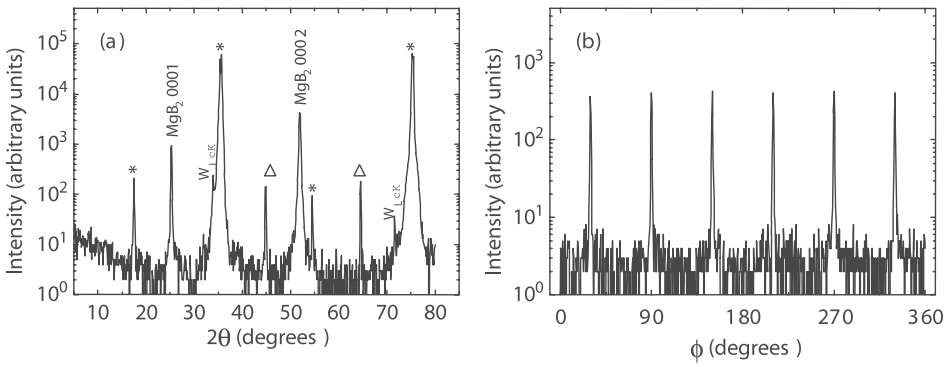

Figure 3. X-ray diffraction spectra of a MgB_2 thin film on a (0001) 4H-SiC substrate. (a) θ–2θ scan and (b) ϕ scan of the $10\bar{1}2$ MgB_2 reflection. The substrate peaks are marked by $*$, while the unidentifiable substrate peaks are marked as $\triangle$. (From [72].)

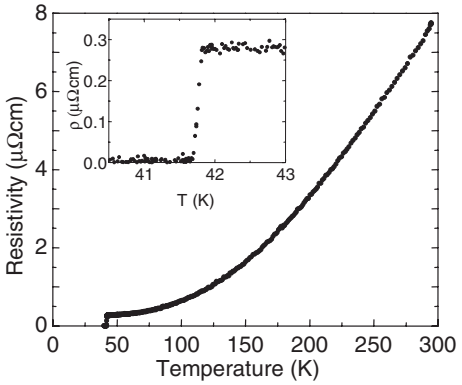

Figure 4. Resistivity versus temperature for a 2250 Å-thick MgB_2 film on 4H-SiC. The inset shows details at the superconducting transition. (From [71].)

defined in this paper. In principle, it can be extended to lower temperatures. The current reactor design does not allow that since the Mg vapour pressure is tied to the substrate temperature. The new generation of HPCVD system, where the substrate temperature and Mg vapour pressure are independently controlled, would allow intermediate and low temperature operations of HPCVD.

4.2. Thin film properties

The high deposition temperatures in HPCVD, made possible by the high Mg vapour pressure, result in excellent epitaxy and crystallinity in the deposited MgB_2 films. Figure 3 shows (a) the θ–2θ scan and (b) the ϕ scan of x-ray diffraction from a MgB_2 film on a (0001) 4H-SiC substrate. 4H-SiC (as well as 6H-SiC) has a hexagonal lattice that matches well with MgB_2 [72]. The θ–2θ scan shows a c-axis orientation, and the ϕ scan shows that the films are in-plane aligned with the substrate lattice. The rocking curves for both θ–2θ and ϕ scans are sharp, indicating good crystallinity. The MgB_2 film on SiC has its hexagonal lattice directly aligned with that of the substrate. Similar epitaxy is also obtained on (0001) sapphire substrate, however the hexagonal lattice of the film is rotated by 30° around the c axis to reduce the large lattice mismatch with the sapphire substrate [69].

The superconducting and normal-state transport properties of the MgB_2 thin films grown by HPCVD are excellent, characterized by $T_{c0} = 41.8$ K, $\rho_0 = 0.26$ $\mu\Omega$ cm, $RRR > 30$ [71], and self-field $J_c = 3.4 \times 10^7$ A cm^{-2} [72]. The resistivity versus temperature curve for a MgB_2 thin film on a 4H-SiC substrate is shown in figure 4. The low resistivity indicates that the film is very clean.

5. Heterostructures of MgB_2 with other materials

MgB_2 Josephson devices and integrated circuits require multilayers of MgB_2 with other insulating and metallic materials. After the successes in the deposition of single-layer MgB_2 thin films, the focus of the research naturally shifts to the deposition of multilayers, in particular the MgB_2/barrier/MgB_2 structures. The structural, chemical and electrical properties at the interfaces are critical for device and circuit development.

We have studied multilayers of MgB_2 thin films with several materials with hexagonal structures, including AlN and TiB_2. Both materials lattice match well with MgB_2 and are chemically stable against reaction with MgB_2. AlN has been

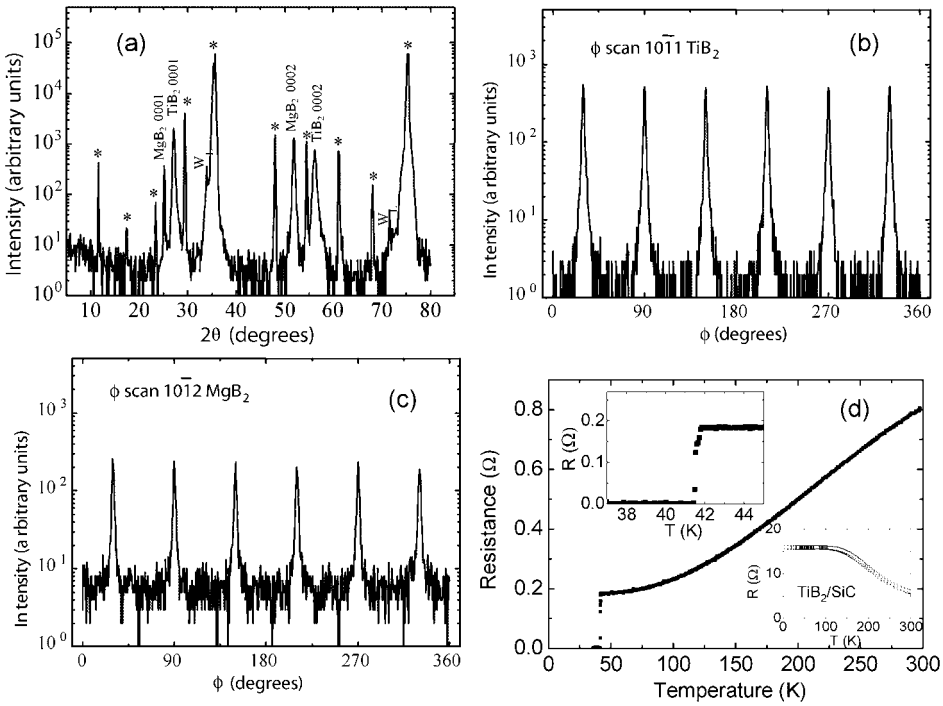

Figure 5. X-ray diffraction spectra and R versus T curve of a MgB_2/TiB_2 bilayer on a (0001) 6H-SiC substrate. (a) The θ–2θ scan, (b) the ϕ scan of the 10$\bar{1}$1 TiB_2 reflection, (c) the ϕ scan of the 10$\bar{1}$2 MgB_2 reflection, and (d) the R versus T curve. The insets to (d) are the details near the superconducting transition and the resistance of the TiB_2 layer.

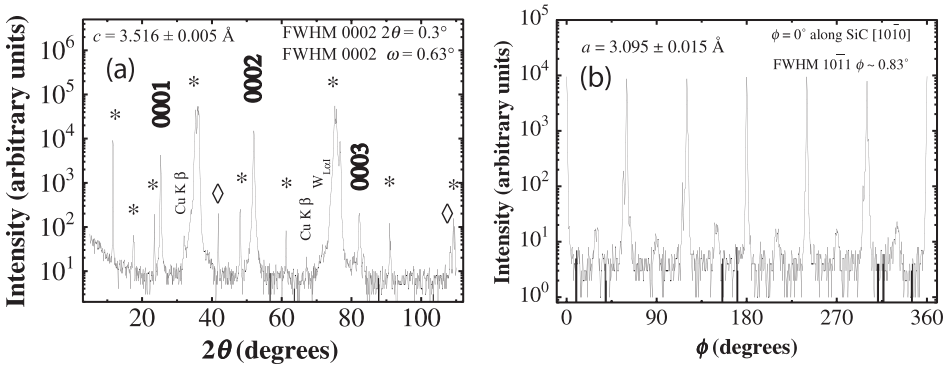

Figure 6. X-ray diffraction spectra of a MgB_2/AlN bilayer on a SiC substrate. (a) The θ–2θ scan, (b) the ϕ scan of the 10$\bar{1}$1 MgB_2 reflection.

used as a barrier layer for MgB_2 Josephson junctions [17]. TiB_2 is a highly conductive material with excellent mechanical, tribological, chemical and thermal properties [73].

The 1500 Å thick TiB_2 layer was grown by pulsed laser deposition [74]. The background during the deposition was 2×10^{-4} Torr of Ar/4% H_2 and the substrate temperature was 600 °C. A KrF excimer laser (wavelength: 248 nm) was used at a repetition rate of 10 Hz, leading to a growth rate of 0.1–0.4 Å. After the film was cooled to room temperature, it was then taken out of the deposition chamber and loaded to the HPCVD reactor. A MgB_2 film of 1200 Å was grown on the TiB_2 layer with a substrate temperature of 720 °C.

Figure 5 shows the structural and superconducting properties of the MgB_2/TiB_2 bilayer film on the SiC substrate. The θ–2θ scan in figure 5(a) shows that both layers are c-axis oriented. The ϕ scans in figure 5(b) for the TiB_2 layer, of the 10$\bar{1}$1 reflection, and figure 5(c) for the MgB_2 layer, of the 10$\bar{1}$2 reflection, indicate that both layers are in-plane aligned with each other and with the substrate. Because TiB_2 is conducting, it is difficult to calculate the resistivity of the MgB_2 film, however it shows a superconducting transition at above 40 K, indicating a good superconducting property. After etching off the MgB_2 layer, the resistance of the TiB_2 layer is measured and plotted in the inset, which shows a low resistance.

The AlN epitaxial layers were deposited by MOCVD on SiC substrates. Similar processes for the growth of the MgB_2/TiB_2 bilayer films were used for the growth of MgB_2/AlN bilayer films. Figure 6 shows (a) the θ–2θ scan and (b) the ϕ scan of the 10$\bar{1}$1 MgB_2 reflection for a MgB_2/AlN bilayer film with a thickness of the MgB_2 layer of 1200 Å. The results show that both AlN and MgB_2 layers are c-axis oriented and are in-plane aligned with each other and with the substrate, except for a small amount of 30° rotational twinning. Figure 7 shows a superconducting transition at above 40 K and a high RRR value, indicating a good superconducting property in the MgB_2 layer on the AlN layer.

6. Conclusion

After two years of intensive research around the world, the key materials issues in the deposition of MgB_2 thin films, namely the volatility of Mg and phase stability of MgB_2, the low sticking coefficients of Mg at elevated temperatures, and the reactivity of Mg with oxygen, have been understood, and successful deposition techniques have been developed. The superconducting properties of the single layer MgB_2 films by several techniques are very good and Josephson junctions of MgB_2 with other low-T_c superconductors as the counter electrodes have been demonstrated. The next goal of research is all-MgB_2 Josephson junctions that can operate above 20 K. For this purpose, appropriate MgB_2/barrier/MgB_2 trilayer structures need to be developed.

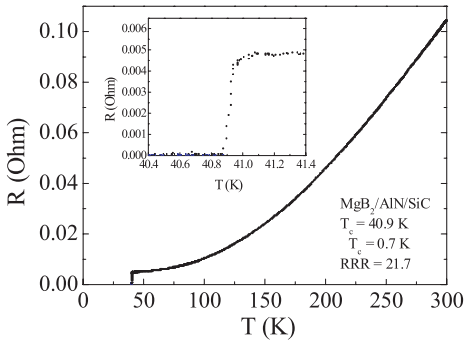

Figure 7. Resistivity versus temperature for a MgB_2/AlN bilayer on a SiC substrate. The inset shows details at the superconducting transition.

(This figure is in colour only in the electronic version)

Acknowledgments

This work is supported in part by ONR under grant Nos N00014-00-1-0294 (Xi) and N0014-01-1-0006 (Redwing), by NSF under grant Nos DMR-9876266 and DMR-9972973 (Li), DMR-9983532 (Liu), and by DOE through grant DE-FG02-97ER45638 (Schlom). Work at ORNL is supported by DOE Office of Energy Efficiency and Renewable Energy and Office of Power Technologies-Superconductivity Program.

References

[1] Nagamatsu J, Nakagawa N, Muranaka T, Zenitani Y and Akimitsu J 2001 *Nature* **410** 63
[2] Rowell J 2002 *Nature Mater.* **1** 5
[3] Bud'ko S L, Lapertot G, Petrovic C, Cunningham C E, Anderson N and Canfield P C 2001 *Phys. Rev. Lett.* **86** 1877

Structural and transport properties of epitaxial Na_xCoO_2 thin films

A. Venimadhav
Department of Physics, The Pennsylvania State University, University Park, Pennsylvania 16802

A. Soukiassian
Department of Materials Science and Engineering, The Pennsylvania State University, University Park, Pennsylvania 16802

D. A. Tenne and Qi Li[a)]
Department of Physics, The Pennsylvania State University, University Park, Pennsylvania 16802

X. X. Xi
Department of Physics and Department of Materials Science and Engineering, The Pennsylvania State University, University Park, Pennsylvania 16802

D. G. Schlom, R. Arroyave, and Z. K. Liu
Department of Materials Science and Engineering, The Pennsylvania State University, University Park, Pennsylvania 16802

H. P. Sun and Xiaoqing Pan
Department of Materials Science and Engineering, The University of Michigan, Ann Arbor, Michigan 48109

Minhyea Lee and N. P. Ong
Department of Physics, Princeton University, New Jersey 08544

(Received 16 May 2005; accepted 27 August 2005; published online 20 October 2005)

We have studied structural and transport properties of epitaxial Na_xCoO_2 thin films on (0001) sapphire substrate prepared by topotaxially converting an epitaxial Co_3O_4 film to Na_xCoO_2 with annealing in Na vapor. The films are *c*-axis oriented and in-plane aligned with $[10\bar{1}0]Na_xCoO_2$ rotated by 30° from $[10\bar{1}0]$ sapphire. Different Na vapor pressures during the annealing resulted in films with different Na concentrations, which showed distinct transport properties. © *2005 American Institute of Physics*. [DOI: 10.1063/1.2117619]

Layered cobaltate Na_xCoO_2 has attracted much attention recently due to its exceptional properties.[1] It has an unusually high thermoelectric power with low mobility, low resistivity, and high carrier density.[1] The Fermi surface[2] and electrical properties[3] of Na_xCoO_2 depend on the Na concentration: $Na_xCoO_2 \cdot 1.3H_2O$ is a superconductor for x around 0.3;[4,5] at $x=0.5$, it is a charge-ordered insulator;[6] and at higher Na concentrations it becomes a metal following the Curie–Weiss law.[3,7] The triangular structure of the CoO_2 planes and the strong electron correlation effect have been recognized as sources of rich properties of Na_xCoO_2.[8] For example, the large thermopower in Na_xCoO_2 has been attributed to the spin entropy due to the strong electron correlation effects.[9] Na_xCoO_2 has been prepared in polycrystalline and single-crystalline forms, but there are very few reports on Na_xCoO_2 thin films.[10–12] Recently, Ohta *et al.*[10] reported epitaxial Na_xCoO_2 films by reactive solid phase epitaxy; however, the Na concentration in the films was not well controlled. In this letter, we describe the structural and transport properties of epitaxial Na_xCoO_2 thin films fabricated by a process which is similar to that used by Ohta *et al.*,[11] but allows some degree of control of the Na concentration in the film. Films with different Na concentrations showed very different transport properties.

The epitaxial Na_xCoO_2 films were fabricated using a two-step process. First, an epitaxial Co_3O_4 film was grown by pulsed laser deposition (PLD) on a (0001) sapphire substrate. A KrF excimer laser was used with an energy density of 3.7 J/cm^2 on a CoO target. The substrate was kept at 650–700 °C during the deposition in 200 mTorr flowing oxygen. At a repetition rate of 8 Hz, the deposition rate is 0.11 Å/s. The Co_3O_4 film was then sealed in an alumina crucible with sodium bicarbonate ($NaHCO_3$) or sodium acetate ($NaOOCCH_3$) powder and heated to 800 °C for 2.5 h to form the Na_xCoO_2 film. A topotaxial conversion occurred, during which the crystallographic alignment of Co_3O_4 was inherited by Na_xCoO_2. The thickness of the Co_3O_4 film was around 1600 Å, which became ~3000 Å following the topotaxial conversion to Na_xCoO_2.

X-ray diffraction scans of an epitaxial Co_3O_4 film on a (0001) sapphire substrate are shown in Fig. 1. Co_3O_4 has a spinel structure with a space group Fd3m. The θ-2θ scan in Fig. 1(a) shows only peaks arising from diffraction off (111) Co_3O_4 planes apart from the substrate peak, indicating a phase-pure Co_3O_4 film with [111] direction normal to the substrate surface. The rocking curve of the Co_3O_4 111 peak had a full width at half maximum (FWHM) of 0.24° in ω, equal to our instrumental resolution. A lattice parameter $a = 8.087 \pm 0.001$ Å was obtained. A ϕ scan of the 220 Co_3O_4 peak is shown in Fig. 1(b), where $\phi=0°$ is aligned parallel to the $[10\bar{1}0]$ in-plane direction of the sapphire substrate. The presence of six 220 peaks (where a single crystal would show only three) indicates an epitaxial Co_3O_4 film with two twinned variants related by a 60° rotation. The FWHM in ϕ is 0.55°. The in-plane epitaxial relationship is that [110] Co_3O_4 is rotated by ±30° from $[10\bar{1}0]Al_2O_3$.

[a)]Electronic mail: qil1@psu.edu

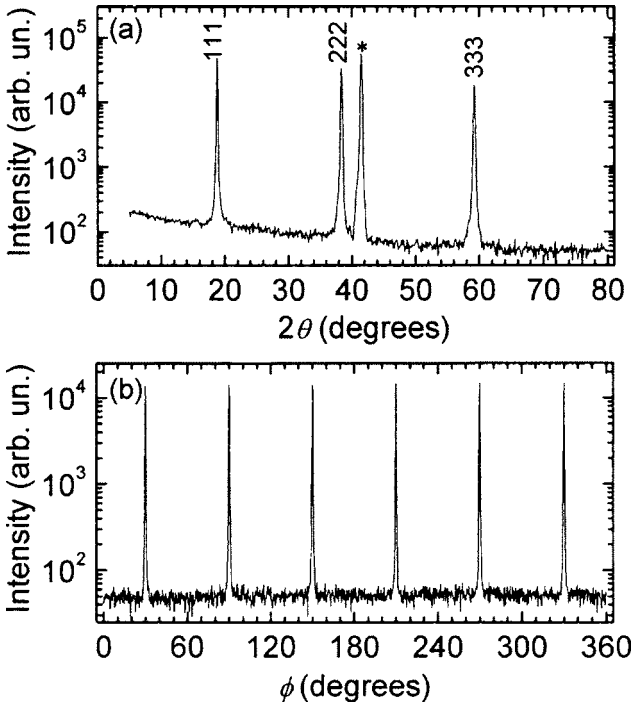

FIG. 1. (a) θ-2θ x-ray diffraction scan of a Co_3O_4 film grown on a (0001) sapphire substrate. The 0006 sapphire substrate peak is marked by an asterisk (*). (b) ϕ-scan of the 220 Co_3O_4 peak at $\chi=54.7°$, indicating that the film is epitaxial. $\phi=0$ is parallel to the $[10\bar{1}0]$ in-plane direction of the substrate.

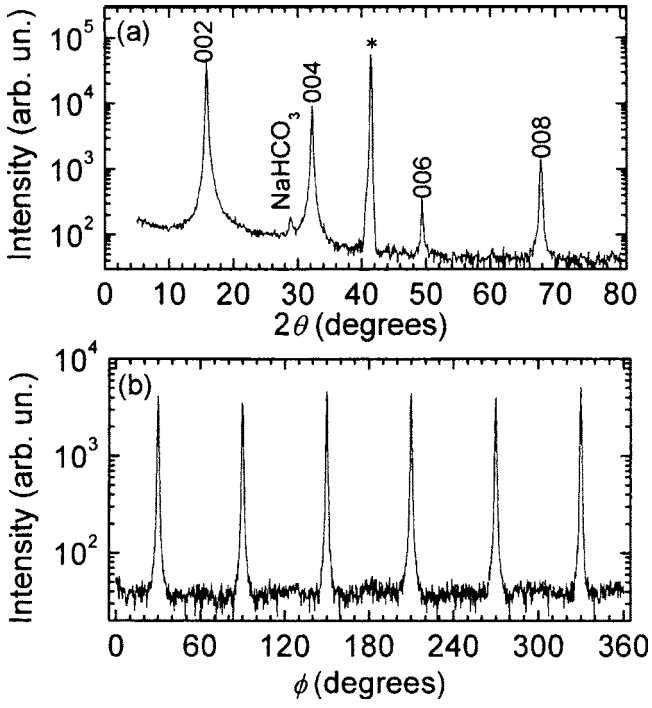

FIG. 2. (a) θ-2θ x-ray diffraction scan of a Na_xCoO_2 film on a (0001) sapphire substrate. The 0006 sapphire substrate peak is marked by an asterisk (*). (b) ϕ-scan of the $10\bar{1}2$ Na_xCoO_2 peak at $\chi=23.6°$, indicating that the film is epitaxial. $\phi=0$ is parallel to the $[10\bar{1}0]$ in-plane direction of the substrate.

The crystallinity and phase purity of the film after the topotaxial conversion depend sensitively on the annealing conditions. Under the optimized condition (800 °C for 2.5 h), the film is completely converted into Na_xCoO_2 without decomposition. X-ray diffraction scans of a Na_xCoO_2 film, which was converted from a Co_3O_4 film by annealing with $NaHCO_3$ powder, are shown in Fig. 2. Na_xCoO_2 has a hexagonal $P6_322$ structure. In the θ-2θ scan in Fig. 2(a), 00ℓ peaks of Na_xCoO_2 are observed beside a substrate peak, indicating a c-axis-oriented film. A weak peak of $NaHCO_3$ is also present due to the $NaHCO_3$ dust on the film surface resulting from the annealing process, which is also confirmed by a Raman scattering measurement. The ϕ-scan of the $10\bar{1}2$ Na_xCoO_2 peak is shown in Fig. 2(b), where $\phi=0$ is parallel to the $[10\bar{1}0]$ direction of the sapphire substrate. The six-fold symmetry indicates a topotaxial conversion from the epitaxial Co_3O_4 film with the angle between $[10\bar{1}0]$ Na_xCoO_2 and $[10\bar{1}0]$ sapphire being 30°. Lattice constants $c=11.02\pm0.003$ Å and $a=2.456\pm0.003$ Å were obtained. The rocking curves showed a broad FWHM of 2° in ω and 1.02° in ϕ. These values indicate that the crystalline quality of the topotaxially converted Na_xCoO_2 film is not as high as that of the starting Co_3O_4 film.

Figure 3(a) is a bright-field cross-sectional transmission electron microscopy (TEM) image of a Na_xCoO_2 film. It shows the film with a smooth surface. An x-ray energy dispersive spectroscopy (EDS) analysis shows a generally uniform distribution of Na concentration in the film. Occasionally, thin layers of amorphous material, such as the white line shown in Fig. 3(a), occur in the film, which have higher Na concentration than that in the crystalline Na_xCoO_2 film. A much thicker amorphous layer, nonuniform and discontinuous, was observed at the film/substrate interface, whose chemical composition is similar to the substrate (Al_2O_3). Figures 3(b) and 3(c) are selected area electron diffraction (SAED) patterns corresponding to the film and the substrate, respectively. They show an epitaxial relationship between the Na_xCoO_2 film and the substrate of $Na_xCoO_2(0001)\times[10\bar{1}0]\|$ sapphire $(0001)[2\bar{1}\bar{1}0]$, which is consistent with the x-ray diffraction analysis. The smeared intensity distribution of reflections in Fig. 3(b) indicates distortions of crystal

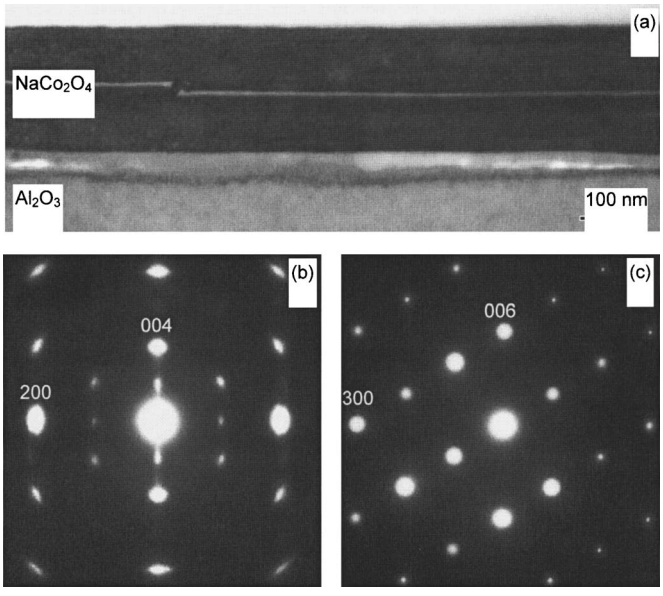

FIG. 3. (a) Bright-field TEM image of a Na_xCoO_2 film on a sapphire substrate. The white line in the middle of the film corresponds to a thin layer of Na-rich amorphous material. (b) SAED pattern from the film. (c) SAED pattern corresponding to the substrate.

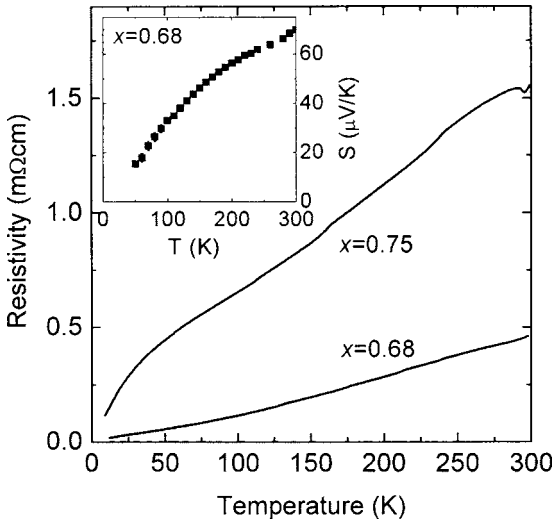

FIG. 4. Resistivity vs temperature curves for two Na_xCoO_2 films with different Na concentrations. Inset: Thermopower vs temperature for a Na_xCoO_2 film with $x=0.68$.

planes in the thin film, consistent with high-resolution TEM observations of waviness in the Na_xCoO_2 lattice planes. Details of the microstructure investigation of the Na_xCoO_2 films will be published elsewhere.

The Na concentration of the Na_xCoO_2 films depends on the powder used for the annealing. At 800 °C, the equilibrium vapor pressure is 0.155 Torr for $NaHCO_3$ and 444 Torr for $NaOOCCH_3$. EDS measurements show that the Na concentration is always $x=0.68\pm0.03$ for films annealed in $NaHCO_3$. The x value in films annealed in $NaOOCCH_3$ depends on the annealing conditions, and for the optimized condition given above (800 °C for 2.5 h) $x=0.75\pm0.02$. Figure 4 shows the resistivity versus temperature curves of two Na_xCoO_2 films with different Na concentrations. The temperature dependence for the film annealed in $NaOOCCH_3$, marked by "$x=0.75$," is characteristic of bulk and single-crystal Na_xCoO_2 samples with $x=0.75$.[3,12] The downturn at low temperatures has been attributed to a phase transition to an antiferromagnetic spin-density wave.[13] The resistivity behavior of the film annealed in $NaHCO_3$, marked by "$x=0.68$," is consistent with single crystals with lower Na concentrations.[3] The inset to Fig. 4 shows the thermopower, S, versus temperature for a film with $x=0.68$. A temperature gradient was generated by a resistive heater attached on one end of the film while the other end was mounted on a cold finger. A pair of type-E (chrome-constantan) thermocouples and a pair of 25 μm gold wires were used to measure the temperature gradient and the difference of electric potential, respectively, to obtain the thermoelectric power. The magnitude of S at 300 K, as well as the overall temperature dependence shown in the figure, is consistent with the result from the in-plane measurement of single crystals with $x=0.7$.[9] These results further confirm the Na concentration measurements by EDS.

In conclusion, epitaxial thin films of Na_xCoO_2 were prepared by annealing PLD-grown epitaxial Co_3O_4 films in Na vapor. The Na compounds used during annealing, $NaHCO_3$ and $NaOOCCH_3$, have different Na vapor pressures, resulting in Na_xCoO_2 films of two different Na concentrations. The topotaxial conversion led to a poorer crystallinity in the Na_xCoO_2 films than in Co_3O_4 films. Nevertheless, the films are c-axis oriented with in-plane alignment with the substrate. The temperature dependent transport properties are distinctly different for films of different Na concentrations, and they are consistent with the bulk results. Our results demonstrate that some degree of control of the Na concentration in the Na_xCoO_2 films can be achieved by using Na compounds of different vapor pressures during annealing.

The work was partially supported by the NSF under Grant Nos. DMR-0405502 (for Q.L.), DMR-0103354 (for X.X.X. and D.G.S.), DMR-0205232 (for Z.K.L.), and DMR-0308012 (for X.P.), by the U.S. DOE under Grant Nos. DE-FG02-01ER45907 (for X.X.X.) and DE-FG02-97ER45638 (for D.G.S.), and by the ONR under Grant No. N00014-04-1-0057 (for N.P.O.).

[1] I. Terasaki, Y. Sasago, and K. Uchinokura, Phys. Rev. B **56**, R12685 (1997).
[2] P. H. Zhang, W. D. Luo, M. L. Cohen, and S. G. Louie, Phys. Rev. Lett. **93**, 236402 (2004).
[3] M. L. Foo, Y. Wang, S. Watauchi, H. W. Zandbergen, T. He, R. J. Cava, and N. P. Ong, Phys. Rev. Lett. **92**, 247001 (2004).
[4] K. Takada, H. Sakurai, E. Takayama-Muromachi, F. Izumi, R. A. Dilanian, and T. Sasaki, Nature (London) **422**, 53 (2003).
[5] R. E. Schaak, T. Klimczuk, M. L. Foo, and R. J. Cava, Nature (London) **424**, 527 (2003).
[6] K. W. Lee, J. Kunes, P. Novak, and W. E. Pickett, Phys. Rev. Lett. **94**, 026403 (2005).
[7] I. R. Mukhamedshin, H. Alloul, G. Collin, and N. Blanchard, Phys. Rev. Lett. **93**, 167601 (2004).
[8] J. Sugiyama, J. H. Brewer, E. J. Ansaldo, H. Itahara, T. Tani, M. Mikami, Y. Mori, T. Sasaki, S. Hebert, and A. Maignan, Phys. Rev. Lett. **92**, 017602 (2004).
[9] Y. Y. Wang, N. S. Rogado, R. J. Cava, and N. P. Ong, Nature (London) **423**, 425 (2003).
[10] H. Ohta, S.-W. Kim, S. Ohta, K. Koumoto, M. Hirano, and H. Hosono, Cryst. Growth Des. **5**, 25 (2005).
[11] W. D. Si, S. M. Park, and P. Johnson, in *Proceedings of the 2004 MRS Fall Meeting Technical Program* (Materials Research Society, Pittsburgh, PA, 2004), p. 204.
[12] Y. Krockenberger, I. Fritsch, G. Cristiani, A. Matveev, L. Alff, H.-U. Habermeier, and B. Keimer, Appl. Phys. Lett. **86**, 191913 (2005).
[13] B. C. Sales, R. Jin, K. A. Affholter, P. Khalifah, G. M. Veith, and D. Mandrus, Phys. Rev. B **70**, 174419 (2004).

Investigations of MgB_2/MgO and MgB_2/AlN Heterostructures for Josephson Devices

P. Orgiani, Y. Cui, A. V. Pogrebnyakov, J. M. Redwing, V. Vaithyanathan, D. G. Schlom, and X. X. Xi

***Abstract*—We report structural and transport proprieties of MgB_2/MgO and MgB_2/AlN multilayers for MgB_2 Josephson junctions. The MgB_2 layers were grown by hybrid physical chemical vapor deposition (HPCVD). The epitaxial $MgB_2/MgO/MgB_2$ trilayers were grown in situ in the HPCVD system. The AlN layers were grown at room temperature by pulsed laser deposition, and the $MgB_2/AlN/MgB_2$ trilayers were deposited ex situ with the deposition of the AlN layer between the depositions of the top and bottom MgB_2 layers. Although slightly less perfect than in films grown directly on sapphire and SiC substrates, excellent superconducting and transport properties were obtained in the MgB_2 layers in both heterostructures. The result addressed only the first of many issues about the adequacy of using MgO and AlN as the barrier materials for all-MgB_2 planar Josephson junctions, i.e. the ability to obtain good structural and superconducting properties in both electrode layers using the trilayer deposition process. It allows us to further investigate the conditions for better wetting and coverage of the insulator layers, as well as other critical issues in the fabrication of all-MgB_2 planar Josephson junctions.**

***Index Terms*—Heterostructures, Josephson junctions, magnesium diboride.**

I. Introduction

SUPERCONDUCTING electronics based on low temperature superconductors (LTS) have been making impressive progress in recent years [1]. However, the low operating temperature of such devices ($T = 4.2$ K) has represented a major problem for widespread practical applications. With the discovery of conventional superconductivity in magnesium diboride MgB_2 [2], which shows a critical temperature of about 40 K, such an obstacle can be significantly alleviated [3].

MgB_2 Josephson devices and integrated circuits require multilayers of MgB_2 with other insulating and metallic materials. In the last few years several types of MgB_2 Josephson junctions have been made. These include MgB_2 nanobridges formed by focused ion beam [4], [5], planar MgB_2 junctions created by local ion damage [6]–[8], $MgB_2/Ag/MgB_2$ step-edge junctions [9], and ramp-type junctions [10]. Planar trilayer junctions with one electrode being MgB_2 and the other a low temperature superconductor (S/I/S' junctions) have been reported by several groups [11]–[13]. However, trilayer all-MgB_2 Josephson junctions are still to be realized.

In order to fabricate MgB_2 planar trilayer junctions, we have studied multilayers of MgB_2 thin films with several materials that lattice-match with MgB_2. In this paper, we report results on MgO and AlN, which have excellent lattice matching with MgB_2 and are chemically stable against reaction with MgB_2. Besides, AlN [12] has been successfully used as a barrier layer in $MgB_2/AlN/NbN$ Josephson junctions and MgO in $Au/MgO/MgB_2$ junctions [13]. We have followed a completely in situ approach for $MgB_2/MgO/MgB_2$ heterostructures and an ex situ approach for $MgB_2/AlN/MgB_2$ heterostructures. For all the samples, we have found that both the top and bottom MgB_2 layers have excellent superconducting properties, which is important for the realization of all-MgB_2 Josephson junctions.

II. Growth of Heterostructures

The MgB_2 crystal structure resembles that of graphite ($P6/mmm$ space group). It shows an in-plane lattice constants of $a = 3.08$ Å and an out-of-plane $c = 3.52$ Å, respectively [2]. The in-plane lattice constant of MgO is 4.217 Å, which corresponds to a lattice spacing in the triangular lattice of the (111) plane of 2.982 Å. The in-plane lattice constant of AlN is 3.113 Å. The lattice mismatch between MgB_2 and (111)MgO and (0001)AlN are -3.2% and 1.1%, respectively.

The MgB_2 films were made by hybrid physical chemical vapor deposition (HPCVD) on (0001) sapphire or (0001)SiC. Details of the HPCVD technique have been reported elsewhere [14]. For MgB_2 thin films, the growth temperature ranges from 680°C to 720°C under a pressure (mainly hydrogen) of 100 Torr. The required Mg partial pressure for thermodynamic phase stability of MgB_2 [15] is provided by the heating of Mg pieces placed on the heater next to the substrate. The MgB_2 film growth begins when the boron precursor gas, 1% diborane (B_2H_6) in H_2, starts to flow into the reactor. XRD showed that the films on both (0001) sapphire and (0001)SiC are c-axis oriented and epitaxial [14], [16]. The a-axis of MgB_2 is parallel with the a-axis of SiC [16], but is rotated by 30° with respect to the a-axis of sapphire [14].

Manuscript received October 3, 2004. This work was supported in part by ONR under Grants N00014-00-1-0294 and N0014-01-1-0006, in part by NSF under Grant DMR-0306746, and in part by DOE under Grant DE-FG02-03ER46063.

P. Orgiani is with the Department of Physics, The Pennsylvania State University, University Park, PA 16802 USA, and also with INFM Coherentia, Universita' di Napoli Federico II, Dipartimento di Fisica, Napoli, Italy (e-mail: puo2@psu.edu).

Y. Cui is with the Department of Physics, The Pennsylvania State University, University Park, PA 16802 USA.

A. V. Pogrebnyakov and X. X. Xi are with the Department of Physics and Department of Materials Science and Engineering, The Pennsylvania State University, University Park, PA 16802 USA.

J. M. Redwing, V. Vaithyanathan, and D. G. Schlom are with the Department of Materials Science and Engineering, The Pennsylvania State University, University Park, PA 16802 USA.

Digital Object Identifier 10.1109/TASC.2005.849764

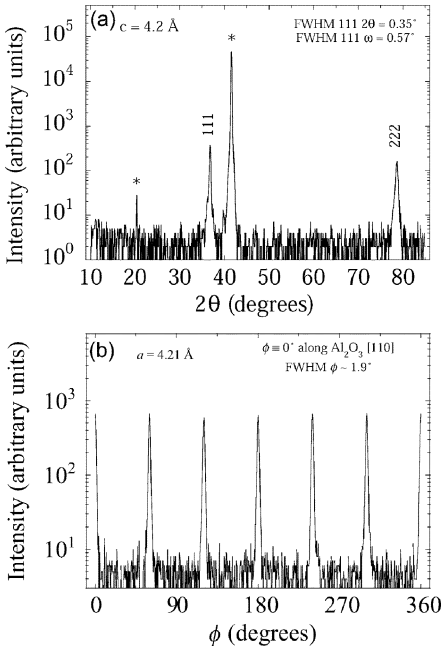

Fig. 1. (a) XRD $\theta - 2\theta$ scan and (b) ϕ scan of a MgO film grown on (0001) Al_2O_3 substrate.

A. MgB_2/MgO *Heterostructures*

The $MgB_2/MgO/MgB_2$ trilayer were grown in situ by HPCVD. One of the major problems in the deposition of magnesium diboride is the strong capability of Mg to react with oxygen to form MgO. It has been shown that a oxygen partial pressure of 10^{-6} torr is sufficient to form MgO phase at 300°C [17]. MgB_2 films grown by HPCVD are very pure, indicated by the low residual resistivity values of 0.26 $\mu\Omega$cm [18]. This feature has been attributed to the absence of MgO contamination due to the reducing hydrogen ambient in the deposition process and the high purity Mg and B sources. However, MgO formation can be intentionally introduced by replacing H_2 carrier gas with N_2 during the process. Even in the ultra-high purity N_2 gas some trace of oxygen is present, which is enough to react with Mg to form MgO.

Fig. 1 shows (a) $\theta - 2\theta$ scan and (b) ϕ scan of a MgO layer grown in the HPCVD reactor at 600° on (0001)sapphire by replacing H_2 with N_2. It shows that MgO grows with (111) orientation and is aligned in-plane as well with (0001)sapphire. The full widths at half maximum (FWHM) of the 111 peak were 0.35° and 0.57° in 2θ and ω, respectively. The ϕ-scan of the 220 peak, where $\phi = 0°$ is aligned parallel to [110] direction of the sapphire substrate, reveals a six-fold symmetry characteristic of an in-plane epitaxy. The FWHM of this peak in ϕ is 1.9°. The in-plane and out-of-plane lattice parameters were found to be $a = 4.21$ Å and $c = 4.2$ Å, respectively. MgO can be deposited using this technique between 550–700°C. The thickness of the MgO film seems to be self-limiting at about 250 Å except for films deposited at around $\sim 600°C$, which is about 450 Å. The crystallographic quality of such films change as a function of deposition temperature, showing a minimum FWHM at 600°C.

Fig. 2(a) shows a $\theta - 2\theta$ scan of an MgB_2 film grown in situ on a MgO buffer layer on a (0001) 4H-SiC substrate. Apart from the peaks from the substrate and the shoulder from the (111)MgO

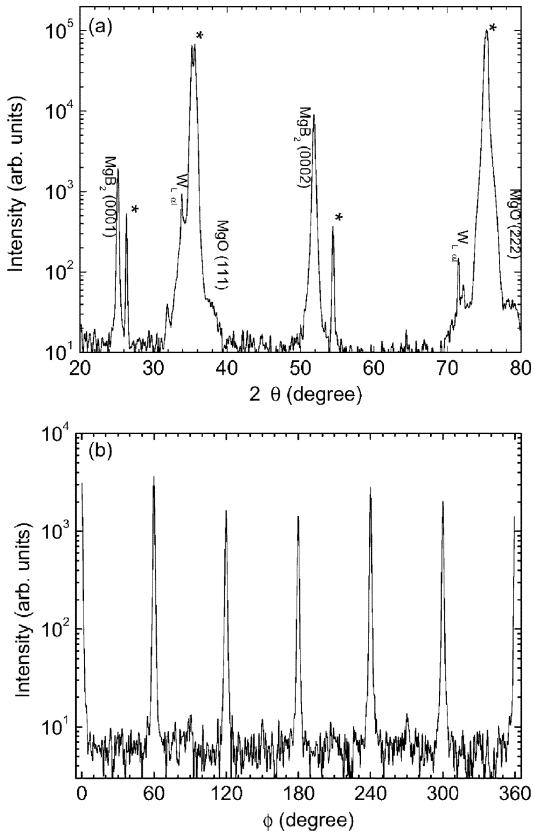

Fig. 2. (a) XRD $\theta - 2\theta$ scan and (b) ϕ scan of a MgB_2 film grown on a MgO/SiC heterostructure.

buffer layer, only the $(000l)$ peaks of MgB_2 are observed. The c lattice constant was 3.523 Å, with FWHM values of the 0002 MgB_2 peak to be 0.33° and 0.72° in 2θ and ω, respectively. The ϕ-scan of the MgB_2 101 reflection, $\phi = 0°$ is aligned parallel to [210] direction of the SiC substrate, displays again a six-fold symmetry indicating an in-plane epitaxy. The FWHM of this peak in ϕ is 1.1°. The result shows that c-axis epitaxial MgB_2 films can be grown on the epitaxial MgO buffer layers.

To grow the complete $MgB_2/MgO/MgB_2$ trilayer, we stopped the B_2H_6 precursor gas and replace H_2 with N_2 after the bottom MgB_2 layer was deposited. The trace amount of oxygen in the ultra high purity N_2 gas allowed the growth of an epitaxial MgO layer on the bottom MgB_2 layer. After this step, the N_2 gas was removed from the reactor, and the top MgB_2 layer was grown by re-introducing the H_2 gas and B_2H_6 into the reactor. It is difficult to distinguish the top and bottom MgB_2 layers in an x-ray diffraction spectra. From the results of Fig. 1 and Fig. 2, we can infer that the $MgB_2/MgO/MgB_2$ trilayers grown in situ by HPCVD are epitaxial.

B. MgB_2/AlN *Heterostructures*

Thermodynamic shows that MgB_2 decomposes at elevated temperatures if the Mg vapor pressure is not sufficiently high [15]. Although Fan *et al.* has shown that there is a significant kinetic barrier to the thermal decomposition of MgB_2 [19], [20], it is not preferred to grow the MgB_2 heterostructure in vacuum at high temperatures. In order to grow $MgB_2/AlN/MgB_2$ trilayers, we deposit the AlN layer ex situ at room temperature

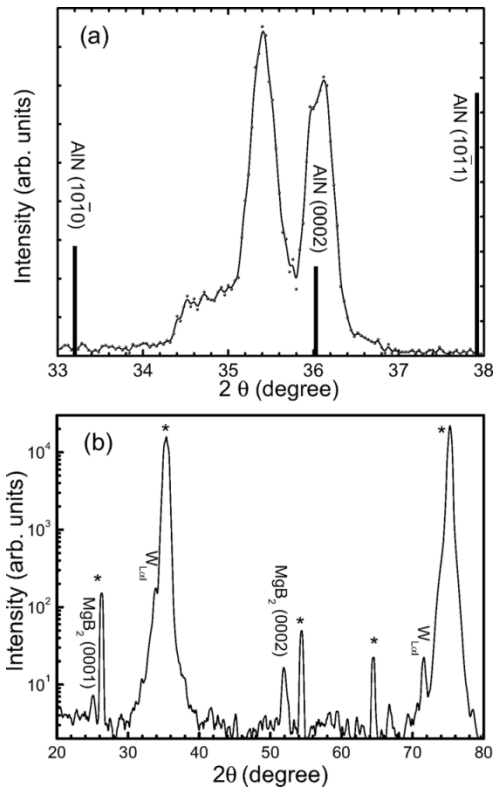

Fig. 3. (a) XRD $\theta-2\theta$ spectrum of an AlN film grown on (0001)SiC substrate. (b) XRD $\theta-2\theta$ spectrum of a $\mathrm{MgB_2}$ film grown on an AlN/SiC heterostructure.

by pulsed laser deposition (PLD). It has been shown that the AlN epitaxial growth at room temperature can be achieved by PLD [21]. In our experiment, the background pressure was in the range of 10^{-8} Torr. An excimer laser (248 nm) was used with a repetition rate of 5 Hz and an energy density of about 3 $\mathrm{J/cm^2}$. The AlN deposition was performed under a ultra high purity (99.999%) nitrogen pressure of 10 mTorr. The deposition rate was about 0.2 $\mathrm{\AA/pulse}$.

A $\theta-2\theta$ XRD spectrum of an AlN film (1800 Å) is shown in Fig. 3(a). Because of the extreme proximity of the AlN peaks to those from the SiC substrate, the measurement was made with a slight misalignment (0.2°) off the film normal so that the substrate peak intensity is substantially reduced. The diffraction pattern shows the 0002 peak of the AlN reflection and no other peaks are seen (the positions of the strongest AlN peaks are indicated in the figure). This indicates that the film is mainly c-axis oriented. The lattice constant c for this film is 4.879 Å, which is close to the literature value for the bulk AlN. We have not obtained similar ϕ scans to that in Fig. 1(b) in the room-temperature deposited AlN films. Most likely these AlN films are randomly in-plane oriented.

Fig. 3(b) shows a $\theta-2\theta$ scan of a $\mathrm{MgB_2}$/400 Å AlN bilayer on a (0001)4H-SiC substrate. The diffractions from the thin AlN buffer layer are too weak to observe. Besides the peaks from the 4H-SiC substrate, we see peaks from the $000l$ planes of $\mathrm{MgB_2}$, indicating that the $\mathrm{MgB_2}$ film grows with the c axis normal to the film surface. The c lattice constant is 3.521 Å, slightly smaller than the bulk value of 3.524 Å, with a FWHM of the 0002 $\mathrm{MgB_2}$ peak in $\theta-2\theta$ of 0.59°. Finally the $\mathrm{MgB_2/AlN/MgB_2}$ heterostructures were deposited in a

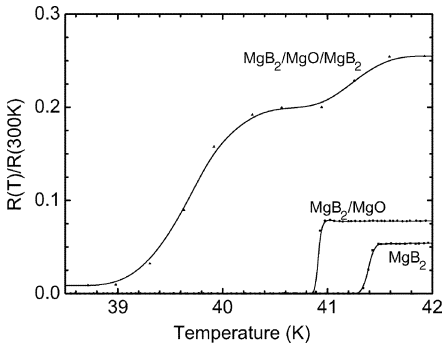

Fig. 4. Resistance vs. temperature curves of a $\mathrm{MgB_2/MgO/MgB_2}$ trilayer structure, a $\mathrm{MgB_2}$ layer on MgO/SiC, and a $\mathrm{MgB_2}$ layer directly on SiC substrate.

three-step ex situ procedure: after the deposition of the bottom $\mathrm{MgB_2}$ layer, an AlN was deposited at room temperature by PLD; the $\mathrm{AlN/MgB_2}$ bilayer was then placed into the HPCVD system for the deposition of the top $\mathrm{MgB_2}$ layer.

III. Electrical Measurements

We have measured electrical properties of $\mathrm{MgB_2}$ films grown on MgO and AlN buffer layers. Compared to films of the same thickness deposited directly on SiC substrates, the residual resistance ratio, RRR, is lower for $\mathrm{MgB_2}$ films on MgO and AlN layers than that on the SiC substrate. For example, for three 1500 Å-thick $\mathrm{MgB_2}$ films, RRR is 12.9, 3.9, and 18.7 for films on MgO, AlN, and directly on SiC, respectively. The lower RRR indicates enhanced scattering from impurities and defects in films on the MgO and AlN buffer layers. The zero-resistance $\mathbf{T}_c$ is also slightly lower (see Fig. 4 and Fig. 5). The slightly decreased critical temperatures for the films on buffer layers could be explained by either the different strain in $\mathrm{MgB_2}$ films or the lower crystallographic quality of $\mathrm{MgB_2}$ films on MgO and AlN buffer layers.

For a $\mathrm{MgB_2}$ trilayer Josephson junction, it is important to know the superconducting properties of both the top and bottom $\mathrm{MgB_2}$ layers. On one hand, the impact of the top $\mathrm{MgB_2}$ deposition on the bottom $\mathrm{MgB_2}$ layer needs to be evaluated, and on the other hand, the results of $\mathrm{MgB_2}$ layers on MgO and AlN buffer layers may not represent the properties of the top $\mathrm{MgB_2}$ layer in the $\mathrm{MgB_2/MgO/MgB_2}$ and $\mathrm{MgB_2/AlN/MgB_2}$ trilayers. For the purpose of characterizing both the top and bottom $\mathrm{MgB_2}$ layers, we defined a 200 $\mu\mathrm{m}\times 400$ $\mu\mathrm{m}$ trilayer area by ion milling and removed the top $\mathrm{MgB_2}$ and the MgO or AlN layer elsewhere. The resistance between the top and bottom $\mathrm{MgB_2}$ layers were then measured, which should include the contributions from both the top and bottom $\mathrm{MgB_2}$ layers as well as those from the insulator layer and interfaces.

Fig. 4 shows a resistance vs. temperature curve, normalized by R(300 K), for a trilayer measurement, marked by "$\mathrm{MgB_2/MgO/MgB_2}$". The thickness of the MgO layer is not precisely known, but should be less than 300–400 Å. The results of $\mathrm{MgB_2}$ on $\mathrm{MgO/MgB_2}$, and $\mathrm{MgB_2}$ directly on SiC substrate are also plotted for comparison. Two transitions are seen for the $\mathrm{MgB_2/MgO/MgB_2}$ trilayer, and we can assume that one is that of the top layer and the other of the bottom layer. We cannot determine definitively which one is for the top or

MgB_2 Thin Films Grown at Different Temperatures by Hybrid Physical-Chemical Vapor Deposition

B. T. Liu, X. X. Xi, V. Vaithyanathan, and D. G. Schlom

***Abstract*—We have grown MgB_2 films at different substrate temperatures by hybrid physical-chemical vapor deposition. X-ray diffraction analysis shows epitaxial growth at all temperatures, as measured at the substrate surface, between 550–700°C. An optimal deposition temperature was found around 650°C, at which the rocking curve is the narrowest, the residual resistivity is the lowest, and T_c is the highest. For the films deposited at lower temperatures, the rocking curve broadens, indicating a decreasing quality of crystallinity. The residual resistivity increases but the superconducting transition temperature remains nearly constant around 40 K when the deposition temperature is decreased to 550°C. The deposition of epitaxial films with excellent superconducting properties at low substrate temperatures is important for device and circuit processing utilizing MgB_2.**

***Index Terms*—Hybrid physical-chemical vapor deposition, magnesium diboride, substrate temperatures, thin films.**

I. Introduction

THE POTENTIAL of MgB_2 in Josephson junctions and integrated circuits [1] has been one of the driving forces behind the development of MgB_2 thin film technologies. It is a phononmediated superconductor [2] with a relatively long coherence length [3], thus promising to behave like conventional low temperature superconductors, such as Nb, in terms of fabrication and characteristics of Josephson junctions. The possibility of 20-K operation and potentially higher speeds than Nb-based integrated circuits make MgB_2 digital circuits very attractive. For superconducting integrated circuits, an in situ process in which multilayers of MgB_2 and other materials are formed directly on the substrate is desirable. We have accomplished the in situ deposition of MgB_2 films using a hybrid physical-chemical vapor deposition (HPCVD) technique [4]. It produces epitaxial MgB_2 films with T_c above 40 K and a residual resistivity at T_c as low as 0.26 $\mu\Omega$cm, [4], [5].

The deposition of multilayers of superconducting, insulating and resistive films for superconducting integrated circuits also prefers a low temperature process so that the reaction or interdiffusion between the different layers are avoided or minimized. The standard HPCVD process requires relatively high deposition temperatures, around 650–700°C. There are MgB_2 deposition techniques that grow films at lower temperatures. For example, several groups have demonstrated in situ growth of superconducting MgB_2 thin films below about 300°C in ultrahigh vacuum background using molecular beam epitaxy [6]–[9], sputtering [10], or co-evaporation [11]. Even in moderately high vacuum, superconducting films of MgB_2 have been grown by co-evaporation [12] and combined sputtering and Mg evaporation [13] at 440–550°C. These films made at low temperatures, however, do not have the high degree of crystallinity and excellent superconducting properties as in HPCVD films deposited at higher temperatures. In this paper, we present results of HPCVD MgB_2 films deposited at different temperatures with an emphasis on the low deposition temperatures. We show that epitaxial MgB_2 films with T_c above 40 K can be grown at temperatures as low as 550°C.

II. Control of Substrate Temperature

The principles and setup of the HPCVD system have been briefly described previously [4], [14]. The schematics of the HPCVD system are shown in Fig. 1. The HPCVD reactor consists of a water cooled vertical quartz tube with a cup-shaped susceptor placed inside the reactor. The susceptor is heated by an inductance heater. The carrier gas is H_2 and the boron precursor gas is a mixture of 1000 ppm B_2H_6 in H_2, which are introduced from the top and exhausted from the bottom of the reactor. Heated bulk Mg (99.95%) chips are used as the Mg source. For this work, 300 sccm of H_2 carrier gas was maintained at 100 Torr during the deposition. When the susceptor, along with the substrate and Mg pieces, were heated to the deposition temperature, 150 sccm of B_2H_6/H_2 mixture was introduced into the reactor to initiate growth.

The limit of the standard HPCVD system to the high deposition temperatures arises from the thermodynamic conditions of the MgB_2 deposition [15]. Liu *et al.* have shown that the process window for in situ MgB_2 deposition, where the thermodynamically-stable phases are MgB_2 and gas phases, is located at very high Mg pressures. For example, for a deposition temperature of 750°C, a Mg pressure greater than 44 mTorr is necessary to keep the MgB_2 phase thermodynamically stable. For the HPCVD technique, this is achieved by heating pure Mg chips which are placed near the substrate. In the standard HPCVD configuration (Fig. 1, left), the susceptor is heated by inductance heating and Mg is heated primarily through thermal contact with the susceptor. The Mg vapor pressure generated in this way depends

Manuscript received October 3, 2004. The work of X. X. Xi was supported in part by the Office of Naval Research under Grant N00014-00-1-0294 and in part by the National Science Foundation under Grant DMR-0306746. The work of D. G. Schlom was supported by the U.S. Department of Energy under Grant DE-FG02-03ER46063.

B. T. Liu is with the Department of Physics, The Pennsylvania State University, University Park, PA 16802 USA.

X. X. Xi is with the Department of Physics and the Department of Materials Science and Engineering, The Pennsylvania State University, University Park, PA 16802 USA (e-mail: xxx4@psu.edu).

V. Vaithyanathan and D. G. Schlom are with the Department of Materials Science and Engineering, The Pennsylvania State University, University Park, PA 16802 USA.

Digital Object Identifier 10.1109/TASC.2005.848844

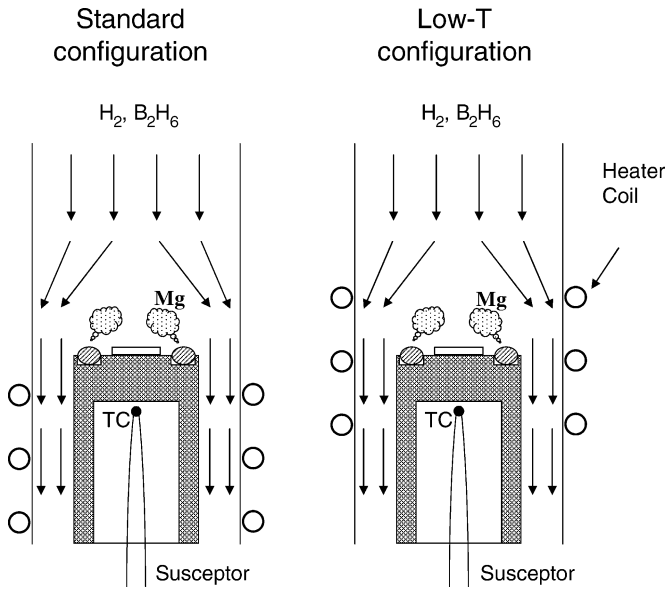

Fig. 1. Schematics of a standard HPCVD system (left) and an HPCVD system for low temperature deposition (right). The top of the susceptor is outside of the inductance heater in the standard configuration, while it is inside the inductance heater in the low-T configuration.

on the temperature of the susceptor and lower deposition temperature leads to lower Mg pressure. If the Mg pressure is too low, $\mathrm{MgB_2}$ is thermodynamically not stable and the conditions are not suitable for $\mathrm{MgB_2}$ deposition.

The Mg chips on the susceptor are also heated by inductance heating, and the efficiency of this heating mechanism depends on how well the electromagnetic field due to the inductive coil couples to the Mg chips. In the standard configuration, the Mg chips are well outside of the electromagnetic field generated by the inductance hater coil, therefore they are not effectively heated by this heating mechanism. In order to deposit $\mathrm{MgB_2}$ films at lower temperatures we position the top of the susceptor right in the middle of the inductance coil (Fig. 1, right). In this case, the electromagnetic field of the heater coil fully penetrates the Mg chips and the inductance heating of the Mg chips is highly effective. As a consequence, a high Mg vapor pressure can be achieved even when the susceptor temperature is lower. By varying the position of the susceptor with respect to the inductance heater coil, we can deposit $\mathrm{MgB_2}$ films at different substrate temperatures.

Special attention was paid to the measurement of the substrate temperature, T_s. In our HPCVD setup, the temperature is measured by a thermocouple (TC) placed inside the cup-shaped susceptor (see Fig. 1). The temperature reading from the thermocouple, T_{TC}, is different from the temperature reading from an infrared pyrometer, T_{Pyro}, measured at the top of the susceptor. For the purpose of process control, the thermocouple reading is sufficient while the Mg deposit on the reactor wall hinders the optical measurement using a pyrometer. In all our publications on the standard HPCVD system, T_{TC} is used as T_s. However, when the susceptor position is changed, the difference between T_{TC} and T_{Pyro} also changes. Fig. 2 shows the $T_{TC} - T_{Pyro}$ correlation for three different susceptor positions marked as A, B, and C. Since T_{Pyro} is influenced less by the difference in the susceptor position, we use T_{Pyro} as T_s throughout this paper.

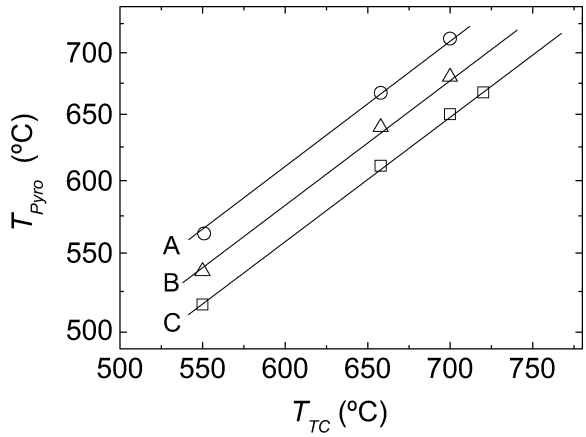

Fig. 2. Correlation between the temperatures from the thermocouple reading, T_{TC}, and the pyrometer reading, T_{Pyro}, for different susceptor positions A (the "Low-T configuration" in Fig. 1), B, and C (the "Standard configuration" in Fig. 1).

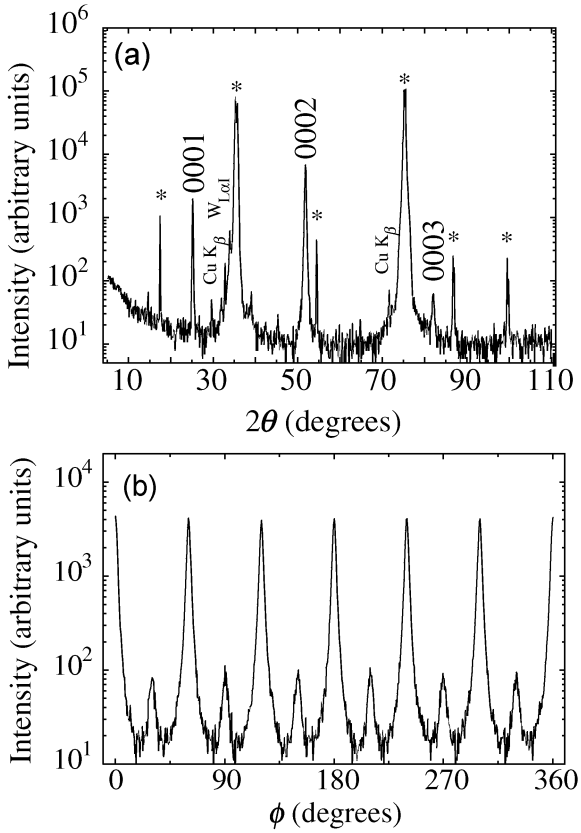

Fig. 3. X-ray diffraction spectra of a $\mathrm{MgB_2}$ thin film deposited at 550°C on a (0001) 4H-SiC substrate. (a) $\theta - 2\theta$ scan and (b) ϕ scan of the $10\bar{1}1$ $\mathrm{MgB_2}$ reflection. The substrate peaks are marked by "$*$".

III. Results and Discussion

The lowest temperature at which superconducting $\mathrm{MgB_2}$ films were deposited using the low-T configuration is 550°C. Fig. 3 shows (a) a $\theta - 2\theta$ scan and (b) a ϕ-scan of the $10\bar{1}1$ reflection of a $\mathrm{MgB_2}$ film deposited at 550°C on a (0001) 4H-SiC substrate. In the $\theta - 2\theta$ scan, the only peaks beside those of the substrate, marked by "$*$", are the $(000l)$ peaks of $\mathrm{MgB_2}$, indicating that the $\mathrm{MgB_2}$ film grows with c-axis normal to the substrate surface. The c lattice constant is 3.52 ± 0.02 Å,

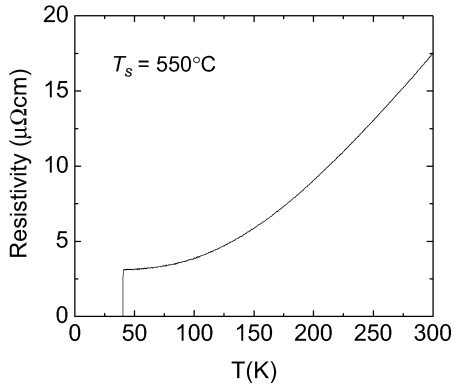

Fig. 4. Resistivity vs. temperature curve for a 2000 Å-thick MgB_2 films deposited at 550°C.

in agreement with the bulk value [16]. The full widths at half maximum (FWHM) of the 0002 peak were 0.37° and 2.1° in 2θ and ω, respectively. The ϕ-scan, where $\phi = 0°$ is aligned parallel to $[10\bar{1}0]$ direction of the SiC substrate, reveals a six-fold symmetry characteristic of a (0001) oriented MgB_2 film with in-plane epitaxy. The a lattice constant is 3.10 ± 0.02 Å, similar to the bulk value of 3.086 Å, [16]. The FWHM of this peak in ϕ is 2.8°. The plot also reveals weaker peaks at $30° \pm n\ 60°$ (where n is an integer), indicating 30° rotational twinning. The dominant in-plane epitaxial relationship is $[2\bar{1}\bar{1}0]\ MgB_2 \| [2\bar{1}\bar{1}0]$ SiC, i.e. the hexagonal lattice of MgB_2 grows directly on top of the hexagonal lattice of SiC. In a small amount of grains the hexagonal MgB_2 lattice is rotated by 30°, i.e. $[10\bar{1}0]\ MgB_2 \| [2\bar{1}\bar{1}0]$ SiC. As a comparison, for MgB_2 films deposited at 650°C in the standard configuration, there is no rotational twinning and the a axis of the MgB_2 film is parallel to the a axis of the SiC substrate [17].

The superconducting transition of the MgB_2 films deposited at 550°C is similar to those in the best thin film samples. Fig. 4 is a resistivity vs. temperature curve, which shows a sharp superconducting transition and a zero-resistance T_{c0} of 40.3 K, which is higher than in the bulk samples. We have shown previously that a tensile strain in the MgB_2 films deposited by HPCVD, caused primarily by the coalescence of grains during the film growth, results in T_c values higher than the bulk [18]. The result here shows that the growth mode at 550°C is likely the same as in films deposited in the standard configuration at higher T_s. The resistivity of the film in Fig. 4 is 17.6 $\mu\Omega$cm at 300 K and 3.2 $\mu\Omega$cm before the superconducting transition, giving a residual resistance ratio $RRR = R(300\ \mathrm{K})/R(40\ \mathrm{K})$ of 5.5. These are low resistivity values indicating good transport properties, although as a reference, the best values obtained in MgB_2 films deposited under the standard conditions are a residual resistivity of 0.26 $\mu\Omega$cm and RRR over 30 [5].

We have deposited a series of MgB_2 films at different temperatures by changing the position of the susceptor with respect to the inductance heater coil. The deposition and film parameters of a series of MgB_2 films grown on SiC substrates are summarized in Table I. The "Position" refers to those in Fig. 2. As the deposition temperature changes, the deposition rate also changes, which is not fully understood. The films also have different thicknesses, and we have found previously that larger

TABLE I
DEPOSITION AND FILM PARAMETERS FOR SAMPLES IN FIG. 5

Sample	Position	T_s, °C	Growth Rate, Å/s	Thickness, Å
B012004a	C	700	13.5	2020
B012004b	C	650	7.0	1680
B012004c	B	600	18.8	5630
B012004f	A	550	16.5	5930

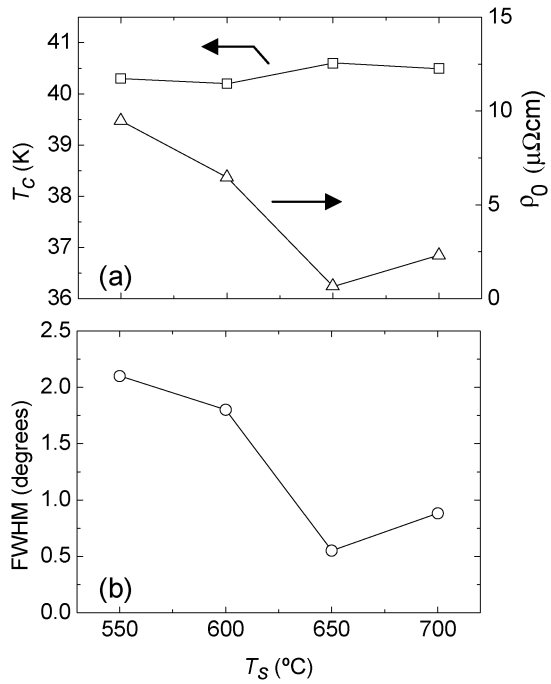

Fig. 5. The deposition temperature dependence of (a) T_c and residual resistivity, and (b) FWHM in ω for MgB_2 films deposited at different temperatures.

film thickness corresponds to higher T_c and lower resistivity [5]. Fig. 5 shows the dependence of the transport, superconducting, and structural properties of this series of MgB_2 films on T_s. The best film properties, $T_c = 40.6$ K, residual resistivity $\rho_0 = 0.67$ $\mu\Omega$cm, and the FWHM in ω of 0.55°, are found in the film deposited at 650°C, which corresponds to the thermocouple reading of $T_{TC} = 720$°C as we reported in our other publications. The film deposited at this temperature shows the best results despite that it is the thinnest film in this series. As the substrate temperature decreases, the crystallinity of the films becomes worse, as indicated by the increasing FWHM in the rocking curve. The residual resistivity also increases with decreasing temperature and closely resembles the trend of the FWHM in the rocking curve, indicating an enhanced scattering due to defects. The transition temperature T_c, on the other hand, is less sensitive to the decreased crystallinity as its dependence on T_s is very weak. Increasing the deposition temperature above 650°C also leads to poorer film qualities in T_c, resistivity, and FWHM.

There are three major issues in the deposition of MgB_2 films: the phase stability conditions of MgB_2 that requires high Mg vapor pressures [15]; the low sticking coefficient of Mg above

250°C that also demands a large Mg flux [9]; and contaminations from oxygen [6], [8] and carbon [19]. In HPCVD, the reducing hydrogen ambient during the deposition suppresses the oxidation of Mg, and the use of pure Mg and B_2H_6 as source materials eliminates the carbon contamination. Heating of the Mg chips produces a high Mg vapor pressure which satisfies the thermodynamic phase stability condition and provides an abundance of Mg to react with B. When the deposition temperature is lowered, the heating of the Mg chips by the susceptor alone is not enough to generate a high enough Mg pressure. By moving the top of the susceptor to the middle of the inductance heater coil, this problem is alleviated by the additional inductance heating of the Mg chips. However, the power of inductance heating also decreases for lower susceptor temperature such that the additional inductive heating of the Mg chips becomes insufficient below 550°C.

The kinetics of crystal growth prefers film deposition to occur at sufficiently high temperatures. The optimum temperature for epitaxial growth is typically about one half of the melting temperature, T_m (in Kelvin), although the minimum temperature can be much lower [20], for example, about $T_m/8$ for metals [21]. MgB_2 melts congruently at 2430°C (~2700 K) with an equilibrium vapor pressure exceeding 49 000 Torr. Therefore, the deposition of MgB_2 could take place between ~ 1080°C (1350 K) and ~ 70°C (340 K). The lower deposition often results in poorer crystallinity and degraded transport and superconducting properties. However, higher deposition temperature requires higher Mg pressure. In the current HPCVD setup, lower deposition temperature also causes lower Mg pressure. Therefore, we could not deposit films at temperatures below 550°C. To deposit MgB_2 films at even lower temperature, a Mg source separate from the substrate heater is needed.

IV. Conclusions

Epitaxial MgB_2 films with excellent transport and superconducting properties have been grown by HPCVD at different substrate temperatures. To meet the thermodynamic phase stability requirement for a high Mg vapor pressure, we moved the top of the susceptor to the middle of the inductance heater coil. In this susceptor position the heating of the Mg chips, which are placed near the substrates, is achieved by both thermal contact with the susceptor and the inductance heating. We were able to lower the deposition temperature to 550°C, 100° lower than that in the standard HPCVD configuration. For multilayer processing for MgB_2 Josephson junctions and integrated circuits, the lowering of the deposition temperature while maintaining the excellent superconducting properties in the films is technologically significant.

Acknowledgment

The authors acknowledge helpful discussions with J. M. Redwing and A. V. Pogrebnyakov.

References

[1] J. Rowell, "Magnesium diboride: superior thin films," *Nature Mater.*, vol. 1, p. 5, 2002.

[2] S. L. Bud'ko, G. Lapertot, C. Petrovic, C. E. Cunningham, N. Anderson, and P. C. Canfield, "Boron isotope effect in superconducting MgB_2," *Phys. Rev. Lett.*, vol. 86, pp. 1877–1880, 2001.

[3] D. K. Finnemore, J. E. Ostenson, S. L. Bud'ko, G. Lapertot, and P. C. Canfield, "Thermodynamic and transport properties of superconducting $Mg^{10}B_2$," *Phys. Rev. Lett.*, vol. 86, pp. 2420–2422, 2001.

[4] X. H. Zeng, A. V. Pogrebnyakov, A. Kotcharov, J. E. Jones, X. X. Xi, E. M. Lysczek, J. M. Redwing, S. Y. Xu, Q. Li, J. Lettieri, D. G. Schlom, W. Tian, X. Q. Pan, and Z. K. Liu, "In situ epitaxial MgB_2 thin films for superconducting electronics," *Nature Mater.*, vol. 1, pp. 35–38, 2002.

[5] A. V. Pogrebnyakov, J. M. Redwing, J. E. Jones, X. X. Xi, S. Y. Xu, Q. Li, V. Vaithyanathan, and D. G. Schlom, "Thickness dependence of the properties of epitaxial MgB_2 thin films grown by hybrid physical-chemical vapor deposition," *Appl. Phys. Lett.*, vol. 82, pp. 4319–4321, 2003.

[6] K. Ueda and M. Naito, "As-grown superconducting MgB_2 thin films prepared by molecular beam epitaxy," *Appl. Phys. Lett.*, vol. 79, pp. 2046–2048, 2001.

[7] W. Jo, J.-U. Huh, T. Ohnishi, A. F. Marshall, M. R. Beasley, and R. H. Hammond, "Thin film superconducting MgB_2 as-grown by MBE without post-anneal," *Appl. Phys. Lett.*, vol. 80, pp. 3563–3565, 2002.

[8] A. J. M. van Erven, T. H. Kim, M. Muenzenberg, and J. S. Moodera, "Highly crystallized as-grown smooth and superconducting MgB_2 films by molecular-beam epitaxy," *Appl. Phys. Lett.*, vol. 81, p. 4982, 2002.

[9] J. Kim, R. K. Singh, N. Newman, and J. M. Rowell, "Surface electronic structures of superconducting thin film MgB_2 (0001)," *IEEE Trans. Appl. Supercond.*, vol. 13, p. 3238, 2003.

[10] A. Saito, A. Kawakami, H. Shimakage, and Z. Wang, "As-grown deposition of superconducting MgB_2 thin films by multiple-target sputtering system," *Jpn. J. Appl. Phys.*, vol. 41, p. L127, 2002.

[11] H. Shimakage, A. Saito, A. Kawakami, and Z. Wang, "Preparation of as-grown MgB_2 thin films by co-evaporation method at low substrate temperature," *IEEE Trans. Appl. Supercond.*, vol. 13, p. 3309, 2003.

[12] B. H. Moeckly and W. S. Ruby, "Growth of high quality in situ MgB_2 thin films by reactive evaporation," in *2003 Fall Meeting Technical Program*, 2003, p. 759.

[13] R. Schneider, J. Geerk, F. Ratzel, G. Linker, and A. G. Zaitsev, "In situ synthesis of MgB_2 thin films for tunnel junctions," *Appl. Phys. Lett.*, submitted for publication.

[14] X. X. Xi, X. H. Zeng, A. V. Pogrebnyakov, S. Y. Xu, Q. Li, Y. Zhong, C. O. Brubaker, Z.-K. Liu, E. M. Lysczek, J. M. Redwing, J. Lettieri, D. G. Schlom, W. Tian, and X. Q. Pan, "In situ growth of MgB_2 thin films by hybrid physical-chemical vapor deposition," *IEEE Trans. Appl. Supercond.*, vol. 13, p. 3233, 2003.

[15] Z. K. Liu, D. G. Schlom, Q. Li, and X. X. Xi, "Thermodynamics of the Mg-B system: implications for the deposition of MgB_2 thin films," *Appl. Phys. Lett.*, vol. 78, pp. 3678–3680, 2001.

[16] J. Nagamatsu, N. Nakagawa, T. Muranaka, Y. Zenitani, and J. Akimitsu, "Superconductivity at 39 K in magnesium diboride," *Nature (London)*, vol. 410, pp. 63–64, 2001.

[17] X. H. Zeng, A. V. Pogrebnyakov, M. H. Zhu, J. E. Jones, X. X. Xi, S. Y. Xu, E. Wertz, Q. Li, J. M. Redwing, J. Lettieri, V. Vaithyanathan, D. G. Schlom, Z. K. Liu, O. Trithaveesak, and J. Schubert, "Superconducting MgB_2 thin films on silicon carbide substrates by hybrid physical-chemical vapor deposition," *Appl. Phys. Lett.*, vol. 82, pp. 2097–2099, 2003.

[18] A. V. Pogrebnyakov, D. A. Tenne, A. Soukiassian, X. X. Xi, J. M. Redwing, V. Vaithyanathan, D. G. Schlom, S. Y. Xu, Q. Li, M. D. Johannes, D. Kasinathan, and W. E. Pickett, "Enhancement of superconducting transition temperature in MgB_2 by strain-induced bond-stretching mode softening," *Phys. Rev. Lett.*, to be published.

[19] S. Lee, T. Masui, A. Yamamoto, H. Uchiyama, and S. Tajima, "Carbon-substituted MgB_2 single crystals," *Physica C*, vol. 397, pp. 7–13, 2003.

[20] M. H. Yang and C. P. Flynn, "Growth of alkali halides from molecular beams: global growth characteristics," *Phys. Rev. Lett.*, vol. 62, p. 2476, 1989.

[21] C. P. Flynn, "Constraints on the growth of metallic superlattices," *J. Phys. F*, vol. 18, p. L195, 1988.

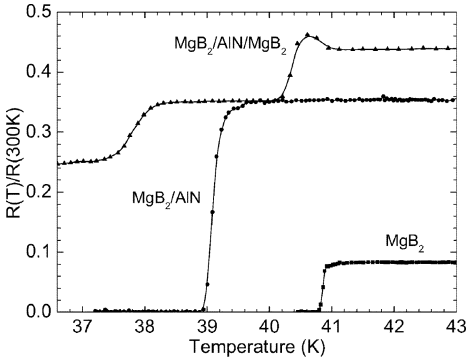

Fig. 5. Resistance vs. temperature curves of a $MgB_2/AlN/MgB_2$ trilayer structure, a MgB_2 layer on AlN/SiC, and a MgB_2 layer directly on SiC substrate.

the bottom layer, however, both transitions are suitable for an all-MgB_2 Josephson junction to work at above 20 K. There is a small resistance below the two transitions, which we attribute to the contributions of the MgO layer and the interfaces. The small value of the resistance may be an indication of poor wetting of MgO on the bottom MgB_2 layer or pinholes in the MgO layer. It may also be due to poor insulating property of the MgO layer. The detailed properties of the MgO layer on MgB_2 require further studies.

Fig. 5 shows the result of the same measurement for a $MgB_2/AlN/MgB_2$ trilayer. The thickness of the AlN layer is 400 Å. As in the case of the $MgB_2/MgO/MgB_2$ trilayer, two transitions are seen for the $MgB_2/AlN/MgB_2$ trilayer, and we cannot determine definitively which one is for the top or the bottom layer. The slightly lower transition temperatures in the $MgB_2/AlN/MgB_2$ trilayer than those in epitaxial $MgB_2/MgO/MgB_2$ may be due to additional defects from the ex situ process. The higher resistance below the two transitions than that in Fig. 4 may indicate a better insulating property or coverage of the AlN layer than the MgO layer.

IV. Conclusions

We have demonstrated that high quality $MgB_2/MgO/MgB_2$ and $MgB_2/AlN/MgB_2$ heterostructures can be grown using the HPCVD technique in combination with either an in situ (in the case of MgO) or an ex situ (in the case of AlN) procedures. The trilayers with MgO are epitaxial, while the room-temperature grown AlN is c-axis oriented but random in-plane. The superconducting properties of both the top and bottom MgB_2 layers are excellent. However, to make MgO and AlN layers suitable as barriers for all-MgB_2 Josephson junctions, many more issues remain to be addressed. For example, the results in Figs. 4 and 5 suggest poor wetting and coverage of the barrier layer, or the existence of pinholes between the electrodes. We need to better control the thickness and coverage of the insulator layers, and to understand and control the structural, electrical, and chemical properties of the interface between MgB_2 and the insulator layer. Nevertheless, the results are a promising first step toward using MgO and AlN as the barrier materials for all-MgB_2 Josephson junctions.

References

[1] D. K. Brock, E. K. Track, and J. M. Rowell, "Superconductor ICs: the 100-GHz second generation," *IEEE Spectrum*, vol. 37, no. 12, pp. 40–46, Dec. 2000.

[2] J. Nagamatsu, N. Nakagawa, T. Muranaka, Y. Zenitani, and J. Akimitsu, "Superconductivity at 39 K in magnesium diboride," *Nature (London)*, vol. 410, pp. 63–64, 2001.

[3] J. Rowell, "Magnesium diboride: superior thin films," *Nature Mater.*, vol. 1, p. 5, 2002.

[4] A. Brinkman, D. Veldhuis, D. Mijatovic, G. Rijnders, D. H. A. Blank, H. Hilgenkamp, and H. Rogalla, "Superconducting quantum interference devices (SQUID's) based on MgB_2 nanobridges," *Appl. Phys. Lett.*, vol. 79, p. 2420, 2001.

[5] A. Malisa, M. Valkeapää, L.-G. Johansson, and Z. Ivanov, "Josephson effects in magnesium diboride based Josephson junctions," *Supercond. Sci. Technol.*, vol. 17, p. S345, 2004.

[6] G. Burnell, D.-J. Kang, H. N. Lee, S. H. Moon, B. Oh, and M. G. Blamire, "Planar superconductor-normal-superconductor Josephson junctions in MgB_2," *Appl. Phys. Lett.*, vol. 79, p. 3464, 2001.

[7] D.-J. Kang, N. H. Peng, R. Webb, C. Jeynes, J. H. Yun, S. H. Moon, B. Oh, G. Burnell, E. J. Tarte, D. F. Moore, and M. G. Blamire, "Realization and properties of MgB_2 metal-masked ion damage junctions," *Appl. Phys. Lett.*, vol. 81, p. 3600, 2002.

[8] D. A. Kahler, J. Talvacchio, J. M. Murduck, A. Kirschenbaum, R. E. Brooks, S. B. Bu, J. Choi, D. M. Kim, and C.-B. Eom, "Planar josephson junctions fabricated with magnesium diboride films," *IEEE Trans. Appl. Supercond.*, vol. 13, p. 1063, 2003.

[9] J.-I. Kye, H. N. Lee, J. D. Park, S. H. Moon, and B. Oh, "Josephson effect in $MgB_2/Ag/MgB_2$ step-edge junctions," *IEEE Trans. Appl. Supercond.*, vol. 13, p. 1075, 2003.

[10] D. Mijatovic, A. Brinkman, I. Oomen, G. Rijnders, H. Hilgenkamp, H. Rogalla, and D. H. A. Blank, "Magnesium-dioboride ramp-type Josephson junctions," *Appl. Phys. Lett.*, vol. 80, p. 2141, 2002.

[11] G. Carapella, N. Martucciello, G. Costabile, C. Ferdeghini, V. Ferrando, and G. Grassano, "Josephson effect in $Nb/Al_2O_3/Al/MgB_2$ large-area thin-film heterostructures," *Appl. Phys. Lett.*, vol. 80, p. 2949, 2002.

[12] A. Saito, A. Kawakami, H. Shimakage, H. Terai, and Z. Wang, "Fabrication of josephson junctions with as-grown MgB_2 thin films," *IEEE Trans. Appl. Supercond.*, vol. 13, p. 1067, 2003.

[13] T. H. Kim and J. S. Moodera, "Demonstration of all in situ magnesium diboride superconductor thin-film tunnel junctions," *Appl. Phys. Lett.*, vol. 85, p. 434, 2004.

[14] X. H. Zeng, A. V. Pogrebnyakov, A. Kotcharov, J. E. Jones, X. X. Xi, E. M. Lysczek, J. M. Redwing, S. Y. Xu, Q. Li, J. Lettieri, D. G. Schlom, W. Tian, X. Q. Pan, and Z. K. Liu, "In situ epitaxial MgB_2 thin films for superconducting electronics," *Nature Mater.*, vol. 1, pp. 35–38, 2002.

[15] Z. K. Liu, D. G. Schlom, Q. Li, and X. X. Xi, "Thermodynamics of the Mg-B system: implications for the deposition of MgB_2 thin films," *Appl. Phys. Lett.*, vol. 78, pp. 3678–3680, 2001.

[16] X. H. Zeng, A. V. Pogrebnyakov, M. H. Zhu, J. E. Jones, X. X. Xi, S. Y. Xu, E. Wertz, Q. Li, J. M. Redwing, J. Lettieri, V. Vaithyanathan, D. G. Schlom, Z. K. Liu, O. Trithaveesak, and J. Schubert, "Superconducting MgB_2 thin films on silicon carbide substrates by hybrid physical-chemical vapor deposition," *Appl. Phys. Lett.*, vol. 82, pp. 2097–2099, 2003.

[17] T. Ishiguro, Y. Hiroshima, and T. Inoue, "MgO(200) highly oriented films on Si(100) synthesized by ambient-controlled pulsed KrF excimer laser deposition method," *Jpn. J. Appl. Phys.*, vol. 35, no. 6A, p. 3537, 1996.

[18] A. V. Pogrebnyakov, J. M. Redwing, J. E. Jones, X. X. Xi, S. Y. Xu, Q. Li, V. Vaithyanathan, and D. G. Schlom, "Thickness dependence of the properties of epitaxial MgB_2 thin films grown by hybrid physical-chemical vapor deposition," *Appl. Phys. Lett.*, vol. 82, pp. 4319–4321, 2003.

[19] Z. Y. Fan, D. G. Hinks, N. Newman, and J. M. Rowell, "Experimental study of MgB_2 decomposition," *Appl. Phys. Lett.*, vol. 79, pp. 87–89, 2001.

[20] J. Kim, R. K. Singh, N. Newman, and J. M. Rowell, "Surface electronic structures of superconducting thin film MgB_2 (0001)," *IEEE Trans. Appl. Supercond.*, vol. 13, p. 3238, 2003.

[21] J. Ohta, H. Fujioka, S. Ito, and M. Oshima, "Room-temperature epitaxial growth of AlN films," *Appl. Phys. Lett.*, vol. 81, p. 2373, 2002.

[4] Finnemore D K, Ostenson J E, Bud'ko S L, Lapertot G and Canfield P C 2001 *Phys. Rev. Lett.* **86** 2420
[5] Choi H J, Roundy D, Sun H, Cohen M L and Louie S G 2002 *Nature* **418** 758
[6] Canfield P C and Crabtree G 2003 *Phys. Today* **56** (3) 34
[7] Kleinsasser A W 2001 *IEEE Trans. Appl. Supercond.* **11** 1043
[8] Liu Z K, Schlom D G, Li Q and Xi X X 2001 *Appl. Phys. Lett.* **78** 3678
[9] Liu Z-K, Zhong Y, Schlom D, Xi X X and Li Q 2001 *CALPHAD* **25** 299
[10] Kim J, Singh R K, Newman N and Rowell J M 2003 *IEEE Trans. Appl. Supercond.* **13** 3238
[11] Eom C B *et al* 2001 *Nature* **411** 558
[12] van Erven A J M, Kim T H, Muenzenberg M and Moodera J S 2002 *Appl. Phys. Lett.* **81** 4982
[13] Burnell G, Kang D-J, Lee H N, Moon S H, Oh B and Blamire M G 2001 *Appl. Phys. Lett.* **79** 3464
[14] Mijatovic D, Brinkman A, Oomen I, Rijnders G, Hilgenkamp H, Rogalla H and Blank D 2002 *Appl. Phys. Lett.* **80** 2141
[15] Carapella G, Martucciello N, Costabile G, Ferdeghini C, Ferrando V and Grassano G 2002 *Appl. Phys. Lett.* **80** 2949
[16] Kahler D A, Talvacchio J, Murduck J M, Kirschenbaum A, Brooks R E, Bu S B, Choi J, Kim D M and Eom C-B 2003 *IEEE Trans. Appl. Supercond.* **13** 1063
[17] Saito A, Kawakami A, Shimakage H, Terai H and Wang Z 2003 *IEEE Trans. Appl. Supercond.* **13** 1067
[18] Kye J-I, Lee H N, Park J D, Moon S H and Oh B 2003 *IEEE Trans. Appl. Supercond.* **13** 1075
[19] Brinkman A, Veldhuis D, Mijatovic D, Rijnders G, Blank D H A, Hilgenkamp H and Rogalla H 2001 *Appl. Phys. Lett.* **79** 2420
[20] Burnell G, Kang D-J, Ansell D A, Lee H N, Moon S H, Tarte E J and Blamire M G 2002 *Appl. Phys. Lett.* **81** 102
[21] Brinkman A, Mijatovic D, Hilgenkamp H, Rijnders G, Oomen I, Veldhuis D, Roesthuis F, Rogalla H and Blank D H A 2003 *Supercond. Sci. Technol.* **16** 246
[22] Lee S Y, Lee J H, Lee J H, Ryu J S, Lim J, Moon S H, Lee H N, Kim H G and Oh B 2002 *Appl. Phys. Lett.* **79** 3299
[23] Zhukov A A *et al* 2002 *Appl. Phys. Lett.* **80** 2347
[24] Andreone A, Di Gennaro E, Lamura G, Salluzzo M, Purnell A, Cohen L F, Hao L, Gallop J, Cantoni C and Paranthaman M 2003 *Supercond. Sci. Technol.* **16** 260
[25] Jin B B, Klein N, Kang W, Kim H-J, Choi E-M, Lee S-I, Dahm T and Maki K 2003 *Supercond. Sci. Technol.* **16** 205
[26] Lee S Y, Lee J H, Lim J, Lee H N, Moon S H, Oh B and Hein M A 2003 *IEEE Trans. Appl. Supercond.* **13** 3585
[27] Monticone E, Rajteri M, Portesi C, Bodoardo S and Gonnelli R S 2003 *IEEE Trans. Appl. Supercond.* **13** 3242
[28] Heckingbottom R, Davies G and Prior K 1983 *Surf. Sci.* **132** 375
[29] Hammond R H and Bormann R 1989 *Physica* C **162** 703
[30] Fan Z Y, Hinks D G, Newman N and Rowell J M 2001 *Appl. Phys. Lett.* **79** 87
[31] Brutti S, Ciccioli A, Balducci G, Gigli G, Manfrinetti P and Palenzona A 2002 *Appl. Phys. Lett.* **80** 2892
[32] Ueda K and Naito M 2001 *Appl. Phys. Lett.* **79** 2046
[33] Ueda K and Naito M 2003 *J. Appl. Phys.* **93** 2113
[34] Ishiguro T, Hiroshima Y and Inoue T 1996 *Japan. J. Appl. Phys.* **35** 3537
[35] Zeng X H *et al* 2001 *Appl. Phys. Lett.* **79** 1840
[36] Rowell J, Xu S Y, Zeng X H, Pogrebnyakov A V, Li Q, Xi X X, Redwing J M, Tian W and Pan X 2003 *Appl. Phys. Lett.* **83** 102
[37] Kang W N, Kim H-J, Choi E-M, Jung C U and Lee S-I 2001 *Science* **292** 1521
[38] Shinde S R, Ogale S B, Greene R L, Venkatesan T, Canfield P C, Bud'ko S, Lapertot G and Petrovic C 2001 *Appl. Phys. Lett.* **79** 227
[39] Ferdeghini C *et al* 2001 *Supercond. Sci. Technol.* **14** 952
[40] Berenov A *et al* 2001 *Appl. Phys. Lett.* **79** 4001
[41] Bu S D *et al* 2002 *Appl. Phys. Lett.* **81** 1851
[42] Vaglio R, Maglione M G and Di Capua R 2002 *Supercond. Sci. Technol.* **15** 1236
[43] Tian W, Pan X Q, Bu S D, Kim D M, Choi J H, Patnaik S and Eom C B 2002 *Appl. Phys. Lett.* **81** 685
[44] Maglione M G, Chiarella F, di Capua R, Vaglio R, Salvato M, Maritato L and Prischepa S L 2003 *Int. J. Mod. Phys.* B **17** 779
[45] Paranthaman M *et al* 2001 *Appl. Phys. Lett.* **78** 3669
[46] Moon S H, Yun J H, Lee H N, Kye J I, Kim H G, Chung W and Oh B 2001 *Appl. Phys. Lett.* **79** 2429
[47] Plecenik A, Satrapinsky L, Kúš P, Gaži Š, Beňačka Š, Vávra I and Kostič I 2001 *Physica* C **363** 224
[48] Schiestel S, Carosella C, Horwitz J, Osofsky M, Kendziora C, Qadri S and Knies D 2002 *Surf. Coat. Technol.* **158** 203
[49] Fu X H, Wang D S, Zhang Z P and Yang J 2002 *Physica* C **377** 407
[50] Wang S-F, Zhu Y-B, Liu Z, Zhou Y-L, Zhang Q, Chen Z-H, Lu H-B and Yang G-Z 2003 *Chin. Phys. Lett.* **20** 1356
[51] Wang S F, Zhou Y L, Zhu Y B, Zhang Q, Chen Z H, Lu H B, Dai S Y and Yang G Z 2003 *J. Supercond.* **16** 585
[52] Kim H-J, Kang W N, Choi E-M, Kim M-S, Kim K H P and Lee S-I 2001 *Phys. Rev. Lett.* **87** 087002
[53] Blank D H A, Hilgenkamp H, Brinkman A, Mijatovic D, Rijnders G and Rogalla H 2001 *Appl. Phys. Lett.* **79** 394
[54] Christen H, Zhai H, Cantoni C, Paranthaman M, Sales B, Rouleau C, Norton D, Christen D and Lowndes D 2001 *Physica* C **353** 157
[55] Hikita Y, Fukumura T, Ito T, Kawasaki M and Takagi H 2003 *J. Low Temp. Phys.* **131** 1187
[56] Ferrando V, Amoruso S, Bellingeri E, Bruzzese R, Manfrinetti P, Marre D, Velotta R, Wang X and Ferdeghini C 2003 *Supercond. Sci. Technol.* **16** 241
[57] Zhai H Y, Christen H M, Zhang L, Cantoni C, Paranthaman M, Sales B C, Christen D K and Lowndes D H 2001 *Appl. Phys. Lett.* **79** 2603
[58] Ermolov S N, Indenbom M V, Rossolenko A N, Bdikin I K, Uspenskaya L S, Stepakov N S and Glebovskii V G 2001 *JETP Lett.* **73** 557
[59] Mori Z, Eitoku K, Toshiya D, Koba S and Hakuraku Y 2003 *Physica* C **388/389** 115
[60] Ahn J-R, Lee S-G, Hwang Y, Sung G Y and Kim D K 2003 *Physica* C **388/389** 127
[61] Kus P, Plecenik A, Satrapinsky L, Xu Y and Sobolewski R 2002 *Appl. Phys. Lett.* **81** 2199
[62] Rogai R, Galluzzi V, Mancini A, Celentano G, Petrisor T, Rufoloni A, Varesi E, Grassano G, Boffa V and Gambardella U 2003 *Int. J. Mod. Phys.* B **17** 703
[63] Jergel M, Andrade E, Chromik Š, Jergel M, Falcony C, Štrbík V, Rocha M and Zavala E 2003 *Physica* C **383** 287
[64] Jo W, Huh J-U, Ohnishi T, Marshall A F, Beasley M R and Hammond R H 2002 *Appl. Phys. Lett.* **80** 3563
[65] Saito A, Kawakami A, Shimakage H and Wang Z 2002 *Japan. J. Appl. Phys.* **41** L127
[66] Shimakage H, Saito A, Kawakami A and Wang Z 2003 *IEEE Trans. Appl. Supercond.* **13** 3309
[67] Yata S, Shimizu G, Yamada Y, Kubo S and Matsushita A 2003 *Physica* C **388/389** 155
[68] Jo W, Beasley M R and Hammond R H 2003 *IEEE Trans. Appl. Supercond.* **13** 3257
[69] Zeng X H *et al* 2002 *Nature Mater.* **1** 35
[70] Xi X X *et al* 2003 *IEEE Trans. Appl. Supercond.* **13** 3233
[71] Pogrebnyakov A V, Redwing J M, Jones J E, Xi X X, Xu S Y, Li Q, Vaithyanathan V and Schlom D G 2003 *Appl. Phys. Lett.* **82** 4319
[72] Zeng X H *et al* 2003 *Appl. Phys. Lett.* **82** 2097
[73] Munro R G 2000 *J. Res. Natl Inst. Stand. Technol.* **105** 709
[74] Zhai H Y, Christen H M, Cantoni C, Goyal A and Lowndes D H 2002 *Appl. Phys. Lett.* **80** 1963

Mater. Res. Soc. Symp. Proc. Vol. 902E © 2006 Materials Research Society 0902-T10-55.1

Out-of-phase Boundary (OPB) Nucleation in Layered Oxides

M. A. Zurbuchen,[1,2,3] J. Lettieri,[3,4] Y. Jia,[3] A. H. Carim,[3,5] S. K. Streiffer,[2,6] D. G. Schlom[3]

[1] National Institute of Standards and Technology, Ceramics Division, Gaithersburg, MD, USA
[2] Argonne National Laboratory, Materials Science Division, Argonne, IL, USA
[3] The Pennsylvania State University, Department of Materials Science and Engineering, and Materials Research Institute, University Park, PA, USA
[4] Deceased
[5] currently at U.S. Department of Energy, Office of Science, Germantown, MD, USA
[6] Argonne National Laboratory Center for Nanoscale Materials, Argonne, IL, USA

ABSTRACT

Out-of-phase boundaries (OPBs), planar faults between regions of a crystal that are misaligned by a fraction of a unit cell dimension, occur frequently in materials of high structural anisotropy. Rarely observed in the bulk, OPBs frequently exist in epitaxial films of layered complex oxides, such as $YBa_2Cu_3O_{7-\delta}$-type, Aurivillius, and Ruddlesden-Popper phases, and frequently propagate through the entire thickness of a film, due to their large offset and the improbability of opposite-sign OPB annihilation. OPBs have previously been demonstrated to have a significant impact upon properties, so it is important to understand their generation. These faults arise through the same few mechanisms in the various layered complex oxides.

An effort is made to unify the discussion of nucleation of these defects, common to layered oxide materials. OPBs can nucleate at the film-substrate interface (primary) via steric, chemical, or misfit mechanisms, or post-growth (secondary) through crystallographic shear during decomposition of volatile components. Examples of the mechanisms observed during high-resolution transmission electron microscopy (HRTEM) study of Aurivillius and Ruddlesden-Popper phases are presented. A method for estimating the relative OPB density in a film from correlation of x-ray diffraction (XRD) θ-2θ data with TEM information on OPBs is presented.

INTRODUCTION

Many layered oxides have useful or physically interesting electromagnetic properties, such as ferroelectricity, superconductivity, and electromagnetism, and have been studied intensively over the past two decades, and intermittently over approximately the past 50 years. Their crystal structures are composed of interleaved crystallographic units. Two examples are shown below. Figure 1(a) shows the Ruddlesden-Popper homologous series.[1], with members composed of *n* alternating perovskite and rocksalt-type crystallographic units. Similarly, the Aurivillius homologous series[2,3] phases are composed of perovskite-like units alternating with pyramidal $Bi_2O_2^{2+}$ layers, shown in Fig. 1(b). Other layered oxides follow similar schema, for example the Dion-Jacobson phases[4] and numerous superconducting phases based on variations in the number and stacking sequences of perovskite, rocksalt, and $CaCuO_2$-type layers.[5,6]

Bulk techniques for synthesis often fail due to thermodynamic limitations. Epitaxial film growth enables synthesis of phase-pure samples inaccessible by other means. It is the constraint of epitaxy that can aid in stabilizing higher-*n* members of the homologous series thin films, along with advances in thin film synthesis techniques. Phase-pure Ruddlesden-Popper phases up to

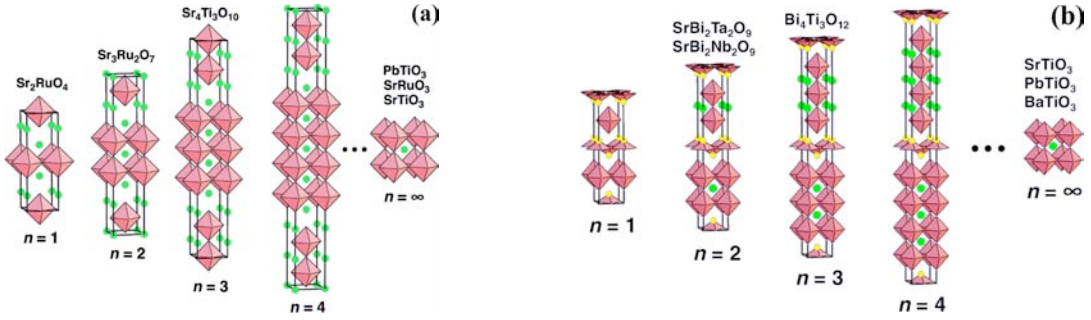

Figure 1. Examples of layered oxides, the (a) Ruddlesden-Popper and (b) Aurivillius homologous series. Some example compositions are shown.

$n = 5$ and Aurivillius phases up to $n = 7$ have recently been synthesized through use of this constraint.[7,8] It is these constraints, however, that lead also to the formation of a class of crystallographic defects in layered oxides, out-of-phase boundaries (OPBs).[9,10]

OPBs are translation boundary defects between identically oriented domains of a crystal or film that are out of registry by a fraction of the long unit cell dimension, depicted in Fig. 2. Depending on the layering period and complexity of the structure, a number of different offsets are possible. The anti-phase boundary (APB) is a special case of an OPB, with an offset of $c/2$.

OPBs were first described by Cowley in 1965,[11] and first imaged by Allpress in 1969 in his pioneering work on lattice imaging by TEM,[12] but have not been the focus of extensive study. They strongly influence material properties, particularly in epitaxial films with otherwise high crystalline perfection, so understanding their nucleation is critical. For example, OPBs have been demonstrated to significantly affect or even quench superconducting and ferroelectric properties of some oxides, and could have an especially severe impact in multiferroic materials.

EXPERIMENTAL DETAILS

All films were grown by pulsed laser deposition on perovskite-type (001) and (110) substrates, epi polished. Treatments of the growth processes and optimizations thereof are available elsewhere.[13,14] The relative phase purity and crystallinity of films was evaluated by four-circle x-ray diffraction scans. Samples for cross-section TEM examination were prepared by sandwiching, slicing, dimpling or wedge polishing, and argon ion milling (cooled or uncooled). Microscopy was performed at 200 keV to 400 keV.

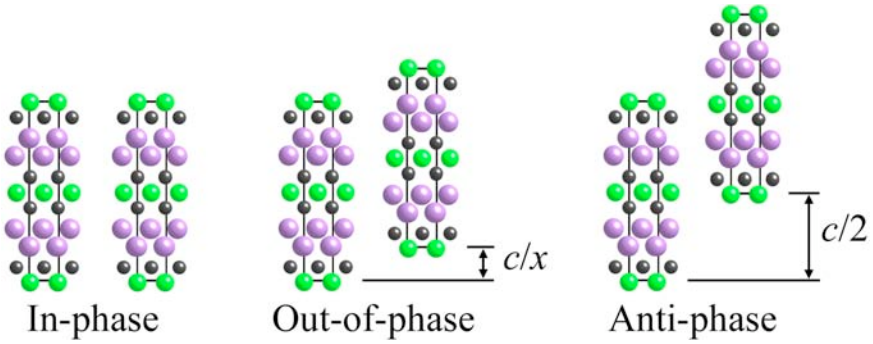

Figure 2. Schematic of in-phase, out-of-phase, and anti-phase alignment of neighboring domains of a crystal. The boundary between the out-of-phase regions is an OPB.

NUCLEATION MECHANISMS

Four primary and one secondary OPB nucleation mechanisms occur in layered oxides, and are generally applicable to layered oxides. Specific examples or particular mechanisms have been reported in the literature variously in specific chemical systems, such as $YBa_2Cu_3O_{7-\delta}$, $SrBi_2Ta_2O_9$, $Bi_4Ti_3O_{12}$, $(Sr_2Bi_4)Ti_5O_{15}$, Sr_2RuO_4, and $Sr_6Ti_5O_{16}$, but the mechanisms have not been described together in a general manner for layered oxides. We present schematics of the mechanisms, with images from our own work on Aurivillius and Ruddlesden-Popper films.

Steric

Nucleation on different steps of a substrate surface can lead to nuclei forming out-of-phase, shown schematically in Fig. 3(a) for both Aurivillius and Ruddlesden-Popper phases on $SrTiO_3$, along with an experimental example observed in a HRTEM image of $SrBi_2Nb_2O_9$,[15,16] Fig. 3(b), with a compressed image on the right, clearly showing the OPB. Nucleation of OPBs by steps in substrate surfaces has been predicted and observed by HRTEM in $YBa_2Cu_3O_{7-\delta}$, $SrBi_2Ta_2O_9$, $Bi_4Ti_3O_{12}$, and $(Ba_2Bi_4)Ti_5O_{18}$. Factors in considering the possibility of this mechanism are film structure, substrate structure, substrate vicinality, substrate surface step height, and density of nuclei for epitaxial growth.

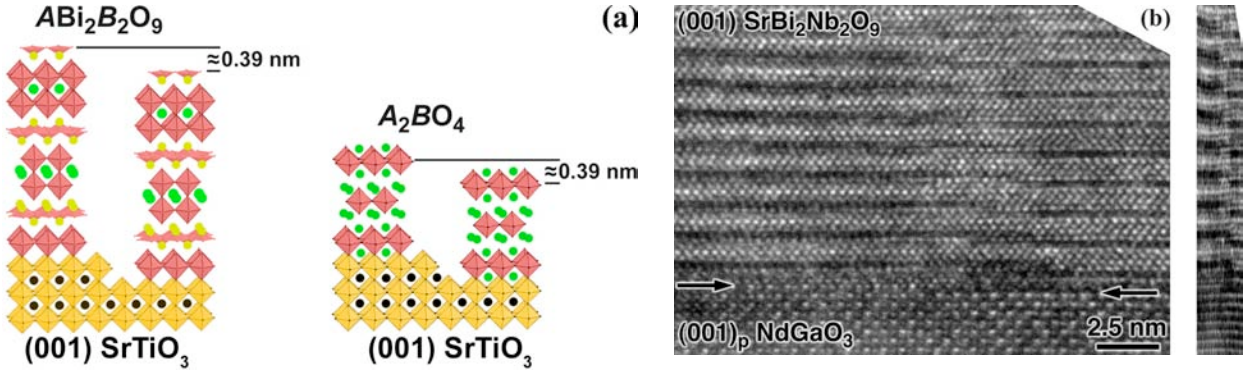

Figure 3. Steric mechanism of OPB formation, shown schematically in (a), and in a cross-section HRTEM image of (001) $SrBi_2Nb_2O_9$ / $(001)_p$ $NdGaO_3$ in (b).

Nucleation Layer

The existence of multiple structurally equivalent layers within the unit cell can lead to out-of-phase nucleation, shown schematically in Fig. 4(a) for Sr_2RuO_4 on $SrTiO_3$. After nucleation with an *A*O layer, growth can continue either with another *A*O or with a BO_2 layer, and neighboring out-of-phase nuclei will generate an OPB.[17] Experimental evidence of this mechanism in a Ruddlesden-Popper phase, Sr_2RuO_4, is shown in the HRTEM image in Fig. 4(b), with a compressed image on the right, clearly showing the OPB.[15] This mechanism has been predicted, observed, and recently used to control OPB density in YBCO-type films. Factors in considering the possibility of this mechanisms are crystal structure of the film, substrate composition, and substrate surface termination.

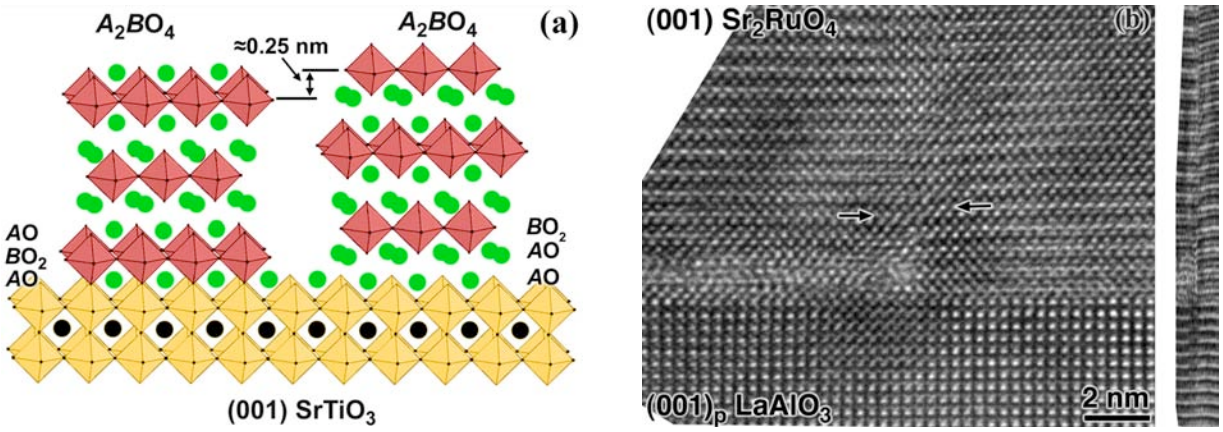

Figure 4. Nucleation Layer mechanism of OPB formation, shown schematically in (a), and in a cross-section HRTEM image of (001) Sr_2RuO_4 / (001)$_p$ $LaAlO_3$ in (b).

Misfit – *c*-axis Film

Interfacial misfit dislocations may nucleate OPBs, shown schematically in Fig. 5 for an $n = 2$ Ruddlesden-Popper phase with a tensile misfit with a $SrTiO_3$ substrate. Three AO layers are present at the core of the defect. Such a defect does not necessitate the formation of any APBs in the *ab* plane, so may be energetically favored in some cases. For the case of compressive misfit, a similar mechanism could occur, with a ≈0.25 nm double-AO layer replacing a ≈0.39 nm ABO_3 octahedron at the dislocation core. The tendency of Ruddlesden-Popper phases to form intergrowths, however, may make such a structure unlikely in those phases. Further, non-coherent nucleation must occur for this mechanism to be active, so large misfit is required. This type of OPB has not been observed experimentally.

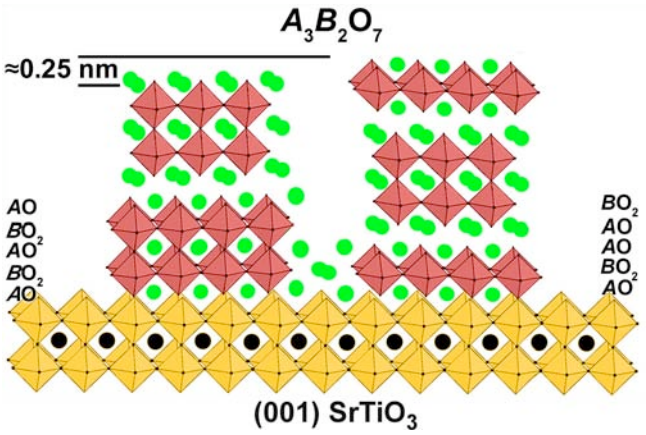

Figure 5. Misfit mechanism of OPB formation for a *c*-axis film, tensile case.

Misfit – Inclined *c*-axis film

Epitaxial films grown with the layering axis inclined to the surface of the substrate (growth front) can nucleate OPBs due to the mismatch in lattice mesh of the film and substrate, shown schematically in Fig. 6(a), and in a HRTEM image in Fig. 6(b).[15,16] This mechanism is not well understood, and does not consistently give rise to OPBs.

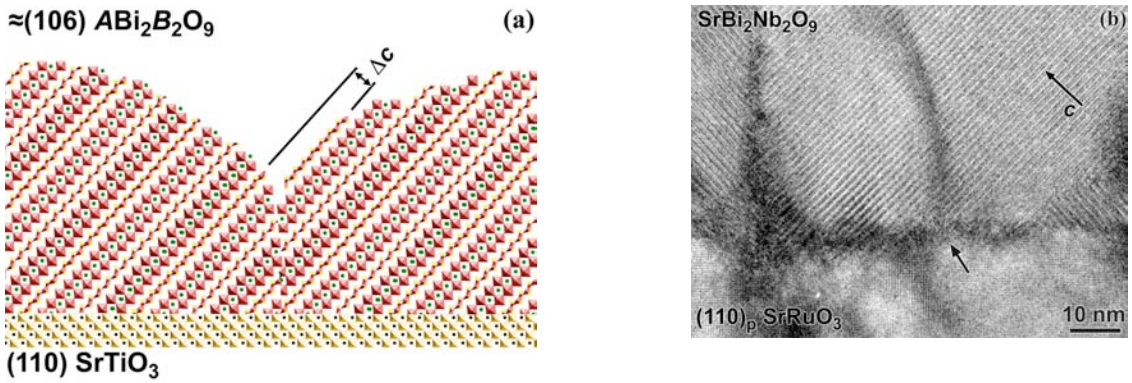

Figure 6. Misfit mechanism of OPB formation for a film with the *c* axis inclined to the substrate surface, shown schematically in (a), and in a cross-section HRTEM image in (b).

Crystallographic Shear

Volatile-component loss from an existing film can lead to OPBs through crystallographic shearing of octahedral blocks to share edges across the OPB and compensate charge. The schematic is shown in Fig. 7(a), with an example observed in a (001) $SrBi_2Ta_2O_9$ film shown in (b).[15,16]

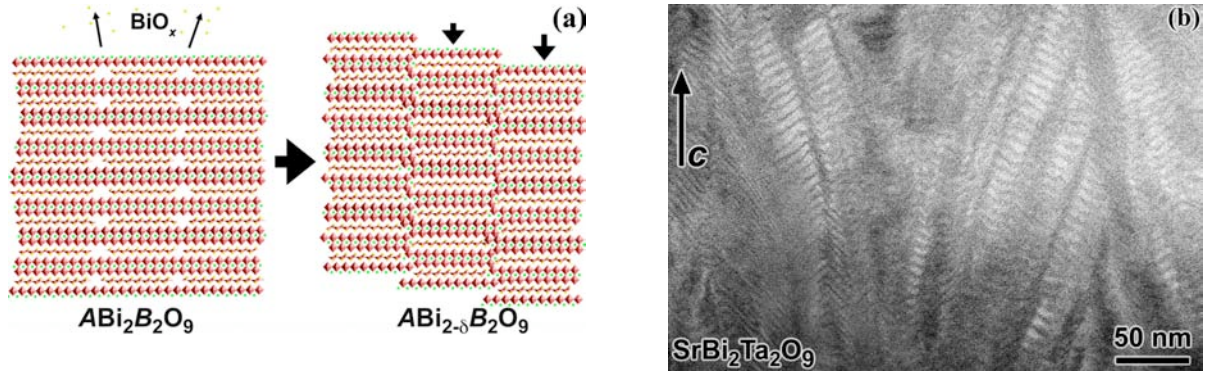

Figure 7. Crystallographic shear mechanism of OPB formation, shown schematically in (a), and in a cross-section HRTEM image of (001) $SrBi_2Ta_2O_9$ / (001) $SrTiO_3$ in (b).

DIFFRACTION ANALYSIS

X-ray diffraction yields a qualitative estimate of the relative OPB density in a film, by measuring peak splitting in θ-2θ scans. XRD θ-2θ scans of all $n = 2$ (001) $SrBi_2B_2O_9$ Aurivillius films we studied exhibit splitting of even-l 00l peaks. The observed trend of peak splitting for these films with the linear OPB density (measured by TEM) is shown in Fig. 8, and is valuable for estimating the relative OPB density in a film for a given system from θ-2θ data.[15,16]

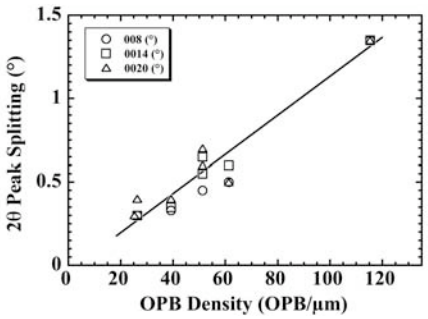

Figure 8. Peak splitting in θ-2θ XRD scans yields an estimate of the OPB density.

CONCLUSIONS

The five mechanisms of OPB formation in layered oxides were presented together as being generally applicable to all epitaxial films of layered oxides. The primary nucleation mechanisms are steric, nucleation layer, and misfit for *c*-axis and inclined-axis films, and the secondary nucleation mechanism is crystallographic shear upon decomposition. Examples showing experimental evidence for several mechanisms were presented. A correlation of θ-2θ peak splitting with OPB density for (001) films was described.

ACKNOWLEDGMENTS

Financial support: U.S. Department of Energy through grant number DE-FG02-03ER46063 and the NAS NRC Postdoctoral Fellowship.. TEM analysis at: The Pennsylvania State University Materials Characterization Lab, The Argonne Electron Microscopy Center, and the University of Michigan Electron Microprobe Analysis Laboratory, and the National Institute of Standards and Technology Electron Microscopy Facility.

REFERENCES

1 S. N. Ruddlesden and P. Popper, *Acta Cryst*. **10**, 538-539 (1957); **11**, 54-55 (1958).
2 B. Aurivillius, *Ark. Kemi* **1**, 463 (1950); **1**, 499 (1950); **2**, 519 (1951); **5**, 39 (1953).
3 B. Aurivillius and P. H. Fang, *Phys. Rev*. **126**, 893 (1962).
4 M. Dion, M. Ganne, and M. Tournoux, *Mater. Res. Bull*. **16**, 1429 (1981); A. J. Jacobson, J. T. Lewandowski, and J. W. Johnson, *J. Less-Common Met.* **116**, 137 (1986).; J. Gopalakrishnan, V. Bhat, and B. Raveau, *Mater. Res. Bull*. **22**, 413 (1987).
5 R. J. Cava, in *Advances in Superconductivity, Proceedings of the 1st International Symposium on Superconductivity*, Eds. K. Kitazawa and T. Ishiguro (Springer-Verlag, Tokyo, 1989), pp 159-164.
6 J. Hauck and K. Mika, *Supercond. Sci. Technol.* **11** 614 (1998).
7 J. H. Haeni, C. D. Theis, D. G. Schlom, W. Tian, X. Q. Pan, H. Chang, I. Takeuchi, and X. D. Xiang, *Appl. Phys. Lett.* **78**, 3292 (2001).
8 M. A. Zurbuchen, J. Schubert, Y. Jia, D. J. Comstock, W. Tian, V. O. Sherman, D. Fong, M. E. Hawley, A. K. Tagantsev, S. K. Streiffer, and D. G. Schlom, *submitted to Nature: Materials* (2005).
9 M. A. Zurbuchen, Y. Jia, S. K. Knapp, A. H. Carim, D. G. Schlom, L-N. Zou, and Y. Liu, *Appl. Phys. Lett*. **78**, 2351 (2001).
10 M. A. Zurbuchen, D. G. Schlom, and S. K. Streiffer*, Appl. Phys. Lett*. **79**, 887 (2001).
11 J. M. Cowley, *Phys. Rev. A* **138**, 1384 (1965).
12 J. G. Allpress, *Mater. Res. Bull.* **4**, 707 (1969).
13 J. Lettieri, Y. Jia, S. J. Fulk, D. G. Schlom, M. E. Hawley, and G. W. Brown, *Thin Solid Films* **379**, 64 (2000).
14 M. A. Zurbuchen, Y. Jia, S. Knapp, A. H. Carim, D. G. Schlom, and X. Q. Pan, *Appl. Phys. Lett.* **83**, 3891 (2003).
15 M. A. Zurbuchen, *Ph. D. Dissertation*, (The Pennsylvania State University, 2002).
16 M. A. Zurbuchen, J. Lettieri, G. Asayama, Y. Jia, S. Knapp, A. H. Carim, D. G. Schlom, X. Q. Pan, and S. K. Streiffer, submitted to *J. Mater. Res.* (2005).
17 M. A. Zurbuchen, Y. Jia, S. K. Knapp, A. H. Carim, D. G. Schlom, and X. Q. Pan, *Appl. Phys. Lett.* **83**, 3891 (2003).

Epitaxial growth and magnetic properties of the first five members of the layered $Sr_{n+1}Ru_nO_{3n+1}$ oxide series

W. Tian, J. H. Haeni, and D. G. Schlom[a)]
Department of Materials Science and Engineering, Pennsylvania State University, University Park, Pennsylvania 16802-5005

E. Hutchinson, B. L. Sheu, M. M. Rosario, P. Schiffer, and Y. Liu
Department of Physics, Pennsylvania State University, University Park, Pennsylvania 16802

M. A. Zurbuchen
Materials Science Division, Argonne National Laboratory, Argonne, Illinois 60439

X. Q. Pan
Department of Materials Science and Engineering, The University of Michigan, Michigan 48109

(Received 23 October 2006; accepted 8 December 2006; published online 12 January 2007)

Epitaxial thin films of the $n=1-5$ members of the layered $Sr_{n+1}Ru_nO_{3n+1}$ oxide series were produced by reactive molecular-beam epitaxy. X-ray diffraction and high-resolution transmission electron microscopy confirm that these films are epitaxially oriented and nearly phase pure ($>98\%$). The Sr_2RuO_4 ($n=1$) and $Sr_3Ru_2O_7$ ($n=2$) samples show no ferromagnetic transition in the range from 5 to 300 K, while the $Sr_4Ru_3O_{10}$ ($n=3$), $Sr_5Ru_4O_{13}$ ($n=4$), and $Sr_6Ru_5O_{16}$ ($n=5$) samples show ferromagnetic transitions at 85, 95, and 130 K, respectively. © *2007 American Institute of Physics*. [DOI: 10.1063/1.2430941]

The discovery of superconductivity[1] and the establishment of spin-triplet pairing[2,3] in single-layer Sr_2RuO_4, quantum metamagnetism in double-layer $Sr_3Ru_2O_7$,[4,5] and the possible presence of momentum-space magnetic monopoles in ferromagnetic, pseudocubic $SrRuO_3$ (Ref. 6) have led to intensive research on the layered $Sr_{n+1}Ru_nO_{3n+1}$ perovskite oxide series (the positive integer n corresponds to the number of perovskite layers sandwiched between double-SrO rocksalt layers). It was suggested that being in close proximity of the ferromagnetic phase $SrRuO_3$ is key for the occurrence of spin-triplet superconductivity in Sr_2RuO_4.[7] The crossover from ferromagnetism in $SrRuO_3$ to paramagnetism and spin-triplet superconductivity in Sr_2RuO_4 appears to originate from a structural crossover from a three-dimensional perovskite network in $SrRuO_3$ to a two-dimensional perovskite sheet in Sr_2RuO_4. Therefore, a systematic study of the behavior of $Sr_{n+1}Ru_nO_{3n+1}$ as dimensionality decreases may provide insight into the interplay between magnetism and superconductivity.

Attempts to explore the magnetic properties of intermediate $Sr_{n+1}Ru_nO_{3n+1}$ members ($1<n<\infty$) have been thwarted by the substantial challenges associated with the synthesis of phase-pure samples. Conflicting results on the magnetic properties of $Sr_3Ru_2O_7$ and $Sr_4Ru_3O_{10}$ have been reported,[4,8–14] even though "single crystals" (as determined by x-ray diffraction) of these phases have been produced.[4,8,10–14] Growing evidence in support of $Sr_3Ru_2O_7$ being a paramagnetic metal in zero field[4,8,13] has led to the widely held belief that intergrowths of higher n members were responsible for the ferromagnetic transition ($T_C=104$ K) previously observed in some $Sr_3Ru_2O_7$ single crystals.[9] Indeed, single crystals deemed phase pure by x-ray diffraction (XRD) were found to contain intergrowths when examined by transmission electron microscopy (TEM).[15] The challenge to the conventional synthesis of phase-pure $Sr_{n+1}Ru_nO_{3n+1}$ compounds considerably restricts access to these materials and lies at the heart of the controversy in the interpretation of existing experimental results.

Here we show that using reactive molecular-beam epitaxy (MBE), i.e., monolayer-by-monolayer deposition with a correct absolute dose of cations, $>98\%$ phase-pure $Sr_{n+1}Ru_nO_{3n+1}$ compounds can be made. The synthesis of nearly phase-pure samples by MBE allows their properties to be characterized.

The first five ($n=1-5$) members of the $Sr_{n+1}Ru_nO_{3n+1}$ series were synthesized by reactive MBE on (001) $SrTiO_3$ and (001) $(LaAlO_3)_{0.29}(SrAl_{1/2}Ta_{1/2}O_3)_{0.71}$ (LSAT) substrates. Prior to growth, the (001) $SrTiO_3$ substrates were etched with a buffered HF solution to achieve a TiO_2-terminated surface.[16] During growth the substrates were held at 620 °C and immersed in a continuous flux of molecular oxygen, yielding a background pressure of 1×10^{-6} Torr. Monolayer doses of Sr and Ru were deposited alternately on the substrates to form the perovskite layers in these structures. For the double-SrO rocksalt layers in these structures, a Sr dose corresponding to twice the monolayer dose was delivered. Shuttered reflection high-energy electron diffraction intensity oscillations during growth were used to monitor film stoichiometry.[17] The duration of the Sr and Ru doses from molecular beams was adjusted to ensure that a complete monolayer of each cation was deposited during each shuttered cycle. The growth of each Ruddlesden-Popper film was begun with a $SrRuO_3$ buffer layer to precisely calibrate the shuttering times.[17] Once calibrated, the shuttering sequence was altered to grow the desired $Sr_{n+1}Ru_nO_{3n+1}$ film. In this letter we focus on five $Sr_{n+1}Ru_nO_{3n+1}$ films with thicknesses of 877, 523, 648, 614, and 670 Å for the $n=1-5$ films, respectively.

Four-circle x-ray diffraction (XRD) studies on these thin films revealed the formation of single-phase and high quality samples with the desired $n=1-5$ Ruddlesden-Popper structures. Figure 1 shows the XRD θ-2θ scans of a Sr_2RuO_4 film

[a)]Electronic mail: schlom@ems.psu.edu

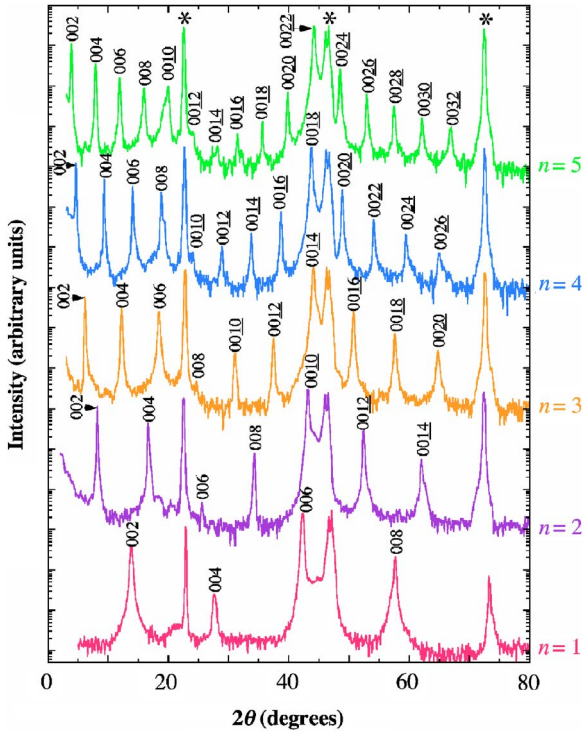

FIG. 1. (Color online) θ-2θ XRD scans of a Sr_2RuO_4 ($n=1$) film grown on a (001) LSAT substrate and $n=2$, 3, 4, and 5 $Sr_{n+1}Ru_nO_{3n+1}$ phases grown on (001) $SrTiO_3$ substrates. Substrate peaks are labeled with an (*), and the plots are offset for clarity.

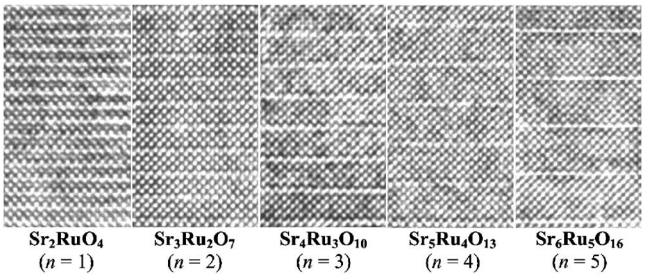

FIG. 2. Cross-sectional HRTEM images (from left to right) of the same $n=1-5$ $Sr_{n+1}Ru_nO_{3n+1}$ films shown in Fig. 1. The two adjacent white rows in the images correspond to the [100] projections of the rocksalt SrO layers. Between the double SrO layers lies the [100] projection of the $SrRuO_3$ perovskite sheet.

grown on a (001) LSAT substrate and $Sr_3Ru_2O_7$, $Sr_4Ru_3O_{10}$, $Sr_5Ru_4O_{13}$, and $Sr_6Ru_5O_{16}$ films grown on (001) $SrTiO_3$ substrates. All of the XRD peaks occur at 2θ positions consistent with the c axis of the films normal to the surface of the substrates. The c-axis lattice constants of these films as determined by a Nelson-Riley analysis[18] of the diffraction peak positions are 12.82 ± 0.02, 20.85 ± 0.05, 28.8 ± 0.2, 37.2 ± 0.4, and 44.7 ± 1.0 Å for the $n=1-5$ phases, respectively. These values are slightly larger than the previously reported bulk values of $Sr_{n+1}Ru_nO_{3n+1}$ phases[11,19,20] with low n and lengthen by the amount expected (two $SrRuO_3$ sheets per unit cell) as n goes from n to $n+1$, consistent with an in-plane biaxial compressive strain being imparted on the films by the epitaxial growth on the (001) LSAT and $SrTiO_3$ substrates. The full width at half maxima of the rocking curves of the 006, 00$\underline{1}$0, 00$\underline{1}$4, 00$\underline{1}$8, and 00$\underline{2}$2 peaks of the $n=1-5$ samples are 0.091°, 0.049°, 0.056°, 0.042°, and 0.045°, respectively, indicating a high degree of structural perfection. XRD ϕ scans of off-axis (asymmetric) peaks were used to establish the in-plane orientations of the films. ϕ scans of the 103, 105, 107, 109, and 10$\underline{1}$1 peaks of the $n=1-5$ films, respectively, indicate an epitaxial in-plane orientation relationship of [100] $Sr_{n+1}Ru_nO_{3n+1}\|$[100] $SrTiO_3$ (LSAT).[23] Although the epitaxial films appear to be single phase by XRD, we used TEM to check for thin aperiodic intergrowths that are difficult to discern by XRD.[21,22]

High-resolution TEM (HRTEM) within a JEOL 4000EX operated at 400 kV was used to characterize the microstructure and atomic structure of the films. Figure 2 shows cross-sectional HRTEM images of the $n=1-5$ films with the incident electron beam along the [100] zone axis of the sample (film and substrate). The two adjacent white rows in the images correspond to the [100] projections of the rocksalt SrO layers. Between double-SrO layers lies the [100] projection of the $SrRuO_3$ perovskite sheet. The alternate stacking of the rocksalt SrO layers and the perovskite sheets observed in the image confirms the formation of the desired Ruddlesden-Popper structures. Selected area electron diffraction studies of these films corroborate the epitaxial orientations established by XRD. All of the imaged areas of the $n=1$ film display the identical contrast characteristic of the region shown in Fig. 2, with no intergrowths observed. Intergrowths of Ruddlesden-Popper layers with other n values (a half-unit-cell in thickness along the c direction) were, however, infrequently observed in the $n=2-5$ films. Such intergrowths exist in very localized regions and have insufficiently ordered volume to give rise to discernable diffraction spots in either XRD or electron diffraction. Although observable, the populations of the intergrowths are very small. Several representative regions imaged by HRTEM, which are typically 200–300 nm wide and span the entire film thickness, of each sample were analyzed to determine the volume fractions of the intergrowths. The statistics showed that the total volume fraction of the intergrowths is less than 2% of the imaged volume in all samples and none of the volume fractions of the individual intergrowths exceeds 0.6%.[23] In addition, the majority of the intergrowths are those with n values less than that of the film phase. In the $n=5$ film, all of the intergrowths have n values less than 5. We believe that the intergrowths in these samples are most likely the result of slight errors and variations in the monolayer doses supplied during the MBE growth. A comprehensive description of the microstructure of the films will be published elsewhere.[23]

The magnetization versus temperature of the *same* films studied by XRD and TEM was measured using a commercial superconducting quantum interference device magnetometer in a 0.005 T magnetic field aligned perpendicular to the sample plane after precooling in a 1 T field. The temperature-dependent magnetization of bare LSAT and $SrTiO_3$ substrates was measured to subtract the magnetic contribution of the magnetic impurities present in the substrates. The contribution of the thin $SrRuO_3$ (ferromagnetic with a $T_C\approx160$ K in bulk[24]) buffer layer to the out-of-plane magnetization was also subtracted by assuming that the magnetic moment per Ru atom in the $SrRuO_3$ buffer layer and its temperature dependence are identical to those obtained from an 847 Å thick $SrRuO_3$ film grown by MBE using the same growth conditions as the $Sr_{n+1}Ru_nO_{3n+1}$ films. This assumption should be valid since all of the $SrRuO_3$ buffer layers have a thickness ($\geqslant$6 pseudocubic $SrRuO_3$ unit cells) that in other studies has been found to yield the out-of-plane mag-

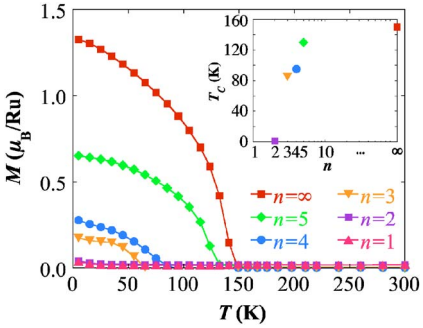

FIG. 3. (Color online) Magnetization as a function of temperature of the same $n=1-5$ $Sr_{n+1}Ru_nO_{3n+1}$ films shown in Figs. 1 and 2 and $n=\infty$ $Sr_{n+1}Ru_nO_{3n+1}$ film. Note that the $n=3$, 4, 5, and ∞ samples show ferromagnetism, while no sign of ferromagnetism is observed for the $n=1$ and $n=2$ samples. The inset shows a plot of the ferromagnetic transition temperatures of the $n=3$, 4, 5, and ∞ $Sr_{n+1}Ru_nO_{3n+1}$ samples vs n. For the sake of comparison, the metamagnetic phase transition temperature ($\sim$1.1 K) of the $n=2$ ($Sr_3Ru_2O_7$) single crystal in a magnetic field of 7.9 T (data from Ref. 5) is also shown.

netization of bulk $SrRuO_3$.[25,26] Figure 3 shows the magnetic moment per Ru atom as a function of temperature in the range from 5 to 300 K for the $n=1-5$ and ∞ samples, after the corresponding substrate and buffer layer subtraction. The curves reveal that the $n=3$, 4, and 5 samples are ferromagnetic, while no sign of ferromagnetism is observed in the $n=1$ and 2 samples. The transition temperatures (T_C) of the ferromagnetic phases were determined by the onset of the magnetization in the $M(T)$ curves. The obtained T_C values are 85, 95, 130, and 150 K for the $n=3$, 4, 5, and ∞ samples, respectively. The n-dependent magnetic behavior is evident (inset in Fig. 3). For the sake of comparison, the metamagnetic phase transition temperature ($\sim$1.1 K) of the $n=2$ ($Sr_3Ru_2O_7$) single crystals[5] in a magnetic field of 7.9 T is also shown in the inset.

The deviation of T_C for the $SrRuO_3$ thin film (150 K) from the bulk value [160±10 K (Ref. 24)] is consistent with previous reports that found such a T_C reduction to be due to the strain imparted by commensurate growth on a $SrTiO_3$ substrate.[27,28] Similarly, the deviation of T_C for the $Sr_4Ru_3O_{10}$ thin film from the reported value [$\sim$100 K (Ref. 29)] of single crystals is believed to be due to epitaxial strain. The saturation moment of the $SrRuO_3$ film ($\sim 1.3\mu_B$/Ru) is comparable to the values previously reported for epitaxial $SrRuO_3$ thin films grown on (001) $SrTiO_3$ substrates.[27,28] In contrast, the saturation moment ($\sim 0.2\mu_B$/Ru) of the $Sr_4Ru_3O_{10}$ thin film is significantly smaller than the values ($\sim 1.5\mu_B$/Ru) reported for single crystals.[29] The origin of the reduced moment for the thin film samples is unclear, although magnetism in the ruthenates is extraordinarily complicated and it is quite possible that the strain from the substrate is responsible for the difference. Further study, perhaps with neutron scattering, would be necessary to explore the details of the magnetic structure.

In closing, our data suggest that reduced dimensionality in the $Sr_{n+1}Ru_nO_{3n+1}$ series leads to a systematic reduction in ferromagnetism. The minimum value of ferromagnetism ($n=3$) corresponds to the case where at least one RuO_2 sheet in the structure is surrounded by RuO_2 sheets from above and below. For $n=1$ and 2 $Sr_{n+1}Ru_nO_{3n+1}$ phases, no RuO_2 sheets are surrounded by RuO_2 sheets, resulting in the loss of ferromagnetism.

The authors acknowledge the financial support of the U.S. Department of Energy through Grant No. DE-FG02-03ER46063 for the three authors (W.T., J.H.H., and D.G.S) and DE-FG02-04ER46159 for the three authors (E.H., M.M.R., and Y.L.) and the National Science Foundation through Grant No. DMR-0401486 for the two authors (B.L.S. and P.S.). The TEM analysis was performed in the Electron Microscopy Center, Materials Science Division, Argonne National Laboratory, Argonne, IL. The authors also acknowledge the help of R. E. Cook, J. M. Hiller, and S. K. Streiffer during the course of the TEM work.

[1] Y. Maeno, H. Hashimoto, K. Yoshida, S. Nishizaki, T. Fujita, J. G. Bednorz, and F. Lichtenberg, Nature (London) **372**, 532 (1994).
[2] A. P. Mackenzie and Y. Maeno, Rev. Mod. Phys. **75**, 657 (2003).
[3] K. D. Nelson, Z. Q. Mao, Y. Maeno, and Y. Liu, Science **306**, 1151 (2004).
[4] S. A. Grigera, R. S. Perry, A. J. Schofield, M. Chiao, S. R. Julian, G. G. Lonzarich, S. I. Ikeda, Y. Maeno, A. J. Millis, and A. P. Mackenzie, Science **294**, 329 (2001).
[5] S. A. Grigera, P. Gegenwart, R. A. Borzi, F. Weickert, A. J. Schofield, R. S. Perry, T. Tayama, T. Sakakibara, Y. Maeno, A. G. Green, and A. P. Mackenzie, Science **306**, 1154 (2004).
[6] Z. Fang, N. Nagaosa, K. S. Takahashi, A. Asamitsu, R. Mathieu, T. Ogasawara, H. Yamada, M. Kawasaki, Y. Tokura, and K. Terakura, Science **302**, 92 (2003).
[7] T. M. Rice and M. Sigrist, J. Phys.: Condens. Matter **7**, L643 (1995).
[8] R. J. Cava, H. W. Zandbergen, J. J. Krajewski, W. F. Peck, B. Batlogg, S. Carter, R. M. Fleming, O. Zhou, and L. W. Rupp, J. Solid State Chem. **116**, 141 (1995).
[9] G. Cao, S. McCall, and J. E. Crow, Phys. Rev. B **55**, R672 (1997).
[10] G. Cao, S. K. McCall, J. E. Crow, and R. P. Guertin, Phys. Rev. B **56**, R5740 (1997).
[11] M. K. Crawford, R. L. Harlow, W. Marshall, Z. Li, G. Cao, R. L. Lindstrom, Q. Huang, and J. W. Lynn, Phys. Rev. B **65**, 214412 (2002).
[12] G. Cao, L. Balicas, W. H. Song, Y. P. Sun, Y. Xin, V. A. Bondarenko, J. W. Brill, S. Parkin, and X. N. Lin, Phys. Rev. B **68**, 174409 (2003).
[13] R. S. Perry, L. M. Galvin, S. A. Grigera, L. Capogna, A. J. Schofield, A. P. Mackenzie, M. Chiao, S. R. Julian, S. I. Ikeda, S. Nakatsuji, Y. Maeno, and C. Pfleiderer, Phys. Rev. Lett. **86**, 2661 (2001).
[14] R. S. Perry, K. Kitagawa, S. A. Grigera, R. A. Borzi, A. P. Mackenzie, K. Ishida, and Y. Maeno, Phys. Rev. Lett. **92**, 166602 (2004).
[15] Y. Xin, G. Cao, and J. E. Crow, J. Cryst. Growth **252**, 372 (2003).
[16] M. Kawasaki, K. Takahashi, T. Maeda, R. Tsuchiya, M. Shinohara, O. Ishiyama, T. Yonezawa, M. Yoshimoto, and H. Koinuma, Science **266**, 1540 (1994).
[17] J. H. Haeni, C. D. Theis, and D. G. Schlom, J. Electroceram. **4**, 385 (2000).
[18] J. B. Nelson and D. P. Riley, Proc. Phys. Soc. London **57**, 160 (1945).
[19] L. Walz and F. Lichtenberg, Acta Crystallogr., Sect. C: Cryst. Struct. Commun. **C49**, 1268 (1993).
[20] H. K. Müller-Buschbaum and J. Z. Wilkens, Z. Anorg. Allg. Chem. **591**, 161 (1990).
[21] J. H. Haeni, C. D. Theis, D. G. Schlom, W. Tian, X. Q. Pan, H. Chang, I. Takeuchi, and X. D. Xiang, Appl. Phys. Lett. **78**, 3292 (2001).
[22] W. Tian, X. Q. Pan, J. H. Haeni, and D. G. Schlom, J. Mater. Res. **16**, 2013 (2001).
[23] W. Tian, J. H. Haeni, M. A. Zurbuchen, X. Q. Pan, and D. G. Schlom (unpublished).
[24] A. Callaghan, C. W. Moeller, and R. Ward, Inorg. Chem. **5**, 1572 (1966).
[25] M. Izumi, K. Nakazawa, Y. Bando, Y. Yoneda, and H. Terauchi, Solid State Ionics **108**, 227 (1998).
[26] M. Izumi, K. Nakazawa, and Y. Bando, J. Phys. Soc. Jpn. **67**, 651 (1998).
[27] C. B. Eom, R. J. Cava, R. M. Fleming, J. M. Philips, R. B. van Dover, J. H. Marshall, J. W. P. Hsu, J. J. Krajewski, and W. F. Peck, Jr., Science **258**, 1766 (1992).
[28] Q. Gan, R. A. Rao, C. B. Eom, J. L. Garrett, and M. Lee, Appl. Phys. Lett. **72**, 978 (1998).
[29] W. Bao, Z. Q. Mao, M. Zhou, J. Hooper, J. W. Lynn, R. S. Freitas, P. Schiffer, Y. Liu, H. Q. Yuan, and F. Salamon, e-print cond-mat/0607428.

REVIEW

This section of Journal of Materials Research is reserved for papers that are reviews of literature in a given area.

Morphology, structure, and nucleation of out-of-phase boundaries (OPBs) in epitaxial films of layered oxides

M.A. Zurbuchen[a)]
Ceramics Division, Materials Science and Engineering Laboratory, National Institute of Standards and Technology (NIST), Gaithersburg, Maryland 20899; and Department of Materials Science and Engineering, The Pennsylvania State University, University Park, Pennsylvania 16802-5005

W. Tian and X.Q. Pan
Department of Materials Science and Engineering, University of Michigan, Ann Arbor, Michigan 48109-2136

D. Fong and S.K. Streiffer
Materials Science Division, Argonne National Laboratory (ANL), Argonne, Illinois 60439

M.E. Hawley
Materials Science and Technology, Los Alamos National Laboratory, Los Alamos, New Mexico 87545

J. Lettieri,[b)] Y. Jia, G. Asayama, S.J. Fulk, D.J. Comstock, S. Knapp, A.H. Carim,[c)] and D.G. Schlom
Department of Materials Science and Engineering, The Pennsylvania State University, University Park, Pennsylvania 16803-6602

(Received 23 July 2006; accepted 26 February 2007)

Out-of-phase boundaries (OPBs) are translation boundary defects characterized by a misregistry of a fraction of a unit cell dimension in neighboring regions of a crystal. Although rarely observed in the bulk, they are common in epitaxial films of complex crystals due to the physical constraint of the underlying substrate and a low degree of structural rearrangement during growth. OPBs can strongly affect properties, but no extensive studies of them are available. The morphology, structure, and nucleation mechanisms of OPBs in epitaxial films of layered complex oxides are presented with a review of published studies and new work. Morphological trends in two families of layered oxide phases are described. The atomic structure at OPBs is presented. OPBs may be introduced into a film during growth via the primary mechanisms that occur at film nucleation (steric, nucleation layer, *a-b* misfit, and inclined-*c* misfit) or after growth via the secondary nucleation mechanism (crystallographic shear in response to loss of a volatile component). Mechanism descriptions are accompanied by experimental examples. Alternative methods to the direct imaging of OPBs are also presented.

I. INTRODUCTION

Many layered complex oxides, including Aurivillius,[1–5] Ruddlesden–Popper,[6,7] and layered cuprate[8] phases, have been intensively studied over the past fifteen years for the interesting and potentially useful behaviors they exhibit, such as superconductivity,[9] colossal magnetoresistance,[10] or ferroelectricity.[11] These phases are of further interest as quasi-two-dimensional systems for study of reduced dimensionality material systems.[12–14] Although the majority of layered complex oxides are inaccessible as large single crystals, they can be prepared for study in epitaxial thin film form to be reasonably pure both chemically and structurally. Lattice-matched substrates provide a structural template enabling high-quality growth, but the physical constraints of epitaxy and the large unit cells of these phases lead to the generation and propagation of out-of-phase boundary (OPB) defects. OPBs can significantly impact properties,

[a)]Address all correspondence to this author.
e-mail: mark_z@mac.com
Present address: Electronics and Photonics Laboratory, The Aerospace Corporation, El Segundo, CA 90245.
[b)]Deceased
[c)]Present address: United States Department of Energy, Germantown, Maryland
DOI: 10.1557/JMR.2007.0198

so an understanding of their genesis is imperative. They frequently nucleate at the film–substrate interface and frequently propagate through the entire thickness of a film, due to their large offset and the improbability of opposite-sign OPB annihilation. As improved deposition techniques make materials with larger and larger unit cells accessible, small-scale interactions causing large-scale defects will play an increasingly greater role in affecting the crystalline perfection and quality of these films.

The crystal structures of layered complex oxides are based on coherently interleaved crystallographic units. Variations in sequence yield different phases, with chemical compositions described by homologous series formulae.[15–17] Two examples are shown in Fig. 1, the Ruddlesden–Popper[6,7] [$A_{n+1}B_nO_{3n+1}$ or $(AO)(ABO_3)_n$] and Aurivillius[1–5] [$(Bi_2O_2)(A_{n-1}B_nO_{3n+1})$ or $(Bi_2BO_6)(ABO_3)_{n-1}$] homologous series of phases. Ruddlesden–Popper phases consist of the repeated layering of $nABO_3$ perovskite sheets alternating with an AO rocksalt sheet along the c axis. Aurivillius phases similarly consist of the repeated layering of $nABO_3$ perovskite sheets alternating units with a $Bi_2O_2^{2+}$-type ($Bi_2O_2^{2+}$ or Pb_2O_2) sheet along the c axis. The room-temperature structures are typically distorted to a lower symmetry than the tetragonal unit cell implied by the prototypes, although many phases are tetragonal at film-growth temperatures.[11,15,18–23] Other layered complex oxides include the Dion–Jacobson phases[24–26] and numerous superconducting phases based on variations in the number and stacking sequences of perovskite, rocksalt and $CaCuO_2$-type layers.[27–29] By convention, the c axis is the layering axis when layered oxides are discussed in general.

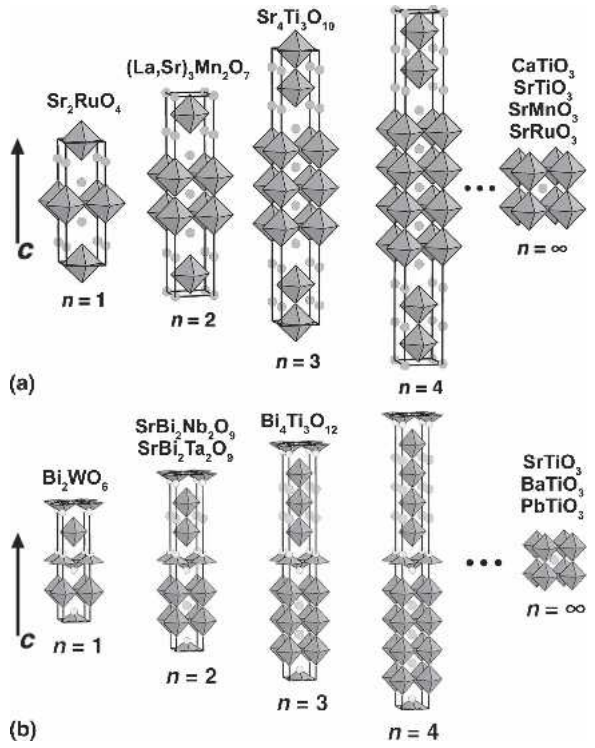

FIG. 1. Examples of two layered complex oxide series of phases: (a) Ruddlesden–Popper phases, $A_{n+1}B_nO_{3n+1}$, are composed of interleaved close-packed AO sheets and n number of ABO_3 perovskite sheets layered along the c axis. (b) Aurivillius phases, $(Bi_2O_2)(A_{n-1}B_nO_{3n+1})$, have a similar structure, composed of interleaved Bi_2O_2 or Pb_2O_2 and n ABO_3 perovskite sheets layered along the c axis.

Bulk and single-crystal synthesis techniques often fail to yield single-phase layered complex oxides due to thermodynamic limitations. Large-period layered oxides of a given series will all have nearly identical formation energies. The case of Ruddlesden–Popper phases has been studied. The enthalpy of formation of Ruddlesden–Popper homologues with $n \geqslant 3$ converges to an effectively constant value,[30] providing no driving force allowing the bulk synthesis of pure phases. A further thermodynamic analysis of the Ruddlesden–Popper system $Sr_{n+1}Ti_nO_{3n+1}$ demonstrated that, for a given composition, a single "solid solution" phase consisting of various n intergrowths was the thermodynamically stable phase for any particular composition.[31] Slopes of phase coexistence tangents between one composition pair and the next differ very little, essentially merging into an envelope and providing a weak driving force for structural rearrangement.[31,32] This is similar to the "swinging shear planes"[33,34] in transition metal oxide shear phases and block structures[35] (based on similar structural principles as layered complex oxides), which have a succession of individual compositions with similar formation energies. It is reasonable to expect that these trends in formation energy hold for all layered oxide homologous series.

Where bulk methods fail, film deposition methods can help extend the range of what is possible. Epitaxial films are the next-best thing for probing new materials. In addition to thermodynamic epitaxial stabilization,[36] kinetic epitaxial stabilization occurs due to the physical constraint, limited atomic rearrangement, and controlled delivery of elements for deposition-based epitaxial film growth techniques such as molecular-beam epitaxy (MBE), pulsed laser deposition (PLD), and chemical vapor deposition (CVD), and have led to considerable success in the synthesis of phase-pure epitaxial films of "new" materials that are impossible to synthesize in phase-pure form by bulk means.[23,37–40] Considerable effort has been directed toward layered oxides, which lend themselves well to epitaxial growth, particularly with the c axis (the long axis) perpendicular to the substrate surface (c-axis films). The constraints of epitaxial growth, though, lead also to the formation of a class of crystallographic defects in layered oxides, OPBs.[41,42]

An OPB can be defined as a boundary between adjacent regions of a crystal that are out of registry by a fraction of a lattice parameter. This is shown schematically in Fig. 2. In other words, an OPB is a translation

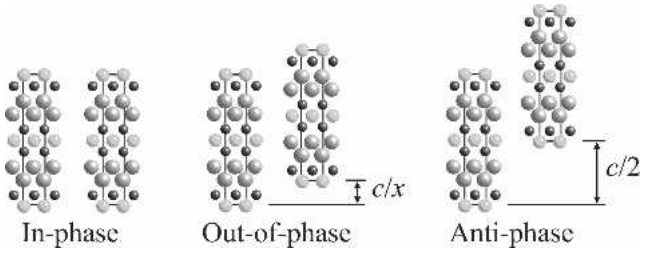

FIG. 2. Two regions of a crystal that are out of registry by a fraction of the unit cell dimension are described as out of phase, and the boundary between the two domains is an OPB. An APB is a special case of an OPB with an offset of 1/2.

boundary defect and can result from of a shift between regions of a crystal that is out of the plane of a substrate used for film growth (the typical case for layered oxides), or in the plane of the substrate. OPBs can also exist in the bulk and can exist generally in any complex structure, although layered oxides are discussed here. Depending upon the dimensions and complexity of the unit cell of a material, a number of different offsets is possible. The simplest case, with only one possible offset, is that of an antiphase boundary (APB), an offset of 1/2 *c*, in a simple structure such as perovskite. The number of possible offsets rises with increasing *n* of a homologous series, i.e., with increasing number of atomic layers in the structure. A distinction is made between the more generic case of a stacking fault in a layered oxide (an atomic plane that is out of sequence of the crystal structure of the layered oxide) and an OPB. An OPB is not simply an inclined stacking fault in a layered oxide. Both are stacking defects, with an associated change in chemistry. The difference lies in the degree of chemistry change on a local scale. A stacking fault in a layered oxide represents a syntactic sub-unit-cell intergrowth of a different-*n* member of the homologous series and is associated with a gross change in chemistry at the defect. An OPB, on the other hand, may have only a local deficiency of a chemical component within the *n*-member of the homologous series. Thus, we will refer to *c* stacking faults in layered oxides as such, in accordance with the conceptualization of layered oxides as being "stacked" along *c*, and not as 0° OPBs.

OPBs were originally discussed by Cowley in 1965[43] and were first observed by Allpress in the WO_3–Nb_2O_5 tungsten-bronze-type system in 1969.[44] Allpress later explicitly described OPBs observed in early high-resolution transmission electron microscopy (HRTEM) images in the TiO_2–Nb_2O_5 and WO_3–Nb_2O_5 systems in his pioneering work on lattice imaging by transmission electron microscopy (TEM).[45,46] The resolving power of microscopes of the time was sufficient to discern only ordered arrays of "blocks" of corner-sharing octahedra, with shared edges between the blocks. More recently, OPBs have been observed in bulk samples of Aurivillius phases[47,48] and other complex oxides[49] but have not been extensively investigated, perhaps because they have not been observed to be present in concentration sufficient to warrant study. Also, they may be less common in the bulk due to the extensive structural rearrangement that occurs during sintering, allowing for the elimination of many defects.

Extended defects in complex crystals are well known but have special significance in the constrained crystal growth that occurs in epitaxial films, where OPBs are much more likely to occur than in the bulk due to a combination of high crystalline anisotropy, a unidirectional growth front, and the limited structural rearrangement at typical film growth temperatures. Temperatures for the growth of epitaxial films are often lower than those needed for bulk synthesis, due to the huge difference in surface diffusion coefficients (relevant to thin film growth) compared to bulk diffusion coefficients (relevant to bulk crystallization) where crystallization occurs as material is deposited on the surface. Under such conditions, structural rearrangement is limited to the surface layers of a growing film, so that insufficient activation exists for the healing of structural defects within the film. Once nucleated, OPBs often propagate through an entire epitaxial film. Post-growth annealing is often not an option.

OPBs strongly influence material properties, particularly in epitaxial films having an otherwise high crystalline perfection. The influence of OPBs on vortex pinning in $YBa_2Cu_3O_{7-\delta}$ is an open question. Line defects such as edge and screw dislocations are known to act as strong vortex pinning sites.[50,51] However, twin boundaries, which may be weakly correlated with OPBs, are not correlated with changes in the volume pinning force in $YBa_2Cu_3O_{7-\delta}$.[52] OPBs have been demonstrated to quench superconductivity in high-purity (001) Sr_2RuO_4/$(001)_p$ $LaAlO_3$ films, where lattice imperfection effects dominated in limiting in-plane resistivity as well as in quenching superconductivity, likely by acting as pair-breaking phonon scattering sites.[41] [The subscript "p" is used to indicate indices of the pseudocubic perovskite subcell of a non-cubic substrate, to simplify comparison.] A trend has been reported for $YBa_2Cu_3O_{7-\delta}$, where the critical temperature (T_c) is lower for films with fewer OPBs.[53] In the zero-strain ferroelectric $SrBi_2Nb_2O_9$, OPBs have been demonstrated to be ferroelectrically inactive regions,[54,55] which would lead to a decrease in remanent polarization in a crystal with a high density of OPBs. Inhomogeneous strain fields associated with defects[56,57] are likely to impact many film properties. This could be particularly important for magnetic multiferroics, where the exchange interaction is strongly dependent on bond lengths and angles. Wide ranges of values for properties are often reported for layered oxide films,[54] but the relative densities of OPBs in the same films are often not reported.

Some variation in OPB morphological trends are observed for films grown using codeposition (e.g., PLD and CVD) versus sequential deposition (e.g., shuttered MBE), although the degree of structural rearrangement for a given growth temperature may be the main reason for this. Beyond the conditions of film growth, sequential deposition methods additionally impose a discontinuous adatom chemistry during growth. This might lead to very different OPB morphologies, but few studies of the defect morphologies in these systems have been reported,[31] so general treatment of OPBs in films made by sequential deposition is reserved until sufficient data exist.

A survey of the literature describing HRTEM studies of layered complex oxides yields some examples that imply that multiple mechanisms of OPB nucleation are shared in common for these structurally similar phases. Nucleation of OPBs by single-unit-cell steps on substrate surfaces has been predicted[58–60] and observed by HRTEM[61,62] for $R\mathrm{Ba_2Cu_3O_{7-\delta}}$ (R = Y, Dy, Nd, and Gd), predicted[63] and observed[64] in $\mathrm{Bi_4Ti_3O_{12}}$, and observed in $\mathrm{Ba_2Bi_4Ti_5O_{18}}$[65] and $\mathrm{SrBi_2Ta_2O_9}$.[66,67] Multiple-unit-cell substrate surface features have also been observed to nucleate OPBs in other layered cuprates,[60,68] although not consistently so.[69,70] OPB nucleation on non-stepped substrate surfaces due to the existence of multiple occurrences of a preferred nucleation layer within the unit cell of layered cuprate films has also been predicted,[58] observed,[71–73] and used to control OPB density.[53] A similar mechanism also has been reported for $\mathrm{Sr_2RuO_4}$ films.[74] Variations in nucleation layer have been predicted to smooth over substrate surface steps in layered cuprates,[58] potentially resulting in films with a surface smoother than that of the substrate. OPBs in $\mathrm{SrBi_2(Nb,Ta)_2O_9}$ exhibit a multimodal statistical distribution of offsets, with values centered around dimensions corresponding to the c dimensions of the crystallographic units, suggesting multiple structurally related nucleation mechanisms for OPB nucleation in that material.[75]

In this paper, an effort is made to organize discussion of OPBs, to review the existing body of work, and to present several new experimental examples. We describe the analysis, morphology, structure, and nucleation mechanisms of OPBs in layered complex oxide films and present exemplary data from the several epitaxial layered complex oxide systems that we have studied: $\mathrm{SrBi_2Nb_2O_9}$, $\mathrm{SrBi_2Ta_2O_9}$, $\mathrm{Bi_7(Mn,Ti)_6O_{21}}$, $\mathrm{Sr_4Bi_4Ti_7O_{24}}$, $\mathrm{Sr_2RuO_4}$, and $\mathrm{Sr_3Ru_2O_7}$. Several open questions are defined. It should be noted that OPBs are a general phenomenon, and although this work is limited to OPBs in layered oxides, the same principles and mechanisms can be applied generally to other classes of complex oxides, as well as to non-oxide or ordered metal systems.

The paper is organized as follows: In Sec. III. A, some useful qualitative and quantitative analysis methods for studying OPBs are described, along with a description of some common pitfalls encountered in OPB imaging and analysis. Section III. B describes the general morphological trends observed for two layered oxide series, Aurivillius and Ruddlesden–Popper phases, based on our own work and that in the literature. Section III. C describes the atomic structure at OPBs and discusses the implications for long-period layered oxides. Finally, Sec. III. D describes the nucleation mechanisms that have been observed or predicted for layered oxides, with examples from our own work. This section also serves as a review of published work on OPB nucleation. It is hoped that this paper will lead to increased attention to these important but often-ignored features and that perhaps reexamination of data in a new light might yield insight into previous discrepancies in the observed properties of layered complex oxides.

II. EXPERIMENTAL

All films used for this study were grown by pulsed laser deposition on perovskite-type (001), (110), and (111) substrates, polished to be atomically smooth [except Fig. 9(b)]. Thorough descriptions of the growth processes and optimizations thereof are available in the literature.[75–79] Briefly, films were grown in a radiatively heated sample chamber[80] using a KrF excimer laser (λ = 248 nm). Parameters for growth of Ruddlesden–Popper phases were: ≈1000 °C, 3.5 μTorr oxygen ambient, 10^4 pulses, 160 mJ/pulse, 2.7 J/cm^2, 2 Hz pulse rate, and a target-to-substrate distance of 7.5 cm with a stoichiometric target. Parameters for growth of Aurivillius phases were: 750–900 °C, 90–150 mTorr O_2/O_3 atmosphere (≈8% O_3), 10^4 pulses, 150 mJ/pulse, 2–3 J/cm^2, a 4 Hz pulse rate, and a target-to-substrate distance of 6.5 cm, with targets 15% rich in bismuth. These films were quenched immediately after growth in 1 atm oxygen, while the Ruddlesden–Popper films were cooled in the same atmosphere in which they were grown.

The relative phase purity and crystallinity of films were evaluated by four-circle x-ray diffraction (XRD) scans using a Picker four-circle x-ray diffractometer with Cu K_α radiation and a graphite incident-beam monochromator. Samples for cross-sectional TEM examination were prepared by standard sandwiching, slicing, dimpling, or wedge polishing, and argon ion milling on either a liquid nitrogen-cooled stage at 4 kV and 8–11°, or on an uncooled stage at 3.0–4.5 kV and 4–7°. Microscopy was performed using various transmission electron microscopes operated at 200–400 keV. For HRTEM imaging, regions of appropriate and consistent thickness were selected, and a series of through-focus images was acquired. For defect modeling and HRTEM simulation, supercells of sufficient size to avoid edge effects were constructed, and simulations were compared with the

acquired series of through-focus images to achieve a good match.

The technique of geometric phase analysis[81] combines real-space and phase-space information, and was utilized to map out-of-phase domain offsets. The technique consists of calculating the power spectrum [fast Fourier transform (FFT)] of a HRTEM image, masking a single spot corresponding to a specific spatial frequency (a lattice periodicity), removing the lattice frequency component, inverse transforming to real space, and mapping the phase component. Each spot in a power spectrum contains low-frequency spatial information, corresponding to the region of an image from which the intensity arose. Removal of the high-frequency information (that of the lattice) reveals this information clearly.

Care must be taken in interpreting HRTEM images of complex oxides. In addition to the usual steps to avoid excessive damage, bending and thickness variation in particular should be avoided, and the degree of contrast delocalization due to defocus condition should be minimized. If only one defocus is used for imaging, thickness-dependent cycling of lattice fringe contrast can lead to misidentification of thickness variations as out-of-phase domains of a crystal, or to mistaking OPBs for other features due to poorly defined imaging conditions.[42] To identify a defect confidently, regions with the same type of contrast on either side of a defect should be visible, and a series of through-focus images acquired. The ideal geometry is one with no thickness variation across an OPB or other lattice feature of interest, but that is not always possible.

All TEM images presented are from cross-sectional samples along the [*hkl*] zone axis of the film that is specified, or along the [100] of the perovskite substructure if not specified. The TEM images are also all oriented with the substrate surface (not visible in all images) horizontal and toward the bottom of the image frame, and the film surface toward the top. To maximize ease of interpretation, the film growth direction is along the vertical direction of images, and sets of related images are presented at a similar scale when possible, with the result that the corners of some images are clipped. Clarity was valued over aesthetics. Many microstructural features are indicated by arrows: black arrows indicate the position of OPBs, white arrows indicate stacking faults, and broad arrows indicate growth twin/grain boundaries. Arrows are oriented parallel to the projected habit plane of the features. Braces indicate OPBs that appear broad in images, unless otherwise indicated. Long, narrow arrows in some images indicate the *c* axis unless otherwise noted. All substrate planes and directions in the text will be referred to using a pseudocubic perovskite subcell, denoted by a subscript p, for substrates with slight distortions from cubic. By convention, *c* is the layering axis.

III. RESULTS AND DISCUSSION

A. Analysis of OPBs

OPBs have been described in the literature using a wide variety of terms, which can obscure discussion of their structural similarities. In $YBa_2Cu_3O_{7-\delta}$ and related systems, a *c*/*n* description is useful because such phases contain crystallographic units of nearly equal dimension. This has been extended to describe OPBs in more complicated layered oxides, describing for example *c*/3 and *c*/6 APBs,[82] wavy *c*/6 translational boundaries,[83,84] ~*c*/12 repeated lattice shifts,[65] and *c*/3 translation boundaries.[68] As more complex and varied phases are studied, the approach becomes insufficient. In other cases, OPBs are referred to as APBs,[60,61,71,72,85] twin boundaries,[86] translational (domain) boundaries,[87,88] or simply as generic lattice defects,[89] although, strictly speaking, an APB is an OPB with an offset of exactly half of a lattice translation vector.

A more general approach to OPB description addressing offset and orientation is helpful. In this manuscript, qualitative descriptions refer to offsets in terms of monolayers, or crystallographic units (ABO_3, AO, rocksalt double layer, $Bi_2O_2^{2+}$ layer, etc.) of structures, where applicable, due to the wide variety of structural units and chemistries of layered complex oxides. Where this is not possible, OPBs are referred to by the absolute linear magnitude of the *c*-axis offset (e.g., 0.39 nm, 0.45 nm), which can imply a structural association if none is explicitly observed, but it is important to recognize that lattice strain local to the defects can shift apparent offsets. OPBs typically have a component of offset in the *a*-*b* plane as well, usually deduced via crystal chemistry principles, due to the difficulty in determining the atomic structure explicitly from an image in projection. Inclination of OPBs is described in relation to the layering plane, the *c* plane. Thus, a 90° OPB would lie parallel to the layering axis, and in this manuscript, parallel to the vertical direction in the cross-section TEM images of this manuscript.

1. Notes on TEM observation of OPBs

Despite having been known for 35 years, OPBs visible in many micrographs in the literature are often attributed to other microstructural features or to sample preparation artifacts. The lack of attention is perhaps primarily because in bulk materials, OPBs are of little importance in relation to other microstructural features, and further, can be removed by annealing. In thin epitaxial films of layered oxides, they are quite common. Indeed, we have observed OPBs in every one of almost 100 films of Ruddlesden–Popper and Aurivillius-phase oxides that we have examined by TEM. They exhibit a reasonably consistent morphology in relation to film and substrate orientation.

OPBs in the TEM appear darker than surrounding material due to increased electron scattering of overlapping crystals and/or disorder at the OPB, and can be casually misinterpreted as sample preparation artifacts or sample thickness fringes. More importantly, some OPBs are shear defects (see Sec. III. C); that is, they are associated with a change in stoichiometry at the fault. The lack of atom mobility at room temperature in a typical perovskite oxide structure makes it unlikely that the mechanical processes involved in TEM sample preparation at room temperature could create such defects, although it has been suggested that they may be associated with a strain-relief mechanism.

In the TEM, thickness variation causes cycling of phase contrast, which can give the appearance of out-of-phase regions when none is present, particularly if the image axis is not parallel to the film layering axis. Careful focus series should be collected, preferably in a region without significant thickness variation. As always with HRTEM, a larger context for anomalous microstructural features is important for conclusive characterization.

Because samples in the TEM are viewed in projection, OPBs frequently have a ribbon-like appearance, undulating and alternately narrow and broad. This morphology is attributable to the OPBs varying orientation about *c*, demonstrated by the two HRTEM images from OPBs in the same $SrBi_2Ta_2O_9$ film in Fig. 3. The OPB in Fig. 3(a) is viewed nearly edge-on, and thus appears very narrow, while the OPB in Fig. 3(b), indicated by braces, is inclined to the viewing axis and appears broad. To reliably identify a feature as an OPB, it is very important to select a region free of features that could be mistaken for OPBs, such as thickness fringes and overlapping grains. Material on either side of the defects in Fig. 3 has the same appearance.

The reverse applies as well: OPBs imaged without context can be mistaken for other features. For example, a small-area image shown as evidence of multiple rocksalt-like layered intergrowths in an Aurivillius phase appears more likely to be an OPB oriented nearly perpendicular to the viewing axis.[90] The area is darker than the surrounding material, and the rows of atoms appear to split, an obviously unlikely physical scenario, more reasonably understood as the superposition of two out-of-phase domains in the projection. A feature in another work described as a stacking fault in $SrBi_2Nb_2O_9$ appears likely to also be an inclined OPB.[91] (See Sec. III. B. 3 for more discussion of stacking faults.) A similar example from our own work is shown in

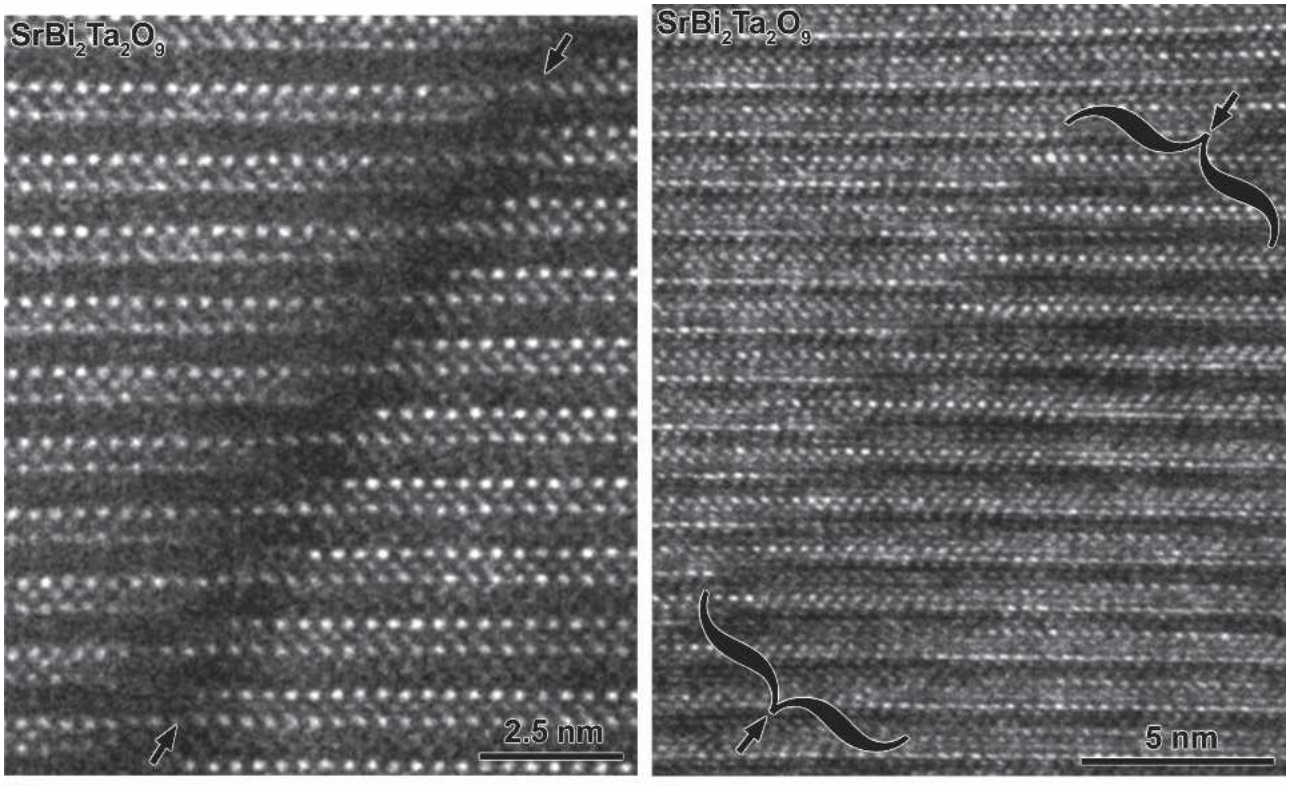

FIG. 3. OPBs can have a ribbonlike appearance due to variation in orientation. Two OPBs are shown (a) edge-on and (b) inclined to the viewing axis in these cross-section HRTEM images. Black arrows indicate the positions of the OPBs and are oriented parallel to the projected habit plane, and braces further indicate the width of broad OPB in (b).

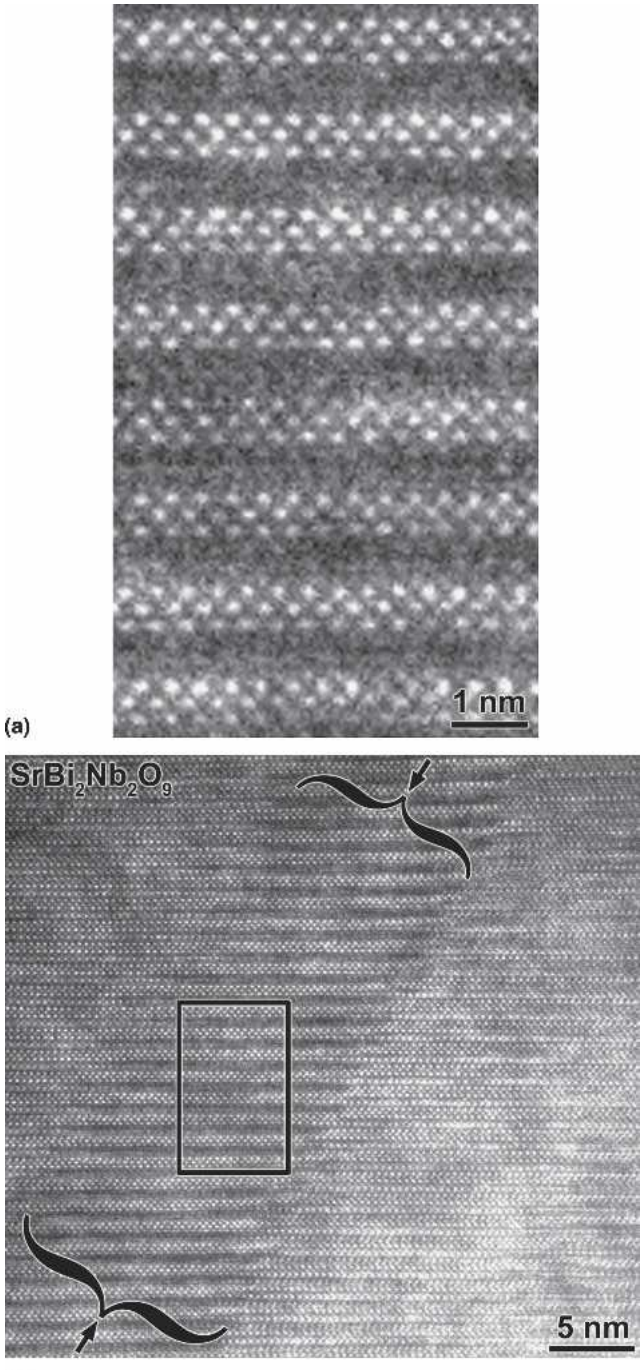

FIG. 4. OPBs can be easily misinterpreted. In this example, (a) appears to be a pure superlattice phase (an $n = 3$ Aurivillius phase in an otherwise $n = 2$ sample in this case), but lower magnification observation of the same feature in (b) shows it to be an OPB inclined to the viewing axis, as indicated by the black arrows and braces. The area of (a) is taken from the inset box in (b).

Fig. 4. What appears to be a clear image of a different phase (an $n = 3$ Aurivillius phase in an otherwise $n = 2$ sample) in Fig. 4(a) is only an OPB, shown clearly in the lower-magnification image of the same region in Fig. 4(b).

2. Geometric phase analysis

A map of the relative phase of out-of-phase domains can be generated using geometric phase analysis,[81] as demonstrated previously.[92] Figure 5(a) shows a HRTEM image of a pair of intersecting OPBs in a Ruddlesden–Popper Sr_2RuO_4 film. Figure 5(b) was calculated from the image by geometric phase analysis using 002-period contrast and clearly shows a map of the offset of the out-of-phase region in a graphical manner. The intensity of the grayscale in the image corresponds to the magnitude of phase offset, ranging from $-\pi$ (black) to π (white), or −0.32 to +0.32 nm, indicating an OPB offset equivalent to a single layer of SrO atoms. The monotonic

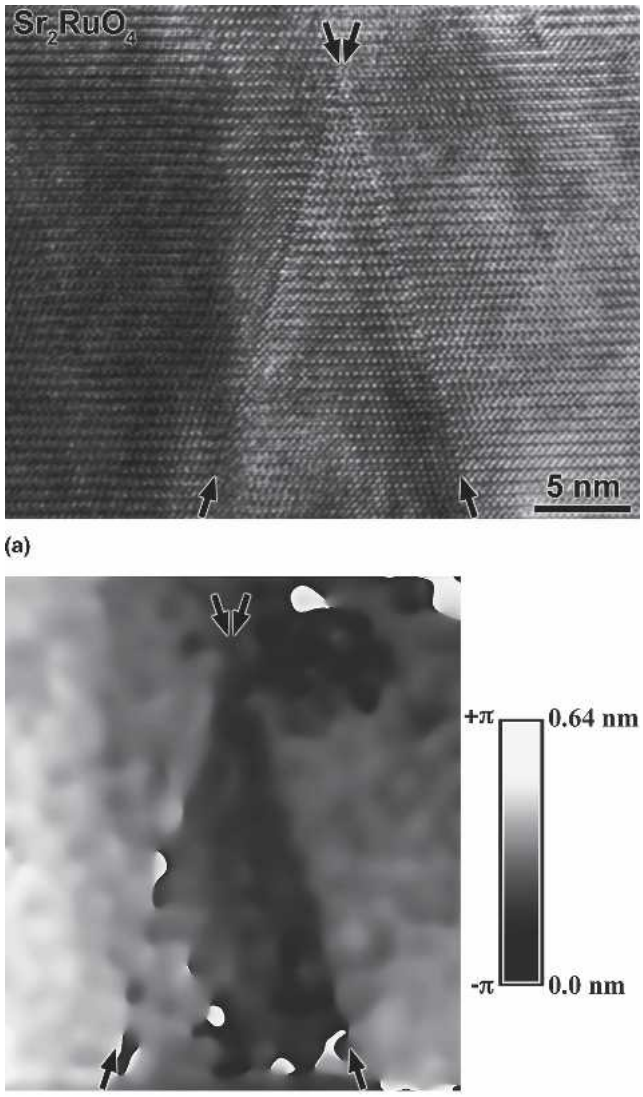

FIG. 5. (a) [100] HRTEM image of a pair of intersecting OPBs in (001) Sr_2RuO_4. (b) The offset at the boundary along the [001] Sr_2RuO_4 direction is made clear by a geometric phase analysis map calculated from (a) using the 002-equivalent peak of the power spectrum. Black arrows indicate the positions of the OPBs.

left-to-right ramp across the entire image of Fig. 5(b) corresponds to thickness variation in the sample.

The method is most suitable for low-n members of the homologous series due to resolution limits imposed on the selection of a single 00l superlattice reflection, and care must be taken to properly analyze results. For example, an OPB was mistaken for an (00l) APB in $(Bi,La)_4Ti_3O_{12}$ (c = 32.9 Å).[90] The 008 peak was selected in the power spectrum to generate the map, and a shift of π at the boundary was interpreted to correspond to an offset of roughly half of the unit cell dimension, 16.4 Å. This shift actually corresponds to ≈0.2 nm, half of d_{008}, corresponding roughly to an OPB with an offset of either half a perovskite (unlikely) or a BiO^+ layer.

3. X-ray analysis

XRD θ-2θ peak splitting provides a qualitative measure of OPB density. XRD θ-2θ scans of all n = 2 Aurivillius-phase films studied exhibit splitting of 00l peaks, with 008, 00$\underline{14}$, and 00$\underline{20}$. The degree of peak splitting gives an indication of OPB density relative to other films of like composition. We have observed extensive peak splitting to result from insufficiently rapid quenching, implying bismuth loss.[79] A region of a θ-2θ XRD scan of the slowly cooled film described in Ref. 79 is shown in Fig. 6(a) [and a TEM image is shown in Fig. 11(f)], demonstrating the high degree of splitting of the 008 reflection. The splitting has a noticeable effect on only a subset of the superlattice reflections.

A predictive trend is observed. Figure 6(b) shows the degree of 2θ peak splitting (peak-to-peak) plotted against the linear density of OPBs in several films, as measured from HRTEM micrographs along c. A strong linear correlation is observed. (Instrumental resolution is ≈0.20°, λ = 0.154 nm.) Thus, one can estimate the relative out-of-phase domain size in layered oxide films by θ-2θ XRD scans, provided effects from other defects are negligible or consistent from sample to sample. One would expect the degree of peak splitting to vary with 2θ, but this is not the observed trend, perhaps due to the small statistical sample size.

Although peak splitting can also be a sign of intergrowths in some materials, it is not believed to be the source of peak splitting in these materials, primarily due to the extremely low incidence and small spatial extent of any stacking faults we have observed, as noted previously. Although the source of the peak splitting is not entirely clear, it is believed to be due to out-of-phase alignment of domains within a diffracting volume. It is known from simple ordered alloys that regions of diffracting volume in antiphase alignment in the diffracting direction give rise to this sort of modulation of diffracted intensity,[93,94] that is, the apparent peak splitting. This does not, however, necessarily imply the presence of antiphase boundaries or stacking faults in the more complicated layered oxides under consideration here, in which any of several crystal defects could give rise to regions in antiphase alignment. For example, it is known that OPBs exhibit discrete shifts along (001) in $SrBi_2(Nb,Ta)_2O_9$, of 2.4, 3.8, and 4.5 Å, corresponding to one or two atomic layers of varying composition. Most combinations of such shifts across two OPBs will put a pair of out-of-phase domains in antiphase alignment, but the two regions will not be adjacent. Therefore they will not have a mutual boundary and thus no antiphase boundary due to an intervening out-of-phase region. Similarly, noncontiguous regions in antiphase alignment can exist without the presence of 00l stacking faults. (A similar effect is described in Sec. III. B. 2. b and Fig. 15.)

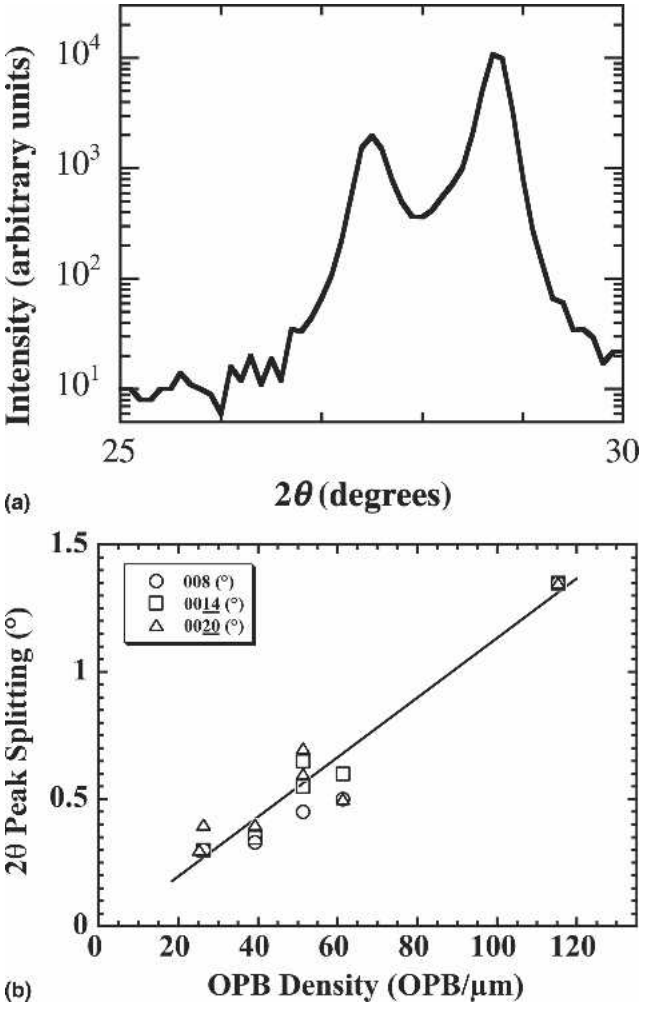

FIG. 6. θ-2θ XRD scans of $SrBi_2(Ta,Nb)_2O_9$ films exhibit peak splitting that correlates with linear OPB density. The 008 peak of a θ-2θ scan of the film shown in Fig. 11(f) is shown here in (a). Peak splitting may arise from constructive interference due to discrete local shifts in the magnitude of the apparent film layering repeat distance. (b) A clear trend is observed for the degree of peak splitting for several films having different linear OPB densities.

Peak splitting in films is most clearly evident when θ-2θ XRD data are plotted on a log intensity scale.

Although many θ-2θ XRD scans of $SrBi_2(Ta,Nb)_2O_9$ reported in the literature are plotted on linear scales or with truncated peaks, splitting is evident in some.[95–97] It would be quite valuable to learn whether other groups find a similar trend in their data upon reexamination. Differing concentrations of OPBs in otherwise high-crystalline-quality films could be the cause of the wide distribution of remanent polarization (P_r) for these films reported in the literature,[54,98–103] as OPBs are volumes of ferroelectrically inactive material.[54,55]

B. Morphology

OPB morphologies for the two systems we studied, Aurivillius and Ruddlesden–Popper phases, are described below. The majority of characterization studies in this work and available in the literature describe only the lowest-*n* members of series, due to the difficulty of synthesizing high-*n* phases, which limits the qualitative data set from which to extract trends. The section will focus on observed morphologies. Predictive trends are discussed later, in the section describing the atomic structure of OPBs (Sec. III. C).

1. Ruddlesden–Popper films

The general morphologic evolution of defects in Ruddlesden–Popper phases, as observed in bulk and thin films, is shown in Fig. 7. (Lines indicate *A*O double layers.) OPBs in (001) films of A_2BO_4 ($n = 1$) are faceted, typically at an angle of 73° to (001), though occasionally also at 90°. The generalized $n = 1$ morphology is shown in Fig. 8(a). OPBs propagate through the film thickness, except when annihilated by another OPB of opposite sign in the growing film. Figure 8(b) shows an example [100] cross-sectional TEM image of a Sr_2RuO_4 film. The two OPBs of opposite sign in the center appear to have annihilated where they met, while the two on the right penetrate the full film thickness. Other HRTEM images of Sr_2RuO_4 films showing the same morphology have been published previously[74] and have shown that the offset of ≈0.25 nm corresponds to a single SrO

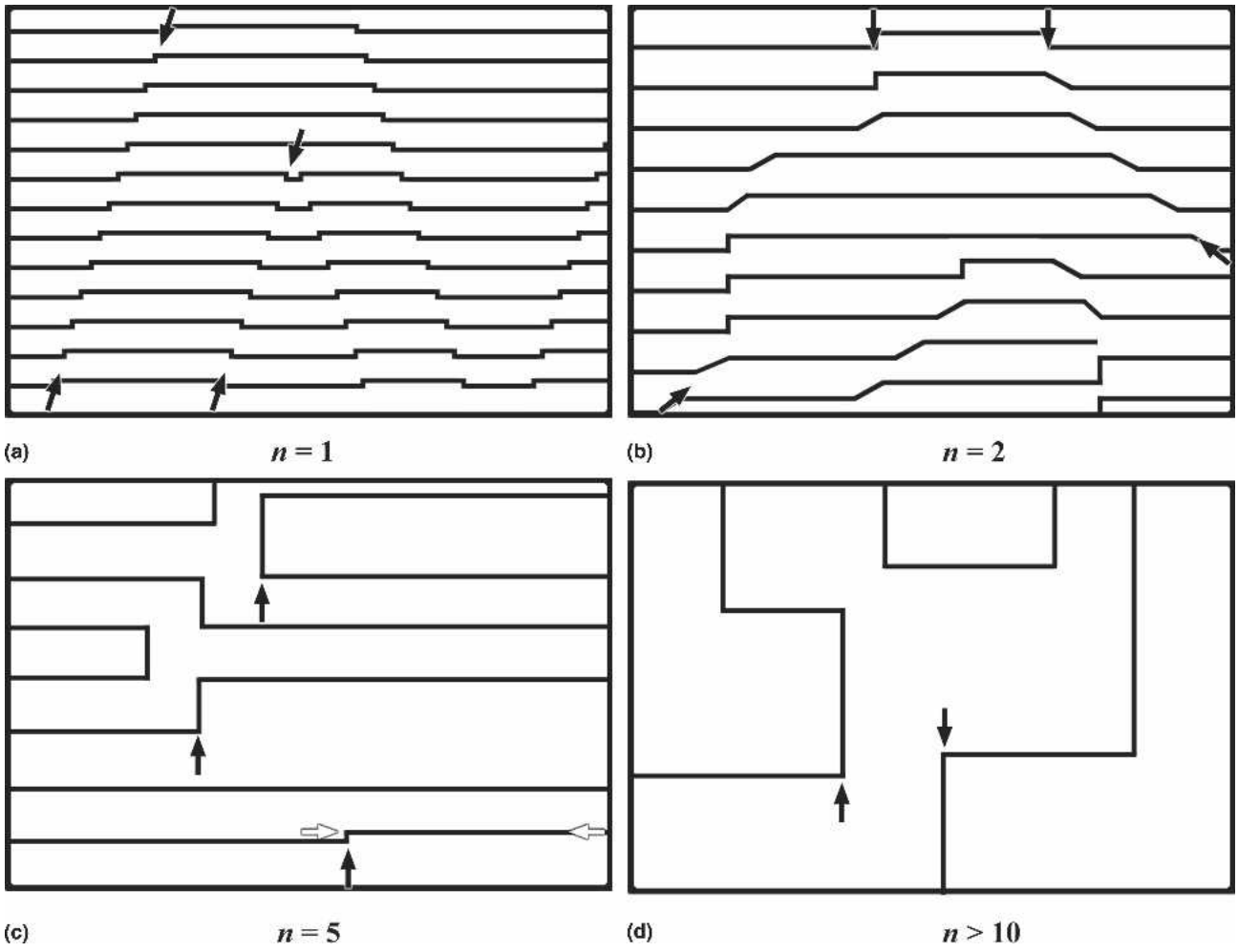

FIG. 7. Schematic illustration of the observed out-of-phase domain morphology in Ruddlesden–Popper phases with increasing layer thickness *n*: (a) is lowest *n*, and (d) is highest *n*. Lines represent the *A*O double layers present between perovskite slabs, and OPBs occur at interruptions of these lines. Some OPBs are indicated by black arrows, and a stacking fault is indicated by white arrows.

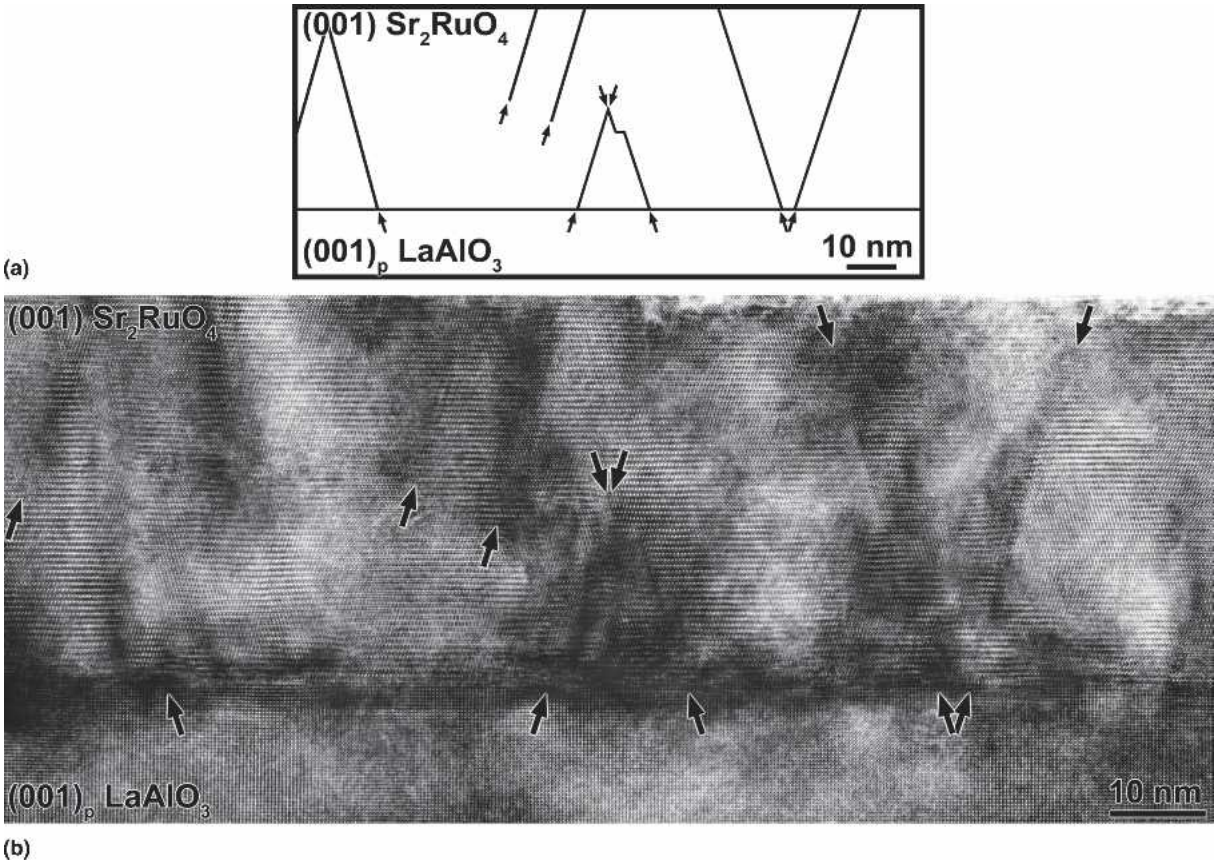

FIG. 8. Out-of-phase domain morphology in an $n = 1$ Ruddlesden–Popper phase, (001) Sr_2RuO_4. OPBs are straight and oriented 73° with respect to the layering plane, shown schematically in (a), with lines representing the OPBs. (b) HRTEM image showing the same OPBs as the schematic illustration. Black arrows indicate the positions of the OPBs.

rocksalt-type layer.[41] Similar Sr_2RuO_4 films have been prepared for TEM by various different means, and all exhibit the same morphology. A feature exhibiting this morphology has also been reported in $n = 1$ $La_2CuO_4F_x$.[104]

An $n = 2$ $Sr_3Ru_2O_7$ film we examined, Fig. 9(a), had a high density of stacking faults, some of which terminated in an OPB. OPBs in this film were typically associated with stacking faults and often separated two different-n regions of a layer where they nucleated. A single OPB is visible in bulk $Sr_3Ti_2O_7$ in Fig. 7 of Takeuchi et al., although of limited enough extent that a general morphology cannot be discerned.[105]

Ruddlesden–Popper phases with $n > 2$ appear to have little tendency to form OPBs, being more prone to syntactic intergrowths[106] due to the aforementioned thermodynamic limitations, so very few epitaxial films of high-n Ruddlesden–Popper phases have been grown. The complexity of OPBs should increase with n, as larger cells have more possible offsets. For example, Sr_2RuO_4 consists of three composition planes, two structurally equivalent, the symmetry of which yields only two structurally unique OPBs. Further discussion is presented in Sec. III. C.

In MBE-deposited $n = 1$ to 5 films of $Sr_{n+1}Ti_nO_{3n+1}$, some 90° OPBs with an offset of one SrO layer are observed. More frequently, 90° SrO double layers separate syntactic intergrowths of Ruddlesden–Popper phases of integer multiples of n. Such defects usually occur in pairs, resolving the antiphase alignment of the perovskite-like slabs that they separate.[31] An example is shown in Fig. 9(b), where 90° OPBs separate $n = 8$ and $n = 13$ regions in an otherwise $n = 4$ $Sr_5Ti_4O_{13}$ film. This morphology is also observed in bulk $Sr_{n+1}Ru_nO_{3n+1}$,[107] $(Sr,Ca)_{n+1}Ti_nO_{3n+1}$,[108,109] $(La,Sr)_3Mn_2O_7$,[110] $Sr_{n+1}Ti_nO_{3n+1}$,[111] and $(Sr,Ln)_3Mn_2O_7$.[112]

Near $n = \infty$, in an A-rich ABO_3 perovskite, excess AO precipitates topotactically as AO double-layers (where A = Ca or Sr) to form meandering (100) Ruddlesden–Popper defects of $(100)_p$ habit in bulk[113–116] and thin film[117] samples. No more than two consecutive layers of AO have ever been observed in Ruddlesden–Popper phases and defects.[118] AO double layers (Ruddlesden–Popper defects) are not usually observed to terminate, nor to branch, but instead meander through the perovskite slabs as OPBs and syntactic intergrowths. Branching of an AO layer is depicted in the model of mosaic Ruddlesden–Popper faults presented by Suzuki

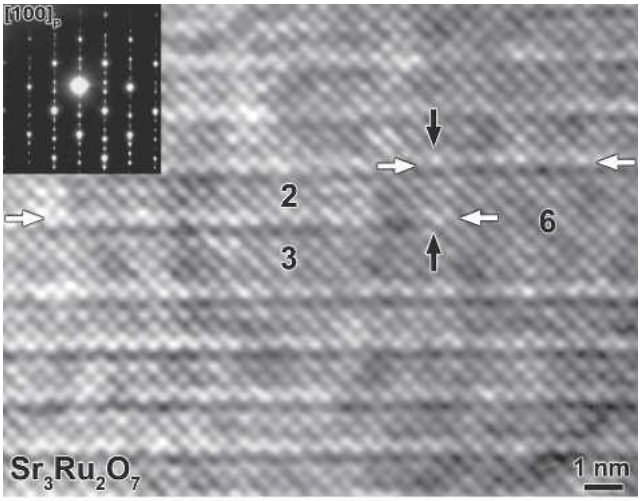

(a)

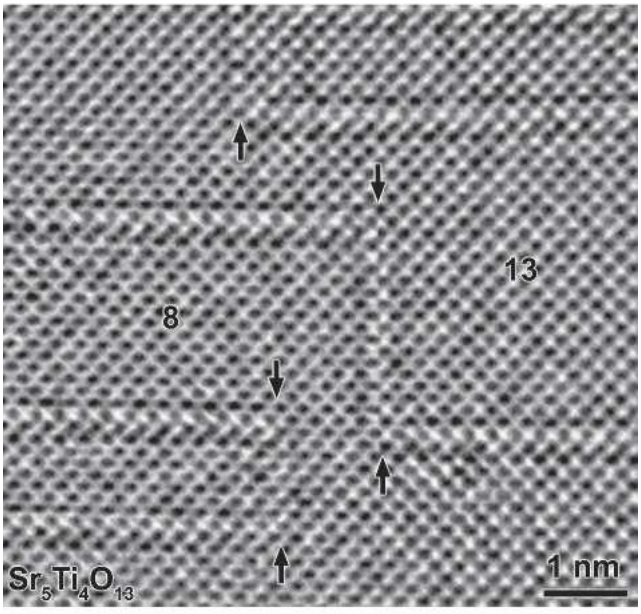

(b)

FIG. 9. OPBs in higher-n films of Ruddlesden–Popper phases: (a) An OPB extending for half of a unit cell, accompanied by an intergrowth and stacking fault in the $n = 2$ $Sr_3Ru_2O_7$. An electron diffraction pattern of the film is inset, showing long-range order. A magnified model of this defect is shown in Fig. 19(a). (b) 90° OPBs terminating other-n intergrowth layers in the $n = 4$ $Sr_5Ti_4O_{13}$. A schematic illustration of this image is shown in Fig. 19(b). Numbers indicate local n. Black arrows indicate the positions of the OPBs, and white arrows indicate stacking faults.

et al.[117] Some permutations of the offset for a given-n Ruddlesden–Popper phase exhibit branching AO layers, although it is not clear how common particular configurations are relative to others (see Sec. III. C. 4).

2. Aurivillius films

a. $n = 2$

By far the most widely studied epitaxial Aurivillius films are $ABi_2B_2O_9$ phases with A = Sr and B = Nb, Ta, mostly in the (001) orientation. OPBs exhibit a wide range of morphologies in as-grown films, which can be grouped into the four categories shown in Fig. 10. In the type-A morphology, OPBs are largely uncorrelated and ribbonlike. In the type-B morphology, OPBs are still ribbonlike but correlated, with an appearance reminiscent of an egg crate. The type-C morphology has straighter OPBs correlated in a W-like arrangement. The type-D morphology has a very high density of OPBs, with tendrils of strongly correlated OPBs converging to highly disordered columns of material. Experimental images of the four morphologies in (001) $SrBi_2(Nb,Ta)_2O_9$ films grown by PLD are shown in Figs. 11(a)–11(f).

The type-A OPBs in Fig. 11(a) and the type-B OPBs in Figs. 11(b) and 11(c) are continuous across the films, with low curvature at peaks and high curvature in valleys.

OPBs in $SrBi_2Ta_2O_9$ grown by CVD exhibit the type-A morphology,[99] although they have been observed to have straighter walls, perhaps due to more controlled cooling (10 °C/min) to allow slight structural rearrangement. Crystallographic faults in (001) $SrBi_2Nb_2O_9$ films grown by sol-gel were studied in the detailed XRD work of Boulle et al.[57] The results appear consistent with a type-A OPB morphology. Plots of domain sizes as a function of the angle of fault planes to [001] showed a nonuniform distribution with orientation,[57] in contrast to the $1/\cos\theta$ relation that might be expected from geometric consideration of an ideal crystal with only 00l stacking faults. Annealing in air at 700 °C resulted in a concentration of the diffuse scattering around 00l peaks, consistent with a reduction of the number of stacking faults.[57] A reduction of diffuse scattering halo in both Q_x and Q_z was also observed, which would be consistent with a lowered density of OPBs of all orientations.[57] These results differ from our observation of an increase in OPB density due to bismuth loss on annealing.[55] In other studies, $SrBi_2(Ta,Nb)_2O_9$ annealed in contact with excess bismuth, presumably having lost no bismuth, did not exhibit XRD peak broadening. Broadening would have been indicative of the presence of stacking faults.[119,120] A combined annealing study using both TEM imaging and x-ray reciprocal space mapping on the same samples could yield more explicit correlations.

Contrary to intuition, the type-A and type-B OPBs are not the outlines of growth islands seen in AFM images of $SrBi_2Ta_2O_9$.[79] The peak-to-valley height of growth islands is ≈10 nm, an order of magnitude greater than the height of the OPBs. [Note that the as-grown film surface is visible in Figs. 11(a), 11(b), 11(c), and 11(e), demonstrating the planarity of the growth front.] OPBs could, however, form when adjacent, out-of-phase nuclei meet during growth. The as-grown surfaces of films with type-A morphology are very smooth, and OPBs do not penetrate to the film surface. No easy diffusion path to

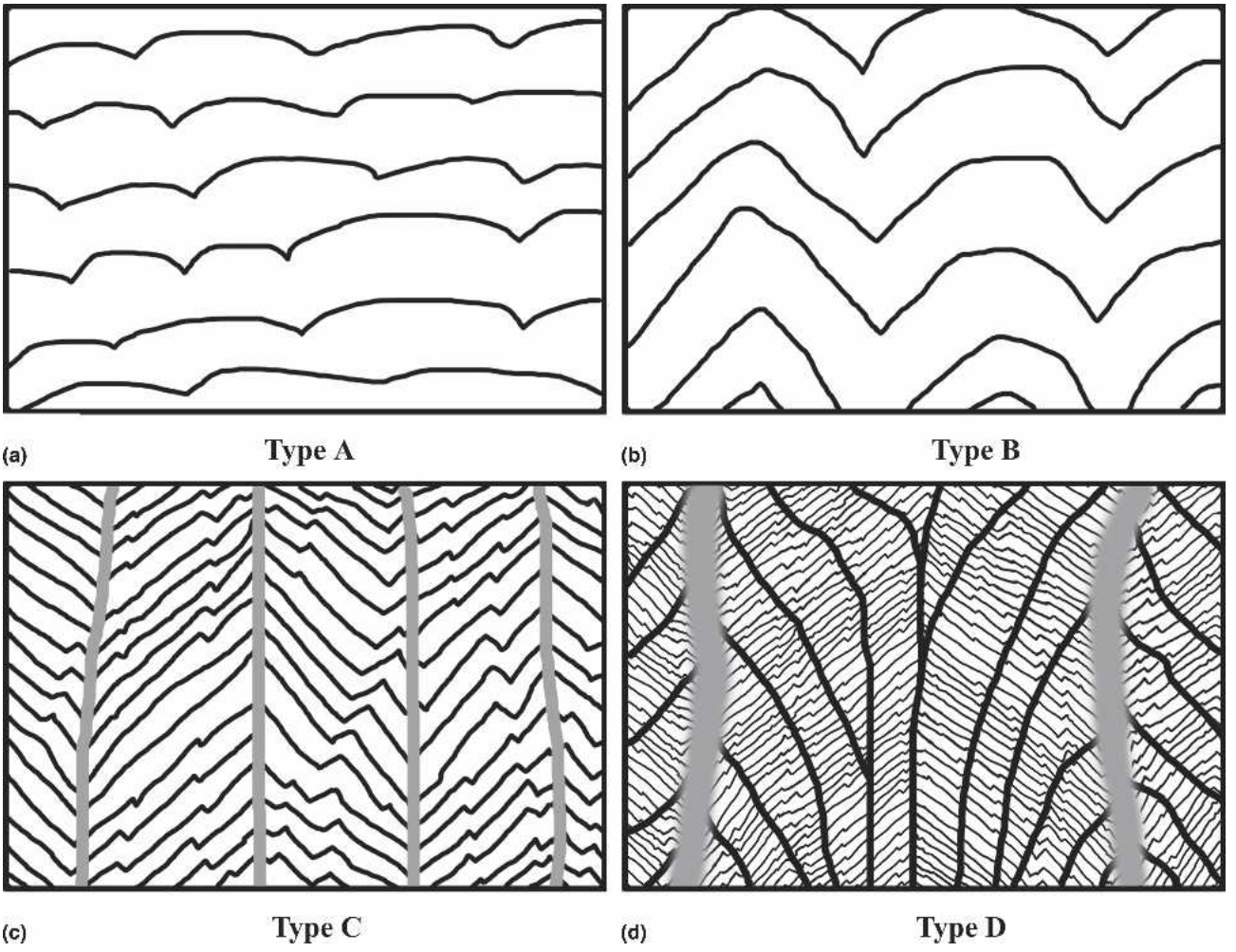

FIG. 10. Schematic illustration of the observed out-of-phase domain morphology in $n = 2$ Aurivillius phases. Lines represent the OPBs. (a) Type-A OPBs are continuous with low curvature. (b) Type-B OPBs are continuous with low curvature and are weakly correlated. (c) Type-C OPBs are straight and strongly correlated, with columns of disordered material (gray bands) where the inclination of OPB groups changes sign. (d) Type-D OPBs are straight and strongly correlated, with tendril-like columns of OPBs, merging into columns of highly disordered material (gray bands). Note that the morphology does not always correspond to the relative bismuth stoichiometry.

the surface is evident, implying that the OPBs were likely formed in situ during growth.

Figures 11(d) and 11(e) show films of type-C OPB morphology with straight, strongly correlated OPBs and regions of high curvature meeting in columns. Run-to-run variations in OPB morphology for identical conditions can be attributed to variations in quenching times. Our films are quenched immediately after growth by drop-transfer to a metal heat sink (the water-cooled PLD chamber walls), to maintain as-grown crystallinity, as measured by decreased rocking curve widths in θ-2θ XRD scans. Slight delays can result in bismuth loss. The columnar features in the type-C films are the result of the intersection of many OPBs and are not grain boundaries. The type-C film for which the as-grown surface is visible, in Fig. 11(e), exhibits roughness correlated with the locations of the defective, columnar regions. The film has receded in the regions of these columns, from which the greatest amount of bismuth has been lost.

The type-D morphology results from massive bismuth loss from a film. An otherwise typical film was cooled slowly in the growth atmosphere over a period of two minutes, immediately after growth.[79] A cross-sectional TEM image of this film is shown in Fig. 11(f). Strongly correlated tendril-like groups of OPBs, separated by disordered regions, converge to highly disordered chimneys of material that reach the film surface. The decomposition indicates that $SrBi_2Ta_2O_9$ is not stable at the film growth temperature and atmosphere without a supply of excess bismuth, in our case from the bismuth-rich laser target. A study of OPB morphology development for films annealed in a bismuth-saturated atmosphere would be very informative. It would also address the degree to which OPB density can be decreased in a particular film/substrate system.

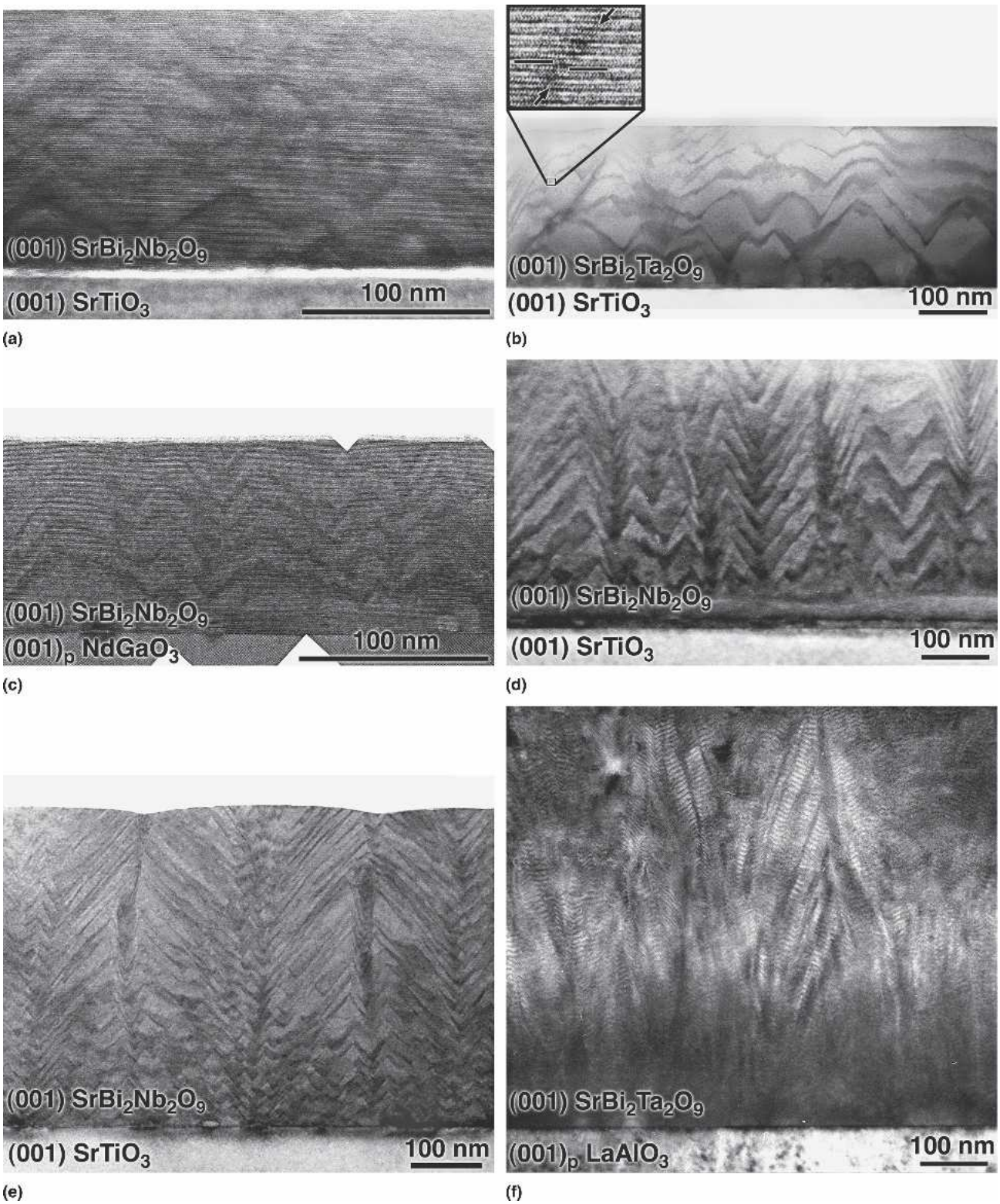

FIG. 11. Examples of the observed out-of-phase domain morphologies in $n = 2$ Aurivillius phases. TEM images showing (a) type-A, (b, c) type-B, (d, e) type-C, (f) and type-D. The dark wavy features in all of the images are OPBs, as demonstrated by the inset in (b), a HRTEM image of the area of the small box, showing a single OPB. Bars in the inset of (b) indicate the $Bi_2O_2^{2+}$ layers in the two out-of-phase domains, demonstrating the offset, and black arrows indicate the OPB.

All four types of OPBs exhibit variable inclination to the layering axis, *c*. They also exhibit variable orientation about *c*, as evidenced by the variation in apparent width of OPBs in the projection of the TEM images. Three-dimensional imaging of OPBs via electron tomography would provide a much fuller understanding of these morphological trends. Correlation of OPB orientation appears to increase with increasing density. Ordering

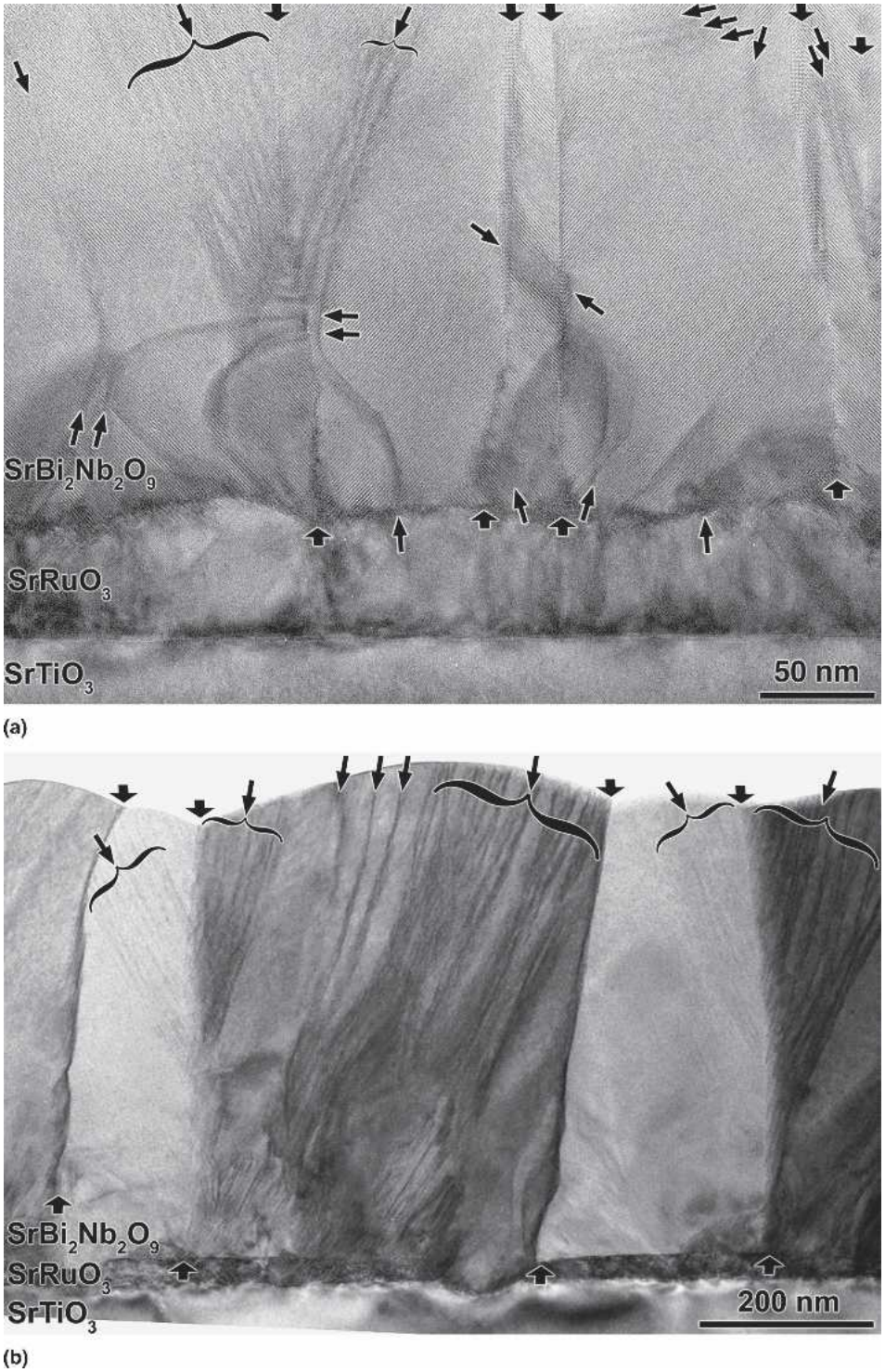

FIG. 12. Examples of OPBs in $n = 2$ Aurivillius phases with the layering axis inclined to the substrate surface, where the OPB morphology takes on a more complex character. TEM images of (a) $SrBi_2Nb_2O_9/(110)_p$ $SrRuO_3/(110)$ $SrTiO_3$, imaged along $[110]_p$, and (b) (103) $SrBi_2Nb_2O_9/(111)_p$ $SrRuO_3/(111)$ $SrTiO_3$. Black arrows indicate the positions of the OPBs, braces indicate groups of OPBs, and broad arrows indicate growth twin boundaries.

of OPBs due to interaction potentials is an Ising-type problem, based on the interaction potentials between neighboring OPBs.[121]

The concentration of OPBs varies with the history of bismuth stoichiometry of the film, along with other factors. As-grown films have an intrinsic or primary OPB density generated during growth. Insufficiently quenched films (i.e., films that lose bismuth at the end of growth) undergo secondary OPB generation. For example, the films in Figs. 11(a) and 11(d) nucleated with an excess of bismuth at the film-substrate interface, visible in the images, but Fig. 11(d) nonetheless shows a high density of OPBs, which appear to be a mixture of primary and secondary OPBs (See Sec. III. D).

Films grown on (110) and (111) perovskite substrates also contain OPBs, and several such high-quality films grown by PLD have been studied. Figures 12(a) and 12(b) are TEM images showing typical OPB morphology in $SrBi_2(Nb,Ta)_2O_9$ films grown on (110) and (111) substrates, respectively, with OPBs frequently present in bunches. Note that these films grow with twinned orientations in accordance with the surface symmetry[75,101] and that the vertical walls are growth twin boundaries due to the multiple orientations. They are not grain boundaries. For these substrate orientations, the growth front does not proceed along the layering direction of the layered oxide. The result is a complex OPB morphology that merits further study. HRTEM images of $SrBi_2Ta_2O_9$

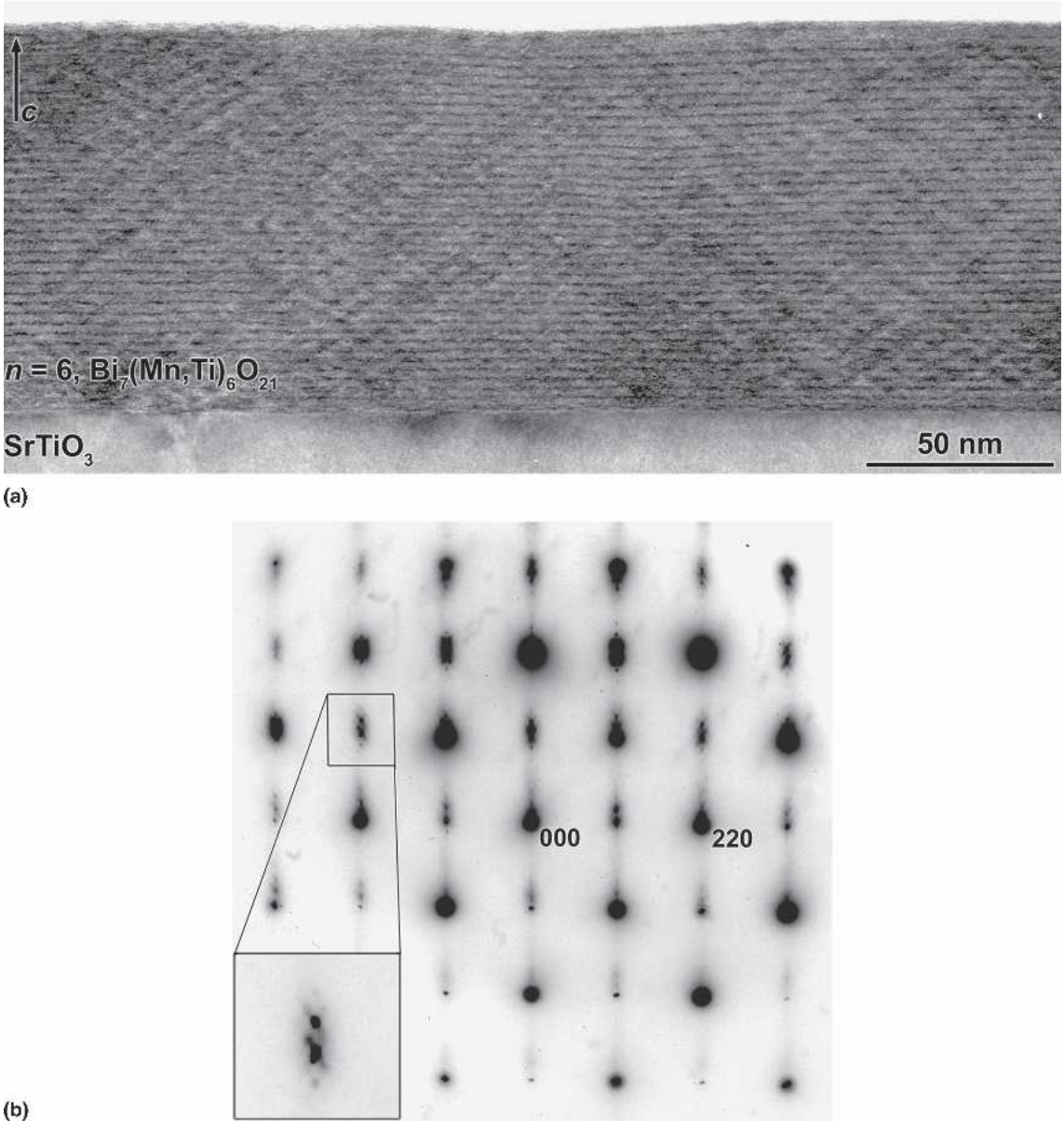

FIG. 13. (a) An $n = 6$ Aurivillius phase, $Bi_7(Mn,Ti)_6O_{21}$, with a high density of OPBs, oriented 35° with respect to the layering plane. (b) Electron diffraction pattern from the same film, showing streaking due to the high defect density.

grown by CVD on (110) and (111) substrates show a very similar OPB morphology.[83]

b. $n > 2$

Too few high-n Aurivillius phases have been synthesized and studied by HRTEM to show trends clearly. Some observations, however, can be noted. A few OPBs in $n = 3$ Aurivillius films have been studied. In MBE-grown (001) $Bi_4Ti_3O_{12}$ ($c = 32.83$ Å), OPBs have been reported to exhibit a meandering morphology, oriented nominally at 55°.[64] In [001] images, APBs were also noted, which can be associated with OPBs (See Sec. III. C. 4).[64] HRTEM imaging of $n = 5$ $Ba_2Bi_4Ti_5O_{18}$ ($c = 50.3$ Å) by Hesse et al. revealed large-offset OPBs dissociated into stepped clusters of OPBs, each having an offset of ≈0.42 nm, nearly equivalent to a double-BiO^+

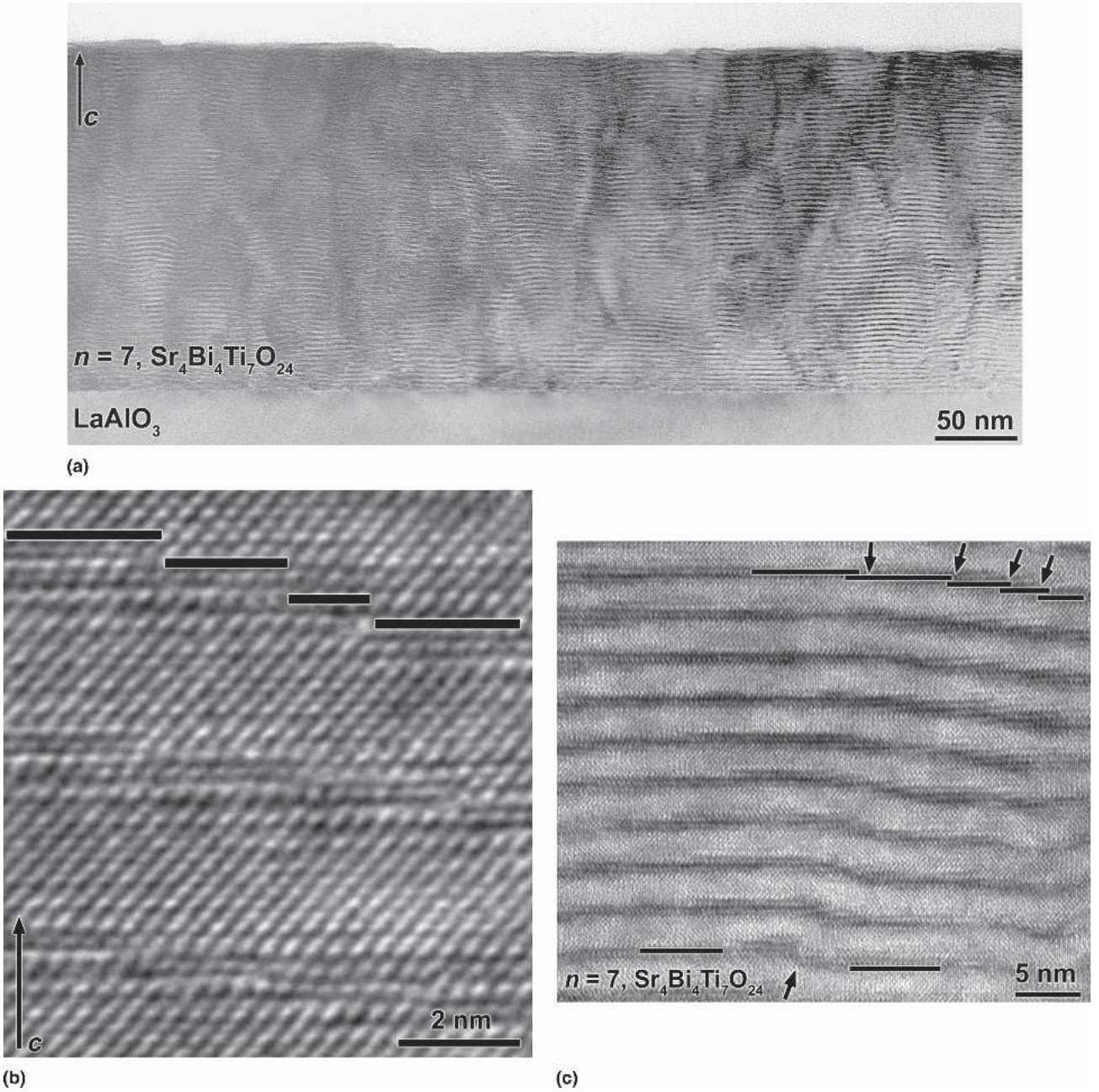

FIG. 14. OPBs in an $n = 7$ Aurivillius phase, the highest-n Aurivillius phase ever synthesized. (a) A low density of OPBs is present, despite the large repeat unit, ≈64 Å. (b) The apparent bending of the $Bi_2O_2^{2+}$ layers (horizontal bands of contrast) in the material is actually a series of atomically stepped OPBs. (c) In another location, a large-scale physical feature has nucleated a large-offset OPB that quickly dissociated into a series of four smaller-offset OPBs. Bars indicate the $Bi_2O_2^{2+}$ layers in neighboring out-of-phase domains, demonstrating the offset, and black arrows indicate the positions of the OPBs.

layer.[85] At low magnification, the clusters gave the appearance of ribbon-like $Bi_2O_2^{2+}$ layers that were bent. A TEM image of the $n = 6$ Aurivillius phase $Bi_7(Mn,Ti)_6O_{21}$ is shown in Fig. 13(a), with a very high density of OPBs having similar alignment, oriented at approximately ±35°, with an offset of ≈0.2 nm. Very few areas with a single visible OPB exist in the film. The [110] diffraction pattern from the film in Fig. 13(b) exhibits strong streaking due to the similar orientation of the planar faults.

TEM images of the $n = 7$ Aurivillius phase $Bi_4Sr_4Ti_7O_{24}$ are shown in Fig. 14. As can be seen in Fig. 14(a), the film has a low density of OPBs of meandering shape that penetrate the full film thickness. The $Bi_2O_2^{2+}$ layers have a ribbonlike appearance, but closer examination reveals the features to be clusters of OPBs, shown in Fig. 14(b), similar to the stepped clusters above. In Fig. 14(c), a sharp OPB of unknown origin, having an offset of 4 monolayers, is visible at the bottom of the image. After the growth of four more unit cells, the OPB has dissociated and spread to form a cluster of stepped OPBs 160 Å in width, implying that a single-monolayer OPB is the lower-energy configuration.

XRD analysis of high-n films such as these becomes less useful with increasing n because even a low density of OPBs can result in most cells of the high-n phase being crossed by at least one OPB, leading to diffraction patterns that are difficult to interpret. At the least, OPBs in such phases will lead to stronger modulation of 00$\underline{l}$ superlattice reflections in 00l θ-2θ scans due to decreased order along [001], and strong modulation of these reflection intensities is used as a metric of general disorder. Such patterns can be difficult to index to a particular lattice parameter c.

Potential misidentification of the lattice parameter in a film with strongly modulated superlattice reflections is addressed in the following thought experiment. Consider the schematic illustration in Fig. 15(a), showing a cross-section of an idealized $n = 7$ Aurivillius phase, with seven perovskite units between $Bi_2O_2^{2+}$ layers, and a c of ≈65 Å. A high density of OPBs is present, ≈300 OPB/μm, spaced relatively evenly. Measuring along c, a period corresponding to $c \approx 69$ Å, or roughly to $n = 8$, is noted. Thus, a 00l θ-2θ XRD scan of such a material might appear to indicate an $n = 8$ Aurivillius phase, with low apparent quality due to strong modulation of 00$\underline{l}$ superlattice reflections. Figure 15(b) shows the difference in the real and apparent c for a single slab. In a real sample, such OPBs would likely be irregularly spaced, leading to increased diffuse scattering perpendicular to the defect planes. A diffraction simulation study of this kind of defect structure would be useful for understanding data from such films. An experimental approach to avoid the issue is to use a smaller probe for diffraction, as is accessible in the TEM or with focused synchrotron radiation.

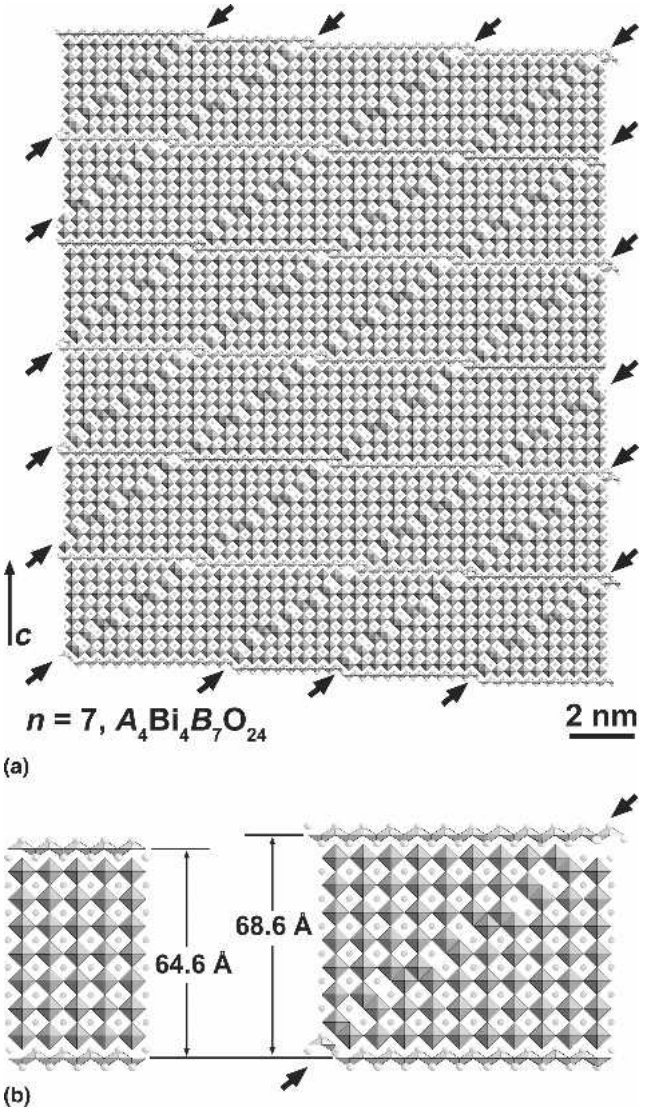

FIG. 15. The presence of OPBs can complicate proper phase identification by XRD of layered oxides with large repeat units. (a) In this hypothetical example, a high density of OPBs in an $n = 7$ Aurivillius phase convolutes the c-axis period spacing such that it appears to be more closely associated with an $n = 8$ Aurivillius phase, shown clearly in (b). Black arrows indicate the positions of the OPBs.

3. Stacking faults

There has been considerable discussion of stacking faults in layered oxides. Their existence in Ruddlesden–Popper phases is well established, and in fact "Ruddlesden–Popper defects" are often described in perovskite and perovskite-related phases. Far less has been said about stacking faults in Aurivillius phases.

Stacking faults are indeed observed in Aurivillius phases, but very few have been imaged directly and convincingly in published reports, and they are far less common than is widely believed. We have observed very few stacking faults in HRTEM studies of numerous Aurivillius phase films, which have in all cases been of

very short spatial extent, and always terminated by OPBs. Three of the four clear published images of stacking faults in $SrBi_2(Nb,Ta)_2O_9$ are terminated by an OPB,[42,85,122] and the fourth does not show a wide enough area to tell.[123] The evidence points strongly to stacking faults in Aurivillius phases being energetically disfavored.

X-ray studies of 00*l* peak spreading, indicative also of *c* faults (in addition to the above), have been reported for sol-gel polycrystalline and epitaxial films of $SrBi_2Nb_2O_9$.[124] Peak profile shapes were analyzed to infer the domain shape. The tendency toward Lorentzian or Voigtian peak shape was used to determine the presence or absence of stacking faults along various axes, with domain sizes measured by the degree of peak spreading.[124] It is possible that in the polycrystalline system, stacking faults extended to grain edges, otherwise, both 00*l* and *h*00 reflections would have exhibited Lorentzian profiles, rather than the Voigt peak shape which was observed for the *h*00 reflections. Stacking faults terminating within crystals (epitaxial films) have been reported to have strong strain fields.[57] A compositional analysis of these films would be very valuable for understanding the potential chemistry of such stacking faults. Even more exciting would be the combination of this type of XRD analysis[124] with HRTEM analysis of the same film.

A very important difference exists between Ruddlesden–Popper and Aurivillius phases: layer charge. In a typical Ruddlesden–Popper phase, the *A*O layer is uncharged, and often the ABO_3 layers are as well. Electrostatics does not play a significant role in determining the organization of crystallographic units in most Ruddlesden–Popper phases. Syntactic intergrowths of other-*n* members of a series are common.

In contrast, for all bismuth-containing Aurivillius phases, the Bi_2O_2 layer has a 2+ formal charge. Thus, a stacking fault (along *c*) requires a significantly different composition than simply that of the next *n*-member of the homologous series to achieve charge balance, making such intergrowths in a nominally stoichiometric film less likely. For example, insertion of an "extra" perovskite block, $SrNbO_3^+$, in $n = 2$ $SrBi_2Nb_2O_9$, would be a single-slab $n = 3$ intergrowth. This would not be charge-balanced, and compensation by an entire layer of oxygen interstitials would be required, which seems unlikely. Compensation by vacancies of half of the Sr^{2+} sites, or *B*-site occupancy by $Bi^{3+/5+}$ and a lower number of Sr^{2+} vacancies, have also been proposed.[122] But in all cases, significant local charge compensation would be required. For a Sr-poor film, an intergrowth of a single layer of an $n = 1$ Aurivillius phase, Bi_2NbO_6, might be possible.

A strontium-rich film of an Aurivillius phase might possibly contain a single Ruddlesden–Popper defect within the double perovskite block of the otherwise single-phase Aurivillius film. Such an unlikely sounding defect may have already been observed. Yan et al. analyzed a stacking fault in $SrBi_2Ta_2O_9$ by Z-contrast imaging, and attributed two adjacent layers of intensity in their image to strontium.[123] Although they concluded that the layer was a Sr_2 metal bilayer, no measurement of the oxygen content accompanied the analysis. Metallic strontium in $SrBi_2Ta_2O_9$ is highly unlikely from a thermodynamic perspective since strontium is the easiest of the constituent cations to oxidize.[125] A reinterpretation of these results as a Ruddlesden–Popper defect is consistent with the published data. A more thorough analysis of such defects could prove informative. Further, the existence of this type of structure implies the exciting possibility of using layer charge to mediate the phase-pure synthesis of high-*n* Aurivillius or Ruddlesden–Popper phases.[23] It also hints that a homologous series of intergrowths between Aurivillius and Ruddlesden–Popper homologous series could be possible.

4. Growth spirals

It has been suggested that OPB nucleation and growth could be due to spiral growth about a screw dislocation with a large Burgers vector,[126] and surface imaging reveals growth spirals in (001) $SrBi_2Ta_2O_9$[79] and $(Sr_4Bi_4)Ti_7O_{24}$.[127] It has also been suggested that neighboring out-of-phase nuclei (Sec. III. D. 1) could lead to the formation of spirals,[58] and edge dislocations with a Burgers vector contained in the surface (i.e., misfit dislocations) can also lead to growth spirals if the edge dislocation line is inclined to the surface.[128] An example of growth spirals in an Aurivillius film is shown in Fig. 16. The areal density of growth spirals is $\approx 10^9$ per cm^2, which is comparable to the density of threading OPBs seen in cross-sectional TEM in these same films. The incoherent meeting of growth fronts thought to be responsible for the nucleation of growth spirals in other layered oxides is also likely to be the nucleation mechanism for these dislocations with screw component.[129–135] The growth fronts on all terraces of a spiral extend during growth, so spirals become larger until the point that they merge with other spirals. OPBs could be the result of the intersections between growth spirals. The observed dissociation of the large-displacement edge dislocation in Fig. 14 suggests that any screw dislocation of similar magnitude would also have a dissociated core, with both edge and screw components, making direct observation exceptionally unlikely.

C. Structure

HRTEM imaging, structural modeling, and simulation reveal the atomic structure at OPBs in both Aurivillius and Ruddlesden–Popper phases to diverge from stoichiometric compositions.[54] The interruption of the lattice is compensated in both cases by deficiency or excess of the *A*-site or bismuth cations.

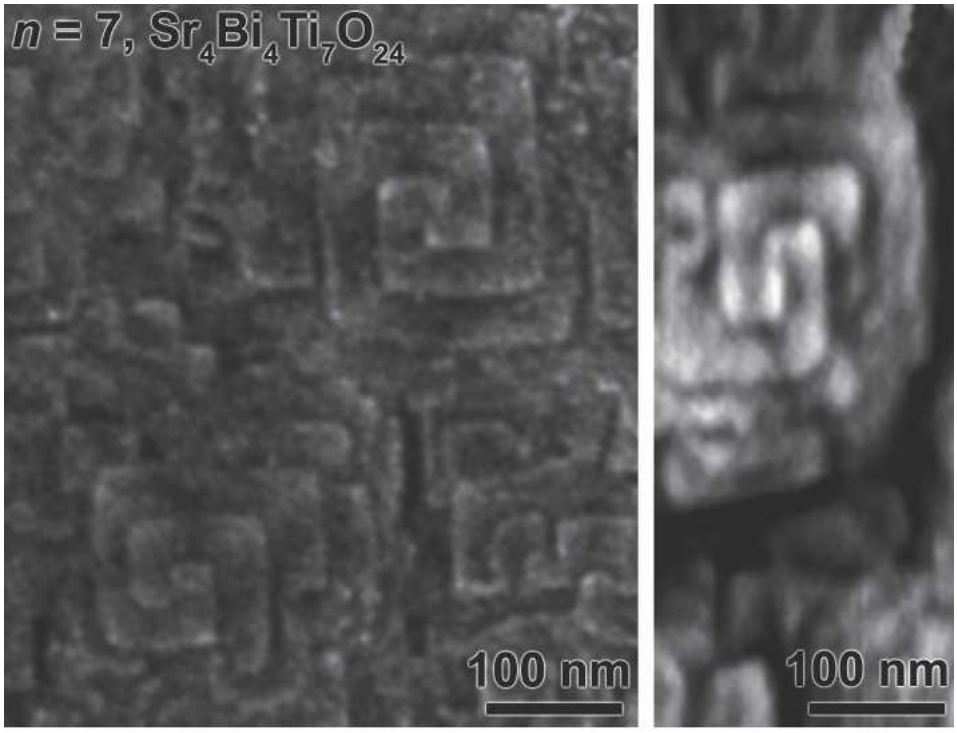

FIG. 16. Growth spirals are visible in (a) SEM and (b) AFM images of the surface of an $n = 7$ Aurivillius-phase (001) $Sr_4Bi_4Ti_7O_{24}$/(001) $SrTiO_3$ film. The images are identically scaled.

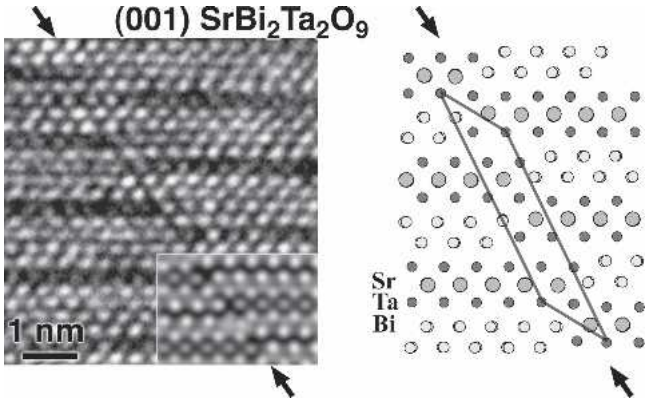

FIG. 17. $[100]_p$ HRTEM image and model of an OPB in the $n = 2$ Aurivillius phase $SrBi_2Ta_2O_9$. A simulation of the model is inset in the lower-right corner of the image. The OPB is bismuth deficient, so NbO_6 octahedra share edges across the boundary in every other layer to achieve charge balance. The rhomboid on the model shows the unit cell of the OPB. Black arrows indicate the position of the OPB.

1. Aurivillius phases

In an Aurivillius-phase (001) $SrBi_2Ta_2O_9$ film, tantalum coordination octahedra share edges across the OPB. The cross-sectional HRTEM image in Fig. 17 shows the film, with an OPB oriented parallel to the imaging axis, making it possible to model the structure in the area. The two domains are out of registry by two composition planes along c. The model on the right is consistent with the observed images, and a simulation of the model is inset in the HRTEM image. Calculation of the stoichiometry of the unit cell of the defect indicates that it is deficient in bismuth. Charge imbalance is compensated by half of the niobium octahedra sharing edges across the fault. This also maintains continuity of the structure in this orientation. OPBs in $SrBi_2Nb_2O_9$ and $SrBi_2Ta_2O_9$ show a high variability in orientation, with apparently curved morphology, implying a low difference in the energy associated with mixed edge- and corner-sharing niobium oxygen coordination octahedra across these faults. This variation in atomic stepping of faults is similar to the behavior of "swinging shear planes" observed in $Nb_2O_{5-\delta}$ with slight variations in oxygen activity.[136] It is also similar to the regularly stepped and collapsed structures reported in Bi-2212-type structures.[137] In a similar fashion, because these OPBs are crystallographic shear defects, the orientation and concentration of OPBs may vary proportionally with the degree of nonstoichiometry in a film.

2. Ruddlesden–Popper phases

In an $n = 1$ Ruddlesden–Popper phase, (001) Sr_2RuO_4, a close-packed layer of SrO exists along the OPB. The cross-sectional HRTEM image in Fig. 18 shows a region of the film with a single OPB, viewed edge-on. The model, on the right, is consistent with the

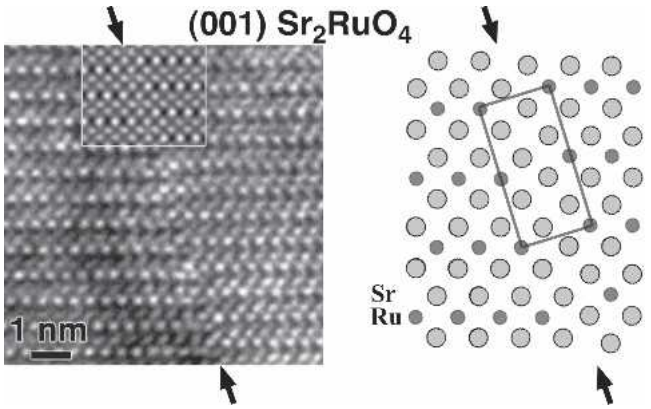

FIG. 18. [100] HRTEM image and model of an OPB in the $n = 1$ Ruddlesden–Popper phase Sr_2RuO_4. A simulation of the model is inset in the top of the image. An *A*O double layer is present at the OPB, disrupting continuity of the RuO_2 octahedral substructure. The rectangle on the model shows the unit cell of the OPB. Black arrows indicate the position of the OPB.

observed images, and a simulation of the model is inset in the HRTEM image. Calculation of the stoichiometry of the unit cell of the defect indicates that it is rich in strontium. The density of OPBs in the film is low, so non-stoichiometry induced by the defects would constitute a change in composition of less than 1%.

The fault in the $n = 2$ Ruddlesden–Popper epitaxial film, $Sr_3Ru_2O_7$, shown in Fig. 9(a), was also modeled. A schematic illustration and the simulation of the model are shown in Fig. 19(a), indicating a good match with the observed image. A 90° OPB forms but is terminated half of a unit cell later in a SrO double layer. This is an atypical form for a fault in a Ruddlesden–Popper phase, as discussed in Sec. III. B. 1. Figure 19(b) is a model of the area shown in Fig. 9(b), made using the same structural principles.

3. Structural interactions

Because OPBs propagate through a growing layered oxide film, they may encounter others and interact. The complexity of OPB interactions should increase with *n*, as larger cells have a commensurately larger number of possible offsets. This interaction can take various forms. In a simple $n = 1$ Ruddlesden–Popper phase with chemical formula A_2BO_4, consisting of three composition planes (two structurally equivalent), only two unique OPB misregistries are possible. The OPBs are also straight and therefore likely to encounter other OPBs in a growing film, which will result in the annihilation of both, as seen previously in Figs. 5 and 8.

The stacking of the $n = 2$ Aurivillius phases $SrBi_2Nb_2O_9$ and $SrBi_2Ta_2O_9$ consists of five composition planes, of which two pairs are structurally equivalent, yielding several possible phase offsets. OPBs in these films exhibit a high variability in orientation but tend to not interact directly, although they do appear to correlate due to strain interactions.

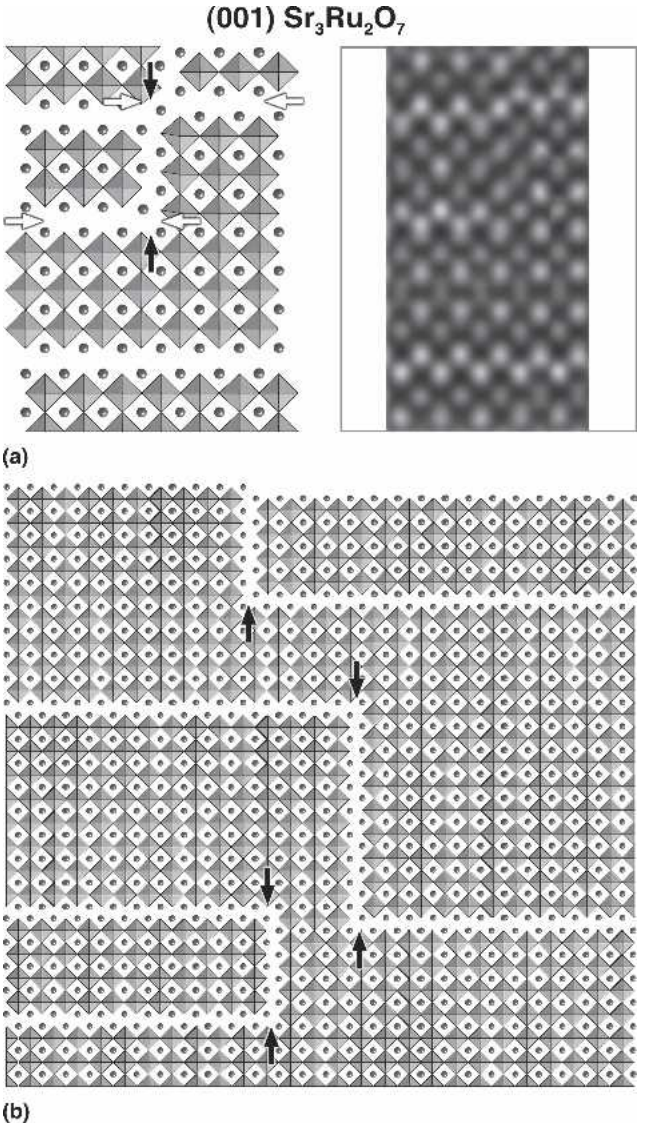

FIG. 19. $[100]_p$ HRTEM model and simulation of the defect in the $n = 2$ $Sr_3Ru_2O_7$ Ruddlesden–Popper film in Fig. 9(a). The stacking fault terminates in an OPB, which terminates in the next *A*O layer of the film. The simulated image has been cropped to remove edge artifacts, as indicated by the frame. (b) Model of the area shown in Fig. 9(b), developed on the same structural principles as the model in (a). Black arrows indicate the positions of the OPBs, and white arrows indicate the stacking faults.

Generally, the complexity of OPBs in layered oxides is expected to increase with *n*, as more structurally unique OPB offsets exist in larger cells, with a commensurate rise in possible interactions. Many structures and complex cumulative interactions are possible. The probability of oppositely signed OPBs annihilating one another drops precipitously with increasing *n*.

4. Structural permutations with *n*

Trends become apparent when the geometrically possible offsets and corresponding structures of OPBs are considered as the repeat cell of layered oxides increases

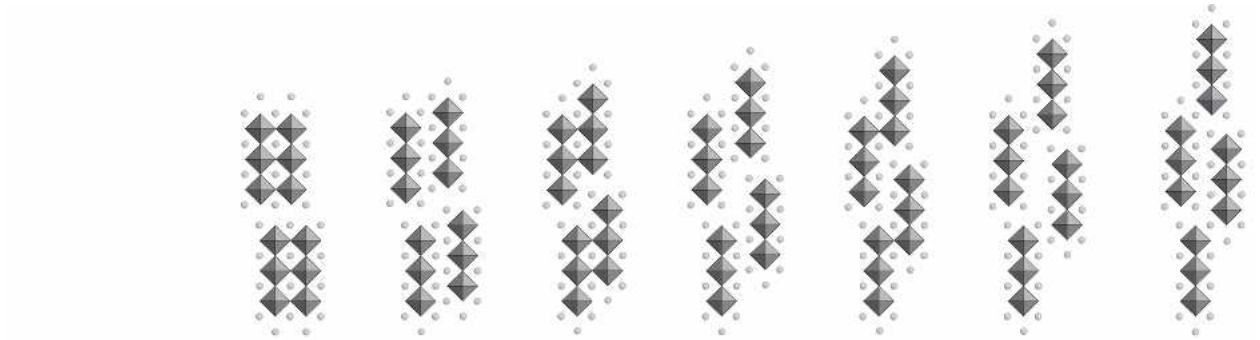

***c* offset (ML)**	0	1	2	3	4	5	6
***ab* offset**	–	APB	–	APB	–	APB	–
***A*O continuity**	cont.	branches	jogs	jogs	jogs	?	branches
***ABO*$_3$ continuity**	3/3	discont.	2/3	discont.	1/3	discont.	discont.

FIG. 20. The possible permutations of OPB offsets increases dramatically with n, increasing the complexity of OPB interactions commensurately. For the $n = 3$ Ruddlesden–Popper phase example shown, the images show all possible OPB offsets in terms of atomic monolayers. The table lists the corresponding offset in the *a*-*b* plane for each, as well as the effects on the continuity of the *A*O and ABO_3 substructures.

in size. The possible number of interactions is the permutation of n ($_nP_n = n!$) for a given Ruddlesden–Popper or Aurivillius phase. An example of a layered oxide with slab layers three perovskite cells thick is shown in Fig. 20, corresponding to an $n = 3$ Ruddlesden–Popper phase. The six possible out-of-phase offsets are shown with idealized structures at the OPBs for each. No particular atomic arrangement at the OPBs is assumed.

The table in Fig. 20 lists the corresponding offset in the *a*-*b* plane for each and also lists the effects on the continuity of the *A*O and ABO_3 substructures. Offsets of an odd number of monolayers result in an APB in the *c* plane, (1/2,1/2,0), in addition to the *c* offset. In contrast, OPBs of an even number of monolayers allow some number of octahedra of the perovskite slab to be continuous across the OPB. Variation in the continuity of the perovskite substructure could have implications for materials in which correlated behaviors of the perovskite are responsible for the behavior of interest, such as in multiferroic layered oxides. The *A*O double layer jogs at the OPB, and in some cases branches, which could be important for transport behavior, and for studies of reduced dimensionality, if slab layers are expected to be continuous in the plane. Note that offsets of 2 and 5 ML (and of 3 and 4 ML) are not equivalent. For an offset of 2 ML, the octahedra of the domain on the right are in phase along the viewing axis. For an offset of 5 ML, the octahedra of the domain on the right must be in antiphase alignment, along the viewing axis, with those on the left. Certain offsets might be energetically preferred over others. The lack of observations of branching *A*O layers in Ruddlesden–Popper phases implies that such configurations might be energetically disfavored. Atomistic simulation studies of these defects could be informative. Study of films of identical composition grown on vicinal substrates having steps of varying numbers of monolayers in height could address the questions regarding the effect on properties of each of these degrees of offset.

D. Nucleation mechanisms

In the layer-by-layer growth of epitaxial layered-oxide films, the growing crystal is physically constrained by the substrate, with a nearly planar growth front proceeding along essentially a single direction. This limits the amount of structural reorganization and amplifies the effects of substrate–film interactions, leading to the prominence of microstructural features not commonly observed in bulk samples. Chemical and physical interactions between a nucleating film and the substrate play key roles in the generation of crystallographic defects such as OPBs. The common outcome of these nucleation events is to introduce a phase shift along the layering axis between neighboring nuclei in a growing film. The result is that faults associated with this shift, often only one atomic layer thick, can propagate through an entire film of half a micron or more in thickness.

Five mechanisms have been identified that can nucleate out-of-phase domains in layered oxides, four primary and one secondary. These are depicted schematically in Fig. 21, and are described in more detail in the following sections. We refer to them by the following names: nucleation layer, steric, *a*-*b* misfit, inclined-*c* misfit, and crystallographic shear. Specific examples of these

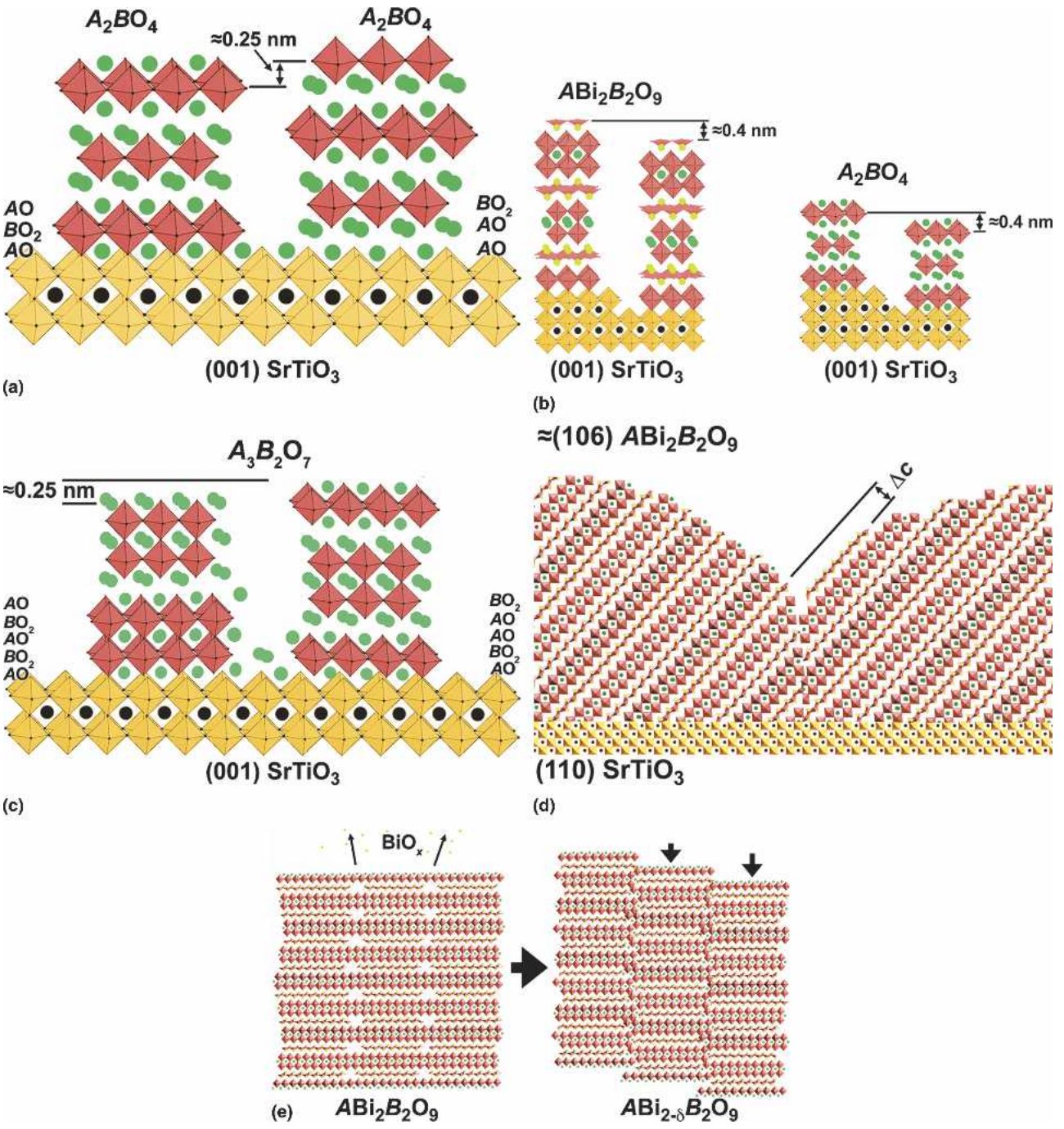

FIG. 21. (a–d) Four primary mechanisms and (e) one secondary mechanism of OPB nucleation in epitaxial films of layered complex oxides. (a) Nucleation layer: multiple occurrences of the preferred nucleation layer within the unit cell, in this case SrO in Sr_2RuO_4, leads to neighboring nuclei that are out of phase. (b) Steric: out-of-phase nuclei on different terraces of a surface generate an OPB where they meet. (c) *a-b* Misfit: A misfit dislocation in a nucleation layer leads to a loss of structural correlation between two regions of the layer, which splits into two nuclei that happen to continue growth with different layer ordering. The tensile case is shown, for which *A*O in sixfold coordination replaces the BO_6 octahedron. (d) Inclined-*c* misfit: layered oxides with the *c* axis inclined to a surface generate OPBs as a result of the incommensurate surface mesh at the heteroepitaxial interface. (e) Crystallographic shear: complex oxides containing a volatile component can undergo crystallographic shear as material is lost at high temperature, resulting in the generation of OPBs.

particular mechanisms have been reported in many chemical systems, such as $YBa_2Cu_3O_{7-\delta}$, $Bi_2Sr_2CaCu_2O_{8+\delta}$, $SrBi_2(Nb,Ta)_2O_9$, $Bi_4Ti_3O_{12}$, $(Sr_2Bi_4)Ti_5O_{15}$, Sr_2RuO_4, and $Sr_6Ti_5O_{16}$ (all described in detail below), but the mechanisms have not been described together in a general manner for layered oxides. We present schematics of the mechanisms, with images from our own work on Aurivillius and Ruddlesden–Popper films, with the

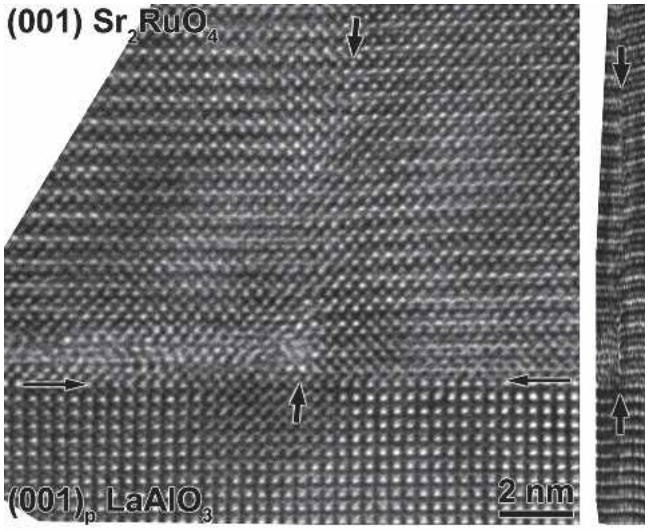

FIG. 22. Example of the nucleation layer mechanism. (a) Cross-sectional HRTEM image of a (001) $Sr_2RuO_4/(001)_p$ $LaAlO_3$ film with a single OPB nucleated at the substrate. The $(001)_p$ $LaAlO_3$ substrate is terminated by the AlO_2 layer and growth of Sr_2RuO_4 starts with the SrO layer. However, growth on the left continued with a RuO_2–SrO–SrO growth order, while growth on the right continued with a SrO–RuO_2–SrO growth order. The resulting ≈0.24 nm offset resulted in the generation of an OPB where the nuclei met. Strain contrast in the $LaAlO_3$ at the defect is also visible. (b) A horizontally compressed version of the same image clearly shows the *c*-direction offset. The images have been enhanced slightly by Fourier techniques. The very thin arrows indicate the film-substrate interface in (a), and the black arrows indicate the position of the OPB.

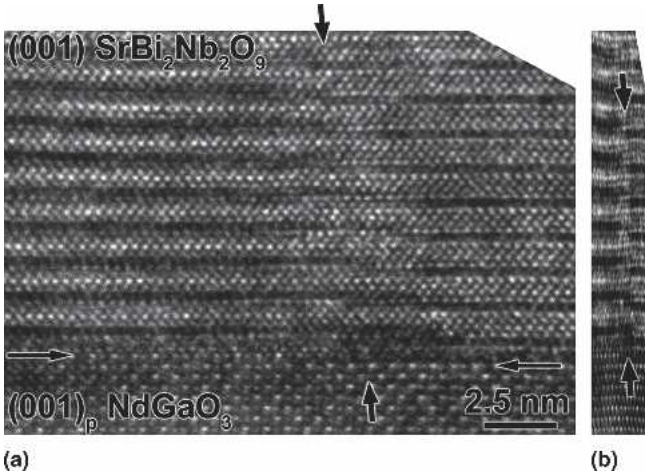

FIG. 23. Canonical example of the steric mechanism. (a) HRTEM image of a (001) $SrBi_2Nb_2O_9/(001)_p$ $NdGaO_3$ film with a single OPB nucleated at a substrate surface step. Neighboring nuclei meeting at a single-unit-cell step in the $NdGaO_3$ surface are out of phase by ≈0.39 nm along *c*, resulting in the generation of an OPB. (b) A highly compressed version of the same image clearly shows the *c*-direction offset. The very thin arrows indicate the film-substrate interface in (a), and the black arrows indicate the position of the OPB.

understanding that they are applicable to layered oxides in general.

1. Nucleation layer

Complex oxides consist of alternating sequences of composition planes. For a given film-substrate system, nucleation by one composition plane will generally be energetically preferred, depending upon substrate termination and thermodynamic parameters. If the nucleating layer has more than one structurally equivalent occurrence in the unit cell, growth after the nucleating layer can proceed in more than one order, resulting in the generation of OPBs. This is shown schematically in Fig. 21(a) for (001) $A_2BO_4/(001)$ $SrTiO_3$ (a common perovskite substrate), which has nucleated with an *A*O layer on TiO_2-terminated (001) $SrTiO_3$. The second atomic layer of the two domains differs—BO_2 on the left, and a second *A*O layer on the right—and will result in the generation of an OPB with an offset equivalent to one *A*O layer, ≈0.25 nm.

The nucleation layer mechanism has been reported for (001) $YBa_2Cu_3O_{7-\delta}/(001)$ MgO,[73] $RBa_2Cu_3O_{7-\delta}/(001)$ $SrTiO_3$ (R = Y, Dy, Nd, and Gd),[58,71,72] and (001) $Sr_2RuO_4/(001)_p$ $LaAlO_3$.[74] For the layered cuprates, although growth on TiO_2-terminated (001) $SrTiO_3$ always begins with the BaO layer, growth can proceed from there in two different orders. HRTEM data supporting the Sr_2RuO_4 case are shown in Fig. 22(a) with a horizontally compressed version of the same image to the right, Fig. 22(b), in which the offset due to the OPB is more clearly seen. In the domain on the left, growth has proceeded with a SrO–SrO–RuO_2 growth order, and in the domain on the right with a SrO–RuO_2–SrO order. The OPB has an offset of ≈0.24 nm, equal to the dimension of a single SrO layer in the unit cell. Disorder at the defect core and the associated strain field are also visible in the phase contrast image. Because only two growth orders are possible, OPBs of differing growth order nucleated on the same plane will annihilate if they intersect, as shown previously in Figs. 5 and 8. Also, because these OPBs occur at the intersection of neighboring film nuclei, the OPB density would be expected to scale negatively with increasing deposition temperature, as greater surface mobility at higher temperatures leads to wider terraces in the growing film.

The substrate termination can also be deduced from these data. The $(001)_p$ $LaAlO_3$ substrate was terminated by AlO_2 at the film growth temperature, and SrO was determined to be the preferred nucleation layer by modeling HRTEM imaging, and simulation.[74]

Knowing the preferred nucleation layer for a given film–substrate system provides a basis for predicting whether the nucleation layer mechanism will occur. The details of nucleation for many systems are unknown and would be an informative line of inquiry. It also depends on the termination layer of the substrate. The best-studied

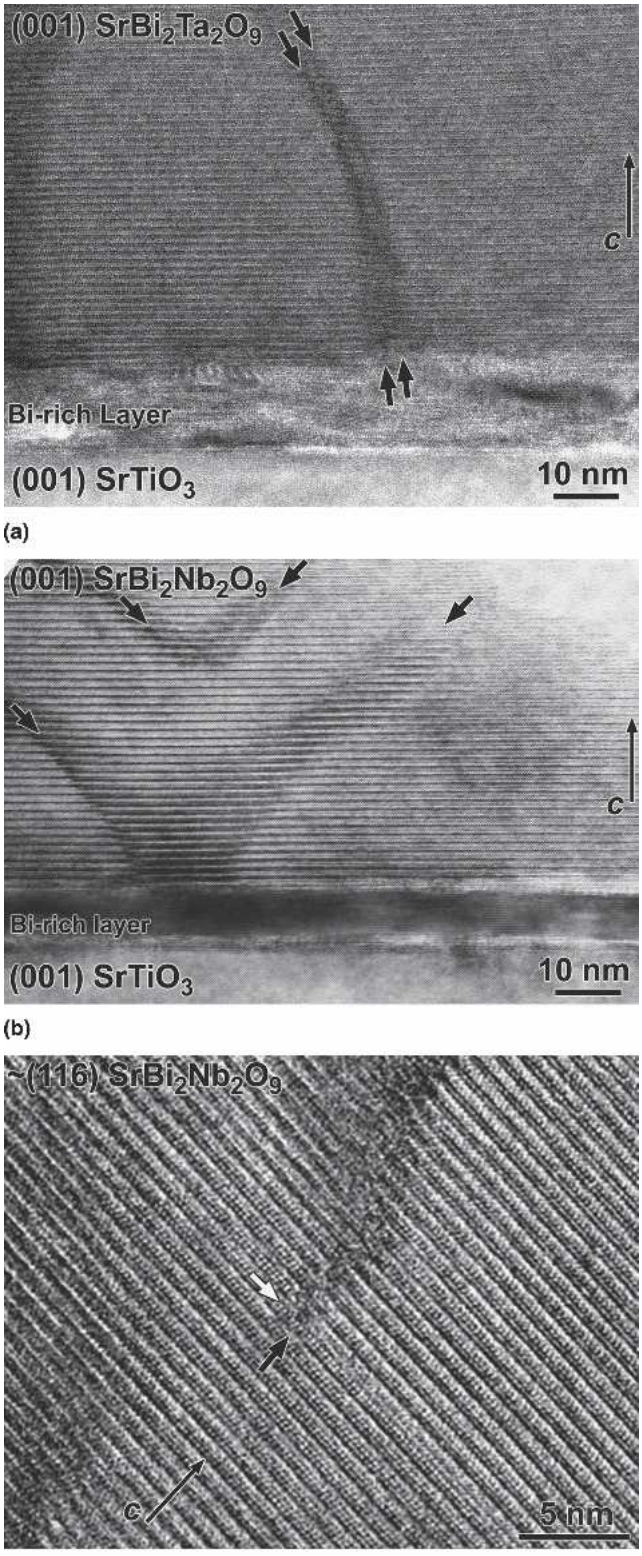

FIG. 24. Additional examples of the steric mechanism. HRTEM images of OPBs nucleated at (a, b) a step in an epitaxial bismuth-rich layer between the film and substrate, and (c) the termination of a stacking fault. Black arrows indicate the positions of the OPBs, and the white arrow indicates the stacking fault.

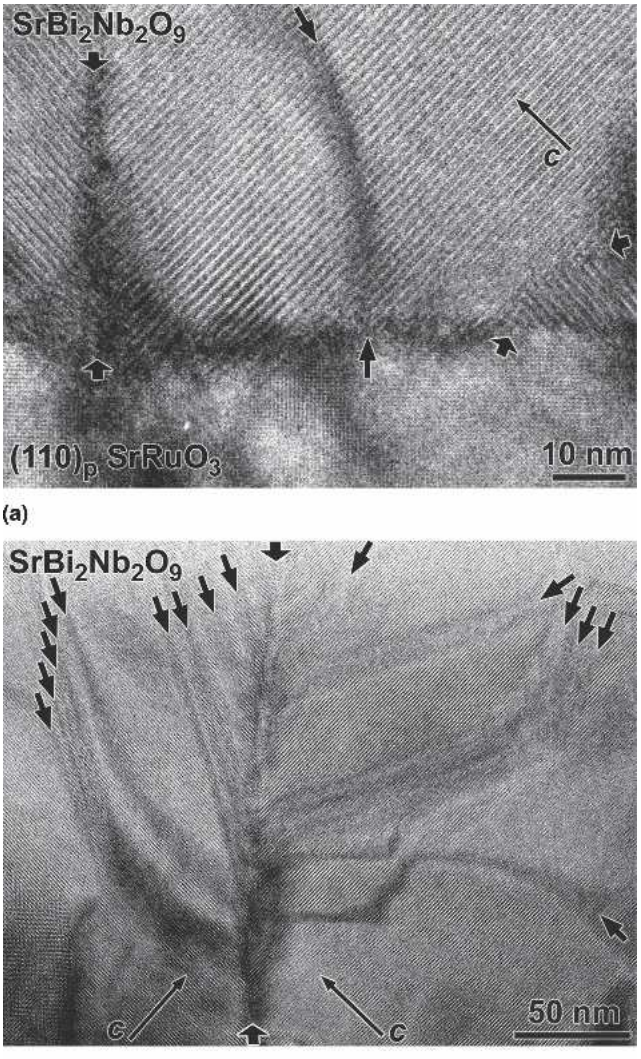

FIG. 25. Examples of the inclined-*c* misfit mechanism for a film with the layering axis inclined to the substrate surface in a $SrBi_2Nb_2O_9$/$(110)_p$ $SrRuO_3$/(110) $SrTiO_3$ film. HRTEM images of (a) OPBs nucleated at the film-substrate interface and (b) OPBs nucleated at a growth twin boundary of the film. Black arrows indicate the positions of the OPBs, and broad arrows indicate the growth twin boundaries.

substrate is (001) $SrTiO_3$ that terminates with a TiO_2 layer.[138,139] When grown on that termination, (001) $YBa_2Cu_3O_{7-\delta}$/(001) $SrTiO_3$ has a single nucleation layer[61] and is susceptible to the nucleation layer OPB nucleation mechanism due to two possible stacking sequences.[58] Nucleation of (001) $Bi_4Ti_3O_{12}$/(001) $SrTiO_3$ has been shown to occur preferably with the central TiO_2 layer of the perovskite block and is therefore not expected to nucleate OPBs via this mechanism.[64] Recently, (001) $SrBi_2Ta_2O_9$/(001) $SrTiO_3$ was shown to grow with a SrO–TaO_2–Bi_2O_2-TaO_2–SrO layer order, indicating that the nucleation layer mechanism is not likely to occur in this system, either.[83]

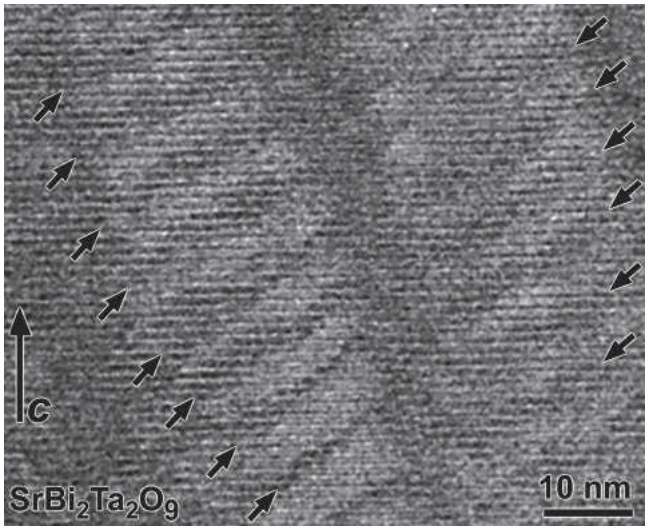

FIG. 26. Example of the crystallographic shear mechanism. An otherwise typical film of $SrBi_2Ta_2O_9$ was allowed to cool slowly in the growth chamber after growth, resulting in bismuth loss from the film. The HRTEM image shows a very high density of OPBs that was generated by crystallographic shear to compensate for the bismuth loss. Arrows indicate the positions of the OPBs.

2. Steric

The atomic-scale topography of the surface on which a film nucleates can also lead to the nucleation of out-of-phase domains in a growing film. The mechanism is shown schematically for a substrate surface step in Fig. 21(b) for two systems, (001) $ABi_2B_2O_9$ and (001) A_2BO_4, both on (001) $SrTiO_3$. In either case, nuclei on different terraces of the substrate are out of phase along *c* by the substrate step height and will generate an OPB where they meet (assuming identical nucleation layers for both domains). In this case, the offset is ≈0.4 nm, or one perovskite subunit of the film structure. Other cases can be envisioned for various other substrates and substrate surface morphologies. OPBs present as a result of the steric mechanism on substrate surface steps have been reported in $YBa_2Cu_3O_{7-\delta}$,[58,61,62] $DyBa_2Cu_3O_{7-\delta}$,[60] $SrBi_2(Nb,Ta)_2O_9$,[66,67] $Bi_4Ti_3O_{12}$,[64] and $(Ba_2Bi_4)Ti_5O_{18}$.[65] Intergrowths of other-*n* homologous series members have been reported as chemical stacking faults, which nucleate OPBs via the steric mechanism, in $Bi_2Sr_2CaCu_2O_{8+\delta}$.[86,140] Factors in considering the possibility of this mechanism are film structure, substrate structure, substrate vicinality, substrate surface step height, and the density of nuclei on the substrate.

We have observed OPBs nucleated at step edges in a (001) $SrBi_2Nb_2O_9$/$(001)_p$ $NdGaO_3$ film, shown in the cross-sectional HRTEM image in Fig. 23(a), with a horizontally compressed version of the same image to the right, Fig. 23(b), in which the offset due to the OPB is more clearly seen. The step edge and OPB are inclined to the imaging axis, so some apparent disorder due to phase overlap exists at the step. The epitaxial relationship of the two regions of the crystal is clearly visible at the interface on the far left and right sides of the image. This mechanism is expected to be active at step edges in any system for which the film has a significantly different lattice parameter than the substrate, in a direction perpendicular

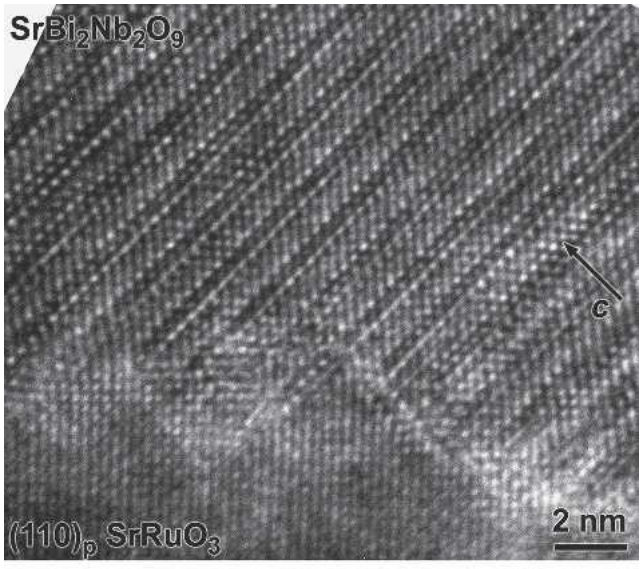

(a)

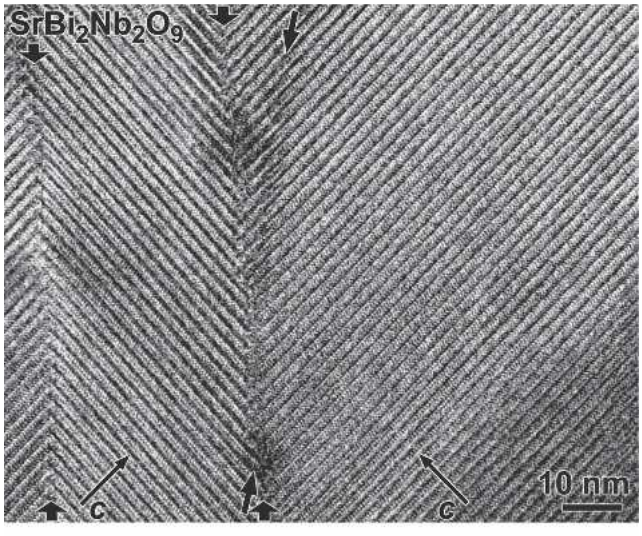

(b)

FIG. 27. The roughness of internal interfaces influences OPB generation. (a) A very rough $SrRuO_3$ surface resulted in significant structural disorder at the interface, which has allowed the film to heal over asperities, with no OPB nucleation. (b) A growth twin boundary has resulted in the generation of an OPB in $SrBi_2Nb_2O_9$, not due to the steric mechanism, but because the (001) terraces on the left presented a (001) perovskite surface, which is misfit relative to the (110) plane of the twin on the right. Black arrows indicate the positions of the OPBs, and broad arrows indicate the growth twin boundary.

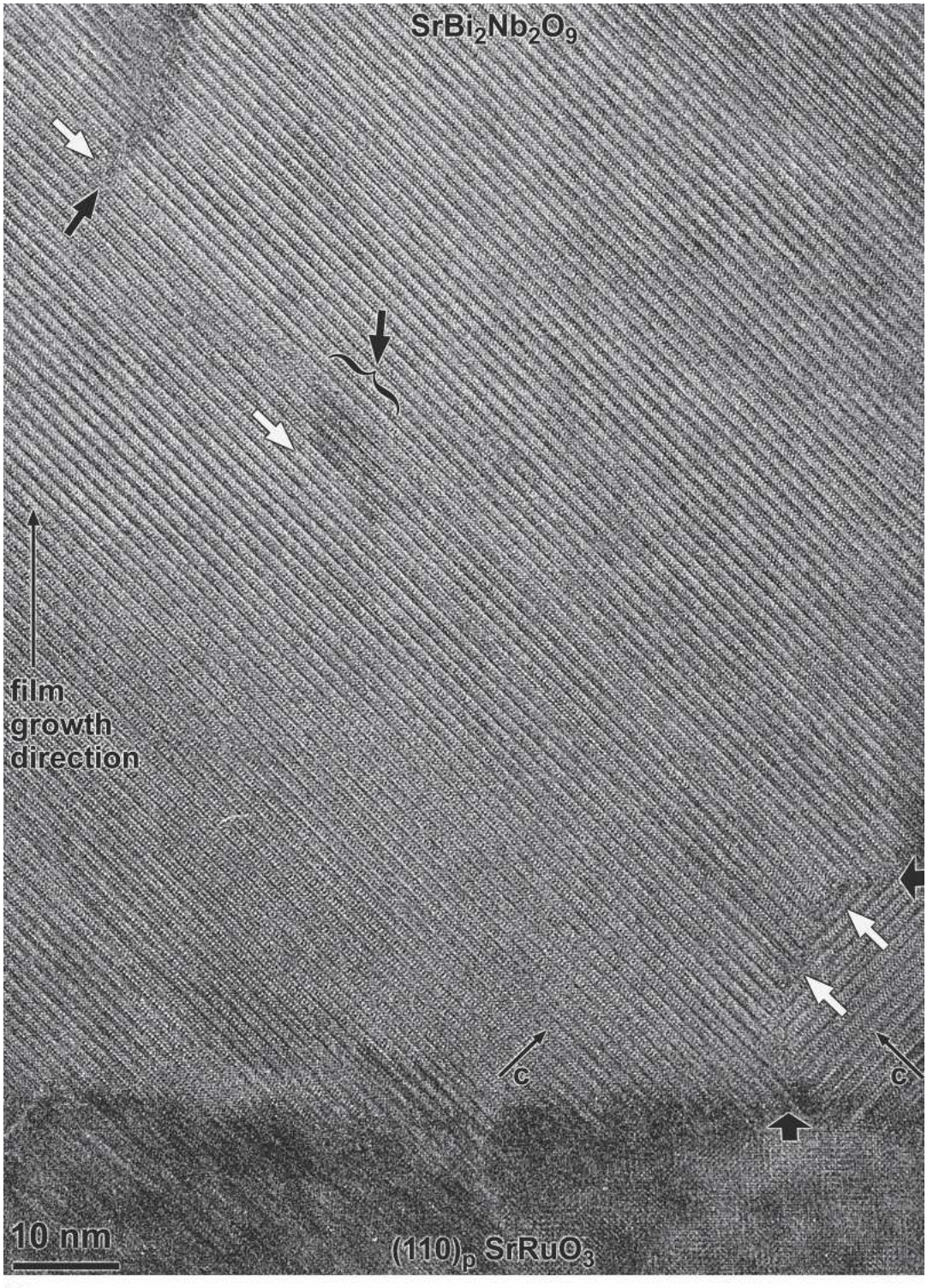

(a)

FIG. 28. The interaction of OPB nucleation mechanisms can lead to complicated defect structures. In the HRTEM image in (a), and the schematic illustration of (a) in (d), a large growth twin has overgrown a differently oriented growth twin in the early stages of film growth, providing a (001) perovskite surface. Broad arrows indicate the growth twin boundary at the bottom right of the image. In this case, the misfit has resulted in the generation of a pair of closely correlated *c* stacking faults, indicated by white arrows oriented parallel to the plane of the stacking fault. Near the center of the image, one stacking fault jogs along an OPB to combine with the other stacking fault, indicated by the black brace and arrow, creating a single, larger stacking fault. Soon after, on the top left, the large combined stacking fault jogs to form an OPB, indicated by the black arrow which continues through the full thickness of the film. Enlarged views of the arrowed regions are shown in (b), (c), and Fig. 24(c), respectively, (d) is a schematic of the entire defect structure in (a).

(continued on next page)

(b)

(c)

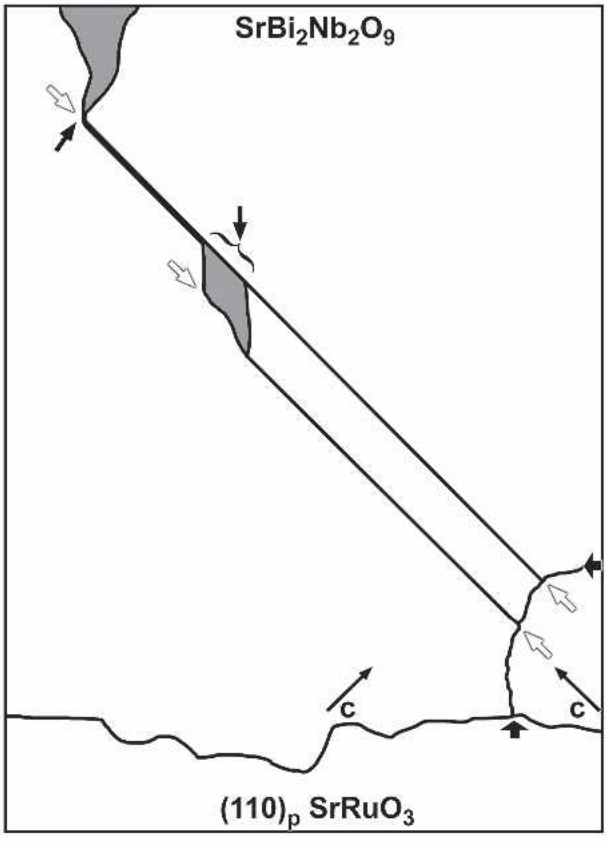

(d)

FIG. 28. *(continued)*

to the substrate. A study of the variation of OPB density across a vicinal substrate series would be informative. Likewise, vicinal substrates could be used to produce films with controlled OPB density, which would be useful for a quantitative study of their impact on properties. Novel morphologies might develop as the terrace width of vicinal substrates approaches the terrace width of nuclei in the growing film.

Some examples of the steric OPB nucleation mechanism at features other than substrate surface steps are shown in Fig. 24. Chemical nonstoichiometry has led to the encapsulation of a bismuth-rich epitaxial layer[54] in the (001) $SrBi_2Ta_2O_9$ and $SrBi_2Nb_2O_9$ films shown in Figs. 24(a) and 24(b), with the subsequent nucleation of OPBs at steps on the surface of the layer. In Fig. 24(c), a stacking fault on the right side of the image in a $SrBi_2Nb_2O_9$ film on (110) $SrTiO_3$ has terminated in an OPB.

3. Misfit

a. *a-b* misfit

Interfacial misfit dislocations may nucleate OPBs, shown schematically in Fig. 21(c) for an $n = 2$ Ruddlesden–Popper phase with tensile misfit to a $SrTiO_3$ substrate. At the core of the defect, the distortion of misfit leads to instability of a BO_6 octahedron, so instead, the space is filled with a larger AO in 6-fold coordination (a Ruddlesden–Popper defect). Such an interruption in the first perovskite slab during growth leads to the splitting of the perovskitic nucleation layer into two separate nuclei, with the growth of each possibly continuing with a different growth order, which is the case shown in Fig. 21(c). A Burgers circuit around this misfit dislocation would have a closure failure due to the extra layer of atoms present in the OPB. Such a defect would not necessitate the formation of any APBs in the *ab* plane, so it may be energetically favored in some cases. For the case of compressive misfit, a similar mechanism could occur, with a ≈0.25 nm double-AO layer replacing a ≈0.39 nm ABO_3 octahedron at the dislocation core and an associated APB in the *c* plane. This mechanism may be applicable only to materials with non-neutral layers, and the tendency of Ruddlesden–Popper phases to form intergrowths may make such a structure unlikely in them. Further, incoherent nucleation must occur for this mechanism to be active at nucleation, so a large misfit would be required, but once a film grows greater than the critical thickness for the nucleation of misfit dislocations, the mechanism could become active in a film that is coherent at the film–substrate interface.

The region between the two out-of-phase nuclei in Fig. 21(c) is left empty, but in a real film, this would be filled with matter, the arrangement of which would be only hypothetical, and so the region is left blank in the schematic illustration. This nucleation mechanism has not been observed experimentally in a layered oxide, although it has been reported to nucleate Ruddlesden–Popper-type defects in stoichiometric $SrRuO_3$.[141] Such a nucleation mechanism might be observable in a (001) $SrBi_2Ta_2O_9$/(001) $SrTiO_3$ film grown without interfacial misfit dislocations, but still containing OPBs,[83] or one simply grown on a substrate with a severe misfit with the film.

b. Inclined-*c* misfit

If the long axis of a complex oxide film is inclined to the substrate surface, OPBs can be generated due to mismatch if the commensurate modulation of the complex oxide structure is not equal to an integral multiple of the substrate structure in a direction parallel to the substrate surface. This is shown schematically in Fig. 21(d). In this case, two neighboring nuclei that are identically oriented but out of registry along a substrate surface-parallel direction can generate an OPB where they meet. This mechanism has the added complication of being influenced by the nucleation layer mechanism.

Depending upon the orientation relationship between the substrate and film, varying numbers of nucleation registries can be possible, and this will in turn influence the number of inclined-*c* misfit-generated OPBs. Like OPBs generated by the nucleation layer mechanism, the frequency of occurrence of OPBs generated by this mechanism would be expected to scale with the nuclei density (negatively with increasing deposition temperature). The mechanism might also be active in OPB generation in *c*-axis films having significant mosaic texture, although that has not been directly observed. An OPB generated in a $SrBi_2Nb_2O_9/(110)_p$ $SrRuO_3/(110)$ $SrTiO_3$ film by this mechanism is shown in Fig. 25(a), although such surfaces do not consistently nucleate these OPBs, as shown later in Sec. III. D. 5 ($SrRuO_3$ is isostructural with $SrTiO_3$ at the film growth temperature). In Fig. 25(b), two differently oriented growth twins in a $SrBi_2Nb_2O_9/(110)_p$ $SrRuO_3/(110)$ $SrTiO_3$ film meet at a growth twin boundary. The mismatch of the (001) to the ~(107) repeat units resulted in the generation of several OPBs. Note that these OPBs proceed along the film growth direction (towards the top of the page) from the growth twin boundary. Other OPBs, which intersect a boundary at their farthest point from the substrate surface have clearly propagated from elsewhere and have terminated at that boundary.

4. Crystallographic shear

After growth, loss of a volatile component through evaporation leads to the secondary generation of OPBs, as shown schematically in Fig. 21(e). Epitaxial films of $SrBi_2(Ta,Nb)_2O_9$ grown at high temperature in an adsorption-controlled growth regime[79] are not stable at the film growth temperature and atmosphere without an

overpressure of bismuth. If deprived of an appropriate bismuth overpressure, they begin decomposing with the evaporation of bismuth and bismuth oxide species. A cross-sectional HRTEM image of the slowly cooled $SrBi_2Ta_2O_9$ film from Fig. 11(f) is shown in Fig. 26. As bismuth is lost, the structure crystallographically shears to form OPBs. In the image, groups of similarly oriented OPBs feed into a larger column of defective material in the center (darker region), which acts as a fast diffusion path for volatilizing bismuth.

5. Nucleation interactions

A complicating factor in analyzing the sources of OPBs in a system is that the various nucleation mechanisms interact, which can reasonably be expected to lead to lower energy barriers for other mechanisms. For example, if a small energy difference exists for the possible nucleation layers of a film, then misfit strain could lead to local energetic preference for a different nucleation layer at a particular location.

Interactions between nucleation mechanisms are also possible in films with the *c* axis inclined to the film growth direction. Non-(100) perovskite substrates often have rough surfaces and may undergo faceting at film growth temperatures. The predeposition of an epitaxial bottom electrode can also yield a rough surface. This roughness would be expected to increase the nucleation of OPBs due to the steric mechanism, described in Sec. III. D. 2, but not in all cases. An unfaulted region of $SrBi_2Nb_2O_9$ has grown over a very rough $(110)_P$ $SrRuO_3$ bottom electrode in Fig. 27(a). Even though the surface has a high density of step edges, no OPBs were nucleated. In this case, the high degree of roughness may have functioned to relieve lattice mismatch strain by introducing a limited amount of structural disorder at the interface.

Roughness at internal boundaries can also lead to OPB generation. The roughness of a growth twin boundary in $SrBi_2Nb_2O_9$/(110) $SrTiO_3$ has resulted in the generation of two OPBs in Fig. 27(b). It is not the step-edge nucleation mechanism, however, that has caused the fault, but structural and lattice mismatch between the (001) and (110) planes of $SrBi_2Nb_2O_9$ as they met at the growth twin boundary, indicated by the presence of strain contrast at the nucleation sites of the two OPBs. OPBs nucleated by a simple step-edge do not typically have a large associated strain field. The large *c*-plane facet on the left side of the twin boundary presents essentially a cubic perovskite surface. It is possible to envision some cases where this would not be a significant source of OPBs, for example in a layered cuprate, with crystallographic units that are approximately equal in their *a*, *b*, and *c* lattice parameters.

A similar interaction of nucleation mechanisms has generated the complex defect structure in a $SrBi_2Nb_2O_9$ film that is pictured in Fig. 28(a) and shown schematically in Fig. 28(d). Once again, a rough $SrRuO_3$ surface has nucleated few OPBs. At the bottom right of the image (near the substrate), a large growth twin has overgrown a differently oriented growth twin in the early stages of growth, providing a square perovskite surface. In this case, the surface mesh mismatch has resulted in the generation of a pair of closely correlated *c*-axis stacking faults, shown clearly in the magnified region in Fig. 28(b), in both cases indicated by white arrows. Near the center of Fig. 28(a), one stacking fault jogs along an OPB to intersect the other, shown magnified in Fig. 28(c), with the OPB indicated by black arrows and a brace, and the stacking fault again indicated by white arrows. Soon after, the large combined stacking fault jogs to form an OPB with the same *c*-axis offset, which continues through the full thickness of the film, shown previously in Fig. 24(c). Incidentally, another pair of stacking faults lies at the bottom left of Fig. 28(a), with one jogging along an OPB to join the other. They also soon terminate in this typical fashion.

The stacking fault in Fig. 28 appears to consist of extra perovskite crystallographic units. Charge imbalance of such a stacking fault in $SrBi_2Nb_2O_9$ could be compensated by crystallographic shear to yield edge-sharing niobium octahedra at the fault. This configuration, however, would create an antiphase relationship along *a* and *b* for material after the stacking fault. For a pair of such faults, only the region between the faults would have this antiphase relationship with the surrounding crystal, so it seems reasonable that these stacking faults are observed in a closely correlated pair, and that lone stacking faults are rarely observed. Once the two individual stacking faults combine into a larger stacking fault, in-phase in the *a-b* plane, it terminates quickly due to its difference in stoichiometry from the arriving material in the laser plume.

IV. CONCLUSIONS

OPBs are prevalent in epitaxial films of layered complex oxides due to their high anisotropy and to the constraints of epitaxial film growth. The general morphology of OPBs in two prototypical homologous series of layered oxides, Aurivillius and Ruddlesden–Popper phases, has been described. The density of OPB defects in films has been correlated to XRD peak splitting, providing a simple method for estimating the relative OPB density in films. The atomic-scale structure of OPBs in these systems has also been determined in two systems and has been found to be non-stoichiometric in both. The mechanisms of OPB nucleation in layered complex oxide systems have been described in detail with examples. The primary mechanisms are nucleation layer, steric, *a-b* misfit, and inclined-*c* misfit. The secondary mechanism is by

crystallographic shear due to the loss of a volatile component. Numerous open questions in the area have been described.

ACKNOWLEDGMENTS

The authors gratefully acknowledge the financial support of the United States Department of Energy (US DOE) through Grant No. DE-FG02-03ER46063, the National Academy of Sciences through the National Research Council Fellowship Program for the work performed at NIST, and, for the work performed at ANL, the US DOE through Contract No. W-31-109-ENG-38. The authors also thank the following people for helpful discussions: Michael A. O'Keefe, Terrence Mitchell, Oliver Eibl, Karl Spear, Dietrich Hesse, Roar Kilaas, Dean Miller, Nicola Spaldin, Hiroshi Funakubo, and Stephen C. Moss. TEM analysis was performed at the Materials Characterization Laboratory at the Pennsylvania State University, the Electron Microscopy Collaborative Research Center at ANL, the Electron Microbeam Analysis Laboratory at the University of Michigan at Ann Arbor, and the Electron Microscopy Facility at NIST.

REFERENCES

1. B. Aurivillius: Mixed bismuth oxides with layer lattices I. The structure type of $CaNb_2Bi_2O_9$. *Ark. Kemi.* **1,** 463 (1950).
2. B. Aurivillius: Mixed bismuth oxides with layer lattices II. Structure of $Bi_4Ti_3O_{12}$. *Ark. Kemi.* **1,** 499 (1950).
3. B. Aurivillius: Mixed bismuth oxides with layer lattices III. Structure of $BaBi_4Ti_4O_{15}$. *Ark. Kemi.* **2,** 519 (1951).
4. B. Aurivillius: The structure of Bi_2NbO_5F and isomorphous compounds. *Ark. Kemi.* **5,** 39 (1953).
5. B. Aurivillius and P.H. Fang: Ferroelectricity in the compound $Ba_2Bi_4Ti_5O_{18}$. *Phys. Rev.* **126,** 893 (1962).
6. S.N. Ruddlesden and P. Popper: New compounds of the K_2NiF_4 type. *Acta Crystallogr.* **10,** 538 (1957).
7. S.N. Ruddlesden and P. Popper: The compound $Sr_3Ti_2O_7$ and its structure. *Acta Crystallogr.* **11,** 54 (1958).
8. H. Müller-Buschbaum: The crystal chemistry of high-temperature oxide superconductors and materials with related structures. *Angew. Chem. Int. Ed. Engl.* **28,** 1472 (1989).
9. J.G. Bednorz, K.A. Müller, and M. Takashige: Superconductivity in alkaline earth-substituted La_2CuO_{4-y}. *Science* **236,** 73 (1987).
10. S. Jin, T.H. Tiefel, M. McCormack, R.A. Fastnacht, R. Ramesh, and L.H. Chen: Thousandfold change in resistivity in magnetoresistive La–Ca–Mn–O films. *Science* **264,** 413 (1994).
11. E.C. Subbarao: A family of ferroelectric bismuth compounds. *J. Phys. Chem. Solids* **23,** 665 (1962).
12. R.A. Mohan Ram, L. Ganapathi, P. Ganguly, and C.N.R. Rao: Evolution of three-dimensional character across the $La_{n+1}Ni_nO_{3n+1}$ homologous series with increase in *n*. *J. Solid State Chem.* **63,** 139 (1986).
13. K.D. Otzschi, D.A. Vander Griend, K.R. Poppelmeier, W. Sinkler, L.D. Marks, and T.O. Mason: Close relationships between doping and layering in pure perovskite. *Chem. Mater.* **10,** 2579 (1998).
14. W. Tian, J.H. Haeni, D.G. Schlom, E. Hutchinson, B.L. Sheu, M.M. Rosario, P. Schiffer, Y. Liu, M.A. Zurbuchen, and X.Q. Pan: Epitaxial growth and magnetic properties of the first five members of the layered $Sr_{n+1}Ru_nO_{3n+1}$ oxide series. *Appl. Phys. Lett.* **90,** 225071 (2007).
15. P.B. Braun: The crystal structures of a new group of ferromagnetic compounds. *Philips Res. Rep.* **12,** 491 (1957).
16. J.S. Anderson and J.L. Hutchison: The study of long-range order in hexagonal barium ferrite layer structures. *Contemp. Phys.* **16,** 443 (1975).
17. D.R. Veblen: Polysomatism and polysomatic series: A review and applications. *Am. Mineral.* **76,** 801 (1991).
18. R.E. Newnham, R.W. Wolfe, and J.F. Dorrian: Structural basis of ferroelectricity in the bismuth titanate family. *Mater. Res. Bull.* **6,** 1029 (1971).
19. A.D. Rae, J.G. Thompson, R.L. Withers, and A.C. Willis: Structure refinement of commensurately modulated bismuth titanate, $Bi_4Ti_3O_{12}$. *Acta Crystallogr. B* **46,** 474 (1990).
20. H. Shaked, J.D. Jorgensen, O. Chmaissem, S. Ikeda, and Y. Maeno: Neutron diffraction study of the structural distortions in $Sr_3Ru_2O_7$. *J. Solid State Chem.* **154,** 361 (2000).
21. M.K. Crawford, R.L. Harlow, W. Marshall, Z. Li, G. Cao, R.L. Lindstrom, Q. Huang, and J.W. Lynn: Structure and magnetism of single crystal $Sr_4Ru_3O_{10}$: A ferromagnetic triple-layer ruthenate. *Phys. Rev. B* **65,** 214412 (2002).
22. R. Kiyanagi, K. Tsuda, N. Aso, H. Kimura, Y. Noda, Y. Yoshida, S-I. Ikeda, and Y. Uwatoko: Investigations of the structure of single crystal $Sr_3Ru_2O_7$ by neutron and convergent beam electron diffractions. *J. Phys. Soc. Jpn.* **73,** 639 (2004).
23. M.A. Zurbuchen, J. Schubert, Y. Jia, D.J. Comstock, W. Tian, V.O. Sherman, D. Fong, M.E. Hawley, A.K. Tagantsev, S.K. Streiffer, and D.G. Schlom: Charge-mediated synthesis of $Sr_4Bi_4Ti_7O_{24}$. (2007, unpublished).
24. M. Dion, M. Ganne, and M. Tournoux: New family of phases $M^{I}M_2^{II}Nb_3O_{10}$ sheet perovskites. *Mater. Res. Bull.* **16,** 1429 (1981).
25. A.J. Jacobson, J.T. Lewandowski, and J.W. Johnson: Ion exchange of the layered perovskite $KCa_2Nb_3O_{10}$ by protons. *J. Less-Common Met.* **116,** 137 (1986).
26. J. Gopalakrishnan, V. Bhat, and B. Raveau: $LaNb_2O_7$: A new series of layered perovskites exhibiting ion exchange and intercalation behavior. *Mater. Res. Bull.* **22,** 413 (1987).
27. F. Santoro, F. Beech, M. Marezio, and R.J. Cava: Crystal chemistry of superconductors: A guide to the tailoring of new compounds. *Physica C* **156,** 693 (1988).
28. Y. Tokura and T. Arima: New classification method for layered copper oxide compounds and its application to design of new high T_c superconductors. *Jpn. J. Appl. Phys.* **29,** 2388 (1990).
29. J. Hauck and K. Mika: Structure families of superconducting oxides and interstitial alloys. *Supercond. Sci. Technol.* **11,** 614 (1998).
30. K.R. Udayakumar and A.N. Cormack: Non-stoichiometry in alkaline earth excess alkaline earth titanates. *J. Amer. Ceram. Soc.* **71,** C469 (1988).
31. W. Tian, X.Q. Pan, J.H. Haeni, and D.G. Schlom: Transmission-electron-microscopy study of $n = 1$–5 $Sr_{n+1}Ti_nO_{3n+1}$ epitaxial thin films. *J. Mater. Res.* **16,** 2013 (2001).
32. J.S. Anderson: Non-stoichiometric and ordered phases: Thermodynamic considerations, in *The Chemistry of Extended Defects in Non-metallic Solids: Proceedings of the Institute for Advanced Study on the Chemistry of Extended Defects in Non-metallic Solids*, edited by L. Eyring and M. O'Keefe (North-Holland, Amsterdam, The Netherlands, 1970), pp. 1–20.
33. L.A. Bursill: The titanium and titanium-chromium oxide systems and swinging shear planes, in *Solid State Chemistry: Proceedings of the 5th Materials Research Symposium,* edited by R.S.

Roth and S.J. Schneider (NBS Special Publication **364,** Gaithersburg, MD, 1972), p. 727.
34. J.G. Allpress: Crystallographic shear in $WO_3 \cdot xNb_2O_5$ (x = 0.03–0.09). *J. Solid State Chem.* **4,** 173 (1972).
35. A.D. Wadsley and S. Andersson: Crystallographic shear and the niobium oxides and oxide fluorides in the composition region MX_x, $2.4 < x < 2.7$, in *Perspectives in Structural Chemistry,* Vol. 3, edited by J.D. Dunitz and J.A. Ibers (Wiley, New York, 1970) pp. 1–58.
36. O. Yu Gorbenko, S.V. Samoilenkov, I.E. Graboy, and A.R. Kaul: Epitaxial stabilization of oxides in thin films. *Chem. Mater.* **14,** 4026 (2002).
37. D.G. Schlom, A.F. Marshall, J.T. Sizemore, Z.J. Chen, J.N. Eckstein, I. Bozovic, K.E. von Dessonneck, J.S. Harris, and J.C. Bravman: Molecular-beam epitaxial-growth of layered Bi–Sr–Ca–Cu–O compounds. *J. Cryst. Growth* **102,** 361 (1990).
38. R. Seshadri, M. Hervieu, C. Martin, A. Maignan, B. Domenges, B. Raveau, and A.N. Fitch: Study of the layered magnetoresistive perovskite $La_{1.2}Sr_{1.8}Mn_2O_7$ by high-resolution electron microscopy and synchrotron x-ray powder diffraction. *Chem. Mater.* **9,** 1778 (1997).
39. D.G. Schlom, J.H. Haeni, J. Lettieri, C.D. Theis, W. Tian, J.C. Jiang, and X.Q. Pan: Oxide nano-engineering using MBE. *Mater. Sci. Eng., B* **87,** 282 (2001).
40. J.H. Haeni, C.D. Theis, D.G. Schlom, W. Tian, X.Q. Pan, H. Chang, I. Takeuchi, and X.D. Xiang: Epitaxial growth of the first five members of the $Sr_{n+1}Ti_nO_{3n+1}$ Ruddlesden–Popper homologous series. *Appl. Phys. Lett.* **78,** 3292 (2001).
41. M.A. Zurbuchen, Y. Jia, S.K. Knapp, A.H. Carim, D.G. Schlom, L-N. Zou, and Y. Liu: Suppression of superconductivity by crystallographic defects in epitaxial Sr_2RuO_4 films. *Appl. Phys. Lett.* **78,** 2351 (2001).
42. M.A. Zurbuchen, D.G. Schlom, and S.K. Streiffer: Comment on "High-resolution electron microscopy investigations on stacking faults in $SrBi_2Ta_2O_9$ ferroelectric thin films" [Appl. Phys. Lett. 78, 973 (2001)]. *Appl. Phys. Lett.* **79,** 887 (2001).
43. J.M. Cowley: Short-range order and long-range order parameters. *Phys. Rev. A* **138,** 1384 (1965).
44. J.G. Allpress: The direct observation of structural features and defects in complex oxides by two-dimensional lattice imaging. *Mater. Res. Bull.* **4,** 707 (1969).
45. J.G. Allpress and J.V. Sanders: n-beam lattice images of complex oxides, in *Electron Microscopy and Structure of Materials, Proceedings of the Fifth International Materials Symposium,* edited by G. Thomas, R.M. Fulrath, and R.M. Fisher (University of California Press, Berkeley, CA, 1972), p. 134.
46. J.G. Allpress: The application of electron optical techniques to high temperature materials, in *Solid State Chemistry: Proceedings of the 5th Materials Research Symposium,* edited by R.S. Roth and S.J. Schneider (NBS Special Publication **364,** Gaithersburg, MD, 1972), p. 87.
47. J.L. Hutchison, J.S. Anderson, and C.N.R. Rao: Electron microscopy of ferroelectric bismuth oxides containing perovskite layers. *Proc. R. Soc. London A* **355,** 301 (1977).
48. N.S. Prasad and K.B.R. Varma: Structural and dielectric properties of ferroelectric $Sr_{1-x}Ba_xBi_2(Nb_{0.5}Ta_{0.5})_2O_9$ and $Sr_{0.5}Ba_{0.5}Bi_2(Nb_{1-y}Ta_y)_2O_9$ ceramics. *Mater. Res. Bull.* **38,** 195 (2003).
49. H. Xu, D.R. Veblen, and G. Luo: A new commensurate modulated structure in orthoclase. *Acta Crystallogr. A* **51,** 53 (1995).
50. J. Mannhart, D. Anselmetti, J.G. Bednorz, A. Catana, C. Gerber, K.A. Muller, and D.G. Schlom: Correlation between J_c and screw dislocation density in sputtered $YBa_2Cu_3O_{7-\delta}$ films. *Z. Phys. B* **86,** 177 (1992).
51. B. Dam, J.M. Huijbregtse, F.C. Klaassen, R.C.F. van der Geest, G. Doornbos, J.H. Rector, A.M. Testa, S. Freisem, J.C. Martinez, B. Stäuble-Pümpin, and R. Griessen: Origin of critical currents in $YBa_2Cu_3O_{7-\delta}$ superconducting thin films. *Nature* **399,** 439 (1999).
52. B.M. Lairson, S.K. Streiffer, and J.C. Bravman: Vortex pinning and twin boundaries in $YBa_2Cu_3O_{7-\delta}$ thin films. *Phys. Rev. B* **42,** 10067 (1990).
53. G. Rijnders, S. Currás, M. Huijben, D.H. Blank, and H. Rogalla: Influence of substrate-film interface engineering on the superconducting properties of $YBa_2Cu_3O_{7-\delta}$. *Appl. Phys. Lett.* **84,** 1150 (2004).
54. M.A. Zurbuchen, G. Asayama, D.G. Schlom, and S.K. Streiffer: Ferroelectric domain structure of $SrBi_2Nb_2O_9$ epitaxial thin films. *Phys. Rev. Lett.* **88,** 107601 (2002).
55. M.A. Zurbuchen, J. Lettieri, S.J. Fulk, Y. Jia, A.H. Carim, D.G. Schlom, and S.K. Streiffer: Bismuth volatility effects on the perfection of $SrBi_2Nb_2O_9$ and $SrBi_2Ta_2O_9$ films. *Appl. Phys. Lett.* **82,** 4711 (2003).
56. M-W. Chu, I. Szafraniak, R. Scholz, C. Harnagea, D. Hesse, M. Alexe, and U. Gösele: Impact of misfit dislocations on the polarization instability of epitaxial nanostructured ferroelectric perovskites. *Nat. Mater.* **3,** 87 (2004).
57. A. Boulle, R. Guinebretiere, and A. Dauger: Highly localized strain fields due to planar defects in epitaxial $SrBi_2Nb_2O_9$. *J. Appl. Phys.* **97,** 073503 (2005).
58. Q.D. Jiang and J. Zegenhagen: $SrTiO_3$ (001) surfaces and growth of ultrathin $GdBa_2Cu_3O_{7-x}$ films studied by LEED/AES and UHV-STM. *Surf. Sci.* **338,** L882 (1995).
59. T. Haage, J. Zegenhagen, H-U. Habermeier, and M. Cardona: Nucleation mechanism of $YBa_2Bu_3O_{7-\delta}$ on $SrTiO_3$ (001). *Phys. Rev. Lett.* **80,** 4225 (1998).
60. S. Bals, G. Rijnders, D.H.A. Blank, and G. Van Tendeloo: TEM of ultra-thin $DyBa_2Cu_3O_{7-x}$ films deposited on TiO_2-terminated $SrTiO_3$. *Physica C* **355,** 225 (2001).
61. J.G. Wen, C. Traeholt, and H.W. Zandbergen: Stacking sequence of $YBa_2Cu_3O_7$ thin film on $SrTiO_3$ substrate. *Physica C* **205,** 354 (1993).
62. H.W. Zandbergen, E. Connolly, I.E. Graboy, V.L. Svetchnikov, and A.R. Kaul: HREM characterisation of interfaces in $YBa_2Cu_3O_{7-\delta}/CeO_2/R\text{-}Al_2O_3$ structures. *Physica C* **329,** 37 (2000).
63. C.D. Theis, J. Yeh, D.G. Schlom, M.E. Hawley, and G.W. Brown: The influence of vicinal $SrTiO_3$ surfaces on the growth and ferroelectric properties of epitaxial $Bi_4Ti_3O_{12}$ thin films. *Mater. Sci. Eng., B* **56,** 228 (1998).
64. X.Q. Pan, J.C. Jiang, C.D. Theis, and D.G. Schlom: Domain structure of epitaxial $Bi_4Ti_3O_{12}$ thin films grown on (001) $SrTiO_3$. *Appl. Phys. Lett.* **83,** 2315 (2003).
65. D. Hesse, N.D. Zakharov, A. Pignolet, A.R. James, and S. Senz: TEM cross-section investigations of epitaxial $Ba_2Bi_4Ti_5O_{18}$ thin films on $LaNiO_3$ bottom electrodes on CeO_2/YSZ-buffered Si(100). *Cryst. Res. Technol.* **35,** 641 (2000).
66. M.A. Zurbuchen, J. Lettieri, Y. Jia, A.H. Carim, S.K. Streiffer, and D.G. Schlom: Out-of-phase boundary (OPB) nucleation in layered oxides, in *Ferroelectric Thin Films XIII*, edited by R. Ramesh, J-P. Maria, M. Alexe, and V. Joshi (Mater. Res. Soc. Symp. Proc. **902E,** Warrendale, PA, 2006), T10-55.1.
67. K. Takahashi, M. Suzuki, M. Yoshimoto, and H. Funakubo: Growth behavior of c-axis oriented epitaxial $SrBi_2Ta_2O_9$ films on $SrTiO_3$ substrates with atomic scale step structure. *Jpn. J. Appl. Phys.* **45,** L138 (2006).
68. R. Ramesh, A. Inam, D.M. Hwang, T.S. Ravi, T. Sands, X.X. Xi, X.D. Wu, Q. Li, T. Venkatesan, and R. Kilaas: The atomic structure of growth interfaces in Y–Ba–Cu–O thin films. *J. Mater. Res.* **6,** 2264 (1991).

69. P.C. McIntyre, M.J. Cima, and A. Roshko: The effects of substrate surface steps on the microstructure of epitaxial $Ba_2YCu_3O_{7-x}$ thin films on (001) $LaAlO_3$. *J. Cryst. Growth* **149,** 64 (1995).
70. O.Y. Gorbenko, I.E. Graboy, A.R. Kaul, and H.W. Zandbergen: HREM and XRD characterization of epitaxial perovskite manganites. *J. Magn. Magn. Mater.* **211,** 97 (2000).
71. M. Salluzzo, C. Aruta, I. Maggio-Aprile, Ø. Fischer, S. Bals, and J. Zegenhagen: Growth of $R_{1+x}Ba_{2-x}Cu_3O_{7-\delta}$ epitaxial films investigated by in situ scanning tunneling microscopy. *Phys. Status Solidi A* **186,** 339 (2001).
72. S. Bals, G. Van Tendeloo, M. Salluzzo, and I. Maggio-Aprile: Why are sputter deposited $Nd_{1+x}Ba_{2-x}Cu_3O_{7\text{-delta}}$ thin films flatter than $NdBa_2Cu_3O_{7-\delta}$ films? *Appl. Phys. Lett.* **79,** 3660 (2001).
73. L.A. Tietz, C.B. Carter, D.K. Lanthrop, S.E. Russek, R.A. Burnham, and J.R. Michael: Crystallography of $YBa_2Cu_3O_{6+x}$ thin film-substrate interfaces. *J. Mater. Res.* **4,** 1072 (1989).
74. M.A. Zurbuchen, Y. Jia, S. Knapp, A.H. Carim, D.G. Schlom, and X.Q. Pan: Defect generation by preferred nucleation in epitaxial Sr_2RuO_4 / $LaAlO_3$. *Appl. Phys. Lett.* **83,** 3891 (2003).
75. M.A. Zurbuchen, J. Lettieri, Y. Jia, D.G. Schlom, S.K. Streiffer, and M.E. Hawley: Transmission-electron-microscopy study of (103)-oriented epitaxial $SrBi_2Nb_2O_9$ films grown on (111) $SrTiO_3$ and (111) $SrRuO_3$ / (111) $SrTiO_3$. *J. Mater. Res.* **16,** 489 (2001).
76. S. Madhavan, D.G. Schlom, A. Dabkowski, H.A. Dabkowska, and Y. Liu: Growth of epitaxial *a*-axis and *c*-axis oriented Sr_2RuO_4 films. *Appl. Phys. Lett.* **68,** 559 (1996).
77. Y. Liu, J.A. Mitchell, S. Madhavan, D.G. Schlom, A. Dabkowski, and H.A. Dabkowska: Electrical transport studies of epitaxial Sr_2RuO_4 films. *Czech. J. Phys.* **46,** 1113 (1996).
78. D.G. Schlom, Y. Jia, L-N. Zou, J.H. Haeni, S. Briczinski, M.A. Zurbuchen, C.W. Leitz, S. Madhavan, S. Wozniak, Y. Liu, M.E. Hawley, G.W. Brown, A. Dabkowski, H.A. Dabkowska, R. Uecker, and P. Reiche: Searching for superconductivity in epitaxial films of copper-free layered oxides with the K_2NiF_4 structure, in *Superconducting and Related Oxides: Physics and Nanoengineering III*, edited by D. Pavuna and I. Bozovic (SPIE Vol. **3481,** Bellingham, WA, 1998), pp. 226–240.
79. J. Lettieri, Y. Jia, S.J. Fulk, D.G. Schlom, M.E. Hawley, and G.W. Brown: Optimization of the growth of epitaxial $SrBi_2Ta_2O_9$ thin films by pulsed laser deposition. *Thin Solid Films* **379,** 64 (2000).
80. J.C. Clark, J-P. Maria, K.J. Hubbard, and D.G. Schlom: An oxygen-compatible radiant substrate heater for thin film growth at substrate temperatures up to 1050 degrees C. *Rev. Sci. Instrum.* **68,** 2538 (1997).
81. M.J. Hÿtch, E. Snoeck, and R. Kilaas: Quantitative measurement of displacement and strain fields from HREM micrographs. *Ultramicroscopy* **74,** 131 (1998).
82. R. Ramesh, D.M. Hwang, J.B. Barner, L. Nazar, T.S. Ravi, A. Inam, B. Dutta, X.D. Wu, and T. Venkatesan: Defect structure of laser deposited Y–Ba–Cu–O thin films on single crystal MgO substrate. *J. Mater. Res.* **5,** 704 (1990).
83. T. Suzuki, Y. Nishi, M. Fujimoto, K. Ishikawa, and H. Funakubo: Interface and defect structures of (001)-oriented $SrBi_2Ta_2O_9$ thin film epitaxially grown on (001) $SrTiO_3$ single crystal. *Jpn. J. Appl. Phys., Part 2* **38,** L1261 (1999).
84. T. Suzuki, Y. Nishi, M. Fujimoto, K. Ishikawa, and H. Funakubo: Interface and domain structures of (116)-oriented $SrBi_2Ta_2O_9$ thin film epitaxially grown on (110) $SrTiO_3$ single crystal. *Jpn. J. Appl. Phys., Part 2* **38,** L1265 (1999).
85. J.H. Choi, J.Y. Lee, and Y.T. Kim: High-resolution transmission-electron-microscopy study on the solid-phase crystallization of amorphous $SrBi_2Ta_2O_9$ thin films on Si. *J. Cryst. Growth* **223,** 161 (2001).
86. O. Eibl: Crystal defects in $Bi_2Sr_2Ca_{n-1}Cu_nO_{4+2n+\delta}$ ceramics. *Physica C* **168,** 249 (1990).
87. R. Ramesh, A. Inam, B. Wilkens, W.K. Chan, T. Sands, D.K. Fork, T.H. Geballe, J. Evans, and J. Bullington: Ferroelectric bismuth titanate/superconductor (Y–Ba–Cu–O) thin-film heterostructures on silicon. *Appl. Phys. Lett.* **59,** 1782 (1991).
88. R. Ramesh, K. Luther, B. Wilkens, D.L. Hart, E. Wang, J.M. Tarascon, A. Inam, X.D. Wu, and T. Venkatesan: Epitaxial growth of ferroelectric bismuth titanate thin films by pulsed laser deposition. *Appl. Phys. Lett.* **57,** 1505 (1990).
89. S. Horiuchi, T. Kikuchi, and M. Goto: Structure determination of a mixed-layer bismuth titanate, $Bi_7Ti_4NbO_{21}$, by super-high-resolution electron microscopy. *Acta Crystallogr. A* **33,** 701 (1977).
90. M-W. Chu, M. Ganne, M.T. Caldes, and L. Brohan: X-ray photoelectron spectroscopy and high resolution electron microscopy studies of Aurivillius compounds: $Bi_{4-x}La_xTi_3O_{12}$ ($x = 0$, 0.5, 0.75, 1.0, 1.5, and 2.0). *J. Appl. Phys.* **91,** 3178 (2002).
91. M. Gilloux-Viry, J-R. Duclere, A. Perrin, J-Y. Laval, and A. Dubon: Evidence of intergrowth in $SrBi_2Nb_2O_9$ (SBN) thin films grown by PLD on (100) $SrTiO_3$ in relation with the composition. *Appl. Surf. Sci.* **186,** 391 (2002).
92. M.A. Zurbuchen: Transmission electron microscopy investigation of defects and domains in epitaxial films of Aurivillius and Ruddlesden–Popper phases, Ph.D. Dissertation, The Pennsylvania State University, University Park, PA (2002).
93. B.E. Warren: *X-ray Diffraction* (Addison-Wesley, Menlo Park, 1969), pp. 216–227.
94. A. Malachias, T.U. Schülli, G. Medeiros-Ribeiro, L.G. Cançado, M. Stoffel, O.G. Schmidt, T.H. Metzger, and R. Magalhaes-Paniago: X-ray study of atomic ordering in self-assembled Ge islands grown on Si(001). *Phys. Rev. B* **72,** 165315 (2005).
95. H. Tabata, H. Tanaka, and T. Kawai: Formation of Bi-based layered perovskite oxide films by a laser ablation technique. *Jpn. J. Appl. Phys., Part 1* **34,** 5146 (1995).
96. K. Ishikawa, N. Nukaga, and H. Funakubo: Metalorganic chemical vapor deposition of epitaxial $SrBi_2Ta_2O_9$ thin films and their crystal structure. *Jpn. J. Appl. Phys., Part 2* **38,** L258 (1999).
97. K. Saito, K. Ishikawa, A. Saiki, I. Yamaji, T. Akai, and H. Funakubo: Residual strain analysis of epitaxial grown SBT thin films prepared by MOCVD. *Integr. Ferroelectrics* **33,** 59 (2001).
98. T.K. Song, J-K. Lee, and H.J. Jung: Structural and ferroelectric properties of the *c*-axis oriented $SrBi_2Ta_2O_9$ thin films deposited by the radio-frequency magnetron sputtering. *Appl. Phys. Lett.* **69,** 3839 (1996).
99. K. Ishikawa and H. Funakubo: Electrical properties of (001)- and (116)-oriented epitaxial $SrBi_2Ta_2O_9$ thin films prepared by metalorganic chemical vapor deposition. *Appl. Phys. Lett.* **75,** 1970 (1999).
100. H.N. Lee, S. Senz, N.D. Zakharov, C. Harnagea, A. Pignolet, D. Hesse, and U. Gösele: Growth and characterization of non-*c*-oriented epitaxial ferroelectric $SrBi_2Ta_2O_9$ films on buffered Si(100). *Appl. Phys. Lett.* **77,** 3260 (2000).
101. J. Lettieri, M.A. Zurbuchen, Y. Jia, D.G. Schlom, S.K. Streiffer, and M.E. Hawley: Epitaxial growth of $SrBi_2Nb_2O_9$ on (110) $SrTiO_3$ and the establishment of a lower bound on the spontaneous polarization of $SrBi_2Nb_2O_9$. *Appl. Phys. Lett.* **77,** 3090 (2000).
102. H.N. Lee, A. Visinoiu, S. Senz, C. Harnagea, A. Pignolet, D. Hesse, and U. Gösele: Epitaxial growth of non-*c*-oriented ferroelectric $SrBi_2Ta_2O_9$ thin films on Si(100) substrates. *J. Appl. Phys., Part 1* **88,** 6658 (2000).
103. K. Ishikawa, H. Funakubo, K. Saito, T. Suzuki, Y. Nishi, and

M. Fujimoto: Crystal structure and electrical properties of epitaxial $SrBi_2Ta_2O_9$ films. *J. Appl. Phys.* **87,** 8018 (2000).
104. G. Kong, M.O. Jones, J.S. Abell, P.P. Edwards, S.T. Lees, K.E. Gibbons, I. Gameson, and M. Aindow: Microstructure of laser-ablated superconducting $La_2CuO_4F_x$ thin films on $SrTiO_3$. *J. Mater. Res.* **16,** 3309 (2001).
105. T. Takeuchi, T. Tani, and T. Satoh: Microcomposite particles $Sr_3Ti_2O_7$–$SrTiO_3$ with an epitaxial core-shell structure. *Solid State Ionics* **108,** 67 (1998).
106. R.J.D. Tilley: An electron microscope study of perovskite-related oxides in the Sr–Ti–O system. *J. Solid State Chem.* **21,** 293 (1977).
107. T. Williams, F. Lichtengerg, A. Reller, and G. Bednorz: New layered perovskites in the Sr-Ru-O system: A transmission electron microscope study. *Mater. Res. Bull.* **26,** 763 (1991).
108. K. Hawkins and T.J. White: Defect structure and chemistry of $(Ca_xSr_{1-x})_{n+1}Ti_nO_{3n+1}$ layer perovskites. *Philos. Trans. R. Soc. London, Sec. A.* **336,** 541 (1991).
109. M. Ceh, V. Krasevec, and D. Kolar: A transmission electron microscope study of SrO-doped $CaTiO_3$. *J. Solid State Chem.* **103,** 263 (1993).
110. R. Seshadri, M. Hervieu, C. Martin, A. Maignan, B. Domenges, and B. Raveau: Study of the layered magnetostrictive perovskite $La_{1.2}Sr_{1.8}Mn_2O_7$ by high-resolution electron microscopy and synchrotron x-ray powder diffraction. *Chem. Mater.* **9,** 1778 (1997).
111. M.A. McCoy, R.W. Grimes, and W.E. Lee: Phase stability and interfacial structures in the SrO–$SrTiO_3$ system. *Philos. Mag. A* **75,** 833 (1997).
112. J. Sloan, P.D. Battle, M.A. Green, M.J. Rosseinsky, and J.F. Vente: A HRTEM study of the Ruddlesden–Popper compositions $Sr_2LnMn_2O_7$ (*Ln* = Y, La, Nd, Eu, Ho). *J. Solid State Chem.* **138,** 135 (1998).
113. M. Fujimoto, J. Tanaka, and S. Shirasaki: Planar faults and grain boundary precipitation in non-stoichiometric $(Sr,Ca)TiO_3$ ceramics. *Jpn. J. Appl. Phys.* **27,** 1162 (1988).
114. M. Ceh and D. Kolar: Solubility of CaO in $CaTiO_3$. *J. Mater. Sci.* **29,** 6295 (1994).
115. M. Rühle, A. Recnik, and M. Ceh: Chemistry and structure of internal interfaces in inorganic materials, in *Solid-State Chemistry of Inorganic Materials,* edited by P.K. Davies, A.J. Jacobson, C.C. Torardi, and T.A. Vanderah (Mater. Res. Soc. Symp. Proc. **453,** Pittsburgh, PA, 1997), p. 673.
116. M. Fujimoto, T. Suzuki, Y. Nishi, and K. Arai: Calcium-ion selective site occupation at Ruddlesden–Popper-type faults and the resultant dielectric properties of *A*-site-excess strontium-calcium titanate ceramics. *J. Am. Ceram. Soc.* **81,** 33 (1998).
117. T. Suzuki, Y. Nishi, and M. Fujimoto: Defect structure in homoepitaxial non-stoichiometric strontium titanate thin films. *Philos. Mag. A* **80,** 621 (2000).
118. C.N.R. Rao and B. Raveau: *Transition Metal Oxides: Structure, Properties, and Synthesis of Ceramic Oxides*, 2nd ed. (Wiley, New York, 1998), p. 61.
119. R. Dinu, M. Dinescu, J.D. Pedarnig, R.A. Gunasekaran, D. Bäuerle, S. Bauer-Gogonea, and S. Bauer: Film structure and ferroelectric properties of in situ grown $SrBi_2Ta_2O_9$ films. *Appl. Phys. A* **69,** 55 (1999).
120. Y-B. Park, S-M. Jang, J-K. Lee, and J-W. Park: Influence of second phases on the ferroelectric properties of $SrBi_2TaNbO_9$ thin films fabricated by radio-frequency magnetron sputtering. *J. Vac. Sci. Technol. A* **18,** 17 (2000).
121. J.M. Cowley: *The Chemistry of Extended Defects in Non-metallic Solids*: *Proceedings of the Institute for Advanced Study on the Chemistry of Extended Defects in Non-Metallic Solids, April, 1969*, edited by L. Eyring and M. O'Keefe (North-Holland, Amsterdam, The Netherlands, 1970), p. 259.
122. Y. Ding, J.S. Liu, J.S. Zhu, and Y.N. Wang: Stacking faults and their effects on ferroelectric properties in strontium bismuth tantalate. *J. Appl. Phys.* **91,** 2255 (2002).
123. Y. Yan, M.M. Al-Jassim, Z. Xu, X. Lu, D. Viehland, M. Payne, and S.J. Pennycook: Structure determination of a planar defect in $SrBi_2Ta_2O_9$. *Appl. Phys. Lett.* **75,** 1961 (1999).
124. A. Boulle, C. Legrand, R. Guinebretiere, J.P. Mercurio, and A. Dauger: Planar faults in Aurivillius compounds: An x-ray diffraction study. *Philos. Mag. A* **82,** 615 (2002).
125. I. Barin: *Thermochemical Data of Pure Substances*, 3rd ed. (John Wiley and Sons, Hoboken, NJ, 1995).
126. F.C. Frank: The growth of carborundum: Dislocations and polytypism. *Philos. Mag.* **42,** 1014 (1954).
127. M.A. Zurbuchen, J. Schubert, Y. Jia, D.J. Comstock, W. Tian, D. Fong, M.E. Hawley, S.K. Streiffer, and D.G. Schlom: Electron microscopy study of $(Sr_4Bi_4)Ti_7O_{24}$. (2006, unpublished).
128. H.P. Strunk: Edge dislocation may cause growth spirals. *J. Cryst. Growth* **160,** 184 (1996).
129. J.C. Fisher, R.L. Fullman, and G.W. Sears: The relation of the disordering of a superlattice to the melting of the disordered alloy. *Acta Metall.* **2,** 344 (1954).
130. G.G. Lemmlein and E.D. Dukova: Formation of screw dislocations in the growth process of a crystal. *Sov. Phys. Crystallogr.* **1,** 269 (1956).
131. M.I. Kozlovskii: Formation of screw dislocations in the growth of a crystal around solid particles. *Sov. Phys. Crystallogr.* **3,** 2006 (1958).
132. M.I. Kozlovskii: Formation of screw dislocations at the junction of two layers spreading over the surface of a crystal. *Sov. Phys. Crystallogr.* **3,** 236 (1958).
133. A. Baronnet: Sur les origines des dislocations vis et des spirales de croissance dans les micas (On the origin of screw dislocations and growth spirals in micas). *J. Cryst. Growth* **19,** 193 (1973).
134. Y. Gatoh and H. Komatsu: On the origin of growth spirals having large step heights. *J. Cryst. Growth* **54,** 163 (1981).
135. D.G. Schlom, D. Anselmetti, J.G. Bednorz, C. Gerber, and J. Mannhart: Epitaxial growth of cuprate superconductors from the gas phase. *J. Cryst. Growth* **137,** 259 (1994).
136. J.G. Allpress, J.V. Sanders, and A.D. Wadsley: Electron microscopy of high-temperature Nb_2O_5 and related phases. *Phys. Status Solidi* **25,** 541 (1968).
137. O. Pérez, H. Leligny, G. Baldinozzi, D. Grebille, M. Hervieu, P. Labbé, D. Groult, and H. Graafsma: Crystal structure of double-collapsed-phase $Bi_{6+x}Sr_{9-x}Fe_5O_{26}$ and its relation to modulated-phase $Bi_2Sr_2CaCu_2O_{8+\delta}$. *Phys. Rev. B* **56,** 5662 (1997).
138. M. Kawasaki, K. Takahashi, T. Maeda, R. Tsuchiya, M. Shinohara, O. Ishiyama, T. Yonezawa, M. Yoshimoto, and H. Koinuma: Atomic control of the $SrTiO_3$ crystal interface. *Science* **266,** 1540 (1994).
139. G. Koster, B.L. Kropman, G.J.H.M. Rijnders, D.H.A. Blank, and H. Rogalla: Quasi-ideal strontium titanate crystal surfaces through formation of strontium hydroxide. *Appl. Phys. Lett.* **73,** 2920 (1998).
140. N.D. Zakharov, D. Hesse, F. Nouvertné, J. Auge, H. Hoffschulz, J. Dreßen, H.G. Roskos, H. Kurz, and G. Güntherodt: Surface topography and bulk structure of $Bi_2Sr_2CaCu_2O_{8+\delta}$ films observed by scanning tunneling microscopy and high-resolution transmission electron microscopy. *Physica C* **245,** 84 (1995).
141. J.S. Wu, C.L. Jia, K. Urban, J.H. Hao, and X.X. Xi: A new mechanism for misfit dislocation generation: Superdislocations associated with Ruddlesden–Popper planar defects. *J. Cryst. Growth* **234,** 603 (2002).

Synthesis and characterization of an $n=6$ Aurivillius phase incorporating magnetically active manganese, $Bi_7(Mn,Ti)_6O_{21}$

M. A. Zurbuchen[a]
Electronics and Photonics Laboratory, The Aerospace Corporation, El Segundo, California 90245

R. S. Freitas,[b] M. J. Wilson, and P. Schiffer
Department of Physics, Pennsylvania State University, University Park, Pennsylvania 16802
and Materials Research Institute, The Pennsylvania State University, University Park, Pennsylvania 16802

M. Roeckerath and J. Schubert
IBN 1-IT, Forschungszentrum Jülich GmbH, 52425 Jülich, Germany and CNI, Forschungszentrum Jülich GmbH, 52425 Jülich, Germany

M. D. Biegalski
Center for Nanophase Material Sciences, Oak Ridge National Laboratory, Oak Ridge, Tennessee 37831

G. H. Mehta, D. J. Comstock, J. H. Lee, Y. Jia, and D. G. Schlom
Department of Materials Science and Engineering, The Pennsylvania State University, University Park, Pennsylvania 16802-5005

(Received 4 January 2007; accepted 14 June 2007; published online 20 July 2007)

Epitaxial films of $Bi_7Mn_{3.75}Ti_{2.25}O_{21}$ were prepared to yield a previously unsynthesized material. The superlattice phase is produced by incorporating the magnetoelectric $BiMnO_3$ into the perovskite substructure of the ferroelectric $Bi_4Ti_3O_{12}$, a strategy which is hoped to yield previously undiscovered multiferroic materials. X-ray diffraction and transmission electron microscopy (TEM) confirm synthesis of an epitaxial $n=6$ Aurivillius phase. Magnetization measurements show ferromagnetic behavior with a Curie point of 55 K, but electronic polarization measurements show no remanent polarization. Rutherford backscattering spectrometry indicates a channeling minimum χ_{min} of 22%, consistent with the high density of out-of-phase domain boundaries observed by TEM. © *2007 American Institute of Physics*. [DOI: 10.1063/1.2756163]

Multiferroic materials exhibit simultaneously two or more of ferroelectricity, magnetism, or ferroelasticity.[1] Magnetoelectric materials [exhibiting both ferroelectric and ferromagnetic (or ferrimagnetic) behaviors] are of particular interest because they hold the potential to control switching of electric polarization via magnetic fields and magnetization via electric fields. Such materials could enable spintronics, magnetic sensors with fewer wires and high sensitivity, and various types of memories and actuators. The physics of such systems is the focus of intense study because the nature of the physical interaction between the order parameters is not thoroughly understood.

Few electric-magnetic (magnetoelectric) materials are known, particularly that are stable at atmospheric pressure.[2,3] So far, these are limited to systems which exhibit weak ferroelectricity or weak ferromagnetism. The resulting magnetoelectric coefficients are also weak.[3–7]

In this letter, we describe the synthesis and characterization of an $n=6$ Aurivillius phase incorporating magnetically active manganese, $Bi_4(Mn,Ti)_6O_{21}$. This phase is a composite of the ferroelectric phase $Bi_4Ti_3O_{12}$ and the ferromagnetic phase $BiMnO_3$. The phase was confirmed by x-ray diffraction (XRD) and transmission electron microscopy (TEM). Crystalline quality was also characterized by Rutherford backscattering spectrometry (RBS). Magnetization behavior was studied as a function of field and temperature.

A composite approach to fabricating two-phase ferroelectric-magnetic composite heterostructures[8] has been demonstrated, and refining the scale to the atomic level is useful for both maximizing elastic coupling and exploring its spatial limits. Macroscale, 3-3 bulk composites[9] have mechanical stability issues and exhibit poor coupling.[10] Micro scale tape cast structures avoid mechanical issues and exhibit stronger coupling,[11] but granular orientation effects likely still reduce coupling. Nanoscale thin film structures have been the most effective in producing multiferroic composites. Although a 2-2 composite (stack of films on a substrate)[9] is convenient for electrical characterization, a nonferroic substrate will clamp the response.[12] A solution is to use a ferroic substrate,[13] but limited selection of substrate materials is problematic. Another solution is to use a 3-1 composite system to maximize out-of-plane mechanical coupling, for example, $BaTiO_3-CoFe_2O_4$.[14] The ultimate level is at the atomic or unit-cell scale, beyond the reach of most physical or phase separation approaches, so natural multiferroics, single-phase materials that can incorporate substructures of both types must be found.

Layered perovskite oxide materials are excellent candidates for the potential synthesis of natural multiferroic materials—nanocomposites at the atomic scale. One approach is to choose a ferroelectric host and to incorporate a magnetically active species. The Aurivillius layered perovskites[15] are chosen because most are ferroelectric,[16] and recently large-celled Aurivillius phases have been stabilized via charge-mediated growth, making them accessible. The phases are members of a homologous series of Bi-

[a]Electronic mail: mark.a.zurbuchen@aero.org and mark_z@mac.com
[b]Also at: Instituto de Física, Universidade de São Paulo, C.P. 66318, São Paulo, São Paulo 05315-970, Brazil.

layered oxides, consisting of $Bi_2O_2^{2+}$ layers alternating with $nABO_3$ perovskite units, described by the formula $Bi_2O_2(A_{n-1}B_nO_{3n+1})$. Typical high-$n$ Aurivillius phases are ferroelectric, such as the $n=3$ $Bi_4Ti_3O_{12}$ (Ref. 15) or the $n=7$ $Sr_4Bi_4Ti_7O_{24}$. Bismuth also occupies the A sites.

The high-n Aurivillius phases cannot be synthesized in bulk form due to small differences in formation energy between related members, or because their free energy is higher than that of a multiphase mixture with the same overall composition. Co-deposition growth of an epitaxial film as we report here using pulsed laser deposition (PLD) can provide the driving force to stabilize a single homologous series member via epitaxial stabilization.[17]

A magnetically active cation that fits into the lattice, while existing in a magnetic oxidation state is needed. Aurivillius structures will accommodate B-site cations from 0.58 to 0.645 Å in radius.[18] Among the magnetically active transition elements, the B-site cation that best fits both criteria is Mn^{3+} ($r_{VI}=0.58$ Å).[19] Fe^{3+} will fit, but $BiFeO_3$ is antiferromagnetic,[19,20] and others [Mn^{2+} ($r_{VI}=0.67$ Å), Co^{3+} ($r_{VI}=0.545$ Å), Ni^{3+} ($r_{VI}=0.56$ Å)] (Ref. 21) do not fit.

Bulk synthesis of a manganese-containing Aurivillius phase, $Bi_2Sr_{1.4}La_{0.6}Nb_2MnO_{12}$, was recently reported,[22] in which the manganese would have an average charge of $Mn^{3.4+}$, perhaps the lower limit of manganese accommodation in the structure. It exhibited spin-glass magnetic behavior on cooling, but was not ferroelectric. An earlier report of $Bi_2Sr_2Nb_2MnO_{12}$ remains unconfirmed,[23] and contained a significant proportion of perovskite impurity phases.[22] Such a composition, with Mn^{4+}, would in any case not be expected to be ferromagnetic. We believe that it is necessary to select a composition compatible with a large proportion of Mn^{3+} in order to synthesize a multiferroic Aurivillius phase. Single crystals or epitaxial films are desirable for study of multiferroic properties, but neither form of any Aurivillius phase containing manganese has been reported.

The interaction of strain with the substrate and the ferroic order parameters of such a film remains unknown. Layered perovskite oxides are known to exhibit magnetostrictive behavior.[24,25] But some show no ferroelectric strain.[26]

Films were synthesized by PLD from 99.99%+ pure single targets, with 10-80% excess bismuth using a KrF excimer laser, $\lambda=248$ nm, under $p_{O_2+O_3}=90$ mTorr at 600–800 °C with a radiatively heated substrate holder[27] onto (001) $SrTiO_3$ and were quenched to avoid decomposition. We performed magnetization measurements using a Quantum Design superconducting quantum interference device magnetometer with the magnetic field parallel to the sample plane. In-plane electronic polarization measurements were taken at 77 K with interdigitated electrodes on an aixACCT ferroelectric tester. Chemical composition and structural perfection were investigated by RBS and channeling using 1.4 MeV He^+-ions.

As-grown films are phase pure and epitaxial, with c perpendicular to the substrate surface, as shown by the θ-2θ XRD scan in Fig. 1. The full width at half maximum (FWHM) of the rocking curve ω scan of the 00$\underline{2}$8 peak and the ϕ scan of (not shown) the 11$\underline{1}$4 peak taken at $2\theta=33.1°$ and $\chi=46.0°$ are 0.10° and 0.13°, respectively. RBS results are consistent with a Bi:Mn:Ti ratio of 28:18:9. This, indicates that the films have composition of $Bi_7Mn_{3.75}Ti_{2.25}O_{21}$. The c-axis lattice parameter, calculated by a regression fit of θ-2θ peak positions, is 56.0±0.1 Å, and $a=b=3.76\pm0.05$ Å based on a tetragonal prototype.

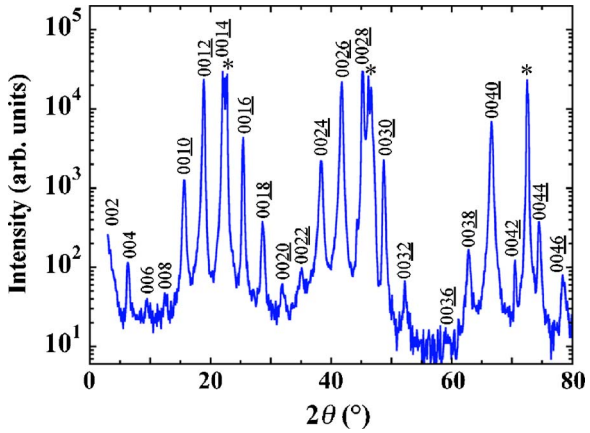

FIG. 1. (Color online) θ-2θ x-ray diffraction scan of the (001) $Bi_7Mn_{3.75}Ti_{2.25}O_{21}$/(001) $SrTiO_3$ film, in which the $SrTiO_3$ substrate peaks are marked by asterisks. The film is phase pure and epitaxial, with a low mosaic of 0.10° FWHM out of plane and 0.13° FWHM in-plane (not shown).

TEM is necessary for structure confirmation of large-period superlattice phases such as this, which are difficult to discern from intergrowths of multiple shorter-period members by XRD alone.[28,29] The cross-section electron diffraction pattern and lattice image in Figs. 2(a) and 2(b), from the same sample shown in Fig. 1, provide confirmation of synthesis of the $n=6$ Aurivillius phase. The film is free of intergrowths of other-n Aurivillius phases, but has a high density of out-of-phase boundaries[29] (OPBs) oriented at ≈55° from [001]. These are visible in the cross-sectional TEM image in Fig. 2(c) and lead to the streaking of spots in the electron diffraction pattern in Fig. 2(b). Measurements confirm the c-axis lattice parameter obtained by XRD, at 54.3±2.7 and

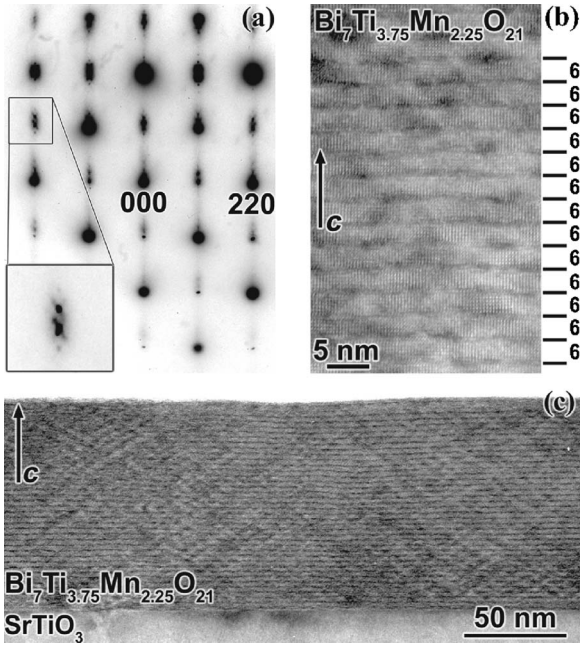

FIG. 2. TEM images taken from a cross section of the same $Bi_7Mn_{3.75}Ti_{2.25}O_{21}$ film shown in Fig. 1. The electron diffraction pattern in (a) and the lattice image in (b) confirm synthesis of an $n=6$ Aurivillius phase. The number of perovskite layers n observed between Bi_2O_2 layers is indicated at the right of the lattice image. (c) Bright-field TEM image of the full film thickness, showing an absence of intergrowths, but a high density of OPBs.

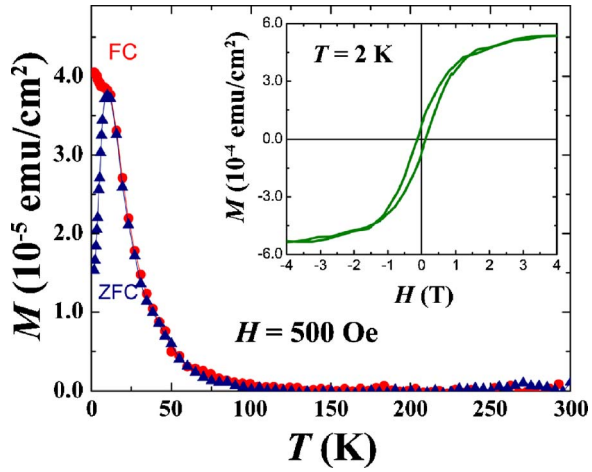

FIG. 3. (Color online) Temperature dependence of the magnetization at $H=50$ Oe. The inset shows the field dependence of the magnetization at $T=2$ K.

55.4±2.8 Å, by substrate-calibrated electron diffraction and high-resolution TEM, respectively. Although OPBs quench ferroelectricity,[26] the effects of OPBs on ferromagnetic superlattices are unknown.

The results of magnetic characterization are shown in Fig. 3. The sample appears to be ferromagnetic with a Curie point (T_C) of approximately 55 K. Measurements of $M(H)$ show typical ferromagnetic behavior below T_C, with a coercive field of approximately 1200 Oe at 2 K. The differences between field-cooled and zero-field-cooled data are probably attributable to domain effects, but could also indicate the presence of some glassiness in the sample. The T_C is significantly lower than that of bulk $BiMnO_3$, 105 K.[30] This is likely due to the reduced dimensionality of the $BiMnO_3$ perovskite sheets in these natural superlattices.

Electronic polarization data showed a primarily linear response to 200 kV/cm in applied field, with some slight curvature which cannot unequivocally be attributed to ferroelectric behavior and is more likely due to leakage and slight nonlinearity in the dielectric response. Although ferroelectric behavior could not be confirmed in this material, the synthesis route enables the exploration of a number of materials of the Aurivillius type, which are typically ferroelectric.[16]

RBS measurements indicate a Mn concentration of 5.36×10^{16} Mn at./cm^2 and a minimum channeling yield ($\chi_{\min}$) of 22%. Saturated value of the magnetization works out to be $1.15\mu_B$ per manganese, in comparison to the $3.8\ \mu_B$ predicted for the average manganese valence of $Mn^{3.2+}$, based on the cation stoichiometry and the low tolerance of oxygen vacancies in Aurivillius phases.[31,32] This suggests that a substantial fraction of the Mn ions are not participating in the ferromagnetic state, perhaps due to antiferromagnetic ordering which might be expected for a perovskite-based superlattice layered along the [001] of the perovskite subcell, considering the *d* orbital geometry.[33] The high structural disorder, in the form of OPBs,[29] might also contribute to frustration of magnetic ordering.

In conclusion, we report natural superlattices as a route to nanocompositing heteroferroic materials. Using single-target PLD, we have synthesized an epitaxial Aurivillius phase containing manganese, $Bi_7Mn_{3.75}Ti_{2.25}O_{21}$. The material is ferromagnetic, but ferroelectric behavior has not been conclusively observed. A discrepancy exists between the predicted and observed magnetization per manganese atom.

The authors acknowledge support of the U.S. Department of Energy through Grant No. DE-FG02-03ER46063, National Science Foundation through Grant No. DMR-0213623, and National Research Council Research Associateship Postdoctoral Award at the National Institute of Standards and Technology. R.S.F. thanks CNPq-Brazil for sponsorship.

[1] N. A. Hill, Annu. Rev. Mater. Res. **32**, 1 (2002).
[2] A. F. M. dos Santos, A. K. Cheetham, W. Tian, X. Q. Pan, Y. Jia, N. J. Murphy, J. Lettieri, and D. G. Schlom, Appl. Phys. Lett. **84**, 91 (2004).
[3] H. Schmid, Ferroelectrics **162**, 317 (1994).
[4] J. Wang, J. B. Neaton, H. Zheng, V. Nagarajan, S. B. Ogale, B. Liu, D. Viehland, V. Vaithyanathan, D. G. Schlom, U. V. Waghmare, N. A. Spaldin, K. M. Rabe, M. Wuttig, and R. Ramesh, Science **299**, 1719 (2003).
[5] J. Dho, C. W. Leung, J. L. MacManus-Driscoll, and M. G. Blamire, J. Cryst. Growth **267**, 548 (2004).
[6] T. Kimura, T. Goto, H. Shintani, K. Ishizaka, T. Arima, and Y. Tokura, Nature (London) **426**, 55 (2003).
[7] N. Hur, S. Park, P. A. Sharma, J. S. Ahn, S. Guha, and S.-W. Cheong, Nature (London) **429**, 392 (2004).
[8] J. Van Suchtelen, Philips Res. Rep. **27**, 28 (1972).
[9] R. E. Newnham, D. P. Skinner, and L. E. Cross, Mater. Res. Bull. **13**, 525 (1978).
[10] J. Van den Boomgard and R. A. J. Born, J. Mater. Sci. **13**, 1538 (1978).
[11] G. Srinivasan, E. T. Rasmussen, A. A. Bush, K. E. Kamentsev, V. F. Mescheryakov, and Y. K. Fetisov, Appl. Phys. A: Mater. Sci. Process. **78**, 721 (2004).
[12] K. Lefki and G. J. M. Dormans, J. Appl. Phys. **76**, 1764 (1994).
[13] M. A. Zurbuchen, S. Saha, T. Wu, J. Mitchell, and S. K. Streiffer, Appl. Phys. Lett. **87**, 232908 (2005).
[14] H. Zheng, J. Wang, S. E. Lofland, Z. Ma, L. Mohaddes-Ardabili, T. Zhao, L. Salamanca-Riba, S. R. Schinde, S. B. Ogale, F. Bai, D. Viehland, Y. Jia, D. G. Schlom, M. Wuttig, A. Roytburd, and R. Ramesh, Science **303**, 661 (2004).
[15] B. Aurivillius, Ark. Kemi **1**, 463 (1950); **1**, 499 (1950); **2**, 519 (1951); **5**, 39 (1953).
[16] E. C. Subbarao, J. Phys. Chem. Solids **23**, 665 (1962).
[17] O. Y. Gorbenko, S. V. Samoilenkov, I. E. Graboy, and A. R. Kaul, Chem. Mater. **14**, 4026 (2002).
[18] R. A. Armstrong and R. E. Newnham, Mater. Res. Bull. **7**, 1025 (1972).
[19] A. Snedden, C. H. Hervoches, and P. Lightfoot, Phys. Rev. B **67**, 092102 (2003).
[20] I. G. Ismailzide, V. I. Nesterenko, F. A. Mirishli, and P. G. Rustamov, Kristallografiya **12**, 400 (1967) [Sov. Phys. Crystallogr.].
[21] R. D. Shannon, Acta Crystallogr., Sect. A: Cryst. Phys., Diffr., Theor. Gen. Crystallogr. **32**, 751 (1976).
[22] E. E. McCabe and C. Greaves, J. Mater. Chem. **15**, 177 (2005).
[23] W. J. Yu, Y. I. Kim, D. H. Ha, J. H. Lee, Y. K. Park, S. Seong, and N. H. Hur, Solid State Commun. **111**, 705 (1999).
[24] J. F. Mitchell, D. N. Argyriou, J. D. Jorgensen, D. G. Hinks, C. D. Potter, and S. D. Bader, Phys. Rev. B **55**, 63 (1997).
[25] M. Medarde, J. F. Mitchell, J. E. Millburn, S. Short, and J. D. Jorgensen, Phys. Rev. Lett. **83**, 1223 (1999).
[26] M. A. Zurbuchen, G. Asayama, D. G. Schlom, and S. K. Streiffer, Phys. Rev. Lett. **88**, 107601 (2002).
[27] J. C. Clark, J.-P. Maria, K. J. Hubbard, and D. G. Schlom, Rev. Sci. Instrum. **68**, 2538 (1997).
[28] J. L. Hutchison, J. S. Anderson, and C. N. R. Rao, Proc. R. Soc. London, Ser. A **355**, 301 (1977).
[29] M. A. Zurbuchen, W. Tian, X. Q. Pan, D. Fong, S. K. Streiffer, M. E. Hawley, J. Lettieri, Y. Jia, G. Asayama, S. J. Fulk, D. J. Comstock, S. Knapp, A. H. Carim, and D. G. Schlom, J. Mater. Res. **22**, 1439 (2007).
[30] T. Atou, H. Chiba, K. Ohayama, Y. Yamaguchi, and Y. Syono, J. Solid State Chem. **145**, 639 (1999).
[31] R. A. Armstrong and R. E. Newnham, Mater. Res. Bull. **7**, 1025 (1972).
[32] A. Snedden, S. M. Blake, and P. Lightfoot, Solid State Ionics **156**, 439 (2003).
[33] N. Spaldin (private communication).

JOURNAL of the American Ceramic Society

Volume 88 | Number 8 | August 2005

journal

J. Am. Ceram. Soc., **91;** [8] 2429–2454 (2008)
DOI: 10.1111/j.1551-2916.2008.02556.x

A Thin Film Approach to Engineering Functionality into Oxides

Darrell G. Schlom,[†,††,‡] Long-Qing Chen,[‡] Xiaoqing Pan,[§] Andreas Schmehl,[‡,¶] and Mark A. Zurbuchen[‖]

[‡]Department of Materials Science and Engineering, Pennsylvania State University, University Park, Pennsylvania 16802-5005

[§]Department of Materials Science and Engineering, University of Michigan, Ann Arbor, Michigan 48109-2136

[¶]Experimentalphysik VI, Elektronische Korrelationen und Magnetismus, Institut für Physik, Universität Augsburg, D-86159 Augsburg, Germany

[‖]The Aerospace Corporation, Microelectronics Technology Department, El Segundo, California 90245

The broad spectrum of electronic and optical properties exhibited by oxides offers tremendous opportunities for microelectronic devices, especially when a combination of properties in a single device is desired. Here we describe the use of reactive molecular-beam epitaxy and pulsed-laser deposition to synthesize functional oxides, including ferroelectrics, ferromagnets, and materials that are both at the same time. Owing to the dependence of properties on direction, it is often optimal to grow functional oxides in particular directions to maximize their properties for a specific application. But these thin film techniques offer more than orientation control; customization of the film structure down to the atomic-layer level is possible. Numerous examples of the controlled epitaxial growth of oxides with perovskite and perovskite-related structures, including superlattices and metastable phases, are shown. In addition to integrating functional oxides with conventional semiconductors, standard semiconductor practices involving epitaxial strain, confined thickness, and modulation doping can also be applied to oxide thin films. Results of fundamental scientific importance as well as results revealing the tremendous potential of utilizing functional oxide thin films to create devices with enhanced performance are described.

I. Oxides Beyond SiO_2

UNTIL recently, the word "oxide" could only mean one thing to anyone working in the semiconductor industry—SiO_2. But as every ceramist knows, oxides are an exciting class of electronic materials in their own right. Oxides exhibit the full spectrum of electronic, optical, and magnetic behavior: insulating, semiconducting, metallic, superconducting, ferroelectric, pyroelectric, piezoelectric, ferromagnetic, multiferroic, and nonlinear optical effects are all possessed by structurally compatible oxides. The unparalleled variety of physical properties of oxides holds tremendous promise for electronic applications. Analogous to today's semiconductor device structures, many device concepts utilizing oxides will likely use alternately layered structures where dimensions are minute enough to observe quantum size effects (nanometer-scale thicknesses).

The physical behavior of oxides confined to quantum size dimensions is not well established, and an understanding of the effect of such confinement (reduced dimensionality) on the physical properties of these structures cannot be achieved without the controlled preparation of well-ordered crystalline samples. Equally exciting are the new functionalities that can emerge at oxide interfaces. For instance, the interface between appropriate antiferromagnetic materials has been shown to be ferromagnetic.[1–7] Similarly, charge transfer at the interface between appropriate nonmagnetic insulators[8] can give rise to a magnetic[9] or superconducting[10] electron gas. These examples offer a glimpse of the new or enhanced functionalities that can be achieved by nanoengineering oxide heterostructures with atomic layer precision. As we show in this article, it is possible to structurally engineer crystalline oxides with a precision that rivals the structural control achieved in today's most advanced semiconductor structures.

Examples of the functional properties of specific oxides are listed in Table I. The oxides chosen were those with exceptional properties for each category. These include the oxide with the highest known electron mobility ($SrTiO_3$),[11] change in resistance at a metal–insulator transition (EuO),[12] superconducting transition temperature ($HgBa_2Ca_2Cu_3O_{8+x}$),[13] switchable spontaneous polarization ($PbZr_{0.2}Ti_{0.8}O_3$[14] and $BiFeO_3$[15–18]), piezoelectric coefficient ($PbZn_{1/3}Nb_{2/3}O_3$–$PbTiO_3$),[19] magnetization (EuO),[20] magnetoresistance ($Pr_{0.7}Sr_{0.04}Ca_{0.26}MnO_{3-\delta}$),[21] magnetostrictive coefficient ($Co_{0.8}Fe_{2.2}O_4$),[22] Verdet constant (EuO)[23]—a measure of the strength of the Faraday effect, spin polarization (CrO_2),[24,25]

D. Green—contributing editor

Manuscript No. 24429. Received March 17, 2008; approved June 1, 2008.
This work was financially supported by the National Science Foundation under grants DMR-0507146 and DMR-0213623, the Office of Naval Research under grant N00014-04-1-0426 monitored by Dr. Colin Wood, and the U.S. Department of Energy through grants DE-FG02-03ER46063 and DE-FG02-07ER46417. This work was supported by The Aerospace Corporation's Independent Research and Development Program.
[†]Author to whom correspondence should be addressed. e-mail: schlom@cornell.edu
[††]Current Address: Department of Materials Science and Engineering, Cornell University, Ithaca, NY 14853-1501

Feature

Table I. Examples of the Properties of Oxides

Property	Value	Oxide material	References
Mobility	$\mu = 22\,000\ cm^2 \cdot (V \cdot s)^{-1}$ (2 K)	$SrTiO_3$	Tufte and Chapman[11]
Metal–insulator transition	$\Delta R/R_{T_{low}} > 10^{13}$	EuO	Petrich *et al.*[12]
Superconductivity	$T_c = 135$ K	$HgBa_2Ca_2Cu_3O_{8+x}$	Schilling *et al.*[13]
Ferroelectricity	$P_s = 105\ \mu C/cm^2$	$PbZr_{0.2}Ti_{0.8}O_3$	Vrejoiu *et al.*[14]
	$P_s = 100\ \mu C/cm^2$	$BiFeO_3$	Wang *et al.*,[15] Li *et al.*[16] Das *et al.*,[17] Dho *et al.*[18]
Piezoelectricity	$d_{33} = 2500$ pC/N	$PbZn_{1/3}Nb_{2/3}O_3$–$PbTiO_3$	Park *et al.*[19]
Ferromagnetism	$M_s = 6.9\ \mu_B$/Eu	EuO	Matthias *et al.*[20]
Colossal magnetoresistance	$\Delta R/R_H > 10^{11}$ (5 T)	$Pr_{0.7}Sr_{0.04}Ca_{0.26}MnO_{3-\delta}$	Maignan *et al.*[21]
Magnetostriction	$\lambda_{100} = -590 \times 10^{-6}$	$Co_{0.8}Fe_{2.2}O_4$	Bozorth *et al.*[22]
Faraday effect	$\nu = 4 \times 10^{5\circ} \cdot (T \cdot cm)^{-1}$	EuO	Ahn and Shafer[23]
Spin polarization	$P > 98\%$	CrO_2	Soulen *et al.*,[24] Anguelouch *et al.*[25]
Ferromagnetic and ferroelectric simultaneously	$T_C = 105$ K	$BiMnO_3$	Hill and Rabe,[29] Moreira dos Santos *et al.*,[28] Sharan *et al.*,[30] Baettig *et al.*[31]
	$T_C = 250$ K	$LuFe_2O_4$, $FeTiO_3$	Ikeda *et al.*, Fennie[27]

and the ferromagnetic ferroelectric with the highest reported[26] ($LuFe_2O_4$) or predicted[27] ($FeTiO_3$) transition temperature. A challenge with materials that are simultaneously ferromagnetic and ferroelectric is that they are often too conductive for the fabrication of conventional ferroelectric switching devices. The ferromagnetic ferroelectric with the highest transition temperature on which a conventional polarization-electric field hysteresis measurement has been reported is $BiMnO_3$ ($TC \sim 105$ K).[28]

(1) Perovskites

The crystal structures of the oxides with the outstanding properties listed in Table I are shown in Fig. 1.[32] Half of the oxides belong to the same structural family—perovskite. The perovskite ABO_3 structure can accommodate with 100% substitution some 30 elements on the *A* site and over half the periodic table on the *B* site, as shown in Fig. 2.[33] Given the chemical and structural compatibility between many perovskites, this malleable structural host offers an opportunity to customize electronic, magnetic, and optical properties in thin films in ways not possible with conventional semiconductors.

The electroceramics industry currently utilizes the diverse electrical properties of oxides in separate components made primarily by bulk synthesis and thick-film methods for capacitors, sensors, actuators, night vision, and other applications. A significant opportunity exists, however, to combine these

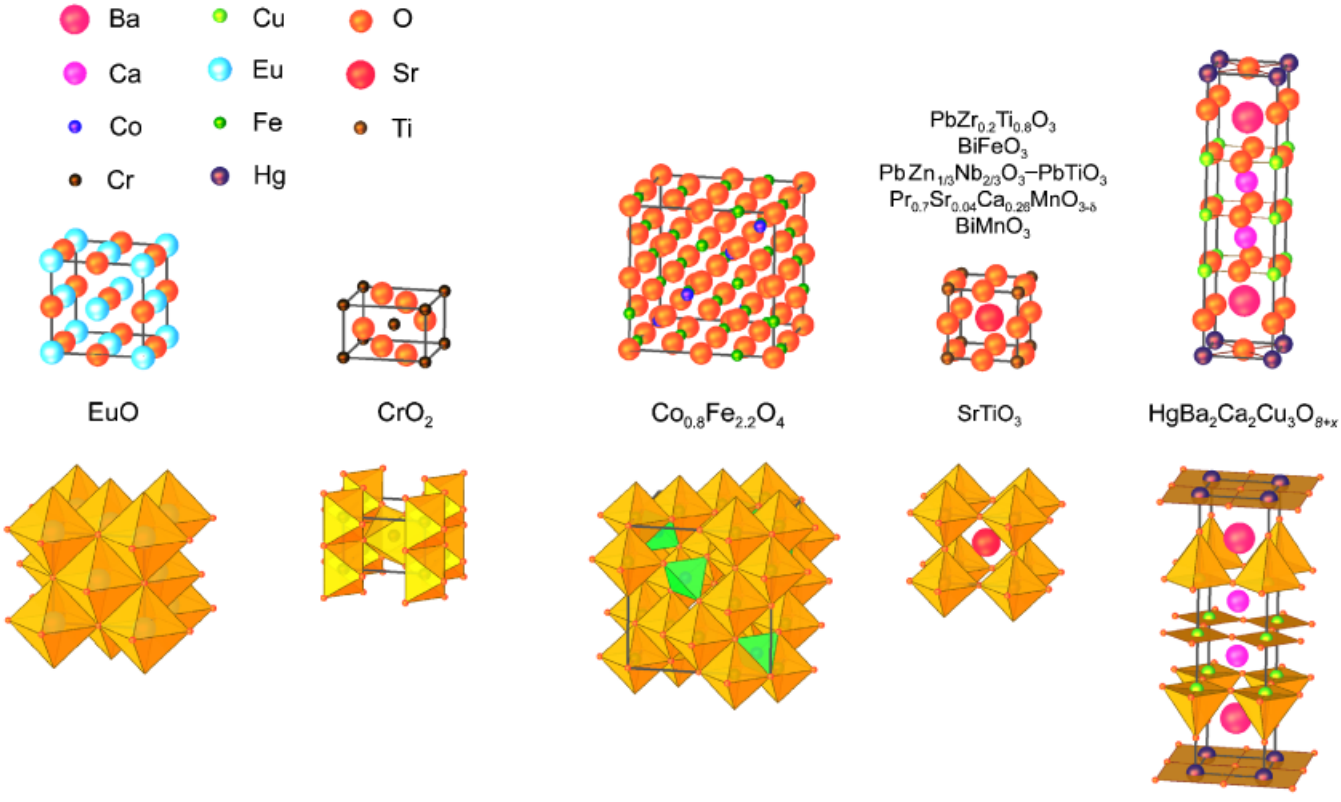

Fig. 1. The crystal structures of the oxides with the exceptional properties described in Table I. Two equivalent representations of these crystal structures are shown: the atomic positions (above) and the coordination polyhedra (below). The oxygen atoms occupy the vertices of the coordination polyhedra. Color is used to distinguish the two types of oxygen coordination polyhedra in $Co_{0.8}Fe_{2.2}O_4$, octahedra (orange), and tetrahedra (green). The pseudocubic subcell of the perovskites $PbZr_{0.2}Ti_{0.8}O_3$, $BiFeO_3$, $PbZn_{1/3}Nb_{2/3}O_3$–$PbTiO_3$, $Pr_{0.7}Sr_{0.04}Ca_{0.26}MnO_{3-\delta}$, and $BiMnO_3$ is shown for clarity. The relative sizes of the atoms reflect their relative ionic radii as given by Shannon.[32]

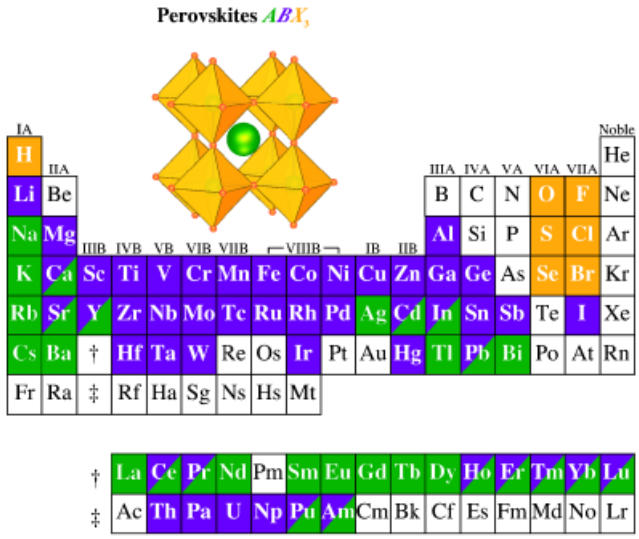

Fig. 2. A compilation of elements of the periodic table that can occupy the three sites (*A*, *B*, and *X*) of the perovskite crystal structure with 100% occupancy (based on the data in Landolt-Boernstein[33]).

properties together in oxide heterostructures where multiple properties can be utilized to yield functional integrated devices. Integration of epitaxial stacks of oxide crystals is motivated by the similarity in crystal structure (the perovskite oxides listed in Table I all have perovskite subcell dimensions in the 3.85–4.05 Å range), the chemical compatibility that exists between many oxides, and the directional dependence of properties that can be optimized for particular applications by controlling the orientation of a single crystalline film. In addition to synthesizing oxide heterostructures that integrate relatively thick layers of different oxides together, new oxides can be engineered at the atomic-layer level. Although now commonplace in the growth of semiconductors, such an ability is relatively new to oxides and makes possible the discovery/engineering of higher performance smart materials by exploiting the exceptional electrical, optical, and magnetic properties of oxides and building a coupling between these properties into oxide heterostructures.

(2) Perovskite-Related Phases

Structure–property relations have been studied for a great many oxides using solid-state synthesis methods. Many cases have been found where the property of a structurally related family of oxides (i.e., a homologous series) changes drastically from one end to the other of the series. Examples include the $Sr_{n+1}Ru_nO_{3n+1}$ Ruddlesden–Popper homologous series[34–36] shown in Fig. 3. In this series the positive integer n corresponds to the number of perovskite layers that are sandwiched between double SrO rock-salt layers. The $n = 1$ (Sr_2RuO_4) member of the series is paramagnetic and at very low temperature (<1.5 K) superconducting,[37] whereas the $n = \infty$ ($SrRuO_3$) member of the series is ferromagnetic.[38] The structural change accompanying this drastic change in properties involves going from a corner sharing RuO_6 octahedral network that is connected in all three dimensions for the $n = \infty$ member ($SrRuO_3$) to the $n = 1$ member (Sr_2RuO_4), where the RuO_6 octahedra are only connected in two dimensions and double SrO layers completely disrupt all corner sharing of the RuO_6 octahedra along the *c*-axis. Many other equally fascinating homologous series exist in perovskite-related oxide structures showing interesting variation in ferromagnetic, ferroelectric, superconducting, and metal–insulator behavior.

An example of an important ferroelectric homologous series is the Aurivillius homologous series with general formula $Bi_2O_2(A_{n-1}B_nO_{3n+1})$ shown in Fig. 4. Here again the positive integer n denotes the number of perovskite layers that in this

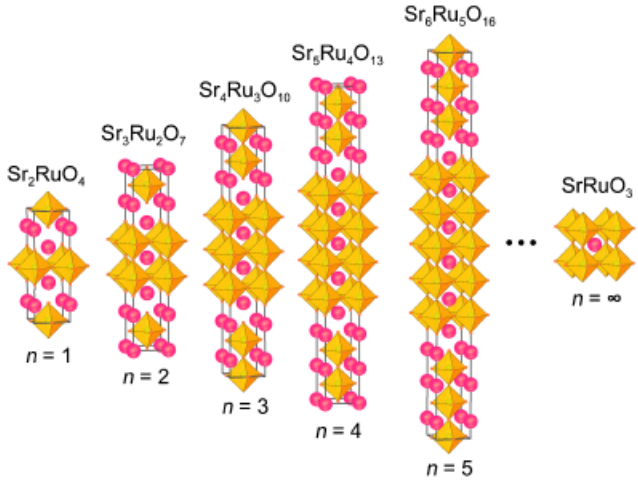

Fig. 3. The $n = 1$ (Sr_2RuO_4), $n = 2$ ($Sr_3Ru_2O_7$), $n = 3$ ($Sr_4Ru_3O_{10}$), $n = 4$ ($Sr_5Ru_4O_{13}$), $n = 5$ ($Sr_6Ru_5O_{16}$), and $n = \infty$ ($SrRuO_3$) members of the homologous Ruddlesden–Popper series of compounds $Sr_{n+1}Ru_nO_{3n+1}$. Ru^{4+} lie at the center of oxygen coordination polyhedra (octahedra). The filled circles represent Sr^{2+} ions (reprinted from Haeni *et al.*,[80] with permission; ©2001 American Institute of Physics).

case are sandwiched between Bi_2O_2 layers. The structures shown include the layered $n = 2$ Aurivillius compound $SrBi_2Ta_2O_9$ widely used in ferroelectric random access memories (FeRAM).[39] Over 500 million FeRAM chips containing either $SrBi_2Ta_2O_9$ or $Pb(Zr,Ti)O_3$ ferroelectrics have been made and worldwide production currently exceeds 70 million units per year.[40] Also included in Fig. 4 is an $n = 6$ Aurivillius compound $Bi_7(Mn,Ti)_6O_{21}$ into which the ferromagnetic perovskite $BiMnO_3$ has been inserted,[41] and at the end of the series is the $n = \infty$ three-dimensional perovskite structure.

When one desires to study the change in a property that occurs as n is varied in detail, however, solid-state synthesis methods often fall short. Invariably researchers have only been able to find conditions of temperature and pressure yielding single-phase products for low values of n and for $n = \infty$. Attempts to make intermediate n values result in uncontrolled intergrowths.[13,41–72] Calculation of the energy of formation of several homologous series of layered oxide phases indicates the reason for this difficulty—differences in formation energy become smaller and smaller as n increases.[73,74] Thus, apart from theoretical calculations, little is known about how the properties of a series of structures vary with n as the dimensionality of the structure changes. Because of correlated electron effects in many

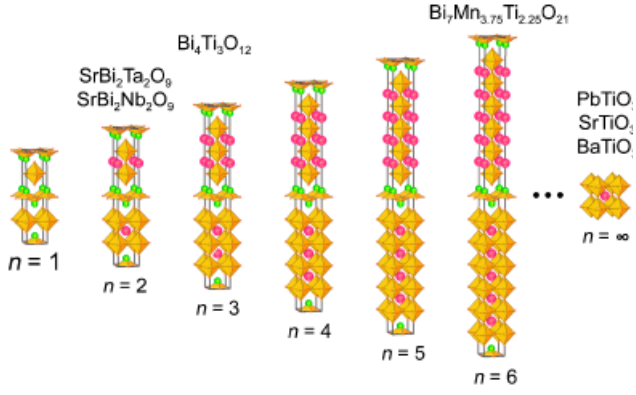

Fig. 4. Examples of the $n = 1$, $n = 2$ ($SrBi_2Ta_2O_9$, $SrBi_2Nb_2O_9$), $n = 3$ ($Bi_4Ti_3O_{12}$), $n = 4$, $n = 5$, and $n = \infty$ ($PbTiO_3$, $SrTiO_3$, and $BaTiO_3$) members of the Aurivillius homologous series of compounds with general formula $Bi_2O_2(A_{n-1}B_nO_{3n+1})$. *B* ions lie at the center of the oxygen coordination polyhedra (octahedra). The filled circles represent *A* ions. These structures consist of alternating sheets of Bi_2O_2 and $nABO_3$ perovskite layers.

homologous series of interest, experimental measurements are an important part of understanding the effect of dimensionality on these oxides.[75]

A key advantage of the use of thin film techniques for the preparation of oxide heterostructures is that single-phase epitaxial films with intermediate n values can often be synthesized even though nearby phases have similar formation energies.[76–80] This is made possible by the ability to supply incident species in any desired sequence with submonolayer composition control. A particular phase can often be grown by supplying the constituents in an ordered sequence corresponding to the atomic arrangement of these constituents in the desired phase.

II. Synthesis of Epitaxial Oxide Films by Pulsed-Laser Deposition (PLD) and Molecular-Beam Epitaxy (MBE)

Significant advances in deposition technologies and substrates over the past two decades have enabled the growth of oxide thin films with high structural perfection and the ability to customize oxide layering down to the atomic layer level. These advances were spurred by the discovery of high-temperature superconductivity over 20 years ago.[81,82] Existing thin film deposition techniques were rapidly adapted to the challenges of functional oxides, including PLD,[83–88] high-pressure[89–94] and off-axis sputtering,[95–102] reactive coevaporation,[103–105] and reactive MBE.[76,106–114] These physical vapor deposition techniques yielded high-quality oxide superconductor films just a few nanometers in thickness,[115–117] superlattices of superconducting oxides with atomic-scale thickness control and abrupt interfaces,[110,118–126] and the construction of new oxide superconducting phases with atomic layer precision.[76,127] Chemical techniques including metal-organic chemical vapor deposition (MOCVD)[128–143] and chemical solution deposition (CSD)[144–148] have also been adapted and applied to functional oxides, particularly ferroelectrics. In recent years, a growing cadre of researchers has applied these physical and chemical techniques with increasing precision to the growth of an ever-broadening set of functional oxide materials. Relevant achievements include the synthesis of oxide superlattices with atomic-scale thickness control and abrupt interfaces[79,113,117,149–157] and the synthesis of metastable oxides.[76,158–161] These advances in thin film deposition technology have made it possible to customize oxide heterostructures with subnanometer precision.

(1) PLD

The PLD technique is ideally suited to the rapid investigation of multicomponent functional oxides because it (1) allows them to be grown in a relatively compact and inexpensive chamber, (2) provides nearly stoichiometric composition transfer from the target to the sample if the growth conditions are optimized, (3) is compatible with oxidant pressures ranging from ultra-high vacuum (UHV) to atmospheric, (4) is amenable to the growth of superlattices with nanometer precision,[126,150,152–155] and (5) is capable of ablating a wide variety of materials.[86,162–165]

A schematic of a PLD system is shown in Fig. 5. The process amounts to flash evaporation of the surface of a multicomponent target. Its key elements are an UV laser capable of vaporizing the surface layer of the multicomponent target when suitably focused down to a high energy density (fluence) by a lens. The vaporized material, containing a variety of atomic, molecular, and excited species, is transported through the low vacuum environment (typically 100 mTorr of O_2) where it condenses on the substrate. If the substrate presents a suitable template for the depositing species, epitaxial growth can occur in which the deposited species follow the crystalline template of the substrate to extend the crystal.

A schematic showing how the presence of a substrate may influence the crystallization of a multicomponent mixture of depositing species is shown in Fig. 6.[166] In the example shown, the growth of $SrBi_2Nb_2O_9$ (or equivalently $SrBi_2Ta_2O_9$) on $SrTiO_3$, the film and substrate have different chemistries and crystal

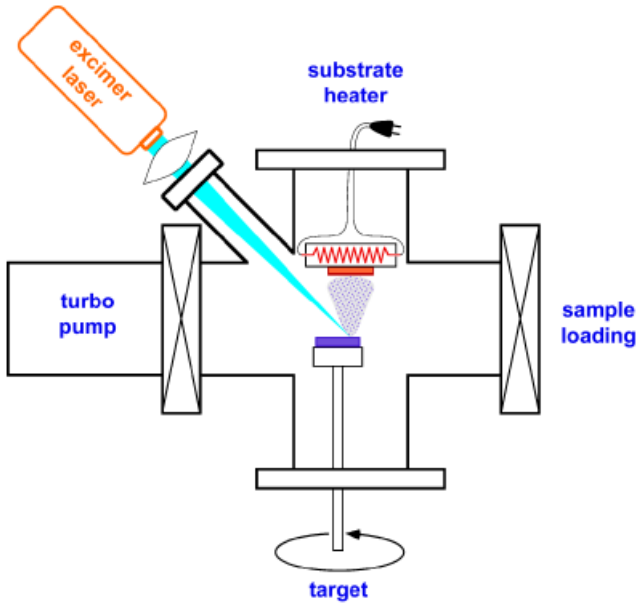

Fig. 5. A schematic diagram of a pulsed-laser deposition system dedicated to the controlled synthesis of oxide heterostructures. The key components are the UV laser whose output is focused by a lens to a sufficient fluence to vaporize the surface of the multicomponent oxide target. The vaporized material from the target is deposited on the heated substrate to form an epitaxial film. For the deposition of multilayers, a multiple-target carousel is used.

structures, yet just like the game Tetris™ the depositing atoms find low-energy configuration(s) to extend the single-crystal substrate into an epitaxial overlayer. In Fig. 6(a) the low-energy configuration is unique and the resulting epitaxial film is single crystalline with an orientation relationship (001) $SrBi_2Nb_2O_9$‖(001) $SrTiO_3$ and [100] $SrBi_2Nb_2O_9$‖ [1$\bar{1}$0] $SrTiO_3$.[‡‡,167] In the other two cases, Figs. 6(b) and (c), several energetically degenerate low-energy configurations exist, leading to an epitaxial film with two or three types of domains related to each other via 180° or 120° rotational twinning, respectively. In Fig. 6(b) the (110) $SrTiO_3$ surface is shown faceted as has been observed to occur at the growth conditions for $SrBi_2Nb_2O_9$ films.[168] Thus, the epitaxy is actually occurring locally on the (100) and (010) faces of the faceted (110) $SrTiO_3$ substrate as has also been reported for the growth of epitaxial films of other perovskite-related phases on (110) $SrTiO_3$.[169–171] The orientation relationship for Fig. 6(b) is ~(116) $SrBi_2Nb_2O_9$‖(110) $SrTiO_3$ and (i) [001] $SrBi_2Nb_2O_9$‖[100] $SrTiO_3$ and (ii) [001] $SrBi_2Nb_2O_9$‖[010]$SrTiO_3$ for the two growth twins.[‡‡,168] For Fig. 6(c) the orientation relationship is (103) $SrBi_2Nb_2O_9$‖(111) $SrTiO_3$ and approximately (i) [001] $SrBi_2Nb_2O_9$‖[100] $SrTiO_3$, (ii) [001] $SrBi_2Nb_2O_9$‖[010] $SrTiO_3$, and (iii) [001] $SrBi_2Nb_2O_9$‖[001] $SrTiO_3$ for the three growth twins.[‡‡,172,173] For clarity, another view of the threefold degenerate epitaxial relationship of the growth of $SrBi_2Nb_2O_9$ on (111) $SrTiO_3$ is shown in Fig. 6(d), where it can be more clearly seen that the three possibilities for the orientation of the c-axis of the $SrBi_2Nb_2O_9$ lie approximately parallel to the ⟨100⟩ axes of the $SrTiO_3$ substrate.

The chief advantages of PLD are its relatively modest cost and, after optimization of the growth conditions, the nearly faithful composition transfer from target to substrate, which allows a single multicomponent target with the same composition as the desired film to be used,[86,162–165] alleviating the need for accurate composition control. PLD offers an extremely

[‡‡]In addition to the *hkl* $SrBi_2Nb_2O_9$ indices given, *khl* $SrBi_2Nb_2O_9$ indices are also implied. The latter indices are omitted for clarity, but arise because of transformation twinning that occurs on cooling as the tetragonal $SrBi_2Nb_2O_9$ (the stable polymorph at growth temperature) goes through a phase transition where it becomes orthorhombic at room temperature with $a \approx b$ and a being the axis of the ferroelectric along which the spontaneous polarization exists.

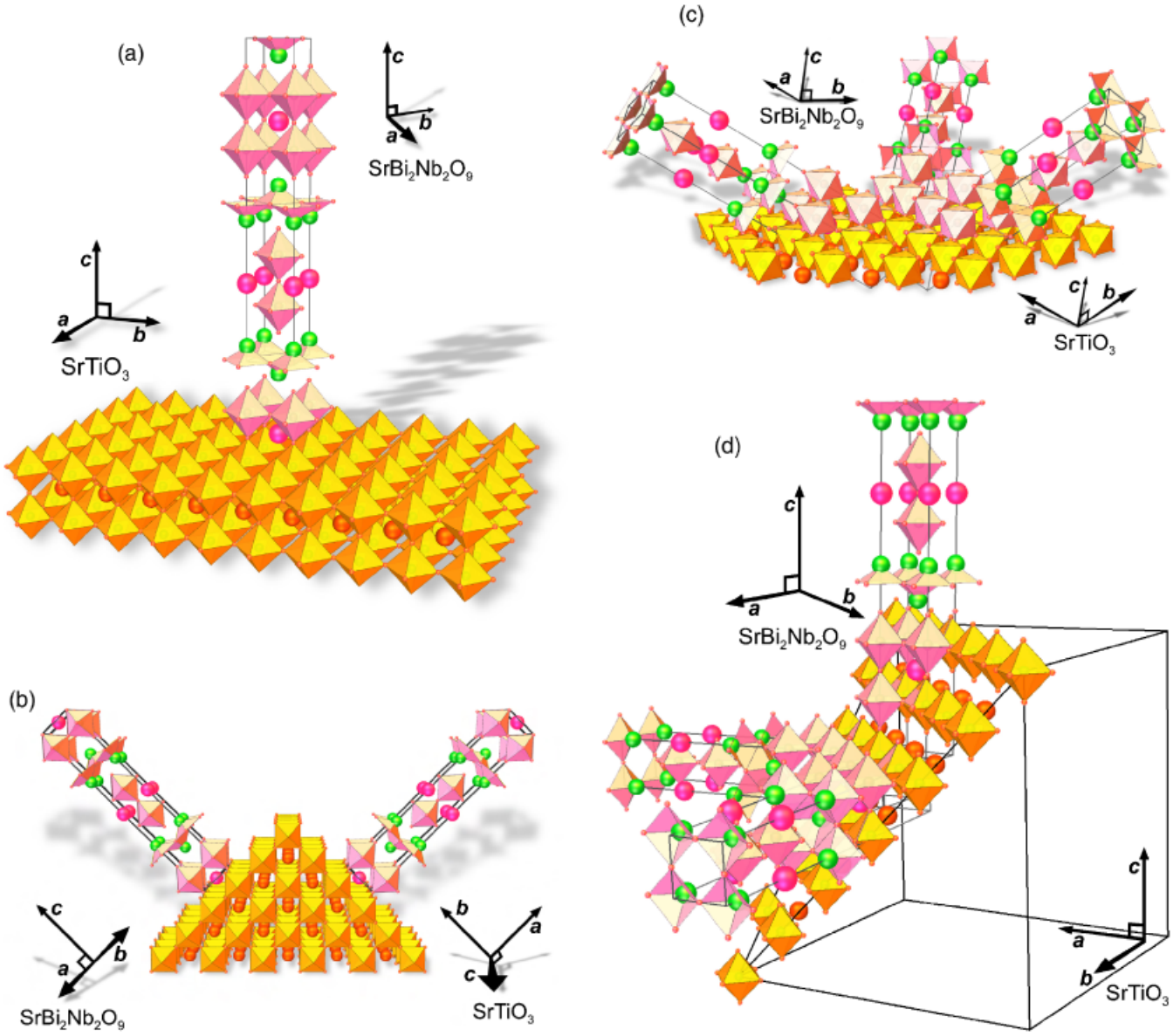

Fig. 6. The crystal structure and orientation of $SrBi_2Nb_2O_9$ (or equivalently $SrBi_2Ta_2O_9$) grown on (a) (001) $SrTiO_3$, (b) (110) $SrTiO_3$, and (c) (111) $SrTiO_3$, showing the low-energy epitaxial orientation relationship(s). Another view of the threefold degenerate epitaxial relationship of $SrBi_2Nb_2O_9$ on (111) $SrTiO_3$ is shown in (d) for clarity (reprinted from Lettieri *et al.*,[172] with permission; ©2000 American Institute of Physics). $SrBi_2Nb_2O_9$ and $SrBi_2Ta_2O_9$ grow epitaxially on (001) $SrTiO_3$ with the *c*-axis parallel to the substrate surface normal, on (110) $SrTiO_3$ in a twofold twin structure with the *c*-axes tilted by $\pm 45^\circ$ from the surface normal, and on (111) $SrTiO_3$ in a threefold twin structure with the *c* axes tilted by 57° away from the surface normal. The $SrBi_2Nb_2O_9$ is drawn and its unit cell is outlined in its tetragonal state above its Curie temperature ($\sim 430^\circ$C, Landolt-Boernstein[166]). Note that the growth temperature is well above the Curie temperature of $SrBi_2Nb_2O_9$, and so the crystallography shown is relevant during nucleation and growth of the epitaxial film. After cooling through the Curie temperature, each of the growth twins shown is twinned further due to *a–b* twinning, leading to a doubling of the expected twin states at room temperature. The orthorhombic axes of only one of the twin variants of the $SrBi_2Nb_2O_9$ films are drawn.

powerful means of scouting for materials with promising properties by enabling the rapid preparation of new materials in epitaxial form: thin single crystalline extensions of the underlying crystalline template provided by the substrate. Its key disadvantages are the micrometer-sized "boulders" common to PLD films[86,162–165] as well as the energetic species present, which can lead to interlayer mixing and extended lattice constants due to ion bombardment effects.[174–179] Stating that PLD provides stoichiometric composition transfer from target to substrate is an oversimplification. Careful studies have shown that only with careful tuning of deposition parameters (chamber pressure, laser fluence, target–substrate distance, etc.) can films with composition near to that of the target be attained.[178]

Techniques that can be used during film deposition to provide information on the nucleation and growth mechanisms in real time, rather than relying on "pathology" after the growth, are extremely useful for improving the quality of oxide thin films. Reflection high-energy electron diffraction (RHEED) is particularly useful in this context. Differential pumping has enabled RHEED to be used at the relatively high pressures of PLD[180,181] leading to tremendous improvements in the ability to tailor oxides at the atomic level. Because of the many possible phases and phase transitions in functional oxide systems, such *in situ* analytical tools that increase our understanding of the growth process and allow the growth conditions to be adjusted *during growth* are crucial to achieving improvements in the atomic layer engineering of oxides.

(2) Oxide MBE

The MBE method of thin film growth may be thought of as atomic spray painting, as shown in Fig. 7 in which an oxide

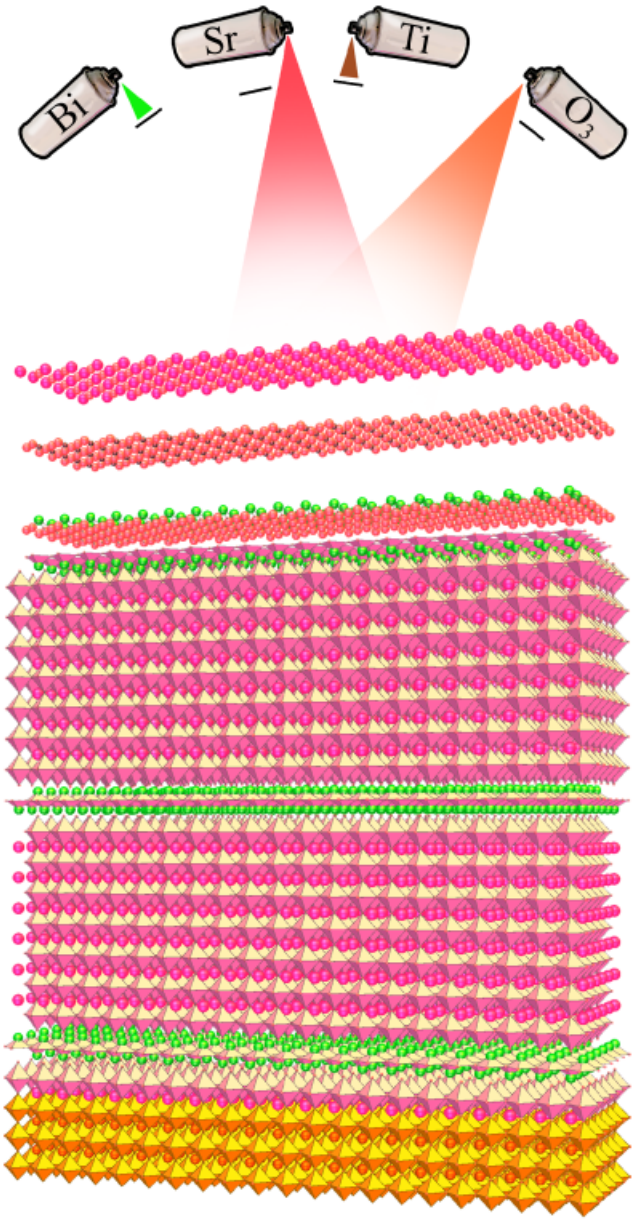

Fig. 7. A highly schematic representation of the molecular-beam epitaxy (MBE) growth of a (001) $Sr_4Bi_4Ti_7O_{24}$ film on a (001) $LaAlO_3$–Sr_2AlTaO_6 (LSAT) substrate by reactive MBE.

ferroelectric structure, e.g., $Sr_4Bi_4Ti_7O_{24}$ (an $n = 7$ Aurivillius phase) is schematically assembled layer by layer. The flux of spray from each atomic or molecular beam is controlled by the temperature (and thus vapor pressure) of the effusion cell in which each species is contained. The duration of spray is individually controlled for each beam by shutters, which control not only the open time (and thus dose), but also the sequence in which species reach the growth surface. By controlling the shutters and temperature of the evaporant (which control dose and flux, respectively), the layering sequence of the desired structure can be customized. This technique is capable of controlling the layering of oxides on a unit cell level.[76–80,110,113,117,119,124,157] A low growth temperature is frequently used to kinetically minimize subsequent bulk reordering and to minimize the loss of the customized (and often metastable) layered structures. The huge difference between surface and bulk diffusion rates in oxides[182,183] enables the growth of films with excellent structural order while at the same time preserving the potentially metastable layering of an oxide superlattice.

MBE is a vacuum deposition method in which well-defined thermal beams of atoms or molecules react at a crystalline surface to produce an epitaxial film. It was originally developed for the growth of GaAs and (Al,Ga)As,[184] but due to its unparalleled ability to control layering at the monolayer level and compatibility with surface-science techniques to monitor the growth process as it occurs, its use has expanded to other semiconductors as well as metals and insulators.[185,186] Epitaxial growth, a clean UHV deposition environment, *in situ* characterization during growth, and the notable absence of highly energetic species are characteristics that distinguish MBE from other thin film methods used to prepare functional oxide thin films. These capabilities are key to the precise customization of oxide heterostructures at the atomic layer level. MBE is traditionally performed in UHV chambers to avoid impurities. In addition to molecular beams emanating from heated crucibles containing individual elements, molecular beams of gases may also be introduced, for example to form oxides or nitrides. This variant of MBE is known as "reactive MBE"[187] in analogy to its similarity to "reactive evaporation," which takes place at higher pressures where well-defined molecular beams are absent. Reactive evaporation has also been extensively used to grow functional oxide films,[188] but here we limit our discussion to reactive MBE.

MBE has enjoyed significant success in the preparation of semiconductor microstructures with nanoscale thickness control and exceptional device characteristics. Examples of the thickness control achieved in semiconductors include interspersing layers as thin as one monolayer (0.28 nm) of AlAs at controlled locations into a GaAs film[189] and alternating monolayers of GaAs and AlAs to make a one-dimensional superlattice.[190] This nanoscale control has enabled tremendous flexibility in the design, optimization, and manufacturing of new devices, especially those making use of quantum effects.[191]

The use of MBE to grow functional oxides dates back to 1985, when it was used to grow $LiNbO_3$ films.[192,193] Since that time it has been used to grow the oxide superconductors $(Ba,K)BiO_3$, $(Ba,Rb)BiO_3$, $(La,Sr)_2CuO_4$, $YBa_2Cu_3O_{7-\delta}$, $NdBa_2Cu_3O_{7-\delta}$, $SmBa_2Cu_3O_{7-\delta}$, $DyBa_2Cu_3O_{7-\delta}$, and $Bi_2Sr_2Ca_{n-1}Cu_nO_{2n+4}$ for $n = 1$–11[76,110,117,119]; the oxide ferroelectrics $LiNbO_3$,[192–195] $LiTaO_3$,[194] $BaTiO_3$,[79,196–205] $PbTiO_3$,[79,112,206] and $Bi_4Ti_3O_{12}$[79,207,208]; the incipient ferroelectric $SrTiO_3$[79,114,197,198,204,209–218]; the ferromagnets $(La,Ca)MnO_3$,[219,220] $(La,Sr)MnO_3$,[219,221] and EuO[222–227]; the ferrimagnet Fe_3O_4[228]; the magnetoelectric Cr_2O_3[228]; the multiferroics $BiFeO_3$[229–231] and $YMnO_3$[232,233]; and superlattices of these phases.[4–7,76,79,110,119,124,157,199,234–237] Although the use of MBE to grow functional oxides is much less mature than its use for compound semiconductors, examples included in this article show how the layering capabilities of MBE can control the composition profile of multicomponent functional oxides along the growth direction with subnanometer precision. This capability is relevant to the fabrication of epitaxial device structures and to the nanoengineering of new functional materials.

The configuration of an MBE system for the growth of ferroelectric oxides differs in several important ways from today's more conventional MBE systems designed for the growth of semiconductors. The major differences are the required presence of an oxidant species, more stringent composition control, and to have adequate pumping to handle the oxidant gas load.

A schematic diagram of the growth chamber of an MBE system used in the growth of functional oxides is shown in Fig. 8. The particular example shown is a Veeco 930 (Veeco Compound Semiconductor Inc., MBE Operations, St. Paul, MN). A single-crystal substrate, heated to the desired growth temperature, is located near the center of the MBE growth chamber. Aimed at the substrate are molecular beams of the constituent elements of the functional oxide to be grown. Each molecular beam is created by a separate effusion cell, each at a different temperature to provide the desired flux of the particular element contained in a crucible within each effusion cell. Elements are used because multicomponent mixtures (especially oxides) rarely evaporate congruently.[238,239] In such

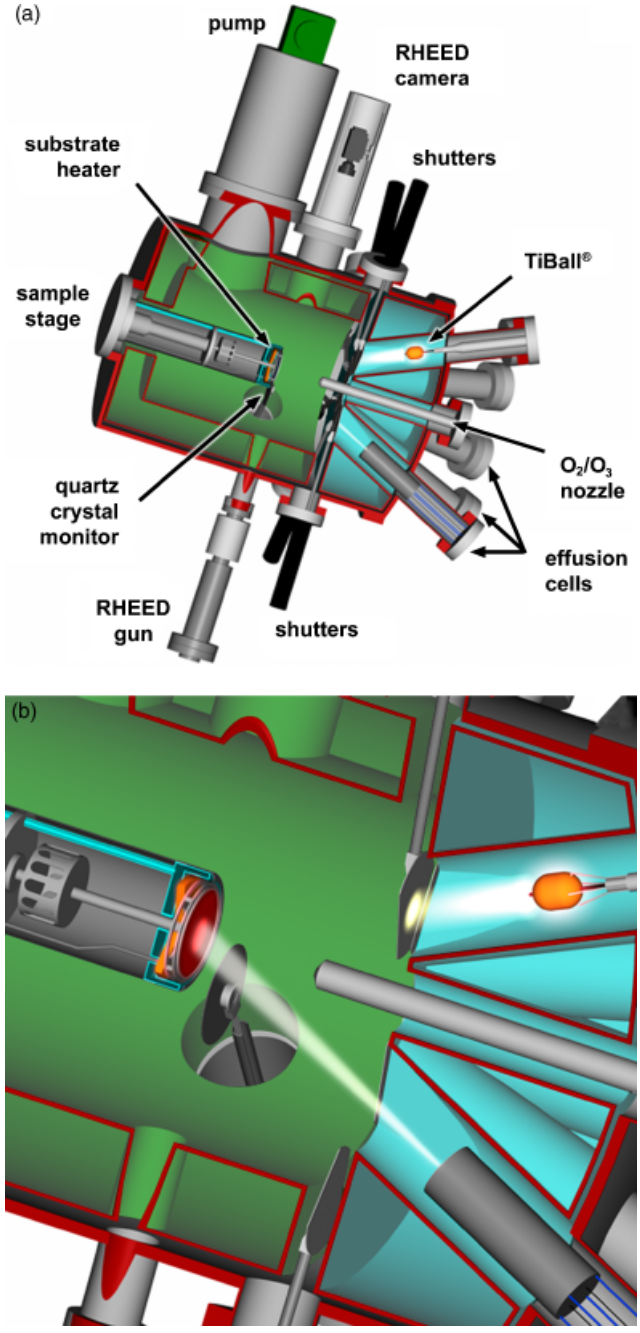

Fig. 8. A schematic diagram of the growth chamber of a molecular-beam epitaxy (MBE) system for the growth of multicomponent oxides. The growth chamber contains molecular beams (emanating from elemental sources), shutters, and ozone distillation and introduction, along with *in situ* characterization by reflection high-energy electron diffraction (RHEED), real-time spectroscopic ellipsometry (RTSE), mass spectrometry, quartz crystal microbalance (QCM), and atomic absorption spectroscopy (AA). The MBE geometry shown corresponds to a Veeco 930.

cases of incongruent evaporation, where the composition of the evaporant is not the same as its source, the composition of the source changes over time, resulting in a change in the absolute fluxes and relative concentrations of the species emitted from it. This would lead to serious composition-control issues. This problem is avoided by using elemental sources. An additional advantage of elemental sources is the completely independent control of the sequence in which the molecular beams of the elemental constituents are supplied to the substrate. The molecular beams impinge upon the substrate unless they are blocked by shutters. These shutters, which are positioned at the output end of each effusion cell, are controlled by a computer, which enables the elemental fluxes to be supplied to the substrate either at the same time (codeposition) or separately (sequential deposition). Because of the long mean free path inherent to MBE, the shutters do not need to seal tightly. Rather they only need to block the line-of-sight transfer of atoms or molecules from the source to the substrate. The chamber walls are kept cool to impede species that collide with the walls from ever reaching the substrate; ideally only the species in the molecular beams emanating from the sources with open shutters ever reach the substrate.

To oxidize the elemental species reaching the substrate to form the desired functional oxide, a molecular beam of oxidant is used. The tolerable pressure of this oxidant is limited so as not to destroy the long mean free path necessary for MBE. The maximum pressure depends on the MBE geometry, the element to be oxidized, and the oxidant species used, but oxidant pressures less than about 10^{-4} Torr are typically required for MBE.[76] While molecular oxygen has been used for the growth of oxides that are easily oxidized,[79,157,192,193,196–205,210–215,217,222–228,232,235–237] oxidants with higher activity are needed for the growth of ferroelectrics containing species that are more difficult to oxidize, e.g., bismuth-, lead-, or copper-containing oxides. For this purpose, purified ozone[4–7,76,79,110,112,114,117,119,203,206–209,216,218,230,231,234] or plasma sources[194,195,199,200,228,229,233] have been successfully used.

Inadequate composition control has been a major problem for previous oxide MBE work,[76] and the success and improvement of MBE for the controlled growth of multicomponent functional oxides is crucially dependent on accurate composition control. The use of atomic absorption spectroscopy (AA) for oxide MBE composition control has allowed fluxes to be measured with an accuracy of better than 1%.[240] The MBE system shown in Fig. 8 also contains a retractable quartz crystal microbalance to provide an absolute *in situ* flux measurement at the position of the wafer (before growth) for calibration of the fluxes before or after growth and calibration of the AA signals. The depositing fluxes of all the sources can be simultaneously monitored during growth by AA. The measured AA signal is fed into the MBE computer control system, which integrates the AA fluxes and closes the appropriate shutters after the desired dose has been delivered to the substrate. In addition, modern oxide MBE systems also contain features found in semiconductor MBE systems: *in situ* RHEED, mass spectrometry, load-locked wafer introduction, real-time spectroscopic ellipsometry,[241] substrate temperature measurement systems that utilize the temperature dependence of the bandgap of oxide substrates,[230,231,242,243] multibeam optical stress sensors (wafer curvature measurements to quantify film strain),[244,245] time-of-flight ion scattering and recoil spectroscopy,[246] and even low-energy electron microscopy.[246]

RHEED is widely used in MBE for the *in situ* characterization of the growing surface. The sensitivity of this grazing angle diffraction technique to surface structure is ideal for monitoring the evolution of growth from initial nucleation to the deposition of each subsequent layer. The formation of intermediate reaction products or impurity phases can be readily monitored and the growth conditions adjusted during growth accordingly.

The multielement deposition control, growth flexibility, and *in situ* monitoring advantages of MBE are well suited to the growth of multicomponent functional oxides that cannot be produced in single-phase form by bulk techniques, including the customized growth of new metastable materials, and heterostructures containing these phases. Other deposition techniques, in particular PLD, are, from an economic and process simplicity perspective, generally better suited than MBE to the synthesis of heterostructures made up of phases, each of which can be produced by bulk techniques in single-phase form (i.e., where the formation energy of each phase is sufficiently favored over other phases that could accommodate its composition).

III. Orientation Control

Except for the most trivial properties (e.g., density), functional properties depend in general on direction. Because of this there

exist in general optimal orientations for an epitaxial oxide film for any particular application. This might be the ones that align the spontaneous polarization of a ferroelectric material with the direction of the applied electric field from the electrodes that surround it to maximize the switchable polarization. Or it might be orientation that minimize the temperature variation of the resonant frequency of a piezoelectric oscillator. Whatever the application, the ability to control the orientation of the epitaxial film through the choice of substrate, its orientation (see, e.g., Fig. 6), and the growth conditions is a key advantage of epitaxial growth.[172,247–253] Orientation control is vital to the preparation of samples suitable for establishing the intrinsic properties of materials, especially those that cannot be prepared as bulk single crystals due to their metastability, high melting temperatures, or phase transitions that occur on cooling. When it comes to applications, techniques that can improve the functional properties of oxide films by controlling film texture through epitaxial growth on a grain-by-grain basis (local epitaxy) are also utilized, e.g., ion-beam-assisted deposition[254,255] and rolling-assisted biaxially textured substrates[256,257] for the growth of $YBa_2Cu_3O_7$ superconducting cables[258] as well as Pb(Zr,Ti)O_3 in FeRAMs.[259]

IV. Integration of Oxides

(1) Substrates and Substrate Preparation

The importance of the quality of the underlying crystalline template, on which an epitaxial film is grown, cannot be overemphasized. For conventional semiconductors (e.g., silicon and GaAs) highly perfect single crystals, chemical mechanical polishing, and chemical etching methods to prepare smooth and damage-free surfaces for epitaxial growth, and detailed knowledge of surface reconstructions all exist, and are a key to the success of semiconductor technology. For the growth of superlattices of functional oxides, tunneling heterostructures, etc., where the intrinsic properties of films with thickness in the nanometer range are desired, the availability of appropriate substrates and methods to prepare smooth and highly perfect surfaces on which epitaxial growth is initiated are also crucial.

For functional oxides with perovskite structures (e.g., $SrTiO_3$, $BiMnO_3$, $BiFeO_3$, Pb(Zr,Ti)O_3, and $PbZn_{1/3}Nb_{2/3}O_3$–$PbTiO_3$), chemically and structurally compatible perovskite substrate materials are needed. Intensive work on high-temperature superconductors stimulated the production of many perovskite single crystals[230–269] to diameters up to 4 in. as well as spawning a number of new perovskite and perovskite-related substrates.[270–273] These single-crystal perovskite and perovskite-related substrates include $YAlO_3$,[265] $LaSrAlO_4$,[270] $LaAlO_3$,[267,269] $LaSrGaO_4$,[271] $NdGaO_3$,[261,266] $(LaAlO_3)_{0.29}$–$(Sr_{1/2}Al_{1/2}TaO_3)_{0.71}$ (LSAT),[272,274] $LaGaO_3$,[260] $SrTiO_3$,[275–278] and $KTaO_3$[263]; many are produced with structural perfection rivaling that of conventional semiconductors. The pseudotetragonal or pseudocubic *a*-axis lattice spacings offered by these commercial substrates, together with the corresponding lattice spacings of several functional oxides with perovskite and perovskite-related structures, are shown in Fig. 9. As can be seen in Fig. 9, the lattice constants of the available perovskite substrates tend to be smaller than many of the ferroelectric and multiferroic[279] perovskites of current interest. This is because most of the commercially available perovskite substrates were developed for high-temperature superconductors, which typically have lattice constants in the 3.8–3.9 Å range. Rare-earth scandate ($REScO_3$) substrates have been recently developed with the larger lattice constants of ferroelectric and multiferroic perovskites in mind.[280–284]

In addition to appropriate substrate single crystals, a method to prepare substrates with a specific chemical termination of the surface is a prerequisite for atomic-layer-controlled thin film growth of epitaxial heterostructures. For example, chemical-mechanically polished (001) $SrTiO_3$ substrates display a mixture of SrO and TiO_2 terminated surfaces. Kawasaki *et al.*[285] showed that an NH_4F-buffered HF solution with controlled pH enables etching of the more basic SrO layer and leaves a completely TiO_2 terminated surface on the substrate.[285] This method of preparing a TiO_2-terminated (001) $SrTiO_3$ surface has been further perfected by Koster *et al.*[286] SrO-terminated (001) $SrTiO_3$ substrates can also be prepared.[287] A means to prepare low-defect surfaces with controlled termination has also been developed for $(001)_p$ $LaAlO_3$,[288,289] (110) $NdGaO_3$,[289] $(001)_p$ LSAT,[289] $KTaO_3$,[290] and (110) $DyScO_3$ substrates.[288] Here the *p* subscript refers to pseudocubic indices.

(2) Epitaxial Oxide Heterostructures

(A) Structural Quality of Epitaxial Films Versus Single Crystals: An example of the structural perfection possible in functional oxide films is shown in Fig. 10(a) where the rocking curve full-width at half-maximum (FWHM) of a strained $SrTiO_3$ film and typical commercial $SrTiO_3$ single crystals are compared. With rocking curve widths as narrow as 7 arc sec,[216,218,291] these epitaxial $SrTiO_3$/$DyScO_3$ films not only have the highest structural quality ever reported in heteroepitaxial films of any oxide grown by any technique, but they even have better structural perfection than $SrTiO_3$ single crystals.[277,278,292] Similarly, as shown in Fig. 10(b), the growth of $BaTiO_3$ films on $GdScO_3$ substrates has achieved films with narrower rocking curves than $BaTiO_3$ single crystals.[291] Epitaxial films of $BiFeO_3$,[293] $BiMnO_3$,[294] $EuTiO_3$, (La,Sr)MnO_3,[295] and $BaTiO_3$/$SrTiO_3$ superlattices[237] all with rocking curve FWHM $\leq$ 10 arc sec have been prepared by MBE on $REScO_3$ substrates. These narrow rocking curves are made possible by the excellent structural perfection of commercially available $REScO_3$ substrates[282,284]; they are grown by the Czochralski method, which is not applicable to either $SrTiO_3$ or $BaTiO_3$. The rocking curve widths of

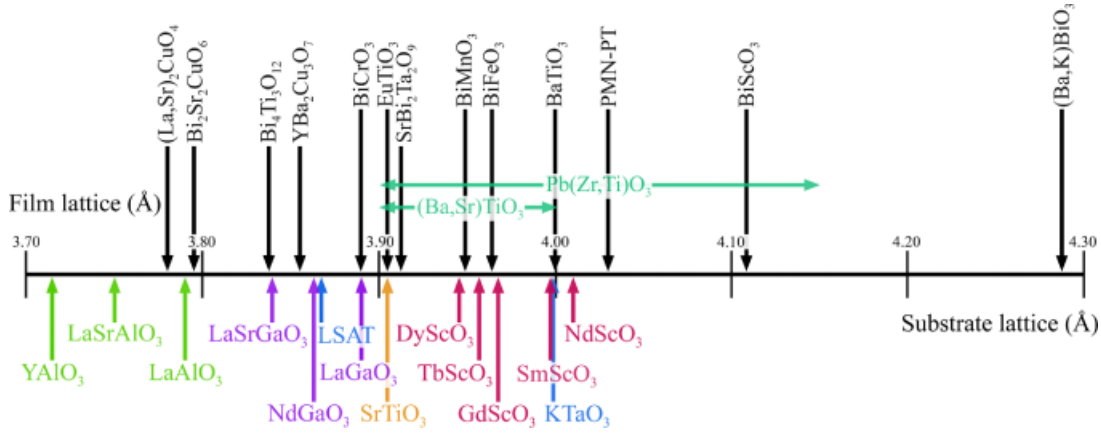

Fig. 9. A number line showing the pseudotetragonal or pseudocubic *a*-axis lattice constants in angstroms of some perovskites and perovskite-related phases of current interest (above the number line) and of some of the perovskite and perovskite-related substrates that are available commercially (below the number line). (Adapted from Schlom *et al.*[345])

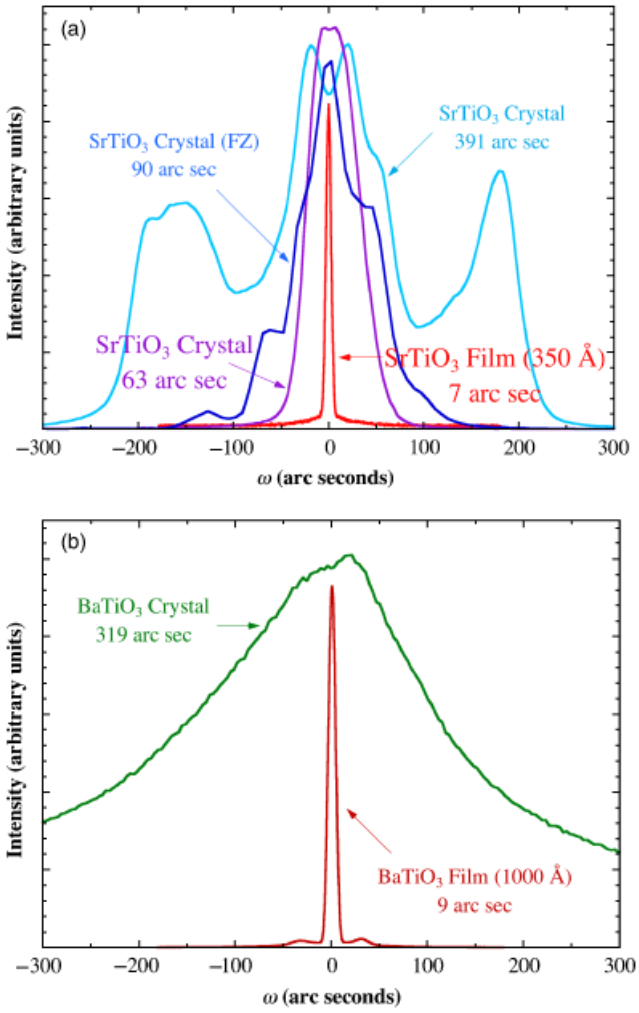

Fig. 10. (a) Rocking curves and full-width at half-maximum (FWHM) of three commercial $SrTiO_3$ single crystals (one grown by floating zone (FZ) and two by flame fusion) showing the variation in structural quality together with an epitaxial 350-Å-thick $SrTiO_3$ film grown on a (110) $DyScO_3$ substrate by molecular-beam epitaxy (MBE) at 650°C under biaxial tension of $\varepsilon_s = +1.1\%$. (b) Rocking curves and FWHM of a commercial $BaTiO_3$ single crystal and an epitaxial 1000-Å-thick $BaTiO_3$ film grown on a (110) $GdScO_3$ substrate by MBE at 650°C under biaxial compression of $\varepsilon_s = -1.0\%$. (From Schlom *et al.*[345])

these functional oxide films are within instrumental error identical to those of the substrates upon which they are grown.

(3) Epitaxial Integration of Oxides with Semiconductors

An important technological enabler is the ability to epitaxially integrate functional oxides with conventional semiconductors. Although the structural quality of films of functional oxides grown on semiconductor substrates is far from the quality of these materials grown on appropriate oxide substrates, significant improvements have been made over the last seven decades (and especially in the last two decades) because oxides were first epitaxially integrated with semiconductors.[296,297] Several routes now exist for the epitaxial integration of functional oxides with semiconductors including (001) Si,[196,204,205,210,212–215,225,226,298–306] (001) Ge,[198,204,307,308] (001) GaAs,[304,309,310] (001) InP,[311,312] and (0001) GaN.[226,313–315] Using these routes a multitude of functional oxides, with conducting top and bottom electrodes when desired, have been epitaxially integrated with semiconductor materials.[196,198,204,205,225,226,298,299,301,304,307–309,313,314,316–326] This capability could play a significant role in future hybrid devices.

Combining functional oxides with existing semiconductor technology greatly enhances the materials properties available for use in microelectronics, optoelectronics, and spintronics, by bringing new functionalities to conventional semiconductor platforms. Epitaxial integration with silicon is particularly important due to it being the backbone of modern semiconductor technology. Unfortunately, direct growth of functional oxides on silicon is frequently accompanied by extensive interdiffusion or chemical reactions that degrade the properties of the oxide, the underlying silicon, or both, and leads to electrically active defects at the semiconductor/oxide interface (D_{it}).[327–333] Such defects at the semiconductor/oxide interface preclude many potential applications, e.g., FeRAMs with a nondestructive readout based on the resistance of the semiconductor channel.[334–343] That $PbTiO_3$, $BaTiO_3$, and $SrTiO_3$ are all unstable in direct contact with silicon is evident from the chemical reactions below[344,345]:

$$3Si + PbTiO_3 \xrightarrow{\Delta G^\circ_{1000\,K} = -79.312 \frac{kJ}{mol}} PbSiO_3 + TiSi_2, \quad (1)$$

$$3Si + BaTiO_3 \xrightarrow{\Delta G^\circ_{1000\,K} = -101.802 \frac{kJ}{mol}} BaSiO_3 + TiSi_2, \quad (2)$$

and

$$3Si + SrTiO_3 \xrightarrow{\Delta G^\circ_{1000\,K} = -87.782 \frac{kJ}{mol}} SrSiO_3 + TiSi_2. \quad (3)$$

For each of these reactions $\Delta G^\circ_{1000\,K}$ is the free energy change of the system when the reaction between reactants and products, all taken to be in their standard state (the meaning of the $^\circ$ superscript), proceeds in the direction indicated at a temperature of 1000 K.[346] Note that all of the above reactions are energetically favorable ($\Delta G < 0$). This is true not only at 1000 K (a typical processing temperature), but at all temperatures between room temperature and the melting point of silicon. Consequently, the focus of a great deal of materials research has been devoted to overcoming this fundamental obstacle through the identification of compatible buffer layers for use between silicon and functional oxides.[234,344,347] Many factors must be considered in selecting materials for use as buffer layers between silicon and a particular oxide: chemical reactions, interdiffusion, crystal structure, and lattice match are some of the most important.[273,304,347,348]

The importance of avoiding interfacial chemical reactions, i.e., the need for a thermodynamically stable interface between the silicon substrate and the functional oxide or the buffer layer leading to the functional oxide is underscored by the observation that nearly all oxides that have been directly epitaxially integrated with silicon are either thermodynamically stable or possibly thermodynamically stable in contact with silicon. A periodic table depicting which elements have binary oxides that are stable or potentially stable in contact with silicon is shown in Fig. 11.[344,349] Also shown in Fig. 11 are those elements with binary oxides that have been epitaxially grown on silicon. BaO is the only binary oxide that thermodynamic data show to be unstable in contact with silicon, yet can be grown epitaxially on it at low temperatures (below ~200°C).[204,210,306] Nonetheless when BaO/Si films are heated or when growth is attempted at higher temperatures, reaction between BaO and silicon is observed as expected.[350–353]

The large difference in thermal expansion coefficient between silicon (which averages 3.8×10^{-6} K^{-1} between room temperature and 700°C)[354] and oxide ferroelectrics (typically 10×10^{-6} K^{-1}) remains a significant problem. Upon cooling after growth, the functional oxide films are in a state of biaxial tension, which can lead to cracking in thick films.[304,355]

V. Customizing Oxides at the Atomic Layer Level

(1) Metastable Phases

(A) $BiMnO_3$, Ba_2RuO_4, $LuScO_3$: Epitaxial growth can be used to create metastable phases by utilizing lattice misfit strain energies and interfacial energies to favor the

desired metastable phase over the equilibrium phase (epitaxial stabilization).[159,356–358] In contrast to bulk synthesis, in epitaxial growth, strain and interfacial energies play a significant role. Specifically, strain energies due to lattice mismatch are often sufficient to shift the energetics of phase stabilities. For sufficiently thin films, the interfacial free energy and strain free energy terms can overcome the volume free energy differences between polymorphs to make a desired metastable form have the lower total free energy (volume+interfacial+strain). Numerous examples of epitaxially stabilized phases exist in semiconductor, metal, and alkali halide systems.[182,356–359] Examples of metastable functional oxides grown by PLD and MBE include Ba_2RuO_4,[158] $BiMnO_3$,[160] and $LuScO_3$.[161] In these examples a substrate with a good lattice and structural match to the desired metastable phase is used to provide the interfacial+strain free energy bias that favors it over the equilibrium phase. Some of these metastable phases have been produced in bulk by high-pressure synthesis[158,160]; others are totally new.[161]

$BiMnO_3$ holds the record (Table I) as the material that is believed to be simultaneously ferromagnetic and ferroelectric at the highest temperature[28–30] on which a conventional polarization-electric field hysteresis loop has been reported.[28] Although it was the suggestion of possible simultaneous ferromagnetism and ferroelectricity in $BiMnO_3$ that started the recent renaissance of activity in multiferroics,[29] advances in computers and first principles methods have allowed these authors to perform more accurate calculations from which they conclude that $BiMnO_3$ is not ferroelectric.[30] At atmospheric pressure $BiMnO_3$ is unstable and phase separates to a mixture of Bi_2O_3 and $Bi_2Mn_4O_9$.[360] In bulk, $BiMnO_3$ is made in powder form at pressures of typically 60 000 atm and a temperature of 1100 K, where it is the stable phase.[361–363] But to establish the properties of $BiMnO_3$ and especially to determine whether or not it is truly ferroelectric, large single crystals or epitaxial films are desired. Using epitaxial stabilization, $BiMnO_3$ films have been prepared with several orientations.[30,160] Although the epitaxial films have the same symmetry as $BiMnO_3$ made at high pressure, they are too leaky (so far) for reliable ferroelectric measurements. Nonetheless, second harmonic generation (SHG) measurements made on metastable $BiMnO_3$ films are consistent with it being ferroelectric.[30]

Because of the unusual properties of the superconductor Sr_2RuO_4,[364] ruthenates with closely related structures are of great interest to help pin down the characteristics of Sr_2RuO_4 responsible for its unusual superconducting behavior. For example, in light of the observation that hydrostatic pressure reduces the superconducting transition temperature (T_c) of Sr_2RuO_4,[365] it is desirable to investigate the properties of Ba_2RuO_4 in which the larger Ba^{2+} ion is substituted for Sr^{2+}, expanding the structure. Utilizing such chemical substitutions to induce "chemical pressure" (negative pressure in this case) is common in superconducting research.[366] The only hitch to its use in this case is that Ba_2RuO_4 is not isostructural with Sr_2RuO_4 when synthesized at atmospheric pressure.[§§,¶¶ 367–373] In bulk, Ba_2RuO_4 powder isostructural with Sr_2RuO_4 has been synthesized using pressures of 65 000 atm.[371] As an alternative to the difficult task of growing extremely pure single crystals at 65 000 atm, epitaxial stabilization has been used to prepare the metastable K_2NiF_4-type polymorph of Ba_2RuO_4.[158]

$LuScO_3$ is another example of a new metastable phase prepared using epitaxial stabilization.[161] All attempts to prepare it using high-pressure synthesis techniques as a perovskite (isostructural to the available $REScO_3$ substrates), using pressures up to 60 000 atm, were unsuccessful.[374,375] But with an appropriate perovskite substrate, the perovskite polymorph of $LuScO_3$ was readily synthesized by epitaxial stabilization.[161]

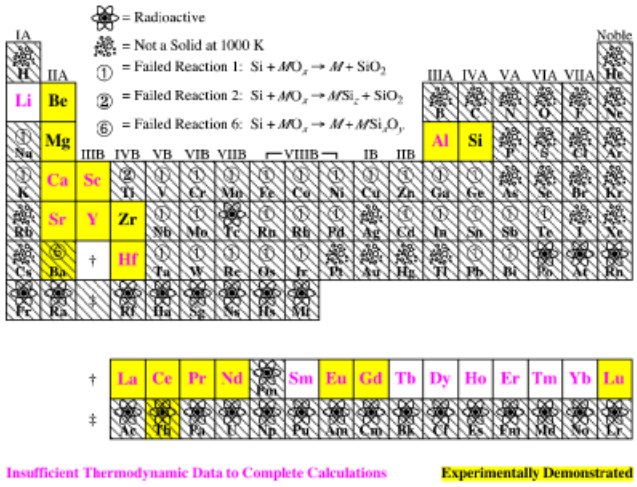

Fig. 11. Pictorial summary of which elements M have an oxide (MO_x) that may be thermodynamically stable in contact with silicon at 1000 K. Elements M having no thermodynamically stable or potentially thermodynamically stable oxide (MO_x) are shaded (hatched), and the reason for their elimination is given. Also shown are the elements M having an oxide (MO_x) that has been experimentally demonstrated to be stable in direct contact with silicon. Performing the thermodynamic analysis over the full range of temperatures for which relevant thermodynamic data are available (as much as 300–1600 K) does not alter the conclusions shown. (Adapted from Schlom and Haeni[349].)

These are just a few of many success stories in the preparation of metastable functional oxides by epitaxial stabilization.[159] An obvious approach to prepare the metastable ferroelectric ferromagnet with the highest predicted transition temperature, $FeTiO_3$ with the $LiNbO_3$ structure (see Table I) is epitaxial stabilization.[27]

(2) *New Phases*

(A) Ruddlesden–Popper Phases: In addition to preparing new metastable phases, MBE can be used to select a particular phase from among a homologous series of phases with nearly equal formation energies. An example is the creation of high-n Ruddlesden–Popper phases. These layered structures can be created by atomic-layer engineering using MBE. An example is the phase-pure growth of the $n = 1$–5 members of the $Sr_{n+1}Ti_nO_{3n+1}$ and $Sr_{n+1}Ru_nO_{3n+1}$ homologous series.[77–80] The crystal structures of the $n = 1$–5 members of this homologous series are shown in Fig. 3.

Complexities of the SrO–TiO_2 phase diagram have frustrated efforts to prepare bulk single crystals of any members of the $Sr_{n+1}Ti_nO_{3n+1}$ series other than the $n = \infty$ end member, $SrTiO_3$. The single-crystal growth of the $n = 1$ member of the series, Sr_2TiO_4, is complicated (if not prohibited) by a phase transition at 1550°C and a peritectic decomposition at 1860°C.[376] The $n = 2$ member, $Sr_3Ti_2O_7$, has a peritectoid decomposition at 1580°C,[376] which prohibits growth of single crystals of this phase from the melt.

Using reactive MBE the first five members of these Ruddlesden–Popper homologous series have been prepared.[77–80] X-ray diffraction (XRD) (Fig. 12) and high-resolution cross-sectional TEM images (Fig. 13) confirm that these films are epitaxially oriented and contain relatively few intergrowths. Detailed investigations using quantitative HRTEM methods reveal that the films have the expected $n = 1$–5 structures.[78] Among these films, the $n = 1$–3 thin films are nearly free of intergrowths, while the $n = 4$ and 5 thin films contain noticeably more antiphase boundaries in their perovskite sheets and intergrowth defects.[78] The $Sr_{n+1}Ru_nO_{3n+1}$ films contain fewer defects than their $Sr_{n+1}Ti_nO_{3n+1}$ counterparts and even the high-n $Sr_{n+1}Ru_nO_{3n+1}$ films are >98% phase pure.[80]

[§§]Although these authors did not determine the crystal structure of the stable form of Ba_2RuO_4 that they synthesized at atmospheric pressure and 1000°–1100°C, they did report the XRD pattern of the Ba_2RuO_4 that they made (which is completely different than the K_2NiF_4 form reported by Kafalas and Longo[367]) and described it as having "low symmetry."

[¶¶]There is one report in the literature of the synthesis of Ba_2RuO_4 with the K_2NiF_4 structure that does not mention the use of high-pressure methods: Prosychev and Shaplygin[370,371] and Gadzhiev and Shaplygin.[372,373] In addition to not stating the synthesis pressure, however, no X-ray or structural data are presented. As Kafalas and Longo[367] and Popova *et al.*[368,369] both contradict this claim and present X-ray data, their results are taken as evidence that Ba_2RuO_4 with the K_2NiF_4 structure is metastable at atmospheric (or lower) pressure and synthesis temperatures of 1000°–1100°C, as used in both Popova *et al.*[368,369] for bulk synthesis and Jia *et al.*[158] for epitaxial films.

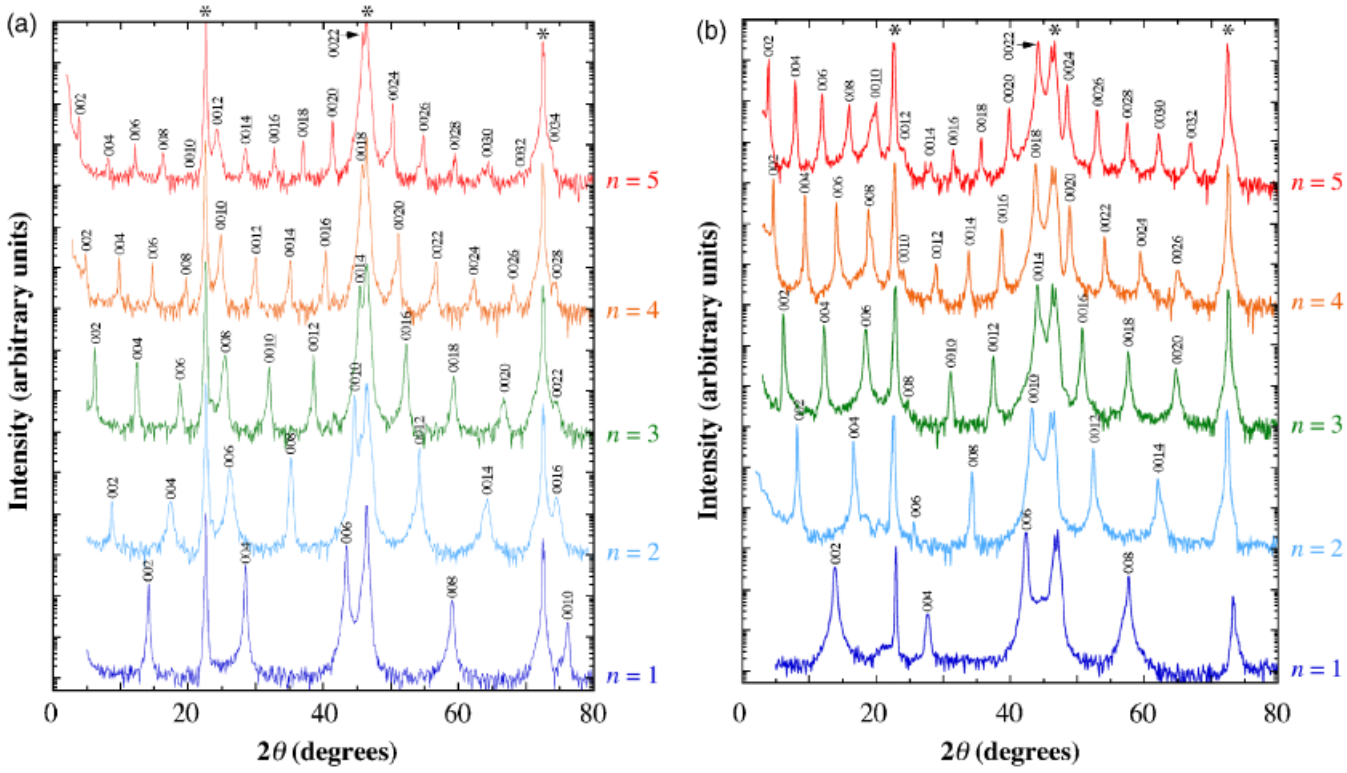

Fig. 12. θ–2θ X-ray diffraction scans of the first five members of the (a) $Sr_{n+1}Ti_nO_{3n+1}$ (reprinted from Haeni *et al.*,[77] with permission; ©2001 American Institute of Physics) and (b) $Sr_{n+1}Ru_nO_{3n+1}$ Ruddlesden–Popper homologous series (reprinted from Tian *et al.*,[80] with permission; ©2007 American Institute of Physics). Substrate peaks are labeled with an (*) and the plots are offset for clarity.

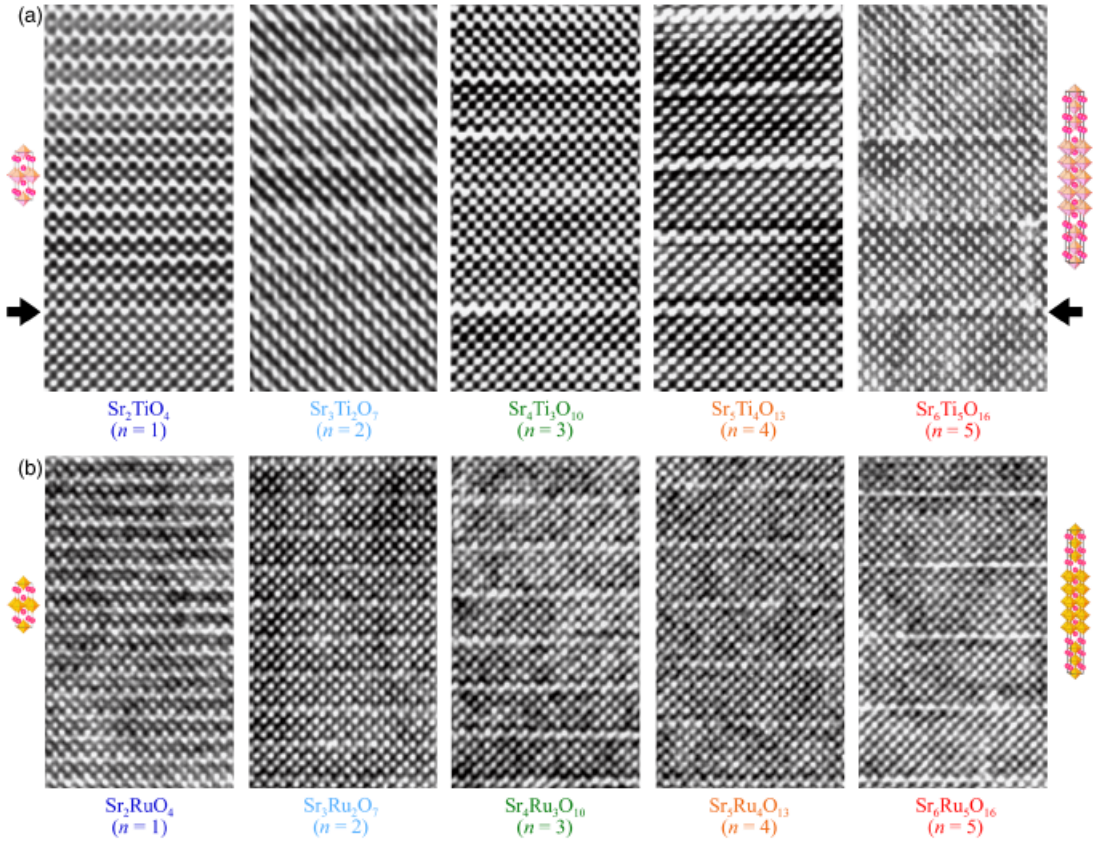

Fig. 13. High-resolution cross-sectional TEM images of the same five members of the (a) $Sr_{n+1}Ti_nO_{3n+1}$ (reprinted from Haeni *et al.*,[77] with permission; ©2001 American Institute of Physics) and (b) $Sr_{n+1}Ru_nO_{3n+1}$ Ruddlesden–Popper homologous series shown in Fig. 12 (reprinted from Tian *et al.*,[80] with permission; ©2007 American Institute of Physics). The two adjacent white rows in the images correspond to the [100] projections of the rock-salt SrO layers. Between the double SrO layers lies the [100] projection of the $SrTiO_3$ and $SrRuO_3$ perovskite sheets. The arrows in (a) indicate the position of the interface between the $Sr_{n+1}Ti_nO_{3n+1}$ films and (100) $SrTiO_3$ substrate on which they were grown.

The preparation of these materials as epitaxial films has allowed their properties to be explored. The full dielectric constant tensor of the $Sr_{n+1}Ti_nO_{3n+1}$ epitaxial films has been measured[377] as a function of frequency and temperature and compared with theory.[378] Preparation of the $n = 1$–5 $Sr_{n+1}Ru_nO_{3n+1}$ Ruddlesden–Popper phases has allowed the effects of dimensionality on the magnetic properties of these phases to be established. It is found that decreasing the dimensionality of this system, i.e., the effect of decreasing n on the magnetic properties of $Sr_{n+1}Ru_nO_{3n+1}$ phases, leads to a systematic reduction in ferromagnetism.[80] The minimum value of n for ferromagnetism is $n = 3$ ($Sr_4Ru_3O_{10}$). This corresponds to the case where at least one RuO_2 sheet in the structure is surrounded by RuO_2 sheets from above and below (see Fig. 3). For $n = 1$ and 2 $Sr_{n+1}Ru_nO_{3n+1}$ phases, no RuO_2 sheets are surrounded by RuO_2 sheets, resulting in the loss of ferromagnetism.

(B) Aurivillius Phases: Just as thin film techniques can be used to prepare and explore the properties of high-n Ruddlesden–Popper phases that cannot be realized by bulk synthesis, they can also be used to prepare high-n Aurivillius phases. An example is the $n = 7$ Aurivillius phase $Sr_4Bi_4Ti_7O_{24}$ whose XRD and cross-sectional TEM are shown in Fig. 14. This film was grown by PLD and is the highest-n Aurivillius phase ever reported.[379] As the schematic shows, this phase contains seven $SrTiO_3$ perovskite layers between Bi_2O_2 sheets.

In addition to increasing the number of perovskite layers between Bi_2O_2 layers in Aurivillius phases, different perovskite layers can be inserted between the Bi_2O_2 layers to alter the properties of the resulting phase as shown schematically in Fig. 4. This can be used, for example, as a composite approach on an atomic scale to the fabrication of a magnetic ferroelectric. Many Aurivillius phases are ferroelectric,[380] e.g., $Bi_4Ti_3O_{12}$, and one could imagine introducing a ferromagnetic perovskite, e.g., $BiMnO_3$, into $Bi_4Ti_3O_{12}$ to construct a ferromagnetic ferroelectric. Although in bulk, manganese has been found to have negligible solubility in $Bi_4Ti_3O_{12}$ itself,[381] this is not a constraint for thin film growth where the targeted phase is a superlattice composite of $BiMnO_3$ and $Bi_4Ti_3O_{12}$. A composite approach to fabricating two-phase ferroelectric–magnetic composite heterostructures[382–385] has been shown to be viable, and refining the scale of the composite down to the atomic scale is a useful goal in terms of both maximizing elastic coupling and exploring the spatial limits of this coupling. At the macroscale, 3–3 bulk composites[386] have mechanical stability issues and exhibit poor coupling.[387] At the microscale, tape-cast structures avoid mechanical issues and exhibit stronger coupling,[388] but granular orientation effects are likely to reduce mechanical coupling efficiency and to complicate analysis of strain within the crystalline lattice. At the nanoscale, thin film structures have been the most effective in producing multiferroic composite behavior. Although a 2–2 composite (stack of films on a substrate)[386] is convenient for electrical characterization, a nonferroic substrate will clamp the response.[389] A solution has been to use a ferroic substrate,[390] but the limited selection of substrate materials can be problematic, as can be domain effects in a noncentrosymmetric substrate crystal. Another solution has been to use a 1–3

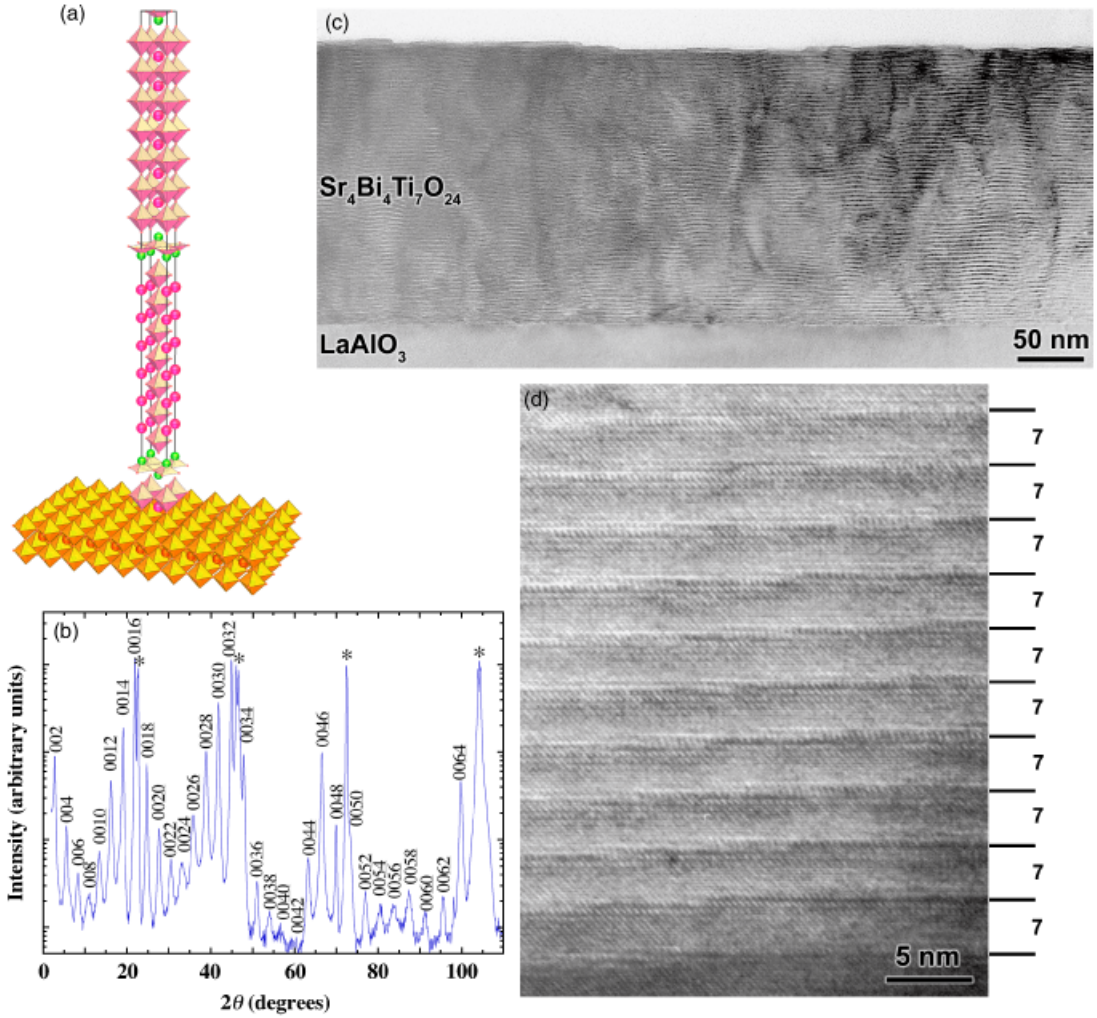

Fig. 14. An epitaxial film of the $n = 7$ Aurivillius phase $Sr_4Bi_4Ti_7O_{24}$. (a) Crystal structure showing the orientation relationship between the (001) $Sr_4Bi_4Ti_7O_{24}$ film and the (001) $LaAlO_3$ substrate, (b) θ–2θ X-ray diffraction scan in which the substrate peaks are labeled with an asterisk, and cross-sectional TEM images (c) showing the full film and (d) an HRTEM image showing the perfection of the layering.

composite system that maximizes out-of-plane mechanical coupling in a film, for example $BaTiO_3$–$CoFe_2O_4$.[391] The ultimate level for forming a composite is at the atomic or unit-cell scale. Most physical or phase separation approaches to composites are not feasible at this scale; hence, natural multiferroics, single-phase materials that can incorporate substructures of both types is a noteworthy approach. This composite strategy was recently applied using PLD to the $n = 6$ Aurivillius phase $Bi_7Mn_{3.75}Ti_{2.25}O_{21}$.[41]

VI. Thin Film Routes to Enhance the Properties of Oxides

(1) Epitaxial Strain

An advantage of using thin films as a platform to explore size effects in ferroelectrics is that they allow huge strains to be applied—strains far larger than where bulk ferroelectrics would crack.[392,393] These strains can be imparted through differences in lattice parameters and thermal expansion behavior between the film and the underlying substrate or arise from defects formed during film deposition.[393–396] Fully coherent, epitaxial films have the advantage that high densities of threading dislocations (e.g., the $\sim 10^{11}$ dislocations/cm^2 observed in partially relaxed $(Ba_xSr_{1-x})TiO_3$ films)[397,398] are avoided. Strain fields around dislocations locally alter the properties of a film, making its ferroelectric properties inhomogeneous and often degraded.[399–401] As the film is clamped to the substrate, but free in the out-of-plane direction, the effect of a biaxial strain state on properties can be dramatic.

The effects of biaxial strain and temperature on ferroelectric transitions and domain structures have been theoretically studied for a number of ferroelectrics.[291] These include $(001)_p$-oriented $PbTiO_3$,[402–406] $BaTiO_3$,[203,402,407,408] and $Pb(Zr_xTi_{1-x})O_3$,[409–411] where the subscript p refers to the pseudocubic index, and even $(001)_p$ $SrTiO_3$,[114,412–415] which is not normally ferroelectric, but can become ferroelectric when strained. Strain phase diagrams for these thin films, which graphically display the ferroelectric phase transition temperatures and domain structures as a function of strain, have been constructed using thermodynamic analysis and phase-field simulations.

The strain phase diagrams in Figs. 15 and 16, for $(001)_p$ $BaTiO_3$ and $(001)_p$ $SrTiO_3$, respectively, imply that ferroelectrics can be very sensitive to strain. These predictions imply that a biaxial tensile strain of order 1% will shift the T_C of $SrTiO_3$, a material that normally is not ferroelectric at any temperature, to the vicinity of room temperature (see Fig. 16).[114,291,412–415] Comparable shifts in transition temperature, roughly 300 K per percent biaxial strain, are expected for $BaTiO_3$ (Fig. 15)[203,291,402,407,408] and $PbTiO_3$.[291,402–406] These predictions have been borne out by experiments on strained $SrTiO_3$,[114,216,291,416–423] $PbTiO_3$,[291,424] and $BaTiO_3$ films[203,291]; large strain effects of comparable magnitude were observed earlier in $KTaO_3/KNbO_3$,[425] $SrTiO_3/SrZrO_3$,[426] and $SrTiO_3/BaZrO_3$ superlattices,[427] and strained $(Ba,Sr)TiO_3$ films.[428,429]

T_C has been determined on strained thin films using several experimental methods. The conventional method of measuring a hysteresis loop is problematic when the electrical leakage current is high, e.g., for extremely thin films where currents due to electron tunneling are high or at elevated temperatures where significant ionic conductivity can occur. It also requires electrodes, which alters the electrical boundary conditions and can impose experimental complications. Two methods that are applicable at high temperatures to extremely thin ferroelectric films have become popular. One method involves measuring the temperature dependence of the out-of-plane lattice parameter of the strained film. A kink in the out-of-plane lattice parameter occurs at T_C. Such kinks at T_C have been observed in a number of coherently strained ferroelectric films[203,424,425] and are expected from theory.[203,424,430] A second method is to use SHG. Only materials that lack inversion symmetry exhibit an SHG signal. All ferroelectrics must lack inversion symmetry, but there are many materials that lack inversion symmetry and are not ferroelectric. This makes SHG a necessary, but insufficient probe for ferroelectricity. A better test for ferroelectricity with SHG is to monitor changes in the symmetry of the SHG response that occur when external electric fields are applied; such changes imply the presence and rearrangement of ferroelectric domains.[431–435]

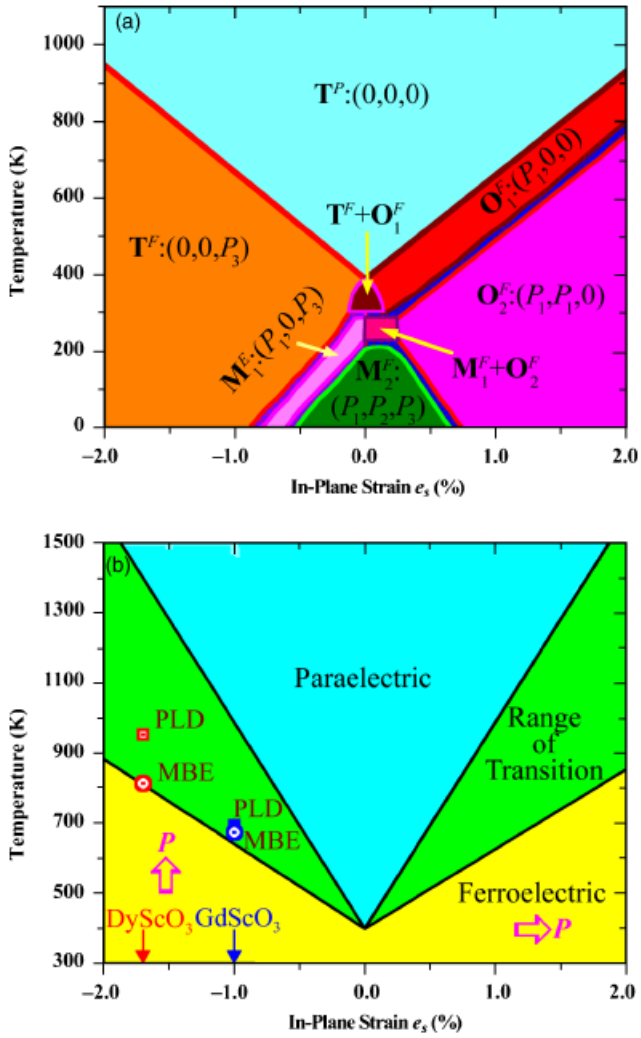

Fig. 15. (a) The strain phase diagram of $(001)_p$-oriented $BaTiO_3$ obtained from phase-field simulations. The letters **T**, **O**, and **M** used in the phase notations indicate tetragonal, orthorhombic, and monoclinic crystallographic symmetries, respectively, under a constraint. The paraelectric and ferroelectric natures of the phases are revealed by the superscript P and F, respectively. $\mathbf{M}_1^F + \mathbf{O}_2^F$ implies a mixture of $\mathbf{M}_1^F$ and $\mathbf{O}_2^F$ phases. The components of the polarization vector $\boldsymbol{P}$ corresponding to the phases (along the crystallographic directions of pseudocubic $BaTiO_3$) are indicated within the parentheses following the phase notation (reprinted from Li and Chen,[408] with permission; ©2006 American Institute of Physics). (b) A simplified strain phase diagram of $BaTiO_3$ showing the error bars of the prediction from thermodynamic analysis as well as the results on commensurately strained $BaTiO_3$ films grown on various substrates (From Choi *et al.*[203] Reprinted with permission from AAAS.)

(A) Strained $SrTiO_3$: Ferroelectricity in strained $SrTiO_3$ films has been inferred from dielectric constant versus temperature measurements,[114,216,291,421,422] the tunability of the dielectric constant through an applied electric field at temperatures just above T_C,[114,291] SHG measurements as a function of temperature and applied fields,[416,417,419,421] transmission IR measurements as a function of temperature showing changes in the soft modes,[423] piezo-force microscopy measurements as a function of temperature,[416] time-resolved confocal scanning optical microscopy,[114,418] electro-optic response measurements,[417,420] and conventional hysteresis loops as a function of

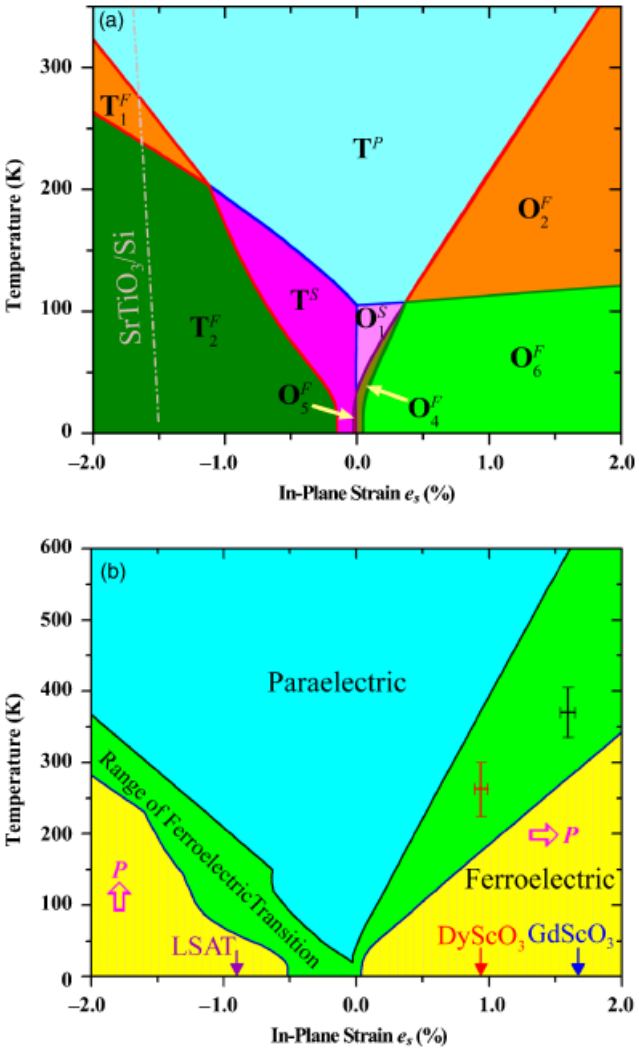

Fig. 16. (a) The strain phase diagram of $(001)_p$-oriented $SrTiO_3$ calculated assuming a single-domain state for all structural and ferroelectric phases (adapted from Li *et al.*[415]). Identical nomenclature as Fig. 15 is used to describe the crystallographic symmetry of the phases and order parameters. This diagram has only a minor difference from that presented in Pertsev *et al.*[412,413] (b) A simplified strain phase diagram of $SrTiO_3$ showing the error bars of the prediction from thermodynamic analysis as well as the results on commensurately strained $SrTiO_3$ films grown on various substrates. (Adapted from Haeni *et al.*[114])

temperature and orientation.[216,421,422] The combined experimental evidence from these methods is consistent with the predicted effect of strain on the ferroelectric transition and antiferrodistortive transition of $SrTiO_3$.[114,412–417,419,421] With strain, $SrTiO_3$ becomes a multiferroic.[416,419,421]

An overlay of the paraelectric-to-ferroelectric transition temperature found in commensurately strained $SrTiO_3$ films grown on different substrates is shown in Fig. 16(b) together with a simplified version of the prediction of strain on $SrTiO_3$ (Fig. 16(a)) that includes the error bars of the thermodynamic analysis. Thermodynamic analysis utilizes the electrostrictive coefficients and elastic constants of $SrTiO_3$. The strain phase diagram shown in Fig. 16(a) was made using a chosen set of these coefficients from the literature for measurements on $SrTiO_3$ single crystals. If instead of using a chosen set of these property coefficients, the range of reported values of the electrostrictive and elastic coefficients of $SrTiO_3$ single crystals are included in the thermodynamic analysis, the uncertainty of the predicted effect of strain on the ferroelectric transition of $SrTiO_3$ emerges. This range is explicitly shown in Fig. 16(b). As is evident, the observed effect of strain on the ferroelectric transition of $SrTiO_3$ is remarkably consistent with theory.

These strained $SrTiO_3$ films grown on (110) $DyScO_3$ substrates show a tunability of the dielectric constant at room temperature of 82% at 10 GHz and dielectric constant maxima near 20 000 at 500 Hz.[114,216,291] Strain enables room temperature access to the high and electric-field-tunable dielectric properties of $SrTiO_3$,[114,216] normally seen only at cryogenic temperatures.[436,437]

(B) Strained $BaTiO_3$: The ferroelectric properties of $BaTiO_3$ thin films have been dramatically enhanced using biaxial compressive strains up to 1.7% imposed by coherent epitaxial film growth on $REScO_3$ substrates.[203] In addition to significantly increasing the remanent polarization (P_r), T_C was increased by nearly 500°C.[203] To establish T_C, a combination of techniques was used because of the high temperatures involved and the electrical leakage of the thin $BaTiO_3$ films at high temperatures. The conventional test for ferroelectricity, hysteresis measurements, was used at room temperature to establish ferroelectricity. Then SHG and the temperature dependence of the out-of-plane lattice parameter was measured from the temperature of the hysteresis loops to where kinks were seen in the temperature-dependent XRD and SHG to establish T_C. The temperatures seen by both methods were in agreement with each other and with the predictions of thermodynamic analysis (Fig. 15).[203,291,402,407,408]

An overlay of the experimentally observed effect of strain on the ferroelectric transition of commensurately strained $BaTiO_3$ films grown on different substrates is shown in Fig. 15(b). Again the range in the theoretical predictions calculated using the range of relevant property coefficients reported for $BaTiO_3$ single crystals is shown and the agreement is again excellent. The epitaxial $BaTiO_3$ films for Fig. 15(b) were grown by both PLD and MBE. The similarity of the results by these two very different thin film preparation techniques is evidence that the observed strain effects represent the intrinsic effect of biaxial strain on $BaTiO_3$.

The first study of the effect of biaxial strain on the ferroelectric properties of $BaTiO_3$ dates more than 50 years when P. W. Forsbergh built a special fixture to biaxially strain a $BaTiO_3$ single crystal.[438] His observations of the effect of biaxial strain on $BaTiO_3$ single crystals are qualitatively similar to those observed in biaxially strained films: biaxial strain increases T_C. A notable difference, however, is that a T_C enhancement of only $\sim$10 K was observed for the strained $BaTiO_3$ single crystals before they broke.[438] A much larger strain effect can be seen in films because they can withstand far greater strains before fracture on account of their thinness,[392,393] which enables a plane stress condition to be controllably applied.

The resulting ferroelectric properties of strained $BaTiO_3$ films are comparable to those exhibited by unstrained $Pb(Zr_xTi_{1-x})O_3$, but in a more environmentally benign composition that is free of lead. These results demonstrate how strain can be used as a route to lead-free ferroelectrics for device applications, e.g., nonvolatile memories and electro-optic devices.

(C) Strained $EuTiO_3$: Strong coupling between the magnetic and ferroelectric order parameters via a spin–phonon interaction was recently predicted to occur in appropriately strained $EuTiO_3$.[439] Although unstrained $EuTiO_3$ is paraelectric and antiferromagnetic at low temperatures, first-principle calculations indicate that $(001)_p$ $EuTiO_3$ under a biaxial compressive strain of about 1% is on the verge of a transition to a ferroelectric and ferromagnetic state. For such strained $EuTiO_3$ films, the application of a modest electric field of order 10^5 V/cm is predicted to induce ferromagnetism with a magnetization of 7 μ_B per europium atom. Similarly, the application of a modest magnetic field of order 1 T is predicted to induce ferroelectricity with a spontaneous polarization of about 10 $\mu C/cm^2$.[439] The predicted coupling between the magnetic and ferroelectric order parameters in this strain-enabled material is orders of magnitude larger than any known multiferroic and a fantastic opportunity for strain tuning. Recent measurements of strained $EuTiO_3$ films show excellent agreement with theory on the dependence of the soft-mode frequencies on strain, and ferroelectricity at room

temperature has been observed in commensurately strained $EuTiO_3$ films.[423]

(2) Modulation Doping

Two-dimensional electron gases (2DEG) have been widely investigated in conventional semiconductors[440] and more recently in the II–VI semiconducting oxide ZnO.[441] But functional oxides have properties drastically different than conventional semiconductors. The perovskite $SrTiO_3$, for example, has an electron effective mass $(m_e^* = 5m_o)$[442,443] and dielectric constant $(\varepsilon_r = 20\,000$ at 4 K$)$[436] orders of magnitude higher than conventional semiconductors and the highest electron mobility $(\mu_n^{bulk} = 22\,000 cm^2/V\,s$ at 2 K$)$[11] of any known oxide. This completely different regime of semiconducting properties, coupled with the occurrence of superconductivity in appropriately electron-doped $SrTiO_3$,[444] makes the study of the behavior of a 2DEG in $SrTiO_3$ of great interest. The desire to study a 2DEG in $SrTiO_3$ was recognized long ago,[445] and was recently achieved experimentally using a $LaAlO_3/SrTiO_3$ heterostructure.[10]

Modulation doping, the dominant technique used to realize 2DEGs in conventional semiconductors,[446] is not foreign to oxides. Indeed it occurs naturally in layered functional oxides, e.g., oxide superconductors, as "charge reservoir" layers donate their carriers to surrounding CuO_2 layers.[447] In addition to the movement of charge (electronic compensation) relevant for the formation of a 2DEG, another way that an oxide may provide compensating charge is via charged defects (ionic compensation). Hence, to achieve modulation doping in oxides, one must overcome ionic compensation mechanisms. Modulation doping has begun to be applied artificially to oxides,[448] although information on the band offsets, a critical element of bandgap engineering, is generally lacking for oxide heterojunctions. This process can be engineered through the controlled growth of oxide heterostructures and due to the functional properties of oxides, the formation, study, and exploitation of 2DEGs in them is an area with tremendous potential. Exploration of the behavior of ferroelectric, magnetic, or even spin-polarized 2DEGs is within reach.

(3) Confined Thickness—Finite Size Effects in Superlattices

Thin film techniques offer powerful ways to assemble new materials, including metastable ones, that cannot be made by other methods. For single layer films, metastable materials may be accessed through epitaxial stabilization.[159,357–359] In multilayer films the tremendous difference between the diffusion coefficient at the surface of the growing thin film compared with the much lower diffusion coefficient within the bulk of the film, including buried interfaces, makes it possible to create two-phase mixtures of end member phases, even for materials that exhibit are fully miscible with each other in bulk form. This is used in the synthesis of many compound semiconductor device structures, e.g., AlAs/GaAs heterostructures, which are metastable heterostructures because their solid solution has a lower free energy over their entire composition range.[449] Similarly, heterostructures involving ferroelectrics such as $PbTiO_3/SrTiO_3$ or $BaTiO_3/SrTiO_3$ are metastable; it is energetically favorable for these oxides to dissolve into each other forming $(Pb,Sr)TiO_3$ and $(Ba,Sr)TiO_3$ solid solutions.[450,451] Although these superlattices are metastable, cation diffusion constants in oxides are sufficiently small that annealing at 1000°C for several hours is typically required before intermixing effects become discernable.[79] As can be seen in Fig. 17, the interface abruptness and layer thickness control of today's oxide superlattices involving functional oxides[79,110,113,117–126,149–157] are comparable to what has become commonplace for AlAs/GaAs superlattices grown by MBE[452] and MOCVD.[453]

Superlattices consisting of a periodic stacking of thin functional oxide layers have been predicted[454–459] or reported[113,155,235,426,427,460–462] to possess many improved physical properties over homogeneous thin films of the same compositions. Among the improved properties are reported enhancements of dielectric constants and remanent polarization in short-period two-component[235,460,461] and three-component[155] superlattices. While such reports need to be carefully evaluated considering that the movement of space charge in the superlattices can spuriously produce an apparent significant enhancement of dielectric constant,[463,464] the improved properties could result from the large lattice mismatch leading to huge strains for commensurate epitaxial growth.[155,235,460,461]

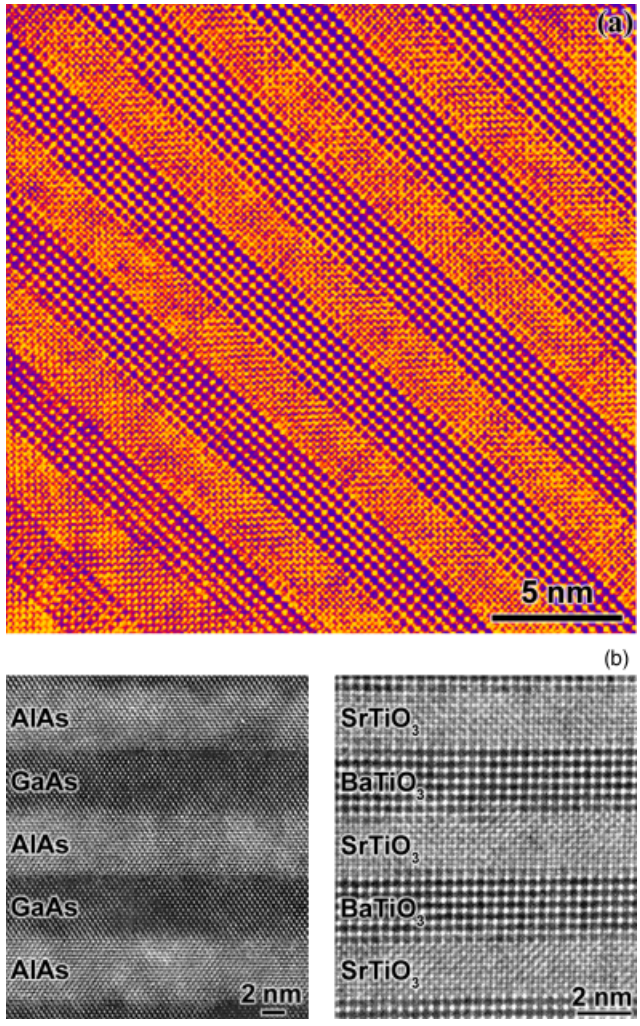

Fig. 17. (a) High-resolution TEM image of a $BaTiO_3/SrTiO_3$ superlattice grown by molecular-beam epitaxy (MBE). (b) A comparison between this same functional oxide superlattice is made with a GaAs/AlAs superlattice (reprinted from Gutakovskii *et al.*,[452] with permission; ©1995 Wiley-VCH). Both superlattices are grown by MBE.

Layered heterostructures including superlattices are just one type of epitaxial composite involving functional oxides. Epitaxial heterostructures that make use of phase separation to form connectivities beyond the 2–2 connectivity[386] of superlattices are also being explored by thin film techniques. These include 1–3 epitaxial nanocomposites involving pillars of magnetic oxides in a ferroelectric matrix[391] or pillars of ferroelectric oxides in a magnetic matrix.[465] These are being explored in ferroelectric systems to enhance the coupling between ferroelectric and magnetic oxides and thus form artificial magneto-electric heterostructures.

Artificially layered superlattices of functional oxides have enormous appeal from both a technological and a fundamental standpoint. With modern deposition techniques the degree of control that can be achieved is astounding and superlattices with essentially perfect interfaces and single-unit-cell constituent layers are well within our grasp. In terms of technology, superlattices of functional oxides with appropriate electrical and mechanical boundary conditions hold the potential of tailoring functional properties precisely for an application; there are some

indications that under certain circumstances the properties of a superlattice of two or more materials may be far superior to the parent materials from which they have been fabricated.

(A) $BaTiO_3/SrTiO_3$ Superlattices: Crucial to the enlightened (non-Edisonian) synthesis of superior materials is an understanding of how the properties of the resulting superlattice material are related to those of the parent materials used. In superlattices of ferroelectric functional oxides where the in-plane lattice parameter of all the constituents is constrained to that of the underlying substrate, the primary interaction that determines the overall properties of the superlattice seems to be electrostatic, with the principle consideration being the minimization of polarization mismatch between layers, any mismatch giving rise to very high electrostatic energy penalties.[456] This does not restrict the possibility of strain engineering, as the elastic constraint imposed by the substrate is an important factor in determining the orientation of the polarization in the superlattice layers and thus has a dramatic effect on the properties of the superlattice. Similarly, should a superlattice suffer relaxation due to misfit dislocations, changes in the orientation of the polarization can arise, as seen in the $SrTiO_3$ layers of relaxed $BaTiO_3/SrTiO_3$ superlattices.[466–468] Beyond the commercial appeal of precisely tailored exceptional materials, these systems also allow an extraordinary opportunity for the exploration of the fundamentals of ferroelectricity. In essence one can produce a system the physics of which is defined by ultra-thin components and interfaces, but with a larger total sample size allowing simple, precise characterization and a detailed exploration of the physics of ferroelectricity in ultra-thin systems.

$(001)_p$ $BaTiO_3/(001)_p$ $SrTiO_3$ superlattices have also been extensively studied to investigate size effects. In a recent study,[157] these superlattices were grown on (001) $SrTiO_3$ substrates and the $(001)_p$ $BaTiO_3$ layer in the superlattice was varied from 1 to 8 unit cells in thickness, while the $(001)_p$ $SrTiO_3$ spacer layer thickness was fixed to be either 4 unit cells or 13 unit cells thick. These superlattices can be denoted by $(BaTiO_3)_n/(SrTiO_3)_m$, where n and m refer to the thickness, in unit cells, of the $(001)_p$ $BaTiO_3$ and $(001)_p$ $SrTiO_3$ layers, respectively. The regularity of these superlattices grown by MBE is demonstrated by the presence and sharpness of all of the superlattice reflections in their XRD patterns. An example is shown in Fig. 18 of the XRD scans of $[(BaTiO_3)_n/(SrTiO_3)_m]_p$ superlattices for (a) $m = 4$ and (b) $m = 13$ $SrTiO_3$ layers separating the $BaTiO_3$ layers in the superlattices.[237] The presence of virtually all satellite peaks in these superlattices attests to their macroscopic structural perfection.

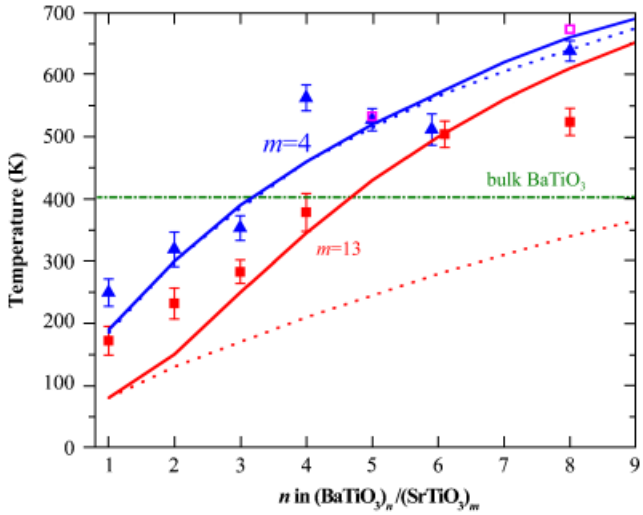

Fig. 19. The dependence of T_C on n and m in $(BaTiO_3)_n/(SrTiO_3)_m$ superlattices. The blue symbols are for $m = 4$ and red symbols are for $m = 13$. T_C was determined by UV Raman (closed symbols) and temperature-dependent X-ray diffraction (open symbols) measurements. A phase-field model with a single-domain assumption yields the dotted curves. The solid lines are from full three-dimensional phase-field calculations. The T_C of bulk unstrained $BaTiO_3$ is also shown (reprinted from Li *et al.*,[469] with permission; ©2007 American Institute of Physics).

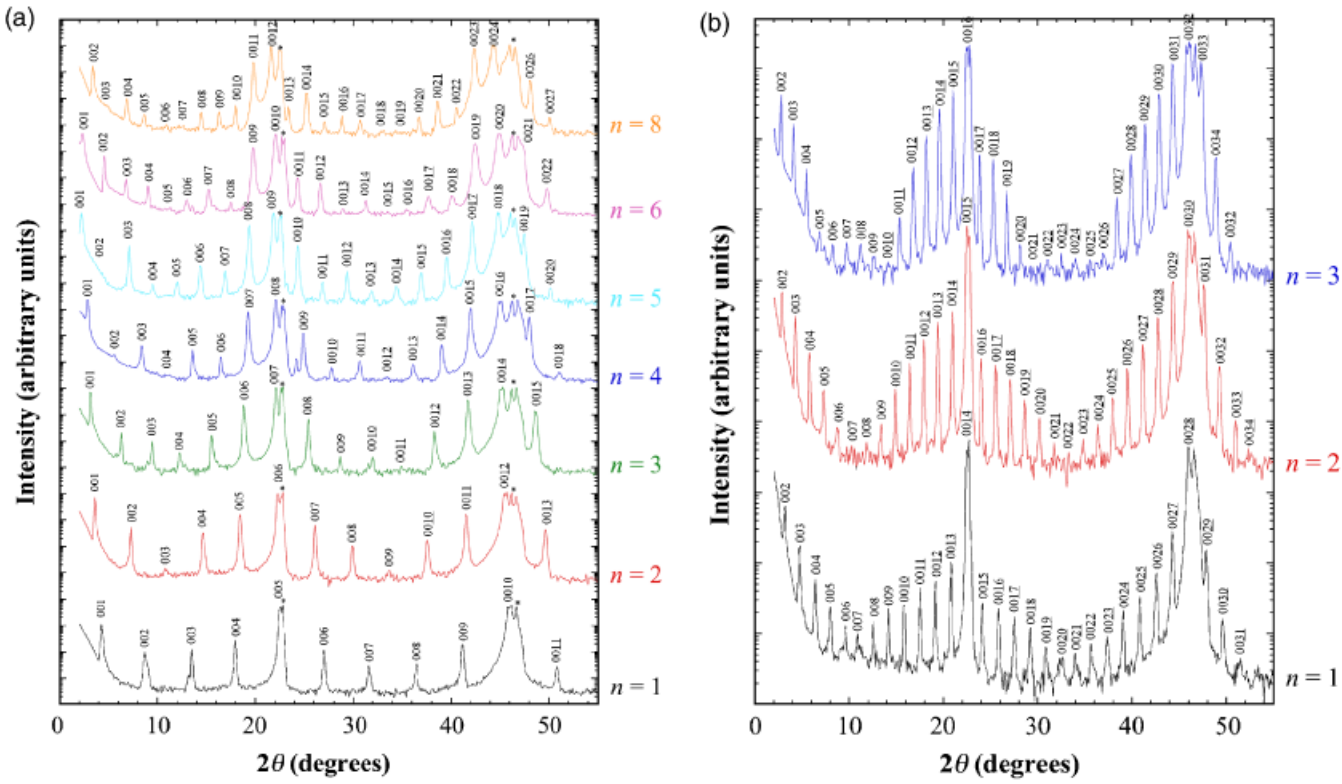

Fig. 18. θ–2θ X-ray diffraction scans of $[(BaTiO_3)_n/(SrTiO_3)_m]_p$ superlattices using CuK_α radiation for (a) $m = 4$ and $n = 1$, 2, 3, 4, 5, 6, and 8 and (b) $m = 13$ and $n = 1$, 2, and 3. Substrate peaks are marked with asterisks (*). (From Soukiassian *et al.*[237])

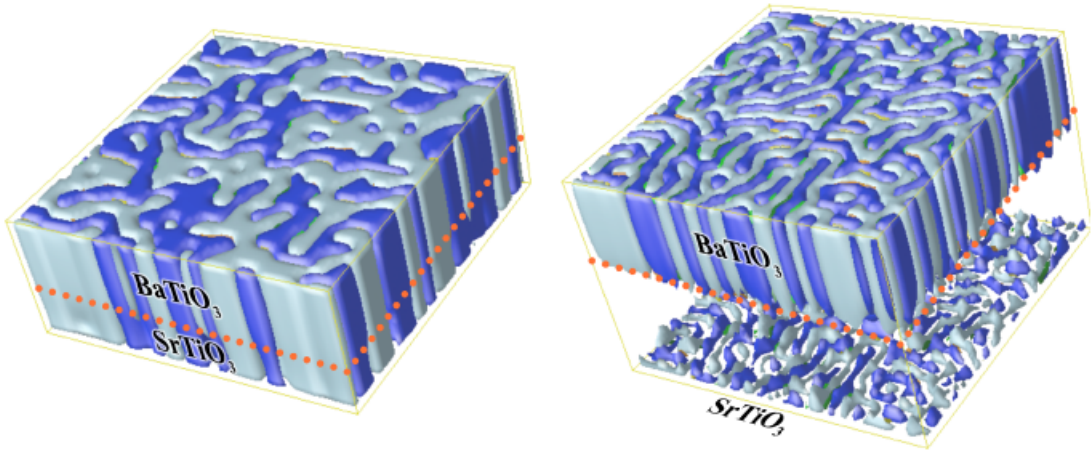

Fig. 20. Calculated multiple domain states of $[(BaTiO_3)_8/(SrTiO_3)_4]_p$ and $[(BaTiO_3)_8/(SrTiO_3)_{13}]_p$ superlattices. The blue and light-blue colors represent the two types of domains with out-of-plane polarization directions. The interfaces between them are 180° domain walls. The induced polarization domains are clearly shown in the $SrTiO_3$ layer of the $[(BaTiO_3)_8/(SrTiO_3)_4]_p$ superlattice with polarization values comparable to the $BaTiO_3$ layer. There is only a small induced polarization in the $SrTiO_3$ layer of the $[(BaTiO_3)_8/(SrTiO_3)_{13}]_p$ superlattice, and hence if we only count regions as domains if their polarization values are above a certain small threshold, there are no observed polarization domains in the $SrTiO_3$ layer for the $[(BaTiO_3)_8/(SrTiO_3)_{13}]_p$ superlattice.

Characterizing the resulting superlattices by UV Raman made it possible to confirm the prediction that the unstrained $SrTiO_3$ layer in these superlattices is polarized due to the electrostatic effect described above and also enabled the T_C of the ferroelectric superlattice to be established. T_C is shown as a function of n for $m = 4$ and $m = 13$ in Fig. 19 together with two different phase-field models of these superlattices. When the phase-field model is limited to a single-domain assumption (dashed lines in Fig. 19), the agreement between theory and experiment is good for $m = 4$, but poor for $m = 13$. Put another way, the $(001)_p$ $BaTiO_3/(001)_p$ $SrTiO_3$ superlattices show disagreement with theory when the $BaTiO_3$ layer is thinner than the $SrTiO_3$ layer, just as was seen for $(001)_p$ $PbTiO_3/(001)_p$ $SrTiO_3$ superlattices.[156] First principles calculations also operate under a single-domain assumption because of the limited number of atoms in the calculation. When a full three-dimensional phase-field simulation is performed (solid lines in Fig. 19), the agreement between theory and experiment becomes good for both $m = 4$ and $m = 13$ over the entire range. These calculations indicate that the low-energy configuration is a multiple-domain state, which allows the polarization in the $(001)_p$ $SrTiO_3$ layers to drop considerably when the $(001)_p$ $BaTiO_3$ layer is thinner than the $(001)_p$ $SrTiO_3$ layer, and results in a significant increase of T_C compared with the single-domain state.[157,469] The calculated multiple domain states of $[(BaTiO_3)_8/(SrTiO_3)_4]_p$ and $[(BaTiO_3)_8/(SrTiO_3)_{13}]_p$ superlattices are shown in Fig. 20. It is found that while the $SrTiO_3$ layer in $[(BaTiO_3)_8/(SrTiO_3)_4]_p$ is fully polarized with polarization values that are comparable to the $BaTiO_3$ layer, the polarization in $SrTiO_3$ for the $[(BaTiO_3)_8/(SrTiO_3)_{13}]_p$ superlattice is much smaller. The 180° walls between the blue domains and light-blue domains in $[(BaTiO_3)_8/(SrTiO_3)_4]_p$ display continuity from $BaTiO_3$ to $SrTiO_3$. Therefore, a single-domain assumption for the $[(BaTiO_3)_8/(SrTiO_3)_4]_p$ superlattice would be reasonable, whereas the same assumption would lead to a large error in the transition temperature for the $[(BaTiO_3)_8/(SrTiO_3)_{13}]_p$ superlattice.

VII. Outlook

The use of thin film techniques for the growth of functional oxides is still in its infancy and many hurdles remain to be overcome for these techniques to develop greater structural control at the atomic layer level, reproducibility, and ultimately precise control of electronic, optical, and spintronic properties. Nonetheless, PLD has become established as an extremely swift and nimble method for rapidly synthesizing epitaxial films and heterostructures of functional oxides. MBE is the premiere synthesis technique for the synthesis of layered oxides with customized layering control down to the atomic layer level. As the complexity and metastability of desired functional oxides and heterostructures involving functional oxides increases, the need to improve these atomic layer engineering techniques will become all the more important. Accurate composition control is key to the controlled growth of such structures and with improvements in composition control, further improvements in the perfection of the layering control attainable in the growth of functional oxides by MBE is expected.

Traditionally the search for new functional materials involves identifying bulk unstrained phases that exist within composition space. But the available configurational space for functional materials in thin films includes additional degrees of freedom: strain and dimensional confinement. Navigating this vastly increased dimensional space in search of functional materials with improved properties is a daunting task without guidance. Luckily today's multiscale modeling techniques are a tremendous aid in identifying likely locations for improved functional materials. This starts with first-principles methods[15,29,157,235,291,416,470–475] to elucidate the potential of new functional oxides including microstructures and strain states that are metastable. Continuum techniques may then be used to extend first-principles predictions to multidomain samples, finite temperatures, and include the dynamics of domain switching.[114,157,203,235,291,402,405,406,408,412,413,415,416,471] The resulting calculated phase diagrams including the effect of large strains are rich and depict how strain can greatly extend the range of functional behavior, performance, and utility beyond bulk compounds.[114,203,291,402,412,413,470,471,476] These modern theoretical methods can target specific compositions, strains, and dimensional confinement for improved functionality and have enjoyed considerable success, e.g., in the fields of ferroelectrics and multiferroics, for predicting the properties of new materials. Many of these new functional oxides are metastable and others attain their improved functionality via strain (strain-enabled). We firmly believe that a theory-driven intelligent approach is imperative for efficiently finding novel or greatly enhanced functional properties in oxides.

Acknowledgments

We gratefully acknowledge our colleagues and collaborators for sharing their insights and helping us to prepare, explore, and better understand the exciting area of functional oxide thin films. We especially thank C. Adamo, O. Auciello, M. D. Biegalski, D. H. A. Blank, I. Bozovic, C. D. Brandle, A. Bruchhausen, A. Cantarero, W. Chang, Y. B. Chen, K. J. Choi, S. Choudhury, H.-M. Christen, B.

Craigo, L. E. Cross, J. A. Eastman, J. N. Eckstein, C. B. Eom, A. Fainstein, C. J. Fennie, D. D. Fong, V. J. Fratello, P. H. Fuoss, V. Gopalan, J. H. Haeni, M. E. Hawley, T. Heeg, J. F. Ihlefeld, P. Irvin, Q. X. Jia, Y. Jia, J.C. Jiang, S. Kamba, R. S. Katiyar, X. Ke, D. M. Kim, S. W. Kirchoefer, H. Kohlstedt, A. Kumar, N. D. Lanzillotti-Kimura, J. H. Lee, J. Lettieri, J. Levy, Y. L. Li, F. Lichtenberg, Y. Liu, H. Z. Ma, J. Mannhart, L. Maritato, R. A. McKee, R. E. Newnham, K. M. Rabe, R. Ramesh, P. Reiche, J. Rodriguez-Contreras, P. Schiffer, J. Schubert, A. Sharan, V. Sherman, A. Soukiassian, N. A. Spaldin, G. B. Stephenson, S. K. Streiffer, H. P. Sun, A. K. Tagantsev, D. A. Tenne, C. D. Theis, C. Thompson, W. Tian, J.-M. Triscone, S. Trolier-McKinstry, R. Uecker, V. Vaithyanathan, A. Vasudevarao, F. J. Walker, M. Warusawithana, P. P. Wu, A. J. Ven Graitis, and X. X. Xi.

References

[1]P. A. Salvador, A.-M. Haghiri-Gosnet, B. Mercey, M. Hervieu, and B. Raveau, "Growth and Magnetoresistive Properties of $(LaMnO_3)_m(SrMnO_3)_n$ Superlattices," *Appl. Phys. Lett.*, **75** [17] 2638–40 (1999).

[2]T. Koida, M. Lippmaa, T. Fukumura, K. Itaka, Y. Matsumoto, M. Kawasaki, and H. Koinuma, "Effect of *A*-Site Cation Ordering on the Magnetoelectric Properties in $[(LaMnO_3)_m/(SrMnO_3)_m]_n$ Artificial Superlattices," *Phys. Rev. B*, **66** [14] 144418 (2002).

[3]H. Yamada, M. Kawasaki, T. Lottermoser, T. Arima, and Y. Tokura, "$LaMnO_3/SrMnO_3$ Interfaces with Coupled Charge-Spin-Orbital Modulation," *Appl. Phys. Lett.*, **89** [5] 052506 (2006).

[4]A. Bhattacharya, X. Zhai, M. Warusawithana, J. N. Eckstein, and S. D. Bader, "Signatures of Enhanced Ordering Temperatures in Digital Superlattices of $(LaMnO_3)_m/(SrMnO_3)_{2m}$," *Appl. Phys. Lett.*, **90** [22] 222503 (2007).

[5]S. J. May, A. B. Shah, S. G. E. te Velthuis, M. R. Fitzsimmons, J. M. Zuo, X. Zhai, J. N. Eckstein, S. D. Bader, and A. Bhattacharya, "Magnetically Asymmetric Interfaces in a $LaMnO_3/SrMnO_3$ Superlattice due to Structural Asymmetries," *Phys. Rev. B*, **77** [17] 174409 (2008).

[6]A. Bhattacharya, S. J. May, S. G. E. te Velthuis, M. Warusawithana, X. Zhai, B. Jiang, J.-M. Zuo, M. R. Fitzsimmons, S. D. Bader, and J. N. Eckstein, "Metal–Insulator Transition and Its Relation to Magnetic Structure in $(LaMnO_3)_{2n}/(SrMnO_3)_n$ Superlattices," *Phys. Rev. Lett.*, **100** [25] 257203 (2008).

[7]C. Adamo, X. Ke, P. Schiffer, A. Soukiassian, M. Warusawithana, L. Maritato, and D. G. Schlom, "Electrical and Magnetic Properties of $(SrMnO_3)_n/(LaMnO_3)_{2n}$ Superlattices," *Appl. Phys. Lett.*, **92** [11] 112508 (2008).

[8]A. Ohtomo and H. Y. Hwang, "A High-Mobility Electron Gas at the $LaAlO_3/SrTiO_3$ Heterointerface," *Nature*, **427** [6973] 423–6 (2004).

[9]A. Brinkman, M. Huijben, M. van Zalk, J. Huijben, U. Zeitler, J. C. Maan, W. G. van der Wiel, G. Rijnders, D. H. A. Blank, and H. Hilgenkamp, "Magnetic Effects at the Interface Between Non-Magnetic Oxides," *Nat. Mater.*, **6** [7] 493–6 (2007).

[10]N. Reyren, S. Thiel, A. D. Caviglia, L. Fitting Kourkoutis, G. Hammerl, C. Richter, C. W. Schneider, T. Kopp, A.-S. Rüetschi, D. Jaccard, M. Gabay, D. A. Muller, J.-M. Triscone, and J. Mannhart, "Superconducting Interfaces Between Insulating Oxides," *Science*, **317** [5842] 1196–9 (2007).

[11]O. N. Tufte and P. W. Chapman, "Electron Mobility in Semiconducting Strontium Titanate," *Phys. Rev.*, **155** [3] 796–802 (1967).

[12]G. Petrich, S. von Molnár, and T. Penney, "Exchange-Induced Autoionization in Eu-Rich EuO," *Phys. Rev. Lett.*, **26** [15] 885–8 (1971).

[13]A. Schilling, M. Cantoni, J. D. Guo, and H. R. Ott, "Superconductivity Above 130 K in the Hg–Ba–Ca–Cu–O System," *Nature*, **363** [6424] 56–8 (1993).

[14]I. Vrejoiu, G. Le Rhun, L. Pintilie, D. Hesse, M. Alexe, and U. Gösele, "Intrinsic Ferroelectric Properties of Strained Tetragonal $PbZr_{0.2}Ti_{0.8}O_3$ Obtained on Layer-by-Layer Grown, Defect-Free Single-Crystalline Films," *Adv. Mater.*, **18** [13] 1657–61 (2006).

[15]J. Wang, J. B. Neaton, H. Zheng, V. Nagarajan, S. B. Ogale, B. Liu, D. Viehland, V. Vaithyanathan, D. G. Schlom, U. V. Waghmare, N. A. Spaldin, K. M. Rabe, M. Wuttig, and R. Ramesh, "Epitaxial $BiFeO_3$ Multiferroic Thin Film Heterostructures," *Science*, **299** [5613] 1719–22 (2003).

[16]J. F. Li, J. Wang, M. Wuttig, R. Ramesh, N. Wang, B. Ruette, A. P. Pyatakov, A. K. Zvezdin, and D. Viehland, "Dramatically Enhanced Polarization in (001), (101), and (111) $BiFeO_3$ Thin Films due to Epitiaxial-Induced Transitions," *Appl. Phys. Lett.*, **84** [25] 5261–3 (2004).

[17]R. R. Das, D. M. Kim, S. H. Baek, C. B. Eom, F. Zavaliche, S. Y. Yang, R. Ramesh, Y. B. Chen, X. Q. Pan, X. Ke, M. S. Rzchowski, and S. K. Streiffer, "Synthesis and Ferroelectric Properties of Epitaxial $BiFeO_3$ Thin Films Grown by Sputtering," *Appl. Phys. Lett.*, **88** [24] 242904 (2006).

[18]J. Dho, X. Qi, H. Kim, J. L. MacManus-Driscoll, and M. G. Blamire, "Large Electric Polarization and Exchange Bias in Multiferroic $BiFeO_3$," *Adv. Mater.*, **18** [11] 1445–8 (2006).

[19]S. E. Park and T. R. Shrout, "Ultrahigh Strain and Piezoelectric Behavior in Relaxor Based Ferroelectric Single Crystals," *J. Appl. Phys.*, **82** [4] 1804–11 (1997).

[20]B. T. Matthias, R. M. Bozorth, and J. H. Van Fleck, "Ferromagnetic Interaction in EuO," *Phys. Rev. Lett.*, **7** [5] 160–1 (1961).

[21]A. Maignan, C. Simon, V. Caignaert, and B. Raveau, "Giant Magnetoresistance Ratios Superior to 10^{11} in Manganese Perovskites," *Solid State Commun.*, **96** [9] 623–5 (1995).

[22]R. M. Bozorth, E. F. Tilden, and A. J. Williams, "Anisotropy and Magnetostriction of Some Ferrites," *Phys. Rev.*, **99** [6] 1788–98 (1955).

[23]K. Y. Ahn and M. W. Shafer, "Relationship Between Stoichiometry and Properties of EuO Films," *J. Appl. Phys.*, **41** [3] 1260–2 (1970).

[24]R. J. Soulen Jr., J. M. Byers, M. S. Osofsky, B. Nadgorny, T. Ambrose, S. F. Cheng, P. R. Broussard, C. T. Tanaka, J. Nowak, J. S. Moodera, A. Barry, and J. M. D. Coey, "Measuring the Spin Polarization of a Metal with a Superconducting Point Contact," *Science*, **282** [5386] 85–8 (1998).

[25]A. Anguelouch, A. Gupta, G. Xiao, G. X. Miao, D. W. Abraham, S. Ingvarsson, Y. Ji, and C. L. Chien, "Properties of Epitaxial Chromium Dioxide Films Grown by Chemical Vapor Deposition Using a Liquid Precursor," *J. Appl. Phys.*, **91** [10] 7140–2 (2002).

[26]N. Ikeda, H. Ohsumi, K. Ohwada, K. Ishii, T. Inami, K. Kakurai, Y. Murakami, K. Yoshii, S. Mori, Y. Horibe, and H. Kito, "Ferroelectricity from Iron Valence Ordering in the Charge-Frustrated System $LuFe_2O_4$," *Nature*, **436** [4039] 1136–8 (2005).

[27]C. J. Fennie, "Ferroelectrically Induced Weak Ferromagnetism by Design," *Phys. Rev. Lett.*, **100** [16] 167203 (2008).

[28]A. Moreira dos Santos, S. Parashar, A. R. Raju, Y. S. Zhao, A. K. Cheetham, and C. N. R. Rao, "Evidence for the Likely Occurrence of Magnetoferroelectricity in the Simple Perovskite, $BiMnO_3$," *Solid State Commun.*, **122** [1–2] 49–52 (2002).

[29]N. A. Hill and K. M. Rabe, "First-Principles Investigation of Ferromagnetism and Ferroelectricity in Bismuth Manganite," *Phys. Rev. B*, **59** [13] 8759–69 (1999).

[30]A. Sharan, J. Lettieri, Y. Jia, W. Tian, X. Q. Pan, D. G. Schlom, and V. Gopalan, "Bismuth Manganite: A Multiferroic with a Large Nonlinear Optical Response," *Phys. Rev. B*, **69** [21] 214109 (2004).

[31]P. Baettig, R. Seshadri, and N. A. Spaldin, "Anti-Polarity in Ideal $BiMnO_3$," *J. Am. Chem. Soc.*, **129** [32] 9854–5 (2007).

[32]R. D. Shannon, "Revised Effective Ionic Radii and Systematic Studies of Interatomic Distances in Halides and Chalcogenides," *Acta Cryst. A*, **32** [5] 751–67 (1976).

[33]K.-H. Hellwege and A. M. Hellwege, *Landolt-Börnstein: Numerical Data and Functional Relationships in Science and Technology, Group III*, **Vol. 12a**, pp. 126–206. Springer-Verlag, Berlin, 1978.

[34]D. Balz and K. Plieth, "Die Struktur des Kaliumnickelfluorids, K_2NiF_4," *Z. Elektrochem.*, **59** [6] 545–51 (1955).

[35]S. N. Ruddlesden and P. Popper, "New Compounds of the K_2NiF_4 Type," *Acta Cryst.*, **10** [8] 538–9 (1957).

[36]S. N. Ruddlesden and P. Popper, "The Compound $Sr_3Ti_2O_7$ and Its Structure," *Acta Cryst.*, **11** [1] 54–5 (1958).

[37]Y. Maeno, H. Hashimoto, K. Yoshida, S. Nishizaki, T. Fujita, J. G. Bednorz, and F. Lichtenberg, "Superconductivity in a Layered Perovskite without Copper," *Nature*, **372** [6506] 532–4 (1994).

[38]A. Callaghan, C. W. Moeller, and R. Ward, "Magnetic Interactions in Ternary Ruthenium Oxides," *Inorg. Chem.*, **5** [9] 1572–6 (1966).

[39]O. Auciello, J. F. Scott, and R. Ramesh, "The Physics of Ferroelectric Memories," *Phys. Today*, **51** [7] 22–7 (1998).

[40]J. F. Scott, "Applications of Modern Ferroelectrics," *Science*, **315** [5814] 954–9 (2007).

[41]M. A. Zurbuchen, R. S. Freitas, M. J. Wilson, P. Schiffer, M. Roeckerath, J. Schubert, M. D. Biegalski, G. H. Mehta, D. J. Comstock, J. H. Lee, Y. Jia, and D. G. Schlom, "Synthesis and Characterization of an $n = 6$ Aurivillius Phase Incorporating Magnetically Active Manganese, $Bi_7(Mn,Ti)_6O_{21}$," *Appl. Phys. Lett.*, **91** [3] 033113 (2007).

[42]B. G. Hyde and S. Andersson, *Inorganic Crystal Structures*. Wiley-Interscience, New York, 1989.

[43]C. N. R. Rao and B. Raveau, *Transition Metal Oxides: Structure, Properties, and Synthesis of Ceramic Oxides*, 2nd edition, pp. 61–226. Wiley-VCH, New York, 1998.

[44]D. R. Veblen, "Polysomatism and Polysomatic Series: A Review and Applications," *Am. Mineral.*, **76** [5–6] 801–26 (1991).

[45]R. J. D. Tilley, "An Electron Microscope Study of Perovskite-Related Oxides in the Sr–Ti–O System," *J. Solid State Chem.*, **21** [4] 293–301 (1977).

[46]J. L. Hutchison, J. S. Anderson, and C. N. R. Rao, "Electron Microscopy of Ferroelectric Bismuth Oxides Containing Perovskite Layers," *Proc. R. Soc. London, Ser. A*, **355** [1682] 301–12 (1977).

[47]J. Drennan, C. P. Tavares, and B. C. H. Steele, "An Electron Microscope Investigation of Phases in the System La–Ni–O," *Mater. Res. Bull.*, **17** [5] 621–6 (1982).

[48]J. Gopalakrishnan, A. Ramanan, C. N. R. Rao, D. A. Jefferson, and D. J. Smith, "A Homologous Series of Recurrent Intergrowth Structures of the Type $Bi_4A_{m+n-2}B_{m+n}O_{3(m+n)+6}$ Formed by Oxides of the Aurivillius Family," *J. Solid State Chem.*, **55** [1] 101–5 (1984).

[49]D. A. Jefferson, M. K. Uppal, C. N. R. Rao, and D. J. Smith, "Elastic Strain at the Solid-Solid Interface in Intergrowth Structures: A Novel Example of Partial Structure Refinement by HREM," *Mater. Res. Bull.*, **19** [11] 1403–9 (1984).

[50]C. N. R. Rao and J. M. Thomas, "Intergrowth Structures: The Chemistry of Solid–Solid Interfaces," *Acc. Chem. Res.*, **18**, 113–9 (1985).

[51]R. A. Mohan Ram, L. Ganapathi, P. Ganguly, and C. N. R. Rao, "Evolution of Three-Dimensional Character across the $La_{n+1}Ni_nO_{3n+1}$ Homologous Series with Increase in *n*," *J. Solid State Chem.*, **63** [2] 139–47 (1986).

[52]J. M. Tarascon, W. R. McKinnon, P. Barboux, D. M. Hwang, B. G. Bagley, L. H. Greene, G. W. Hull, Y. LePage, N. Stoffel, and M. Giroud, "Preparation, Structure, and Properties of the Superconducting Compound Series $Bi_2Sr_2Ca_{n-1}Cu_nO_y$ with $n = 1$, 2, and 3," *Phys. Rev. B*, **38** [13] 8885–92 (1988).

[53]B. Raveau, C. Michel, and M. Hervieu, "Crystal Chemistry of Superconductive Bismuth and Thallium Cuprates"; pp. 151–7 in *Advances in Superconductivity: Proceedings of the 1st International Symposium on Superconductivity (ISS '88)*, Edited by K. Kitazawa, and T. Ishiguro. Springer-Verlag, Tokyo, 1989.

[54]W. T. Fu, H. W. Zandbergen, Q. Xu, J. M. van Ruitenbeek, L. J. de Jongh, and G. van Tendeloo, "Structural and Transport Properties of the Triple-Layer Compounds $Ba_4(Pb_{1-x}Bi_x)_3O_{10}$ $(0 \le x < 0.3)$," *Solid State Commun.*, **70** [12] 1117–21 (1989).

[55]O. Eibl, "Crystal Defects in $Bi_2Sr_2Ca_{n-1}Cu_nO_{4+2n+\delta}$ Ceramics," *Physica C*, **168** [1–2] 249–56 (1990).

[56]R. Ramesh, S. Jin, and P. Marsh, "Superconductor Defect Structure," *Nature*, **346**, 420 (1990).

[57]A. Nozaki, H. Yoshikawa, T. Wada, H. Yamauchi, and S. Tanaka, "Layered Perovskite Compounds $Sr_{n+1}V_nO_{3n+1}$ ($n = 1, 2, 3,$ and ∞)," *Phys. Rev. B*, **43** [1] 181–5 (1991).

[58]M. A. Señaris-Rodriguez, A. M. Chippindale, A. Várez, E. Morán, and M. A. Alario-Franco, "A Novel '126' Phase of the Family of $Y_2Ba_4Cu_{6+n}O_{14+n}$ High-Temperature Superconducting Materials," *Physica C*, **172** [5–6] 477–80 (1991).

[59]R. J. Cava, T. Siegrist, B. Hessen, J. J. Krajewski, W. F. Peck Jr., B. Batlogg, H. Takagi, J. V. Waszczak, L. F. Schneemeyer, and H. W. Zandbergen, "A New Homologous Series of Lanthanum Copper Oxides," *J. Solid State Chem.*, **94** [1] 170–84 (1991).

[60]K. Hawkins and T. J. White, "Defect Structure and Chemistry of $(Ca_xSr_{1-x})_{n+1}Ti_nO_{3n+1}$ Layer Perovskites," *Philos. Trans. R. Soc. London, Ser. A*, **336** [1644] 541–69 (1991).

[61]T. Williams, F. Lichtenberg, A. Reller, and G. Bednorz, "New Layered Perovskites in the Sr–Ru–O System: A Transmission Electron Microscope Study," *Mater. Res. Bull.*, **26** [8] 763–70 (1991).

[62]M. Čeh, V. Kraševec, and D. Kolar, "A Transmission Electron Microscope Study of SrO-Doped $CaTiO_3$," *J. Solid State Chem.*, **103** [1] 263–8 (1993).

[63]S. Adachi, H. Yamauchi, S. Tanaka, and N. Môri, "New Superconducting Cuprates in the Sr–Ca–Cu–O System," *Physica C*, **212** [1–2] 164–8 (1993).

[64]Z. Hiroi, M. Takano, M. Azuma, and Y. Takeda, "A New Family of Copper Oxide Superconductors $Sr_{n+1}Cu_nO_{2n+1+\delta}$ Stabilized at High Pressure," *Nature*, **364** [6435] 315–7 (1993).

[65]X.-J. Wu, S. Adachi, C.-Q. Jin, H. Yamauchi, and S. Tanaka, "Novel Homologous Series of Superconducting Copper Oxides, Cu-12(n−1)n," *Physica C*, **223** [3–4] 243–8 (1994).

[66]P. Laffez, G. Van Tendeloo, R. Seshadri, M. Hervieu, C. Martin, A. Maignan, and B. Raveau, "Microstructural and Physical Properties of Layered Manganites Oxides Related to the Magnetoresistive Perovskites," *J. Appl. Phys.*, **80** [10] 5850–6 (1996).

[67]M. A. McCoy, R. W. Grimes, and W. E. Lee, "Phase Stability and Interfacial Structures in the SrO–$SrTiO_3$ System," *Philos. Mag. A*, **75** [3] 833–46 (1997).

[68]R. Seshadri, M. Hervieu, C. Martin, A. Maignan, B. Domenges, B. Raveau, and A. N. Fitch, "Study of the Layered Magnetoresistive Perovskite $La_{1.2}Sr_{1.8}Mn_2O_7$ by High-Resolution Electron Microscopy and Synchrotron X-Ray Powder Diffraction," *Chem. Mater.*, **9** [8] 1778–87 (1997).

[69]S. D. Bader, R. M. Osgood III, D. J. Miller, J. F. Mitchell, and J. S. Jiang, "Role of Intergrowths in the Properties of Naturally Layered Manganite Single Crystals," *J. Appl. Phys.*, **83** [11] 6385–9 (1998).

[70]J. Sloan, P. D. Battle, M. A. Green, M. J. Rosseinsky, and J. F. Vente, "A HRTEM Study of the Ruddlesden-Popper Compositions $Sr_2LnMn_2O_7$ (Ln = Y, La, Nd, Eu, Ho)," *J. Solid State Chem.*, **138** [1] 135–40 (1998).

[71]K. Szot and W. Speier, "Surfaces of Reduced and Oxidized $SrTiO_3$ from Atomic Force Microscopy," *Phys. Rev. B*, **60** [8] 5909–26 (1999).

[72]G. Trolliard, N. Ténèze, P. Boullay, and D. Mercurio, "TEM Study of Cation-Deficient-Perovskite Related $A_nB_{n-1}O_{3n}$ Compounds: The Twin-Shift Option," *J. Solid State Chem.*, **177** [4–5] 1188–96 (2004).

[73]K. R. Udayakumar and A. N. Cormack, "Structural Aspects of Phase Equilibria in the Strontium-Titanium-Oxygen System," *J. Am. Ceram. Soc.*, **71**, C-469–71 (1988).

[74]K. R. Udayakumar and A. N. Cormack, "Non-Stoichiometry in Alkaline Earth Excess Alkaline Earth Titanates," *J. Phys. Chem. Solids*, **50** [1] 55–60 (1989).

[75]Y. Tokura, "Correlated-Electron Physics in Transition-Metal Oxides," *Phys. Today*, **56** [7] 50–5 (2003).

[76]D. G. Schlom and J. S. Harris Jr., "MBE Growth of High T_c Superconductors"; pp. 505–622 in *Molecular Beam Epitaxy: Applications to Key Materials*, Edited by R. F. C. Farrow. Park Ridge, Noyes, 1995.

[77]J. H. Haeni, C. D. Theis, D. G. Schlom, W. Tian, X. Q. Pan, H. Chang, I. Takeuchi, and X.-D. Xiang, "Epitaxial Growth of the First Five Members of the $Sr_{n+1}Ti_nO_{3n+1}$ Ruddlesden–Popper Homologous Series," *Appl. Phys. Lett.*, **78** [21] 3292–4 (2001).

[78]W. Tian, X. Q. Pan, J. H. Haeni, and D. G. Schlom, "Transmission Electron Microscopy Study of $n = 1$–5 $Sr_{n+1}Ti_nO_{3n+1}$ Epitaxial Thin Films," *J. Mater. Res.*, **16** [7] 2013–26 (2001).

[79]D. G. Schlom, J. H. Haeni, J. Lettieri, C. D. Theis, W. Tian, J. C. Jiang, and X. Q. Pan, "Oxide Nano-Engineering Using MBE," *Mater. Sci. Eng. B*, **87** [3] 282–91 (2001).

[80]W. Tian, J. H. Haeni, D. G. Schlom, E. Hutchinson, B. L. Sheu, M. M. Rosario, P. Schiffer, Y. Liu, M. A. Zurbuchen, and X. Q. Pan, "Epitaxial Growth and Magnetic Properties of the First Five Members of the Layered $Sr_{n+1}Ru_nO_{3n+1}$ Oxide Series," *Appl. Phys. Lett.*, **90** [2] 022507 (2007).

[81]J. G. Bednorz and K. A. Müller, "Possible High T_c Superconductivity in the Ba–La–Cu–O System," *Z. Phys. B*, **64** [2] 189–93 (1986).

[82]J. G. Bednorz, M. Takashige, and K. A. Müller, "Susceptibility Measurements Support High-T_c Superconductivity in the Ba–La–Cu–O System," *Europhys. Lett.*, **3** [3] 379–85 (1987).

[83]D. Dijkkamp, T. Venkatesan, X. D. Wu, S. A. Shaheen, N. Jisrawi, Y. H. Min-Lee, W. L. McLean, and M. Croft, "Preparation of Y–Ba–Cu Oxide Superconductor Thin Films using Pulsed Laser Evaporation from High T_c Bulk Material," *Appl. Phys. Lett.*, **51** [8] 619–21 (1987).

[84]X. D. Wu, A. Inam, T. Venkatesan, C. C. Chang, E. W. Chase, P. Barboux, J. M. Tarascon, and B. Wilkens, "Low-Temperature Preparation of High T_c Superconducting Thin Films," *Appl. Phys. Lett.*, **52** [9] 754–6 (1988).

[85]R. Ramesh, K. Luther, B. Wilkens, D. L. Hart, E. Wang, J. M. Tarascon, A. Inam, X. D. Wu, and T. Venkatesan, "Epitaxial Growth of Ferroelectric Bismuth Titanate Thin Films by Pulsed Laser Deposition," *Appl. Phys. Lett.*, **57** [15] 1505–7 (1990).

[86]D. B. Chrisey, and G. K. Hubler (ed), *Pulsed Laser Deposition of Thin Films*. Wiley, New York, 1994.

[87]T. Frey, C. C. Chi, C. C. Tsuei, T. Shaw, and F. Bozso, "Effect of Atomic Oxygen on the Initial Growth Mode in Thin Epitaxial Cuprate Films," *Phys. Rev. B*, **49** [5] 3483–91 (1994).

[88]G. Koster, G. J. H. M. Rijnders, D. H. A. Blank, and H. Rogalla, "Imposed Layer-by-Layer Growth by Pulsed Laser Interval Deposition," *Appl. Phys. Lett.*, **74** [24] 3729–31 (1999).

[89]U. Poppe, J. Schubert, R. R. Arons, W. Evers, C. H. Freiburg, W. Reichert, K. Schmidt, W. Sybertz, and K. Urban, "Direct Production of Crystalline Superconducting Thin Films of $YBa_2Cu_3O_7$ by High-Pressure Oxygen Sputtering," *Solid State Commun.*, **66** [6] 661–5 (1988).

[90]H. C. Li, G. Linker, F. Ratzel, R. Smithey, and J. Geerk, "*In Situ* Preparation of Y–Ba–Cu–O Superconducting Thin Films by Magnetron Sputtering," *Appl. Phys. Lett.*, **52** [13] 1098–100 (1988).

[91]B. Pachaly, R. Bruchhaus, D. Pitzer, H. Huber, W. Wersing, and F. Koch, "Pyroelectric Properties of Lead Titanate Thin Films deposited on Pt-Coated Si Wafers by Multi-Target Sputtering," *Integr. Ferroelectrics*, **5** [4] 333–8 (1994).

[92]P. Muralt, T. Maeder, L. Sagalowicz, S. Hiboux, S. Scalese, D. Naumovic, R. G. Agostino, N. Xanthopoulos, H. J. Mathieu, L. Patthey, and E. L. Bullock, "Texture Control of $PbTiO_3$ and $Pb(Zr,Ti)O_3$ Thin Films with TiO_2 Seeding," *J. Appl. Phys.*, **83** [7] 3835–41 (1998).

[93]T. Maeder, P. Muralt, and L. Sagalowicz, "Growth of (111)-Oriented PZT on RuO_2(100)/Pt(111) Electrodes by In-Situ Sputtering," *Thin Solid Films*, **345** [2] 300–6 (1999).

[94]N. K. Pervez, P. J. Hansen, and R. A. York, "High Tunability Barium Strontium Titanate Thin Films for RF Circuit Applications," *Appl. Phys. Lett.*, **85** [19] 4451–3 (2004).

[95]H. Koinuma, M. Kawasaki, M. Funabashi, T. Hasegawa, K. Kishio, K. Kitazawa, K. Fueki, and S. Nagata, "Preparation of Superconducting Thin Films of $(La_{1-x}Sr_x)_yCuO_{4-\delta}$ by Sputtering," *J. Appl. Phys.*, **62** [4] 1524–6 (1987).

[96]R. L. Sandstrom, W. J. Gallagher, T. R. Dinger, R. H. Koch, R. B. Laibowitz, A. W. Kleinsasser, R. J. Gambino, B. Bumble, and M. F. Chisholm, "Reliable Single-Target Sputtering Process for High-Temperature Superconducting Films and Devices," *Appl. Phys. Lett.*, **53** [5] 444–6 (1988).

[97]X. X. Xi, G. Linker, O. Meyer, E. Nold, B. Obst, F. Ratzel, R. Smithey, B. Strehlau, F. Weschenfelder, and J. Geerk, "Superconducting and Structural Properties of YBaCuO Thin Films Deposited by Inverted Cylindrical Magnetron Sputtering," *Z. Phys. B*, **74** [1] 13–9 (1989).

[98]C. B. Eom, J. Z. Sun, K. Yamamoto, A. F. Marshall, K. E. Luther, T. H. Geballe, and S. S. Laderman, "*In Situ* Grown $YBa_2Cu_3O_{7-d}$ Thin Films from Single-Target Magnetron Sputtering," *Appl. Phys. Lett.*, **55** [6] 595–7 (1989).

[99]C. B. Eom, R. B. Van Dover, J. M. Phillips, D. J. Werder, J. H. Marshall, C. H. Chen, R. J. Cava, R. M. Fleming, and D. K. Fork, "Fabrication and Properties of Epitaxial Ferroelectric Heterostructures with ($SrRuO_3$) Isotropic Metallic Oxide Electrodes," *Appl. Phys. Lett.*, **63** [18] 2570–2 (1993).

[100]C. H. Ahn, J.-M. Triscone, N. Archibald, M. Decroux, R. H. Hammond, T. H. Geballe, O. Fischer, and M. R. Beasley, "Ferroelectric Field Effect in Epitaxial Thin Film Oxide $SrCuO_2$/$Pb(Zr_{0.52}Ti_{0.48})O_3$ Heterostructures," *Science*, **269** [5222] 373–6 (1995).

[101]J.-M. Triscone, L. Frauchiger, M. Decroux, L. Mieville, O. Fischer, C. Beeli, P. Stadelmann, and G.-A. Racine, "Growth and Structural Properties of Epitaxial $Pb(Zr_xTi_{1-x})O_3$ Films and $Pb(Zr_xTi_{1-x})O_3$-Cuprate Heterostructures," *J. Appl. Phys.*, **79** [8] 4298–305 (1996).

[102]S. D. Bu, M. K. Lee, C. B. Eom, W. Tian, X. Q. Pan, S. K. Streiffer, and J. J. Krajewski, "Perovskite Phase Stabilization in Epitaxial $Pb(Mg_{1/3}Nb_{2/3})O_3$–$PbTiO_3$ Films by Deposition onto Vicinal (001) $SrTiO_3$ Substrates," *Appl. Phys. Lett.*, **79** [21] 3482–4 (2001).

[103]D. K. Lathrop, S. E. Russek, and R. A. Buhrman, "Production of $YBa_2Cu_3O_{7-y}$ Superconducting Thin Films *in Situ* by High-Pressure Reactive Evaporation and Rapid Thermal Annealing," *Appl. Phys. Lett.*, **51** [19] 1554–6 (1987).

[104]T. Terashima, K. Iijima, K. Yamamoto, Y. Bando, and H. Mazaki, "Single-Crystal $YBa_2Cu_3O_{7-x}$ Thin Films by Activated Reactive Evaporation," *Jpn. J. Appl. Phys., Part 2*, **27** [1] L91–3 (1988).

[105]P. Berberich, B. Utz, W. Prusseit, and H. Kinder, "Homogeneous High Quality $YBa_2Cu_3O_7$ Films on 3″ and 4″ Substrates," *Physica C*, **219** [3–4] 497–504 (1994).

[106]D. G. Schlom, J. N. Eckstein, E. S. Hellman, C. Webb, F. Turner, J. S. Harris Jr., M. R. Beasley, and T. H. Geballe, "Molecular Beam Epitaxy of Layered Dy–Ba–Cu–O Compounds"; pp. 197–200 in *Extended Abstracts, High-Temperature Superconductors II*, Edited by D. W. Capone II, W. H. Butler, B. Batlogg, and C. W. Chu. Materials Research Society, Pittsburgh, 1988.

[107]R. J. Spah, H. F. Hess, H. L. Stormer, A. E. White, and K. T. Short, "Parameters for *in Situ* Growth of High T_c Superconducting Thin Films Using an Oxygen Plasma Source," *Appl. Phys. Lett.*, **53** [5] 441–3 (1988).

[108]D. G. Schlom, J. N. Eckstein, E. S. Hellman, S. K. Streiffer, J. S. Harris Jr., M. R. Beasley, J. C. Bravman, T. H. Geballe, C. Webb, K. E. von Dessonneck, and F. Turner, "Molecular Beam Epitaxy of Layered Dy–Ba–Cu–O Compounds," *Appl. Phys. Lett.*, **53** [17] 1660–2 (1988).

[109]J. Kwo, M. Hong, D. J. Trevor, R. M. Fleming, A. E. White, R. C. Farrow, A. R. Kortan, and K. T. Short, "*In Situ* Epitaxial Growth of $Y_1Ba_2Cu_3O_{7-x}$ Films by Molecular Beam Epitaxy with an Activated Oxygen Source," *Appl. Phys. Lett.*, **53** [26] 2683–5 (1988).

[110]J. Eckstein and I. Bozovic, "High-Temperature Superconducting Multilayers and Heterostructures Grown by Atomic Layer-By-Layer Molecular Beam Epitaxy," *Annu. Rev. Mater. Sci.*, **25**, 679–709 (1995).

[111]I. Bozovic and D. G. Schlom, "Superconducting Thin Films: Materials, Preparation, and Properties"; pp. 8955–64 in *The Encyclopedia of Materials: Science and Technology*. Edited by K. H. J. Buschow, R. Cahn, M. C. Flemings, B.

Ilschner, E. J. Kramer, S. Mahajan, and P. Veyssiere. Pergamon, Amsterdam, 2001.
[112]C. D. Theis, J. Yeh, D. G. Schlom, M. E. Hawley, and G. W. Brown, "Adsorption-Controlled Growth of $PbTiO_3$ by Reactive Molecular Beam Epitaxy," *Thin Solid Films* **325** [1–2] 107–14 (1998).
[113]M. R. Warusawithana, E. V. Colla, J. N. Eckstein, with M. B. Weissman, "Artificial Dielectric Superlattices with Broken Inversion Symmetry," *Phys. Rev. Lett*., **90** [3] 036802 (2003).
[114]J. H. Haeni, P. Irvin, W. Chang, R. Uecker, P. Reiche, Y. L. Li, S. Choudhury, W. Tian, M. E. Hawley, B. Craigo, A. K. Tagantsev, X. Q. Pan, S. K. Streiffer, L. Q. Chen, S. W. Kirchoefer, J. Levy, and D. G. Schlom, "Room-Temperature Ferroelectricity in Strained $SrTiO_3$," *Nature*, **430** [7001] 758–61 (2004).
[115]T. Terashima, K. Shimura, Y. Bando, Y. Matsuda, A. Fujiyama, and S. Komiyama, "Superconductivity of One-Unit-Cell Thick $YBa_2Cu_3O_7$ Thin Film," *Phys. Rev. Lett*., **67** [10] 1362–5 (1991).
[116]A. Roelofs, T. Schneller, K. Szot, and R. Waser, "Piezoresponse Force Microscopy of Lead Titanate Nanograins Possibly Reaching the Limit of Ferroelectricity," *Appl. Phys. Lett*., **81** [27] 5231–3 (2002).
[117]I. Bozovic, G. Logvenov, M. A. J. Verhoeven, P. Caputo, E. Goldobin, and T. H. Geballe, "No Mixing of Superconductivity and Antiferromagnetism in a High-Temperature Superconductor," *Nature*, **422** [6934] 873–5 (2003).
[118]J.-M. Triscone, M. G. Karkut, L. Antognazza, O. Brunner, and Ø. Fischer, "Y–Ba–Cu–O/Dy–Ba–Cu–O Superlattices: A First Step Towards the Artificial Construction of High-T_c Superconductors," *Phys. Rev. Lett*., **63** [9] 1016–9 (1989).
[119]D. G. Schlom, J. N. Eckstein, I. Bozovic, Z. J. Chen, A. F. Marshall, K. E. von Dessonneck, and J. S. Harris Jr., "Molecular Beam Epitaxy—A Path to Novel High T_c Superconductors?"; pp. 234–47 in *Growth of Semiconductor Structures and High-T_c Thin Films on Semiconductors*, edited by A. Madhukar, *SPIE*, Vol. 1285. SPIE, Bellingham, 1990.
[120]D. H. Lowndes, D. P. Norton, and J. D. Budai, "Superconductivity in Nonsymmetric Epitaxial $YBa_2Cu_3O_{7-x}/PrBa_2Cu_3O_{7-x}$ Superlattices: The Superconducting Behavior of Cu–O Bilayers," *Phys. Rev. Lett*., **65** [9] 1160–3 (1990).
[121]S. J. Pennycook, M. F. Chisholm, D. E. Jesson, D. P. Norton, D. H. Lowndes, R. Feenstra, H. R. Kerchner, and J. O. Thomson, "Interdiffusion, Growth Mechanisms, and Critical Currents in $YBa_2Cu_3O_{7-x}/PrBa_2Cu_3O_{7-x}$ Superlattices," *Phys. Rev. Lett*., **67** [6] 765–8 (1991).
[122]K. Kamigaki, T. Terashima, K. Shimura, Y. Bando, and H. Terauchi, "Unit Cell-by-Unit Cell Grown $(YBa_2Cu_3O_{7-\delta})_1/(PrBa_2Cu_3O_{7-\delta})_1$ Superlattice," *Physica C*, **183** [4–6] 252–6 (1991).
[123]H. Tabata, T. Kawai, and S. Kawai, "Crystal Structure and Superconductivity of $(La,Sr)_2CuO_4/Sm_2CuO_4$ Superlattices Prepared by Excimer Laser Deposition," *Appl. Phys. Lett*., **58** [13] 1443–5 (1991).
[124]I. Bozovic and J. N. Eckstein, "Superconducting Superlattices"; pp. 99–207 in *Physical Properties of High Temperature Superconductors V*, Edited by D. M. Ginsberg. World Scientific, Singapore, 1996.
[125]J-M. Triscone and Ø. Fischer, "Superlattices of High-Temperature Superconductors: Synthetically Modulated Structures, Critical Temperatures and Vortex Dynamics," *Rep. Prog. Phys*., **60** [12] 1673–721 (1997).
[126]G. Koster, K. Verbist, G. Rijnders, H. Rogalla, G. van Tendeloo, and D. H. A. Blank, "Structure and Properties of $(Sr,Ca)CuO_2$–$BaCuO_2$ Superlattices Grown by Pulsed Laser Interval Deposition," *Physica C*, **353** [3–4] 167–83 (2001).
[127]H. Yamamoto, M. Naito, and H. Sato, "New Superconducting Cuprate Prepared by Low-Temperature Thin-Film Synthesis in a Ba–Cu–O System," *Jpn. J. Appl. Phys., Part 2*, **36** [3B] L341–4 (1997).
[128]B. S. Kwak, E. P. Boyd, and A. Erbil, "Metalorganic Chemical Vapor Deposition of $PbTiO_3$ Thin Films," *Appl. Phys. Lett*., **53** [18] 1702–4 (1988).
[129]M. Okada, S. Takai, M. Amemiya, and K. Tominaga, "Preparation of *c*-Axis-Oriented $PbTiO_3$ Thin Films by MOCVD Under Reduced Pressure," *Jpn. J. Appl. Phys., Part 1*, **28** [6] 1030–4 (1989).
[130]M. de Keijser, G. J. M. Dormans, J. F. M. Cillessen, D. M. de Leeuw, and H. W. Zandbergen, "Epitaxial $PbTiO_3$ Thin Films Grown by Organometallic Chemical Vapor Deposition," *Appl. Phys. Lett*., **58** [23] 2636–8 (1991).
[131]K. Fujii, H. Zama, and S. Oda, "Preparation of $YBa_2Cu_3O_x$ Thin Films by Layer-by-Layer Metalorganic Chemical Vapor Deposition," *Jpn. J. Appl. Phys., Part 2*, **31** [6B] L787–9 (1992).
[132]G. R. Bai, H. L. M. Chang, H. K. Kim, C. M. Foster, and D. J. Lam, "Epitaxy-Induced Phase of Near-Stoichiometry $PbTiO_3$ Films Prepared by Metalorganic Chemical Vapor Deposition," *Appl. Phys. Lett*., **61** [4] 408–10 (1992).
[133]G. J. M. Dormans, P. J. van Veldhoven, and M. de Keijser, "Composition-Controlled Growth of $PbTiO_3$ on $SrTiO_3$ by Organometallic Chemical Vapour Deposition," *J. Cryst. Growth*, **123** [3–4] 537–44 (1992).
[134]Z. Li, C. M. Foster, D. Guo, H. Zhang, G. R. Bai, P. M. Baldo, and L. E. Rehn, "Growth of High Quality Single-Domain Single-Crystal Films of $PbTiO_3$," *Appl. Phys. Lett*., **65** [9] 1106–8 (1994).
[135]M. de Keijser and G. J. M. Dormans, "Modelling of Organometallic Chemical Vapour Deposition of Lead Titanate," *J. Cryst. Growth*, **149** [3–4] 215–28 (1995).
[136]M. de Keijser and G. J. M. Dormans, "Chemical Vapor Deposition of Electroceramic Thin Films," *MRS Bull*., **21** [6] 37–43 (1996).
[137]C. M. Foster, "Chemical Vapor Deposition of Ferroelectric Thin Films;" pp. 167–97 in *Thin Film Ferroelectric Materials and Devices*, Edited by R. Ramesh. Kluwer, Boston, 1997.
[138]G.-R. Bai, I.-F. Tsu, A. Wang, C. M. Foster, C. E. Murray, and V. P. Dravid, "*In Situ* Growth of Highly Oriented $Pb(Zr_{0.5}Ti_{0.5})O_3$ Thin Films by Low-Temperature Metal-Organic Chemical Vapor Deposition," *Appl. Phys. Lett*., **72** [13] 1572–4 (1998).
[139]J. F. Roeder, T. H. Baum, S. M. Bilodeau, G. T. Stauf, C. Ragaglia, M. W. Russell, and P. C. Van Buskirk, "Liquid-Delivery MOCVD: Chemical and Process Perspectives on Ferroelectric Thin Film Growth," *Adv. Mater. Opt. Electron*., **10** [3–5] 145–54 (2000).
[140]M. V. Ramana Murty, S. K. Streiffer, G. B. Stephenson, J. A. Eastman, G.-R. Bai, A. Munkholm, O. Auciello, and C. Thompson, "*In Situ* X-Ray Scattering Study of $PbTiO_3$ Chemical-Vapor Deposition," *Appl. Phys. Lett*., **80** [10] 1809–11 (2002).
[141]K. Saito, I. Yamaji, T. Akai, M. Mitsuya, and H. Funakubo, "Quantitative Effects of Preferred Orientation and Impurity Phases on Ferroelectric Properties of $SrBi_2(Ta_{1-x}Nb_x)_2O_9$ Thin Films Measured by X-ray Diffraction Reciprocal Space Mapping," *Jpn. J. Appl. Phys., Part 1*, **42** [2A] 539–43 (2003).
[142]A. Nagai, H. Morioka, G. Asano, H. Funakubo, and A. Saiki, "Preparing $Pb(Zr,Ti)O_3$ Films Less than 100 nm Thick by Low-Temperature Metalorganic Chemical Vapor Deposition," *Appl. Phys. Lett*., **86** [14] 142906 (2005).
[143]Y. K. Kim, H. Morioka, R. Ueno, S. Yokoyama, and H. Funakubo, "Comparison of Electrical Properties of (100)/(001)-Oriented Epitaxial $Pb(Zr_{0.35},Ti_{0.65})O_3$ Thin Films with the same (001) Domain Fraction Grown on (100)Si and (100)$SrTiO_3$ Substrates," *Appl. Phys. Lett*., **86** [21] 212905 (2005).
[144]J. Fukushima, K. Kodaira, and T. Matsushita, "Preparation of Ferroelectric PZT Films by Thermal Decomposition of Organometallic Compounds," *J. Mater. Sci*., **19** [2] 595–8 (1984).
[145]K. D. Budd, S. K. Dey, and D. A. Payne, "Sol–Gel Processing of $PbTiO_3$, $PbZrO_3$, PZT, and PLZT Thin Films," *Br. Ceram. Proc*., **36**, 107–21 (1985).
[146]R. W. Schwartz, "Chemical Solution Deposition of Perovskite Thin Films," *Chem. Mater*., **9** [11] 2325–40 (1997).
[147]A. I. Kingon and S. Srinivasan, "Lead Zirconate Titanate Thin Films Directly on Copper Electrodes for Ferroelectric, Dielectric and Piezoelectric Applications," *Nat. Mater*., **4** [3] 233–7 (2005).
[148]M. D. Losego, L. H. Jimison, J. F. Ihlefeld, and J.-P. Maria, "Ferroelectric Response from Lead Zirconate Titanate Thin Films Prepared Directly on Low-Resistivity Copper Substrates," *Appl. Phys. Lett*., **86** [17] 172906 (2005).
[149]K. Iijima, T. Terashima, Y. Bando, K. Kamigaki, and H. Terauchi, "Atomic Layer Growth of Oxide Thin Films with Perovskite-Type Structure by Reactive Evaporation," *J. Appl. Phys*., **72** [7] 2840–5 (1992).
[150]H.-M. Christen, L. A. Boatner, J. D. Budai, M. F. Chisholm, L. A. Géa, P. J. Marrero, and D. P. Norton, "The Growth and Properties of Epitaxial $KNbO_3$ Thin Films and $KNbO_3/KTaO_3$ Superlattices," *Appl. Phys. Lett*., **68** [11] 1488–90 (1996).
[151]J. C. Jiang, X. Q. Pan, W. Tian, C. D. Theis, and D. G. Schlom, "Abrupt $PbTiO_3/SrTiO_3$ Superlattices Grown by Reactive Molecular Beam Epitaxy," *Appl. Phys. Lett*., **74** [19] 2851–3 (1999).
[152]A. Ohtomo, D. A. Muller, J. L. Grazul, and H. Y. Hwang, "Artificial Charge-Modulation in Atomic-Scale Perovskite Titanate Superlattices," *Nature*, **419** [6905] 378–80 (2002).
[153]D. A. Muller, N. Nakagawa, A. Ohtomo, J. L. Grazul, and H. Y. Hwang, "Atomic-Scale Imaging of Nanoengineered Oxygen Vacancy Profiles in $SrTiO_3$," *Nature*, **430** [7000] 657–61 (2004).
[154]C. H. Ahn, K. M. Rabe, and J.-M. Triscone, "Ferroelectricity at the Nanoscale: Local Polarization in Oxide Thin Films and Heterostructures," *Science*, **303** [5657] 488–91 (2004).
[155]H. N. Lee, H. M. Christen, M. F. Chisholm, C. M. Rouleau, and D. H. Lowndes, "Strong Polarization Enhancement in Asymmetric Three-Component Ferroelectric Superlattices," *Nature*, **433** [7024] 395–9 (2005).
[156]M. Dawber, C. Lichtensteiger, M. Cantoni, M. Veithen, P. Ghosez, K. Johnston, K. M. Rabe, and J.-M. Triscone, "Unusual Behavior of the Ferroelectric Polarization in $PbTiO_3/SrTiO_3$ Superlattices," *Phys. Rev. Lett*., **95** [17] 177601 (2005).
[157]D. A. Tenne, A. Bruchhausen, N. D. Lanzillotti-Kimura, A. Fainstein, R. S. Katiyar, A. Cantarero, A. Soukiassian, V. Vaithyanathan, J. H. Haeni, W. Tian, D. G. Schlom, K. J. Choi, D. M. Kim, C. B. Eom, H. P. Sun, X. Q. Pan, Y. L. Li, L. Q. Chen, Q. X. Jia, S. M. Nakhmanson, K. M. Rabe, and X. X. Xi, "Probing Nanoscale Ferroelectricity by Ultraviolet Raman Spectroscopy," *Science*, **313** [5793] 1614–6 (2006).
[158]Y. Jia, M. A. Zurbuchen, S. Wozniak, A. H. Carim, D. G. Schlom, L.-N. Zou, S. Briczinski, and Y. Liu, "Epitaxial Growth of Metastable Ba_2RuO_4 Films with the K_2NiF_4 Structure," *Appl. Phys. Lett*., **74** [25] 3830–2 (1999).
[159]O. Y. Gorbenko, S. V. Samoilenkov, I. E. Graboy, and A. R. Kaul, "Epitaxial Stabilization of Oxides in Thin Films," *Chem. Mater*., **14** [10] 4026–43 (2002).
[160]A. F. Moreira dos Santos, A. K. Cheetham, W. Tian, X. Q. Pan, Y. Jia, N. J. Murphy, J. Lettieri, and D. G. Schlom, "Epitaxial Growth and Properties of Metastable $BiMnO_3$ Thin Films," *Appl. Phys. Lett*., **84** [1] 91–3 (2004).
[161]T. Heeg, M. Roeckerath, J. Schubert, W. Zander, C. Buchal, H. Y. Chen, C. L. Jia, Y. Jia, C. Adamo, and D. G. Schlom, "Epitaxially Stabilized Growth of Orthorhombic $LuScO_3$ Thin Films," *Appl. Phys. Lett*., **90** [19] 192901 (2007).
[162]G. K. Hubler (ed), "Pulsed Laser Deposition," *MRS Bull*., **17** [2] 26–9 (1992).
[163]J. Cheung and J. Horwitz, "Pulsed Laser Deposition History and Laser–Target Interactions," *MRS Bull*., **17** [2] 30–6 (1992).
[164]D. B. Chrisey and A. Inam, "Pulsed Laser Deposition of High Tc Superconducting Thin Films for Electronic Device Applications," *MRS Bull*., **17** [2] 37–43 (1992).
[165]T. Venkatesan, X. D. Wu, R. Muenchausen, and A. Pique, "Pulsed Laser Deposition: Future Directions," *MRS Bull*., **17** [2] 54–8 (1992).
[166]K. -H. Hellwege, and A. M. Hellwege (eds), *Landolt-Börnstein: Numerical Data and Functional Relationships in Science and Technology, Part a*, **Vol. 16**, p. 233. Springer-Verlag, Berlin, 1981.
[167]J. Lettieri, Y. Jia, M. Urbanik, C. I. Weber, J-P. Maria, D. G. Schlom, H. Li, R. Ramesh, R. Uecker, and P. Reiche, "Epitaxial Growth of (001)-Oriented and (110)-Oriented $SrBi_2Ta_2O_9$ Thin Films," *Appl. Phys. Lett*., **73** [20] 2923–5 (1998).
[168]J. Lettieri, M. A. Zurbuchen, Y. Jia, D. G. Schlom, S. K. Streiffer, and M. E. Hawley, "Epitaxial Growth of $SrBi_2Nb_2O_9$ on (110) $SrTiO_3$ and the Establishment of a Lower Bound on the Spontaneous Polarization of $SrBi_2Nb_2O_9$," *Appl. Phys. Lett*., **77** [19] 3090–2 (2000).

[169]H. L. Kao, J. Kwo, R. M. Fleming, M. Hong, and J. P. Mannaerts, "*In Situ* Growth and Properties of Single-Crystalline-Like $La_{2-x}Sr_xCuO_4$ Epitaxial Films by Off-Axis Sputtering," *Appl. Phys. Lett*., **59** [21] 2748–50 (1991).
[170]O. Wada, K. Kuroda, J. Tanimura, M. Kataoka, K. Kojima, T. Takami, K. Hamanaka, and T. Ogama, "Defence of Crystal Orientation of BiSrCaCuO Thin Films on Off-Angles of Vicinal $SrTiO_3$ (110) Surfaces," *Jpn. J. Appl. Phys*., **30** [11A] L1881–3 (1991).
[171]J. Tanimura, K. Kuroda, M. Kataoka, O. Wada, T. Takami, K. Kojima, and T. Ogama, "(01*n*)-Oriented BiSrCaCuO Thin Films Formed on CeO_2 Buffer Layers," *Jpn. J. Appl. Phys*., **32** [2B] L254–6 (1993).
[172]J. Lettieri, M. A. Zurbuchen, Y. Jia, D. G. Schlom, S. K. Streiffer, and M. E. Hawley, "Epitaxial Growth of Non-*c*-Oriented $SrBi_2Nb_2O_9$ on (111) $SrTiO_3$," *Appl. Phys. Lett*., **76** [20] 2937–9 (2000).
[173]M. A. Zurbuchen, J. Lettieri, Y. Jia, D. G. Schlom, S. K. Streiffer, and M. E. Hawley, "Transmission Electron Microscopy Study of (103)-Oriented Epitaxial $SrBi_2Nb_2O_9$ Films Grown on (111) $SrTiO_3$ and (111) $SrRuO_3$/(111) $SrTiO_3$," *J. Mater. Res*., **16** [2] 489–502 (2001).
[174]M. Kitabatake, P. Fons, and J. E. Greene, "Molecular Dynamics Simulations of Low-Energy Particle Bombardment Effects During Vapor-Phase Crystal Growth: 10 eV Si Atoms Incident on Si(001)2×1 Surfaces," *J. Vac. Sci. Technol. A*, **8** [5] 3726–35 (1990).
[175]M. Kitabatake and J. E. Greene, "Molecular Dynamics and Quasidynamics Simulations of Low-Energy Particle Bombardment Effects During Vapor-Phase Crystal Growth: Production and Annihilation of Defects Due to 50 eV Si Incident on (2×1)-Terminated Si(001)," *J. Appl. Phys*., **73** [7] 3183–94 (1993).
[176]E. J. Tarsa, E. A. Hachfeld, F. T. Quinlan, J. S. Speck, and M. Eddy, "Growth-Related Stress and Surface Morphology in Homoepitaxial $SrTiO_3$ Films," *Appl. Phys. Lett*., **68** [4] 490–2 (1996).
[177]J.-P. Maria, S. Trolier-McKinstry, D. G. Schlom, M. E. Hawley, and G. W. Brown, "The Influence of Energetic Bombardment on the Structure and Properties of Epitaxial $SrRuO_3$ Thin Films Grown by Pulsed Laser Deposition," *J. Appl. Phys*., **83** [8] 4373–9 (1998).
[178]T. Ohnishi, M. Lippmaa, T. Yamamoto, S. Meguro, and H. Koinuma, "Improved Stoichiometry and Misfit Control in Perovskite Thin Film Formation at a Critical Fluence by Pulsed Laser Deposition," *Appl. Phys. Lett*., **87** [24] 2419191 (2005).
[179]T. Ohnishi, K. Shibuya, T. Yamamoto, and M. Lippmaa, "Defects and Transport in Complex Oxide Thin Films," *J. Appl. Phys*., **103** [10] 103703. (2008).
[180]H. Karl and B. Stritzker, "Reflection High-Energy Electron Diffraction Oscillations Modulated by Laser-Pulse Deposited $YBa_2Cu_3O_{7-x}$," *Phys. Rev. Lett*., **69** [20] 2939–42 (1992).
[181]G. J. H. M. Rijnders, A. G. Koster, D. H. A. Blank, and H. Rogalla, "*In Situ* Monitoring During Pulsed Laser Deposition of Complex Oxides Using Reflection High Energy Electron Diffraction Under High Oxygen Pressure," *Appl. Phys. Lett*., **70** [14] 1888–90 (1997).
[182]M. H. Yang and C. P. Flynn, "Growth of Alkali Halides from Molecular Beams: Global Growth Characteristics," *Phys. Rev. Lett*., **62** [21] 2476–9 (1989).
[183]S. Yadavalli, M. H. Yang, and C. P. Flynn, "Low-Temperature Growth of MgO by Molecular-Beam Epitaxy," *Phys. Rev. B*, **41** [11] 7961–3 (1990).
[184]A. Y. Cho and J. R. Arthur, "Molecular Beam Epitaxy," *Progress in Solid-State Chemistry*, **10** [3] 157–91 (1975).
[185]R. F. C. Farrow (ed), *Molecular Beam Epitaxy: Applications to Key Materials*. Noyes, Park Ridge, 1995.
[186]M. A. Herman and H. Sitter, *Molecular Beam Epitaxy: Fundamentals and Current Status*, 2nd edition, Springer-Verlag, Berlin, 1996.
[187]S. Yoshida, "Reactive Molecular Beam Epitaxy"; pp. 287–316 in *Critical Reviews™ in Solid State and Materials Sciences*, **Vol. 11**, Edited by D. E. Schuele, and R. W. Hoffman. CRC Press, Boca Raton, FL, 1984.
[188]K. Iijima, T. Terashima, K. Yamamoto, K. Hirata, and Y. Bando, "Preparation of Ferroelectric $BaTiO_3$ Thin Films by Activated Reactive Evaporation," *Appl. Phys. Lett*., **56** [6] 527–9 (1990).
[189]T. Sakamoto, H. Funabashi, K. Ohta, T. Nakagawa, N. J. Kawai, T. Kojima, and Y. Bando, "Well Defined Superlattice Structures Made by Phase-Locked Epitaxy Using RHEED Intensity Oscillations," *Superlattices Microstruct*., **1** [4] 347–52 (1985).
[190]A. C. Gossard, P. M. Petroff, W. Weigmann, R. Dingle, and A. Savage, "Epitaxial Structures with Alternate-Atomic-Layer Composition Modulation," *Appl. Phys. Lett*., **29** [6] 323–5 (1976).
[191]A. Y. Cho, "Molecular Beam Epitaxy from Research to Manufacturing," *MRS Bull*., **20** [4] 21–8 (1995).
[192]R. A. Betts and C. W. Pitt, "Growth of Thin-Film Lithium Niobate by Molecular Beam Epitaxy," *Electron. Lett*., **21** [21] 960–2 (1985).
[193]M. Petrucci, C. W. Pitt, and P. J. Dobson, "RHEED Studies on *z*-Cut $LiNbO_3$," *Electron. Lett*., **22** [18] 954–6 (1986).
[194]Z. Sitar, F. Gitmans, W. Liu, and P. Gunter, "Homo and Heteroepitaxial Growth of $LiTaO_3$ and $LiNbO_3$ by MBE"; pp. 255–60 in *Epitaxial Oxide Thin Films II*, **Vol. 401**, Edited by J. S. Speck, D. K. Fork, R. M. Wolf, and T. Shiosaki. Materials Research Society, Pittsburgh, 1996.
[195]W. A. Doolittle, A. G. Carver, and W. Henderson, "Molecular Beam Epitaxy of Complex Metal-Oxides: Where Have We Come, Where Are We Going, and How Are We Going to Get There," *J. Vac. Sci. Technol. B*, **23** [3] 1272–6 (2005).
[196]R. A. McKee, F. J. Walker, J. R. Conner, E. D. Specht, and D. E. Zelmon, "Molecular Beam Epitaxy Growth of Epitaxial Barium Silicide, Barium Oxide, and Barium Titanate on Silicon," *Appl. Phys. Lett*., **59** [7] 782–4 (1991).
[197]R. A. McKee, F. J. Walker, E. D. Specht, G. E. Jellison Jr., and L. A. Boatner, "Interface Stability and the Growth of Optical Quality Perovskites on MgO," *Phys. Rev. Lett*., **72** [17] 2741–4 (1994).
[198]R. A. McKee, F. J. Walker, and M. F. Chisholm, "Physical Structure and Inversion Charge at a Semiconductor Interface with a Crystalline Oxide," *Science*, **293** [5529] 468–71 (2001).
[199]T. Tsurumi, T. Suzuki, M. Yamane, and M. Daimon, "Fabrication of Barium Titanate/Strontium Titanate Artificial Superlattice by Atomic Layer Epitaxy," *Jpn. J. Appl. Phys., Part 1*, **33** [9B] 5192–5 (1994).
[200]H. Shigetani, K. Kobayashi, M. Fujimoto, W. Sugimura, Y. Matsui, and J. Tanaka, "$BaTiO_3$ Thin Films Grown on $SrTiO_3$ Substrates by a Molecular-Beam-Epitaxy Method Using Oxygen Radicals," *J. Appl. Phys*., **81** [2] 693–7 (1997).
[201]H. P. Sun, W. Tian, X. Q. Pan, J. H. Haeni, and D. G. Schlom, "Evolution of Dislocation Arrays in Epitaxial $BaTiO_3$ Thin Films Grown on (100) $SrTiO_3$," *Appl. Phys. Lett*., **84** [17] 3298–300 (2004).
[202]H. P. Sun, X. Q. Pan, J. H. Haeni, and D. G. Schlom, "Structural Evolution of Dislocation Half-Loops in Epitaxial $BaTiO_3$ Thin Films During High-Temperature Annealing," *Appl. Phys. Lett*., **85** [11] 1967–9 (2004).
[203]K. J. Choi, M. D. Biegalski, Y. L. Li, A. Sharan, J. Schubert, R. Uecker, P. Reiche, Y. B. Chen, X. Q. Pan, V. Gopalan, L.-Q. Chen, D. G. Schlom, and C. B. Eom, "Enhancement of Ferroelectricity in Strained $BaTiO_3$ Thin Films," *Science*, **306** [5698] 1005–9 (2004).
[204]F. J. Walker and R. A. McKee, "High-k Crystalline Gate Dielectrics: A Research Perspective"; pp. 607–37 in *High Dielectric Constant Materials: VLSI MOSFET Applications*, Edited by H. R. Huff, and D. C. Gilmer. Springer, Berlin, 2005.
[205]V. Vaithyanathan, J. Lettieri, W. Tian, A. Kochhar, H. Ma, A. Sharan, A. Vasudevarao, V. Gopalan, Y. Li, L. Q. Chen, P. Zschack, J. C. Woicik, J. Levy, and D. G. Schlom, "*c*-Axis Oriented Epitaxial $BaTiO_3$ Films on (001) Si," *J. Appl. Phys*., **100** [2] 024108 (2006).
[206]C. D. Theis and D. G. Schlom, "Epitaxial Lead Titanate Grown by MBE," *J. Cryst. Growth*, **174** [1–4] 473–9 (1997).
[207]C. D. Theis, J. Yeh, D. G. Schlom, M. E. Hawley, G. W. Brown, J. C. Jiang, and X. Q. Pan, "Adsorption-Controlled Growth of $Bi_4Ti_3O_{12}$ by Reactive MBE," *Appl. Phys. Lett*., **72** [22] 2817–9 (1998).
[208]S. Migita, H. Ota, H. Fujino, Y. Kasai, and S. Sakai, "Epitaxial $Bi_4Ti_3O_{12}$ Thin Film Growth using Bi Self-Limiting Function," *J. Cryst. Growth*, **200** [1–2] 161–8 (1999).
[209]I. Bozovic, J. N. Eckstein, and G. F. Virshup, "Superconducting Oxide Multilayers and Superlattices: Physics, Chemistry, and Nanoengineering," *Physica C*, **235–240** [1] 178–81 (1994).
[210]R. A. McKee, F. J. Walker, and M. F. Chisholm, "Crystalline Oxides on Silicon: The First Five Monolayers," *Phys. Rev. Lett*., **81** [14] 3014–7 (1998).
[211]J. H. Haeni, C. D. Theis, and D. G. Schlom, "RHEED Intensity Oscillations for the Stoichiometric Growth of $SrTiO_3$ Thin Films by Reactive Molecular Beam Epitaxy," *J. Electroceram*., **4** [2/3] 385–91 (2000).
[212]K. Eisenbeiser, J. M. Finder, Z. Yu, J. Ramdani, J. A. Curless, J. A. Hallmark, R. Droopad, W. J. Ooms, L. Salem, S. Bradshaw, and C. D. Overgaard, "Field Effect Transistors with $SrTiO_3$ Gate Dielectric on Si," *Appl. Phys. Lett*., **76** [10] 1324–6 (2000).
[213]Z. Yu, J. Ramdani, J. A. Curless, C. D. Overgaard, J. M. Finder, R. Droopad, K. W. Eisenbeiser, J. A. Hallmark, W. J. Ooms, and V. S. Kaushik, "Epitaxial Oxide Thin Films on Si(001)," *J. Vac. Sci. Technol. B*, **18** [4] 2139–45 (2000).
[214]J. Lettieri, "Critical Issues of Complex, Epitaxial Oxide Growth and Integration with Silicon by Molecular Beam Epitaxy"; Ph.D. Thesis, Pennsylvania State University, 2002. Available on-line at http://etda.libraries.psu.edu/theses/approved/WorldWideIndex/ETD-202/index.html
[215]H. Li, X. Hu, Y. Wei, Z. Yu, X. Zhang, R. Droopad, A. A. Demkov, J. Edwards Jr., K. Moore, W. Ooms, J. Kulik, and P. Fejes, "Two-Dimensional Growth of High-Quality Strontium Titanate Thin Films on Si," *J. Appl. Phys*., **93** [8] 4521–5 (2003).
[216]M. D. Biegalski, Y. Jia, D. G. Schlom, S. Trolier-McKinstry, S. K. Streiffer, V. Sherman, R. Uecker, and P. Reiche, "Relaxor Ferroelectricity in Strained Epitaxial $SrTiO_3$ Thin Films on $DyScO_3$ Substrates," *Appl. Phys. Lett*., **88** [19] 192907 (2006).
[217]L. Fitting Kourkoutis, C. S. Hellberg, V. Vaithyanathan, H. Li, M. K. Parker, K. E. Andersen, D. G. Schlom, and D. A. Muller, "Imaging the Phase Separation in Atomically Thin Buried $SrTiO_3$ Layers by Electron Channeling," *Phys. Rev. Lett*., **100** [3] 036101 (2008).
[218]M. D. Biegalski, S. Trolier-McKinstry, D. G. Schlom, D. D. Fong, J. A. Eastman, P. H. Fuoss, S. K. Streiffer, T. Heeg, J. Schubert, W. Tian, X. Q. Pan, M. E. Hawley, M. Bernhagen, P. Reiche, and R. Uecker, "Critical Thickness of High Structural Quality $SrTiO_3$ Films Grown on Orthorhombic (101) $DyScO_3$," *J. Appl. Phys*., in press.
[219]J. N. Eckstein, I. Bozovic, M. Rzchowski, J. O'Donnell, B. Hinaus, and M. Onellion, "Molecular Beam Epitaxy of Single Crystal Colossal Magneto-Resistive Material"; pp. 467–71 in *Epitaxial Oxide Thin Films II*, **Vol. 401**, Edited by J. S. Speck, D. K. Fork, R. M. Wolf, and T. Shiosaki. Materials Research Society, Pittsburgh, 1996.
[220]J. N. Eckstein, I. Bozovic, J. O'Donnell, M. Onellion, and M. S. Rzchowski, "Anisotropic Magnetoresistance in Tetragonal $La_{1-x}Ca_xMnO_\delta$ Thin Films," *Appl. Phys. Lett*., **69** [9] 1312–4 (1995).
[221]L. Maritato and A. Y. Petrov, "High Metal–Insulator Transition Temperature in $La_{1-x}Sr_xMnO_3$ Thin Films Grown in Low Oxygen Partial Pressure by Molecular Beam Epitaxy," *J. Magn. Magn. Mater*., **272–276** [2] 1135–6 (2004).
[222]G. M. Roesler Jr., M. E. Filipkowski, P. R. Broussard, Y. U. Idzerda, M. S. Osofsky, and R. J. Soulen Jr., "Epitaxial Multilayers of Ferromagnetic Insulators with Nonmagnetic Metals and Superconductors"; pp. 285–90 in *Superconducting Superlattices and Multilayers*, **Vol. 2157**, Edited by I. Bozovic. SPIE, Bellingham, 1994.
[223]N. Iwata, G. Pindoria, T. Morishita, and K. Kohn, "Preparation and Magnetic Properties of EuO Thin Films Epitaxially Grown on MgO and $SrTiO_3$ Substrates," *J. Phys. Soc. Jpn*., **69** [1] 230–6 (2000).

[224]P. G. Steeneken, "New Light on EuO Thin Films"; Ph.D. thesis, University of Groningen, 2002.
[225]J. Lettieri, V. Vaithyanathan, S. K. Eah, J. Stephens, V. Sih, D. D. Awschalom, J. Levy, and D. G. Schlom, "Epitaxial Growth and Magnetic Properties of EuO on (001) Si by Molecular-Beam Epitaxy," *Appl. Phys. Lett*., **83** [5] 975–7 (2003).
[226]A. Schmehl, V. Vaithyanathan, A. Herrnberger, S. Thiel, C. Richter, M. Liberati, T. Heeg, M. Röckerath, L. Fitting Kourkoutis, S. Mühlbaur, P. Böni, D. A. Muller, Y. Barash, J. Schubert, Y. Idzerda, J. Mannhart, and D. G. Schlom, "Epitaxial Integration of the Highly Spin-Polarized Ferromagnetic Semiconductor EuO with Silicon and GaN," *Nat. Mater*., **6** [11] 882–7 (2007).
[227]R. W. Ulbricht, T. Heeg, D. G. Schlom, A. Schmehl, and J. Schubert, "Adsorption-Controlled Growth of EuO by Molecular-Beam Epitaxy," *Appl. Phys. Lett*, submitted.
[228]S. A. Chambers, "Epitaxial Growth and Properties of Thin Film Oxides," *Surf. Sci. Rep*., **39** [5–6] 105–80 (2000).
[229]J. Kabelac, S. Ghosh, P. Dobal, and R. Katiyar, "rf Oxygen Plasma Assisted Molecular Beam Epitaxy Growth of $BiFeO_3$ Thin Films on $SrTiO_3$ (001)," *J. Vac. Sci. Technol. B*, **25** [3] 1049–52 (2007).
[230]J. F. Ihlefeld, A. Kumar, V. Gopalan, D. G. Schlom, Y. B. Chen, X. Q. Pan, T. Heeg, J. Schubert, X. Ke, P. Schiffer, J. Orenstein, L. W. Martin, Y. H. Chu, and R. Ramesh, "Adsorption-Controlled Molecular-Beam Epitaxial Growth of $BiFeO_3$," *Appl. Phys. Lett*., **91** [7] 071922 (2007).
[231]J. F. Ihlefeld, N. J. Podraza, Z. K. Liu, R. C. Rai, X. Xu, T. Heeg, Y. B. Chen, J. Li, R. W. Collins, J. L. Musfeldt, X. Q. Pan, J. Schubert, R. Ramesh, and D. G. Schlom, "Optical Band Gap of $BiFeO_3$ Grown by Molecular-Beam Epitaxy," *Appl. Phys. Lett*., **92** [14] 142908 (2008).
[232]S. Imada, S. Shouriki, E. Tokumitsu, and H. Ishiwara, "Epitaxial Growth of Ferroelectric $YMnO_3$ Thin Films on Si(111) Substrates by Molecular Beam Epitaxy," *Jpn. J. Appl. Phys., Part 1*, **37** [12A] 6497–501 (1998).
[233]Y. Chye, T. Liu, D. Li, K. Lee, D. Lederman, and T. H. Myers, "Molecular Beam Epitaxy of $YMnO_3$ on *c*-Plane GaN," *Appl. Phys. Lett*., **88** [13] 132903 (2006).
[234]J. C. Jiang, X. Q. Pan, W. Tian, C. D. Theis, and D. G. Schlom, "Abrupt $PbTiO_3/SrTiO_3$ Superlattices Grown by Reactive Molecular Beam Epitaxy," *Appl. Phys. Lett*., **74** [19] 2851–3 (1999).
[235]W. Tian, J. C. Jiang, X. Q. Pan, J. H. Haeni, Y. L. Li, L. Q. Chen, D. G. Schlom, J. B. Neaton, K. M. Rabe, and Q. X. Jia, "Structural Evidence for Enhanced Polarization in a Commensurate Short-Period $BaTiO_3/SrTiO_3$ Superlattice," *Appl. Phys. Lett*., **89** [9] 092905 (2006).
[236]A. Soukiassian, W. Tian, D. A. Tenne, X. X. Xi, D. G. Schlom, N. D. Lanzillotti-Kimura, A. Bruchhausen, A. Fainstein, H. P. Sun, X. Q. Pan, A. Cros, and A. Cantarero, "Acoustic Bragg Mirrors and Cavities Made Using Piezoelectric Oxides," *Appl. Phys. Lett*., **90** [4] 042909 (2007).
[237]A. Soukiassian, W. Tian, V. Vaithyanathan, J. H. Haeni, L. Q. Chen, X. X. Xi, D. G. Schlom, D. A. Tenne, H. P. Sun, X. Q. Pan, K. J. Choi, C. B. Eom, Y. L. Li, Q. X. Jia, C. Constantin, R. M. Feenstra, M. Bernhagen, P. Reiche, and R. Uecker, "Growth of Nanoscale $BaTiO_3/SrTiO_3$ Superlattices by Molecular-Beam Epitaxy," *J. Mater. Res*., **23** [5] 1417–32 (2008).
[238]R. H. Lamoreaux and D. L. Hildenbrand, "High Temperature Vaporization Behavior of Oxides I. Alkali Metal Binary Oxides," *J. Phys. Chem. Ref. Data*, **13** [1] 151–73 (1984).
[239]R. H. Lamoreaux and D. L. Hildenbrand, "High-Temperature Vaporization Behavior of Oxides II. Oxides of Be, Mg, Ca, Sr, Ba, B, Al, Ga, In, Tl, Si, Ge, Sn, Pb, Zn, Cd, and Hg," *J. Phys. Chem. Ref. Data*, **16** [3] 419–43 (1987).
[240]M. E. Klausmeier-Brown, J. N. Eckstein, I. Bozovic, and G. F. Virshup, "Accurate Measurement of Atomic Beam Flux by Pseudo-Double-Beam Atomic Absorption Spectroscopy for Growth of Thin-Film Oxide Superconductors," *Appl. Phys. Lett*., **60** [5] 657–9 (1992).
[241]B. J. Gibbons, M. E. Hawley, S. Trolier-McKinstry, and D. G. Schlom, "Real-Time Spectroscopic Ellipsometry as a Characterization Tool for Oxide Molecular Beam Epitaxy," *J. Vac. Sci. Technol. A*, **19** [2] 584–90 (2001).
[242]BandiT, k-Space Associates, Ann Arbor, MI.
[243]E. S. Hellman and J. S. Harris, "Infrared Transmission Spectroscopy of GaAs during Molecular Beam Epitaxy," *J. Cryst. Growth*, **81** [1–4] 38–42 (1987).
[244]MOSS, k-Space Associates, Ann Arbor, MI.
[245]C. Taylor, D. Barlett, E. Chason, and J. Floro, "Technology," *Ind. Phys*., **4** [1] 25 (1998).
[246]I. Bozovic and V. Matijasevic, "COMBE: A Powerful New Tool for Materials Science," *Mater. Sci. Forum*, **352**, 1–8 (2000).
[247]S. Y. Wu, W. J. Takei, M. H. Francombe, and S. E. Cummins, "Domain Structure and Polarization Reversal in Films of Ferroelectric Bismuth Titanate," *Ferroelectrics*, **3** [234] 217–24 (1972).
[248]W. J. Takei, S. Y. Wu, and M. H. Francombe, "Optimization of Epitaxial Quality in Sputtered Films of Ferroelectric Bismuth Titanate," *J. Cryst. Growth*, **28** [2] 188–98 (1975).
[249]J. Fujita, T. Yoshitake, A. Kamijo, T. Satoh, and H. Igarashi, "Preferentially Oriented Epitaxial Y–Ba–Cu–O Films Prepared by the Ion Beam Sputtering Method," *J. Appl. Phys*., **64** [3] 1292–5 (1988).
[250]C. B. Eom, A. F. Marshall, S. S. Laderman, R. D. Jacowitz, and T. H. Geballe, "Epitaxial and Smooth Films of *a*-Axis $YBa_2Cu_3O_7$," *Science*, **249** [4976] 1549–52 (1990).
[251]G. Asayama, J. Lettieri, M. A. Zurbuchen, Y. Jia, S. Trolier-McKinstry, D. G. Schlom, S. K. Streiffer, J-P. Maria, S. D. Bu, and C. B. Eom, "Growth of (103) Fiber-Textured $SrBi_2Nb_2O_9$ Films on Pt-Coated Silicon," *Appl. Phys. Lett*., **80** [13] 2371–3 (2002).
[252]R. Ramesh and D. G. Schlom, "Orienting Ferroelectric Films," *Science*, **296** [5575] 1975–6 (2002).
[253]H. N. Lee, D. Hesse, N. Zakharov, and U. Gosele, "Ferroelectric $Bi_{3.25}La_{0.75}Ti_3O_{12}$ Films of Uniform *a*-Axis Orientation on Silicon Substrates," *Science*, **296** [5575] 2006–9 (2002).
[254]Y. Iijima, N. Tanabe, O. Kohno, and Y. Ikeno, "Inplane Aligned $YBa_2Cu_3O_{7-x}$ Thin-Films Deposited on Polycrystalline Metallic Substrates," *Appl. Phys. Lett*., **60** [6] 769–71 (1992).
[255]C. P. Wang, K. B. Do, M. R. Beasley, T. H. Geballe, and R. H. Hammond, "Deposition of In-Plane Textured MgO on Amorphous Si_3N_4 Substrates by Ion-Beam-Assisted Deposition and Comparisons with Ion-Beam-Assisted Deposited Yttria-Stabilized-Zirconia," *Appl. Phys. Lett*., **71** [20] 2955–7 (1997).
[256]A. Goyal, D. P. Norton, J. D. Budai, M. Paranthaman, E. D. Specht, D. M. Kroeger, D. K. Christen, Q. He, B. Saffian, F. A. List, D. F. Lee, P. M. Martin, C. E. Klabunde, E. Hartfield, and V. K. Sikka, "High Critical Current Density Superconducting Tapes by Epitaxial Deposition of $YBa_2Cu_3O_x$ Thick Films on Biaxially Textured Metals," *Appl. Phys. Lett*., **69** [12] 1795–7 (1996).
[257]D. P. Norton, A. Goyal, J. D. Budai, D. K. Christen, D. M. Kroeger, E. D. Specht, Q. He, B. Saffian, M. Paranthaman, C. E. Klabunde, D. F. Lee, B. C. Sales, and F. A. List, "Epitaxial $YBa_2Cu_3O_7$ on Biaxially Textured Nickel (001): An Approach to Superconducting Tapes with High Critical Current Density," *Science*, **274** [5288] 755–7 (1996).
[258]A. P. Malozemoff, J. Mannhart, and D. Scalapino, "High-Temperature Cuprate Superconductors get to Work," *Phys. Today*, **58** [4] 41–6 (2005).
[259]J. Rodriguez, K. Remack, K. Boku, K. R. Udayakumar, S. Aggarwal, S. Summerfelt, T. Moise, H. McAdams, J. McPherson, R. Bailey, M. Depner, and G. Fox, "Reliability Properties of Low Voltage PZT Ferroelectric Capacitors and Arrays"; pp. 200–8 in *2004 IEEE International Reliability Physics Symposium*, Proceedings 42nd Annual IEEE, Piscataway, NJ, 2004.
[260]R. L. Sandstrom, E. A. Giess, W. J. Gallagher, A. Segmüller, E. I. Cooper, M. F. Chisholm, A. Gupta, S. Shinde, and R. B. Laibowitz, "Lanthanum Gallate Substrates for Epitaxial High-Temperature Superconducting Thin Films," *Appl. Phys. Lett*., **53** [19] 1874–6 (1988).
[261]R. W. Simon, C. E. Platt, A. E. Lee, G. S. Lee, K. P. Daly, M. S. Wire, J. A. Luine, and M. Urbanik, "Low-Loss Substrate for Epitaxial Growth of High-Temperature Superconductor Thin Films," *Appl. Phys. Lett*., **53** [26] 2677–9 (1988).
[262]G. Koren, A. Gupta, E. A. Giess, A. Segmüller, and R. B. Laibowitz, "Epitaxial Films of $YBa_2Cu_3O_{7-\delta}$ on $NdGaO_3$, $LaGaO_3$, and $SrTiO_3$ Substrates Deposited by Laser Ablation," *Appl. Phys. Lett*., **54** [11] 1054–6 (1989).
[263]R. Feenstra, L. A. Boatner, J. D. Budai, D. K. Christen, M. D. Galloway, and D. B. Poker, "Epitaxial Superconducting Thin Films of $YBa_2Cu_3O_{7-x}$ on $KTaO_3$ Single Crystals," *Appl. Phys. Lett*., **54** [11] 1063–5 (1989).
[264]E. A. Giess, R. L. Sandstrom, W. J. Gallagher, A. Gupta, S. L. Shinde, R. F. Cook, E. I. Cooper, E. J. M. O'Sullivan, J. M. Roldan, A. P. Segmüller, and J. Angilello, "Lanthanide Gallate Perovskite-Type Substrates for Epitaxial, High-T_c Superconducting $Ba_2YCu_3O_{7-\delta}$ Films," *IBM J. Res. Dev*., **34** [6] 916–26 (1990).
[265]H. Asano, S. Kubo, O. Michikami, M. Satoh, and T. Konaka, "Epitaxial Growth of $EuBa_2Cu_3O_{7-y}$ Films on $YAlO_3$ Single Crystals," *Jpn. J. Appl. Phys., Part 2*, **29** [8] L1452–4 (1990).
[266]G. W. Berkstresser, A. J. Valentino, and C. D. Brandle, "Growth of Single Crystals of Rare Earth Gallates," *J. Cryst. Growth*, **109** [1–4] 457–66 (1991).
[267]G. W. Berkstresser, A. J. Valentino, and C. D. Brandle, "Growth of Single Crystals of Lanthanum Aluminate," *J. Cryst. Growth*, **109** [1–4] 467–71 (1991).
[268]R. W. Ralston, M. A. Kastner, W. J. Gallagher, and B. Batlogg, "Cooperating on Superconductivity," *IEEE Spectrum*, **29** [8] 50–5 (1992).
[269]G. W. Berkstresser, A. J. Valentino, and C. D. Brandle, "Congruent Composition for Growth of Lanthanum Aluminate," *J. Cryst. Growth*, **128** [1–4] 684–8 (1993).
[270]R. Brown, V. Pendrick, D. Kalokitis, and B. H. T. Chai, "Low-Loss Substrate for Microwave Application of High-Temperature Superconductor Films," *Appl. Phys. Lett*., **57** [13] 1351–3 (1990).
[271]S. Hontsu, J. Ishii, T. Kawai, and S. Kawai, "$LaSrGaO_4$ Substrate Gives Oriented Crystalline $YBa_2Cu_3O_{7-y}$ Films," *Appl. Phys. Lett*., **59** [22] 2886–8 (1991).
[272]D. Mateika, H. Kohler, H. Laudan, and E. Volkel, "Mixed-Perovskite Substrates for High-T_c Superconductors," *J. Cryst. Growth*, **109** [1–4] 447–56 (1991).
[273]J. M. Phillips, "Substrate Selection for High-Temperature Superconducting Thin Films," *J. Appl. Phys*., **79** [4] 1829–48 (1996).
[274]B. C. Chakoumakos, D. G. Schlom, M. Urbanik, and J. Luine, "Thermal Expansion of $LaAlO_3$ and $(La,Sr)(Al,Ta)O_3$, Substrate Materials for Superconducting Thin-Film Device Applications," *J. Appl. Phys*., **83** [4] 1979–82 (1998).
[275]L. Merker, "Method of Prepration of Monocrystalline Strontium Titanate Composition of High Refractive Index"; US Patent No. 2,684,910, July 27, 1954.
[276]J. G. Bednorz and H. J. Scheel, "Flame-Fusion Growth of $SrTiO_3$," *J. Cryst. Growth*, **41** [1] 5–12 (1977).
[277]P. I. Nabokin, D. Souptel, and A. M. Balbashov, "Floating Zone Growth of High-Quality $SrTiO_3$ Single Crystals," *J. Cryst. Growth*, **250** [3–4] 397–404 (2003).
[278]H. J. Scheel, J. G. Bednorz, and P. Dill, "Crystal Growth of Strontium Titanate $SrTiO_3$," *Ferroelectrics*, **13** [1–4] 507–9 (1976).
[279]N. A. Spaldin and M. Fiebig, "The Renaissance of Manetoelectric Multiferroics," *Science*, **309** [5733] 391–2 (2005).
[280]J. Schubert, O. Trithaveesak, A. Petraru, C. L. Jia, R. Uecker, P. Reiche, and D. G. Schlom, "Structural and Optical Properties of Epitaxial $BaTiO_3$ Thin Films Grown on $GdScO_3(110)$," *Appl. Phys. Lett*., **82** [20] 3460–2 (2003).
[281]M. D. Biegalski, J. H. Haeni, S. Trolier-McKinstry, D. G. Schlom, C. D. Brandle, and A. J. Ven Graitis, "Thermal Expansion of the New Perovskite Substrates $DyScO_3$ and $GdScO_3$," *J. Mater. Res*., **20** [4] 952–8 (2005).
[282]R. Uecker, H. Wilke, D. G. Schlom, B. Velickov, P. Reiche, A. Polity, M. Bernhagen, and M. Rossberg, "Spiral Formation during Czochralski Growth of Rare-Earth Scandates," *J. Cryst. Growth*, **295** [1] 84–91 (2006).

[283]B. Veličkov, V. Kahlenberg, R. Bertram, and M. Bernhagen, "Crystal Chemistry of $GdScO_3$, $DyScO_3$, $SmScO_3$, and $NdScO_3$," *Z. Kristallogr.*, **222** [9] 466–73 (2007).

[284]R. Uecker, B. Velickov, D. Klimm, R. Bertram, M. Bernhagen, M. Rabe, M. Albrecht, R. Fornari, and D. G. Schlom, "Properties of Rare-Earth Scandate Single Crystals (Re = Nd–Dy)," *J. Cryst. Growth*, **310** [10] 2649–58 (2008).

[285]M. Kawasaki, K. Takahashi, T. Maeda, R. Tsuchiya, M. Shinohara, O. Ishiyama, T. Yonezawa, M. Yoshimoto, and H. Koinuma, "Atomic Control of the $SrTiO_3$ Crystal Surface," *Science*, **266** [5190] 1540–2 (1994).

[286]G. Koster, B. L. Kropman, G. J. H. M. Rijnders, D. H. A. Blank, and H. Rogalla, "Quasi-Ideal Strontium Titanate Crystal Surfaces Through Formation of Strontium Hydroxide," *Appl. Phys. Lett.*, **73** [20] 2920–2 (1998).

[287]A. G. Schrott, J. A. Misewich, M. Copel, D. W. Abraham, and Y. Zhang, "*A*-Site Surface Termination in Strontium Titanate Single Crystals," *Appl. Phys. Lett.*, **79** [12] 1786–8 (2001).

[288]. D. H. A. Blank (private communication).

[289]T. Ohnishi, K. Takahashi, M. Nakamura, M. Kawasaki, M. Yoshimoto, and H. Koinuma, "*A*-Site Layer Terminated Perovskite Substrate: $NdGaO_3$," *Appl. Phys. Lett.*, **74** [17] 2531–3 (1999).

[290]H-J. Bae, J. Sigman, D. P. Norton, and L. A. Boatner, "Surface Treatment for Forming Unit-Cell Steps on the (001) $KTaO_3$ Substrate Surface," *Appl. Surf. Sci.*, **241** [3–4] 271–8 (2005).

[291]D. G. Schlom, L. Q. Chen, C. B. Eom, K. M. Rabe, S. K. Streiffer, and J.-M. Triscone, "Strain Tuning of Ferroelectric Thin Films," *Annu. Rev. Mater. Res.*, **37**, 589–626 (2007).

[292]S. B. Qadri, J. S. Horwitz, D. B. Chrisey, R. C. Y. Auyeung, and K. S. Grabowski, "X-Ray Characterization of Extremely High Quality (Sr,Ba)TiO_3 Films Grown by Pulsed Laser Deposition," *Appl. Phys. Lett.*, **66** [13] 1605–7 (1995).

[293]J. F. Ihlefeld and D. G. Schlom (unpublished).

[294]J. H. Lee and D. G. Schlom (unpublished).

[295]C. Adamo, M. Warusawithana, D. G. Schlom, X. Ke, P. Schiffer, and L. Maritato (unpublished).

[296]T. Yamaguti, "Oxidation of a Crystal Surface Studied by Means of Cathode Ray Reflection," *Proc. Phys. Math. Soc. Jpn.*, **17** [11] 443–53 (1935).

[297]R. Sato, "Surface Oxidation of Zincblende Cleavage Face in the Roasting Atmosphere," *J. Phys. Soc. Jpn.*, **6**, 527–8 (1951).

[298]S. Matsubara, N. Shohata, and M. Mikami, "Epitaxial Growth of $PbTiO_3$ on $MgAl_2O_4$/Si Substrates," *Jpn. J. Appl. Phys.*, **24** [Suppl. 24-3] 10–2 (1985).

[299]S. Miura, T. Yoshitake, S. Matsubara, Y. Miyasaka, N. Shohata, and T. Satoh, "Epitaxial Y–Ba–Cu–O Films on Si with Intermediate Layer by RF Magnetron Sputtering," *Appl. Phys. Lett.*, **53** [20] 1967–9 (1988).

[300]H. Myoren, Y. Nishiyama, H. Fukumoto, H. Nasu, and Y. Osaka, "As-Grown Preparation of Superconducting Epitaxial $Ba_2YCu_3O_x$ Thin Films Sputtered on Epitaxially Grown ZrO_2/Si(100)," *Jpn. J. Appl. Phys., Part 1*, **28** [3] 351–5 (1989).

[301]D. K. Fork, F. A. Ponce, J. C. Tramontana, and T. H. Geballe, "Epitaxial MgO on Si(001) for Y–Ba–Cu–O Thin-Film Growth by Pulsed Laser Deposition," *Appl. Phys. Lett.*, **58** [20] 2294–6 (1991).

[302]H. Mori and H. Ishiwara, "Epitaxial Growth of $SrTiO_3$ Films on Si(100) Substrates Using a Focused Electron Beam Evaporation Method," *Jpn. J. Appl. Phys., Part 2*, **30** [8A] L1415–7 (1991).

[303]A. N. Tiwari, S. Blunier, H. Zogg, P. Lerch, F. Marcenat, and P. Martinoli, "Epitaxial Growth of Superconducting $YBa_2Cu_3O_{7-x}$ on Si(100) with CaF_2 as Intermediate Buffer," *J. Appl. Phys.*, **71** [10] 5095–8 (1992).

[304]D. K. Fork, "Epitaxial Oxides on Semiconductors"; pp. 393–415 in *Pulsed Laser Deposition of Thin Films*, Edited by D. B. Chrisey, and G. K. Hubler. Wiley, New York, 1994.

[305]M.-B. Lee, M. Kawasaki, M. Yoshimoto, and H. Koinuma, "Heteroepitaxial Growth of $BaTiO_3$ Films on Si by Pulsed Laser Deposition," *Appl. Phys. Lett.*, **66** [11] 1331–3 (1995).

[306]J. Lettieri, J. H. Haeni, and D. G. Schlom, "Critical Issues in the Heteroepitaxial Growth of Alkaline-Earth Oxides on Silicon," *J. Vac. Sci. Technol. A*, **20** [4] 1332–40 (2002).

[307]E. G. Jacobs, Y. G. Rho, R. F. Pinizzotto, S. R. Summerfelt, and B. E. Gnade, "Effect of a Ge Barrier on the Microstructure of $BaTiO_3$ Deposited on Silicon by Pulsed Laser Ablation"; pp. 379–84 in *Laser Ablation in Materials Processing: Fundamentals and Applications*, **Vol. 285**, Edited by B. Braren, J. J. Dubowski, and D. Norton. Materials Research Society, Pittsburgh, 1993.

[308]D. P. Norton, J. D. Budai, and M. F. Chisholm, "Hydrogen-Assisted Pulsed-Laser Deposition of (001) CeO_2 on (001) Ge," *Appl. Phys. Lett.*, **76** [13] 1677–9 (2000).

[309]K. Nashimoto, D. K. Fork, and T. H. Geballe, "Epitaxial Growth of MgO on GaAs(001) for Growing Epitaxial $BaTiO_3$ Thin Films by Pulsed Laser Deposition," *Appl. Phys. Lett.*, **60** [10] 1199–201 (1992).

[310]Y. Liang, J. Kulik, T. C. Eschrich, R. Droopad, Z. Yu, and P. Maniar, "Hetero-Epitaxy of Perovskite Oxides on GaAs(001) by Molecular Beam Epitaxy," *Appl. Phys. Lett.*, **85** [7] 1217–9 (2004).

[311]E. Vasco, L. Vazquez, M. Aguilo, and C. Zaldo, "Epitaxial Growth of Y-Stabilised Zirconia Films on (100) InP Substrates by Pulsed Laser Deposition," *J. Cryst. Growth*, **209** [4] 883–9 (2000).

[312]D. P. Norton, S. J. Pearton, H. M. Christen, and J. D. Budai, "Hydrogen-Assisted Pulsed-Laser Deposition of Epitaxial CeO_2 Films on (001) InP," *Appl. Phys. Lett.*, **80** [1] 106–8 (2002).

[313]C.-R. Cho, J.-Y. Hwang, J.-P. Kim, S.-Y. Jeong, S.-G. Yoon, and W.-J. Lee, "Growth and Characterization of $(Ba_{0.5}Sr_{0.5})TiO_3$ Films Epitaxially Grown on (002) GaN/(0006) Al_2O_3 Electrode," *Jpn. J. Appl. Phys., Part 2*, **43** [11A] L1425–8 (2004).

[314]H. S. Craft, J. F. Ihlefeld, M. D. Losego, R. Collazo, Z. Sitar, and J-P. Maria, "MgO Epitaxy on GaN (0002) Surfaces by Molecular Beam Epitaxy," *Appl. Phys. Lett.*, **88** [21] 212906 (2006).

[315]W. Tian, V. Vaithyanathan, D. G. Schlom, Q. Zhan, S. Y. Yang, Y. H. Chu, and R. Ramesh, "Epitaxial Integration of (0001) $BiFeO_3$ with (0001) GaN," *Appl. Phys. Lett.*, **90** [17] 172908 (2007).

[316]D. K. Fork, D. B. Fenner, R. W. Barton, J. M. Phillips, G. A. N. Connell, J. B. Boyce, and T. H. Geballe, "High Critical Currents in Strained Epitaxial $YBa_2Cu_3O_{7-\delta}$ on Si," *Appl. Phys. Lett.*, **57** [11] 1161–3 (1990).

[317]H. Ishiwara, N. Tsuji, H. Mori, and H. Nohira, "Preparation of $YbBa_2Cu_3O_{7x}$ Films on Si(100) Substrates Using $SrTiO_3$ Buffer Layers," *Appl. Phys. Lett.*, **61** [12] 1459–61 (1992).

[318]R. Ramesh, H. Gilchrist, T. Sands, V. G. Keramidas, R. Haakenaasen, and D. K. Fork, "Ferroelectric La–Sr–Co–O/Pb–Zr–Ti–O/La–Sr–Co–O Heterostructures on Silicon via Template Growth," *Appl. Phys. Lett.*, **63** [26] 3592–4 (1993).

[319]K. Nashimoto, D. K. Fork, F. A. Ponce, and J. C. Tramontana, "Epitaxial $BaTiO_3$/MgO Structure Grown on GaAs(100) by Pulsed Laser Deposition," *Jpn. J. Appl. Phys., Part 1*, **32** [9B] 4099–102 (1993).

[320]V. Srikant, E. J. Tarsa, D. R. Clarke, and J. S. Speck, "Crystallographic Orientation of Epitaxial $BaTiO_3$ Films: The Role of Thermal-Expansion Mismatch with the Substrate," *J. Appl. Phys.*, **77** [4] 1517–22 (1995).

[321]T. Maruyama, M. Saitoh, I. Sakai, T. Hidaka, Y. Yano, and T. Noguchi, "Growth and Characterization of 10-nm-Thick *c*-Axis Oriented Epitaxial $PbZr_{0.25}Ti_{0.75}O_3$ Thin Films on (100)Si Substrate," *Appl. Phys. Lett.*, **73** [24] 3524–6 (1998).

[322]A. Lin, X. Hong, V. Wood, A. Verevkin, C. H. Ahn, R. A. McKee, F. J. Walker, and E. D. Specht, "Epitaxial Growth of $Pb(Zr_{0.2}Ti_{0.8})O_3$ on Si and its Nanoscale Piezoelectric Properties," *Appl. Phys. Lett.*, **78** [14] 2034–6 (2001).

[323]B. T. Liu, K. Maki, Y. So, V. Nagarajan, R. Ramesh, J. Lettieri, J. H. Haeni, D. G. Schlom, W. Tian, X. Q. Pan, F. J. Walker, and R. A. McKee, "Epitaxial La-doped $SrTiO_3$ on Silicon: A Conductive Template for Epitaxial Ferroelectrics on Silicon," *Appl. Phys. Lett.*, **80** [25] 4801–3 (2002).

[324]Y. Liang, J. Kulik, Y. Wei, T. Eschrich, J. Curless, B. Craigo, and S. Smith, "Hetero-Epitaxy of Crystalline Perovskite Oxides on GaAs(001)"; pp. 379–84 in *Fundamentals of Novel Oxide/Semiconductor Interfaces*, Vol. 786, Edited by C. R. Abernathy, E. P. Gusev, D. Schlom, and S. Stemmer. Materials Research Society, Warrendale, 2004.

[325]S. Y. Yang, F. Zavaliche, L. Mohaddes-Ardabili, V. Vaithyanathan, D. G. Schlom, Y. J. Lee, Y. H. Chu, M. P. Cruz, Q. Zhan, T. Zhao, and R. Ramesh, "Metalorganic Chemical Vapor Deposition of Lead-Free Ferroelectric $BiFeO_3$ Films for Memory Applications," *Appl. Phys. Lett.*, **87** [10] 102903 (2005).

[326]A. Posadas, J.-B. Yau, C. H. Ahn, J. Han, S. Gariglio, K. Johnston, K. M. Rabe, and J. B. Neaton, "Epitaxial Growth of Multiferroic $YMnO_3$ on GaN," *Appl. Phys. Lett.*, **87** [17] 171915 (2005).

[327]J. K. G. Panitz and C. C. Hu, "Radio-Frequency-Sputtered Tetragonal Barium Titanate Films on Silicon," *J. Vac. Sci. Technol.*, **16** [2] 315–8 (1979).

[328]V. S. Dharmadhikari and W. W. Grannemann, "AES Study on the Chemical Composition of Ferroelectric $BaTiO_3$ Thin Films RF Sputter-Deposited on Silicon," *J. Vac. Sci. Technol. A*, **1** [2] 483–5 (1983).

[329]S. Matsubara, T. Sakuma, S. Yamamichi, H. Yamaguchi, and Y. Miyasaka, "Interface Structure and Dielectric Properties of $SrTiO_3$ Thin Film Sputter-Deposited onto Si Substrates"; pp. 243–53 in *Ferroelectric Thin Films, Materials Research Society Proceedings*, **Vol. 200**, Edited by E. R. Myers, and A. I. Kingon. Materials Research Society, Pittsburgh, PA, 1990.

[330]T. Sakuma, S. Yamamichi, S. Matsubara, H. Yamaguchi, and Y. Miyasaka, "Barrier Layers for Realization of High Capacitance Density in $SrTiO_3$ Thin-Film Capacitor on Silicon," *Appl. Phys. Lett.*, **57** [23] 2431–3 (1990).

[331]H. Yamaguchi, S. Matsubara, and Y. Miyasaka, "Reactive Coevaporation Synthesis and Characterization of $SrTiO_3$ Thin Films," *Jpn. J. Appl. Phys.*, **30** [9B] 2197–9 (1991).

[332]H. Nagata, T. Tsukahara, S. Gonda, M. Yoshimoto, and H. Koinuma, "Heteroepitaxial Growth of CeO_2(001) Films on Si(001) Substrates by Pulsed Laser Deposition in Ultrahigh Vacuum," *Jpn. J. Appl. Phys.*, **30** [6B] L1136–8 (1991).

[333]Y. Shichi, S. Tanimoto, T. Goto, K. Kuroiwa, and Y. Tarui, "Interaction of $PbTiO_3$ Films with Si Substrate," *Jpn. J. Appl. Phys.*, **33** [9B] 5172–7 (1994).

[334]D. H. Looney, "Semiconducting Translating Device"; US Patent No. 2,791,758, May 7, 1957.

[335]W. L. Brown, "Semiconductive Device"; US Patent No. 2,791,759, May 7, 1957.

[336]I. M. Ross, "Semiconducting Translating Device"; US Patent No. 2,791,760, May 7, 1957.

[337]J. A. Morton, "Electrical Switching and Storage"; US Patent No. 2,791,761, May 7, 1957.

[338]J. L. Moll and Y. Tarui, "A New Solid State Memory Resistor," *IEEE Trans. Electron Devices*, **10** [5] 338–9 (1963).

[339]P. M. Heyman and G. H. Heilmeier, "A Ferroelectric Field Effect Device," *Proc. IEEE*, **54** [6] 842–8 (1966).

[340]G. G. Teather and L. Young, "Non-Destructive Readout of Ferroelectrics by Field Effect Conductivity Modulation," *Solid State Electron.*, **11** [5] 527–33 (1968).

[341]S.-Y. Wu, "A New Ferroelectric Memory Device, Metal-Ferroelectric-Semiconductor Transistor," *IEEE Trans. Electron Devices*, **21** [8] 499–504 (1974).

[342]M. Suzuki, "Review on Future Ferroelectric Nonvolatile Memory: Fe-RAM—From the Point of View of Epitaxial Oxide Thin Films," *J. Ceram. Soc. Jpn.*, **103** [11] 1099–111 (1995).

[343]M. Suzuki, "Review on Future Ferroelectric Nonvolatile Memory: FeRAM - From the Point of View of Epitaxial Oxide Thin Films," *J. Ceram. Soc. Jpn. Int. Ed.*, **103** [11] 1088–99 (1995).

[344]K. J. Hubbard and D. G. Schlom, "Thermodynamic Stability of Binary Oxides in Contact with Silicon," *J. Mater. Res.*, **11** [11] 2757–76 (1996).

[345]D. G. Schlom, C. A. Billman, J. H. Haeni, J. Lettieri, P. H. Tan, R. R. M. Held, S. Völk, and K. J. Hubbard, "High-*K* Candidates for Use as the Gate Dielectric in Silicon MOSFETs"; pp. 31–78 in *Thin Films and Heterostructures for Oxide Electronics*, Edited by S. B. Ogale. Springer, New York, 2005.

[346]I. Barin, *Thermochemical Data of Pure Substances*, Vols. I and II, 3rd edition, VCH, Weinheim, 1995.
[347]E. J. Tarsa, K. L. McCormick, and J. S. Speck, "Common Themes in the Epitaxial Growth of Oxides on Semiconductors"; pp. 73–85 in *Epitaxial Oxide Thin Films and Heterostructures, Materials Research Society Proceedings*, Vol. 341, Edited by D. K. Fork, J. M. Phillips, R. Ramesh, and R. M. Wolf. Materials Research Society, Pittsburgh, PA, 1994.
[348]J. M. Phillips, "Substrate Selection for Thin-Film Growth," *MRS Bull.*, **20** [4] 35–9 (1995).
[349]D. G. Schlom and J. H. Haeni, "A Thermodynamic Approach to Selecting Alternative Gate Dielectrics," *MRS Bull.*, **27** [3] 198–204 (2002).
[350]V. V. Il'chenko, G. V. Kuznetsov, V. I. Strikha, and A. I. Tsyganova, "The Formation of a Barium Silicate Layer on Silicon," *Mikroelektron*, **27** [5] 340–5 (1998).
[351]V. V. Il'chenko, G. V. Kuznetsov, V. I. Strikha, and A. I. Tsyganova, "The Formation of a Barium Silicate Layer on Silicon," *Russ. Microelectron.*, **27** [5] 291–6 (1998).
[352]V. V. Il'chenko and G. V. Kuznetsov, "Effect of Oxygen on the Chemical Reactions and Electron Work Function in Ba–Si and BaO–Si Structures," *Pis'ma Zh. Tekh. Fiz.*, **27** [8] 58–63 (2001).
[353]V. V. Il'chenko and G. V. Kuznetsov, "Effect of Oxygen on the Chemical Reactions and Electron Work Function in Ba–Si and BaO–Si Structures," *Sov. Tech. Phys. Lett.*, **27** [4] 333–5 (2001).
[354]Y. S. Touloukian, R. K. Kirby, R. E. Taylor, and T. Y. R. Lee, *Thermal Expansion: Nonmetallic Solids, Vol. 13 of Thermophysical Properties of Matter*, p. 154. Plenum, New York, 1977.
[355]D. K. Fork, F. A. Ponce, J. C. Tramontana, N. Newman, J. M. Phillips, and T. H. Geballe, "High Critical Current Densities in Epitaxial $YBa_2Cu_3O_{7-\delta}$ Thin films on Silicon-on-Sapphire," *Appl. Phys. Lett.*, **58** [21] 2432–4 (1991).
[356]E. S. Machlin and P. Chaudhari, "Theory of 'Pseudomorphic Stabilization' of Metastable Phases in Thin Film Form"; pp. 11–29 in *Synthesis and Properties of Metastable Phases*, Edited by E. S. Machlin, and T. J. Rowland. The Metallurgical Society of AIME, Warrendale, 1980.
[357]C. P. Flynn, "Strain-Assisted Epitaxial Growth of New Ordered Compounds," *Phys. Rev. Lett.*, **57** [5] 599–602 (1986).
[358]R. Bruinsma and A. Zangwill, "Structural Transitions in Epitaxial Overlayers," *J. Phys. (Paris)*, **47** [12] 2055–73 (1986).
[359]R. F. C. Farrow (ed), *Molecular Beam Epitaxy: Applications to Key Materials*. Noyes, Park Ridge, 1995.
[360]E. M. Levin, C. R. Robbins, and H. F. McMurdie (eds), *Phase Diagrams for Ceramists*, **Vol. 1**, p. 127. American Ceramic Society, Columbus, 1964.
[361]F. Sugawara and S. Iida, "New Magnetic Perovskites $BiMnO_3$ and $BiCrO_3$," *J. Phys. Soc. Jpn.*, **20** [8] 1529 (1965).
[362]H. Faqir, H. Chiba, M. Kikuchi, Y. Syono, M. Mansori, P. Satre, and A. Sebaoun, "High-Temperature XRD and DTA Studies of $BiMnO_3$ Perovskite," *J. Solid State Chem.*, **142** [1] 113–9 (1999).
[363]T. Atou, H. Chiba, K. Ohoyama, Y. Yamaguchi, and Y. Syono, "Structure Determination of Ferromagnetic Perovskite $BiMnO_3$," *J. Solid State Chem.*, **145** [2] 639–42 (1999).
[364]Y. Maeno, T. M. Rice, and M. Sigrist, "The Intriguing Superconductivity of Strontium Ruthenate," *Phys. Today*, **54** [1] 42–7 (2001).
[365]N. Shirakawa, K. Murata, S. Nishizaki, Y. Maeno, and T. Fujita, "Pressure Dependence of Superconducting Critical Temperature of Sr_2RuO_4," *Phys. Rev. B*, **56** [13] 7890–3 (1997).
[366]C. W. Chu, P. H. Hor, R. L. Meng, L. Gao, Z. J. Huang, and Y. Q. Wang, "Evidence for Superconductivity above 40 K in the La–Ba–Cu–O Compound System," *Phys. Rev. Lett.*, **58** [4] 405–7 (1987).
[367]J. A. Kafalas and J. M. Longo, "High Pressure Synthesis of $(ABX_3)(AX)_n$ Compounds," *J. Solid State Chem.*, **4** [1] 55–9 (1972).
[368]I. I. Prosychev and I. S. Shaplygin, "Interaction in the BaO–RuO_2 System," *Zh. Neorg. Khim.*, **25**, 876–7 (1980).
[369]I. I. Prosychev and I. S. Shaplygin, *Russ. J. Inorg. Chem.*, **25** [3] 489 (1980).
[370]M. I. Gadzhiev and I. S. Shaplygin, "Reactions in the BaO–RuO_2 System," *Zh. Neorg. Khim.*, **29**, 2154–5 (1984).
[371]M. I. Gadzhiev and I. S. Shaplygin, "Reactions in the BaO–RuO_2 System," *Russ. J. Inorg. Chem.*, **29** [8] 1230–1 (1984).
[372]T. L. Popova, N. G. Kisel, V. I. Krivobok, and V. P. Karlov, "Interaction in the BaO–RuO_2 System," *Ukr. Khim. Zh.*, **48** [5] 457–60 (1982).
[373]T. L. Popova, N. G. Kisel, V. I. Krivobok, and V. P. Karlov, "Interaction in the BaO–RuO_2 System," *Sov. Prog. Chem.*, **48**, 8–10 (1982).
[374]J. B. Clark, P. W. Richter, and L. Du Toit, "High-Pressure Synthesis of $YScO_3$, $HoScO_3$, $ErScO_3$, and $TmScO_3$, and a Reevaluation of the Lattice Constants of the Rare Earth Scandates," *J. Solid State Chem.*, **23** [1–2] 129–34 (1978).
[375]R. P. Liferovich and R. H. Mitchell, "A Structural Study of Ternary Lanthanide Orthoscandate Perovskites," *J. Solid State Chem.*, **177** [6] 2188–97 (2004).
[376]E. M. Levin, C. R. Robbins, and H. F. McMurdie (eds), *Phase Diagrams for Ceramists*, **Vol. 2**, p. 93. American Ceramic Society, Columbus, 1969.
[377]N. Orloff, I. Takeuchi, J. C. Booth, D. Gu, A. Lewandoski, J. Mateu, C. J. Fennie, K. M. Rabe, W. Tian, and D. G. Schlom, "Broadband and Temperature Dependent Permittivity Measurements of Ruddlesden–Popper $Sr_{n+1}Ti_nO_{3n+1}$ (n = 1,2,3) Thin Films"; (unpublished).
[378]C. J. Fennie and K. M. Rabe, "Structural and Dielectric Properties of Sr_2TiO_4 from First Principles," *Phys. Rev. B*, **68** [18] 184111 (2003).
[379]M. A. Zurbuchen, J. Schubert, Y. Jia, W. Tian, V. Cherman, M. D. Biegalski, D. Fong, M. E. Hawley, A. K. Tagantsev, S. K. Streiffer, and D. G. Schlom, "Charge-Mediated Synthesis of $Sr_4Bi_4Ti_7O_{24}$"; (unpublished).
[380]E. C. Subbarao, "A Family of Ferroelectric Bismuth Compounds," *J. Phys. Chem. Solids*, **23**, 665–76 (1962).
[381]R. A. Armstrong and R. E. Newnham, "Bismuth Titanate Solid Solutions," *Mater. Res. Bull.*, **7** [10] 1025–34 (1972).
[382]J.van Suchtelen, "Product Properties: A New Application of Composite Materials," *Philips Res. Rep.*, **27** [1] 28–37 (1972).
[383]J. van den Boomgaard, D. R. Terrell, R. A. J. Born, and H. F. J. I. Giller, "An *in Situ* Grown Eutectic Magnetoelectric Composite Material: Part 1 Composition and Unidirectional Solidification," *J. Mater. Sci.*, **9** [10] 1705–9 (1974).
[384]A. M. J. G. van Run, D. R. Terrell, and J. H. Scholing, "An *in Situ* Grown Eutectic Magnetoelectric Composite Material: Part 2 Physical Properties," *J. Mater. Sci.*, **9** [10] 1710–4 (1974).
[385]L. P. M. Bracke and R. G. van Vliet, "A Broadband Magneto-Electric Transducer using a Composite Material," *Int. J. Electron.*, **51** [3] 255–62 (1981).
[386]R. E. Newnham, D. P. Skinner, and L. E. Cross, "Connectivity and Piezoelectric–Pyroelectric Composites," *Mater. Res. Bull.*, **13** [5] 525–36 (1978).
[387]J. van den Boomgaard and R. A. J. Born, "A Sintered Magnetoelectric Composite Material $BaTiO_3$–$Ni(Co,Mn)Fe_2O_4$," *J. Mater. Sci.*, **13** [7] 1538–48 (1978).
[388]G. Srinivasan, E. T. Rasmussen, A. A. Bush, K. E. Kamentsev, V. F. Meshcheryakov, and Y. K. Fetisov, "Structural and Magnetoelectric Properties of MFe_2O_4-PZT (M = Ni, Co) and $La_x(Ca, Sr)_{1-x}MnO_3$–PZT Multilayer Composites," *Appl. Phys. A*, **78** [5] 721–8 (2004).
[389]K. Lefki and G. J. M. Dormans, "Measurement of Piezoelectric Coefficients of Ferroelectric Thin Films," *J. Appl. Phys.*, **76** [3] 1764–7 (1994).
[390]M. A. Zurbuchen, S. Saha, T. Wu, J. Mitchell, and S. K. Streiffer, "Multiferroic Composite Ferroelectric–Ferromagnetic Films," *Appl. Phys. Lett.*, **87** [23] 232908 (2005).
[391]H. Zheng, J. Wang, S. E. Lofland, Z. Ma, L. Mohaddes-Ardabili, T. Zhao, L. Salamanca-Riba, S. R. Shinde, S. B. Ogale, F. Bai, D. Viehland, Y. Jia, D. G. Schlom, M. Wuttig, A. Roytburd, and R. Ramesh, "Multiferroic $BaTiO_3$–$CoFe_2O_4$ Nanostructures," *Science*, **303** [5658] 661–3 (2004).
[392]E. Klokholm, J. W. Matthews, A. F. Mayadas, and J. Angilello; pp. 105–9 in *Magnetism and Magnetic Materials*, Edited by C. D. Graham Jr., and J. J. Rhyne. American Institute of Physics, New York, 1972.
[393]L. B. Freund and S. Suresh, *Thin Film Materials: Stress, Defect Formation and Surface Evolution*, pp. 60–83, 283–90 Cambridge University Press, Cambridge, 2003.
[394]J. S. Speck, A. C. Daykin, A. Seifert, A. E. Romanov, and W. Pompe, "Domain Configurations due to Multiple Misfit Relaxation Mechanisms in Epitaxial Ferroelectric Thin Films. III. Interfacial Defects and Domain Misorientations," *J. Appl. Phys.*, **78** [3] 1696 (1995).
[395]W. D. Nix and B. M. Clemens, "Crystallite Coalescence: A Mechanism for Intrinsic Tensile Stresses in Thin Films," *J. Mater. Res.*, **14** [8] 3467–73 (1999).
[396]T. R. Taylor, P. J. Hansen, B. Acikel, N. Pervez, R. A. York, S. K. Streiffer, and J. S. Speck, "Impact of Thermal Strain on the Dielectric Constant of Sputtered Barium Strontium Titanate Thin Films," *Appl. Phys. Lett.*, **80** [11] 1978–80 (2002).
[397]C. L. Canedy, H. Li, S. P. Alpay, L. Salamanca-Riba, A. L. Roytburd, and R. Ramesh, "Dielectric Properties in Heteroepitaxial $Ba_{0.6}Sr_{0.4}TiO_3$ Thin Films: Effect of Internal Stresses and Dislocation-Type Defects," *Appl. Phys. Lett.*, **77** [11] 1695–7 (2000).
[398]I. B. Misirlioglu, A. L. Vasiliev, M. Aindow, S. P. Alpay, and R. Ramesh, "Threading Dislocation Generation in Epitaxial $(Ba,Sr)TiO_3$ Films Grown on (001) $LaAlO_3$ by Pulsed Laser Deposition," *Appl. Phys. Lett.*, **84** [10] 1742–4 (2004).
[399]M.-W. Chu, I. Szafraniak, R. Scholz, C. Harnagea, D. Hesse, M. Alexe, and U. Gösele, "Impact of Misfit Dislocations on the Polarization Instability of Epitaxial Nanostructured Ferroelectric Perovskites," *Nat. Mater.*, **3** [2] 87–90 (2004).
[400]S. P. Alpay, I. B. Misirlioglu, V. Nagarajan, and R. Ramesh, "Can Interface Dislocations Degrade Ferroelectric Properties," *Appl. Phys. Lett.*, **85** [11] 2044–6 (2004).
[401]V. Nagarajan, C. L. Jia, H. Kohlstedt, R. Waser, I. B. Misirlioglu, S. P. Alpay, and R. Ramesh, "Misfit Dislocations in Nanoscale Ferroelectric Heterostructures," *Appl. Phys. Lett.*, **86** [19] 192910 (2005).
[402]N. A. Pertsev, A. G. Zembilgotov, and A. K. Tagantsev, "Effect of Mechanical Boundary Conditions on Phase Diagrams of Epitaxial Ferroelectric Thin Films," *Phys. Rev. Lett.*, **80** [9] 1988–91 (1998).
[403]N. A. Pertsev and V. G. Koukhar, "Polarization Instability in Polydomain Ferroelectric Epitaxial Thin Films and the Formation of Heterophase Structures," *Phys. Rev. Lett.*, **84** [16] 3722–5 (2000).
[404]V. G. Koukhar, N. A. Pertsev, and R. Waser, "Thermodynamic Theory of Epitaxial Ferroelectric Thin Films with Dense Domain Structures," *Phys. Rev. B*, **64** [21] 214103 (2001).
[405]Y. L. Li, S. Y. Hu, Z. K. Liu, and L. Q. Chen, "Phase-Field Model of Domain Structures in Ferroelectric Thin Films," *Appl. Phys. Lett.*, **78** [24] 3878–80 (2001).
[406]Y. L. Li, S. Y. Hu, Z. K. Liu, and L. Q. Chen, "Effect of Substrate Constraint on the Stability and Evolution of Ferroelectric Domain Structures in Thin Films," *Acta Mater.*, **50** [2] 395–411 (2002).
[407]O. Diéguez, S. Tinte, A. Antons, C. Bungaro, J. B. Neaton, K. M. Rabe, and D. Vanderbilt, "Ab Initio Study of the Phase Diagram of Epitaxial $BaTiO_3$," *Phys. Rev B*, **69** [21] 212101 (2004).
[408]Y. L. Li and L. Q. Chen, "Temperature–Strain Phase Diagram for $BaTiO_3$ Thin Films," *Appl. Phys. Lett.*, **88** [7] 072905 (2006).
[409]N. A. Pertsev, V. G. Kukhar, H. Kohlstedt, and R. Waser, "Phase Diagrams and Physical Properties of Single-Domain Epitaxial $Pb(Zr_{1-x}Ti_x)O_3$ Thin Films," *Phys. Rev. B*, **67** [5] 54107 (2003).
[410]Y. L. Li, S. Choudhury, Z. K. Liu, and L. Q. Chen, "Effect of External Mechanical Constraints on the Phase Diagram of Epitaxial $PbZr_{1-x}Ti_xO_3$ Thin

Films-Thermodynamic Calculations and Phase-Field Simulations," *Appl. Phys. Lett*., **83** [8] 1608–10 (2003).
[411]S. Choudhury, Y. L. Li, and L. Q. Chen, "A Phase Diagram for Epitaxial $PbZr_{1-x}Ti_xO_3$ Thin Films at the Bulk Morphotropic Boundary Composition," *J. Am. Ceram. Soc*., **88** [6] 1669–72 (2005).
[412]N. A. Pertsev, A. K. Tagantsev, and N. Setter, "Phase Transitions and Strain-Induced Ferroelectricity in $SrTiO_3$ Epitaxial Thin Films," *Phys. Rev. B*, **61** [2] R825–9 (2000).
[413]N. A. Pertsev, A. K. Tagantsev, and N. Setter, "Erratum: Phase Transitions and Strain-Induced Ferroelectricity in $SrTiO_3$ Epitaxial Thin Films [Phys. Rev. B **61**, R825 (2000)]," *Phys. Rev. B*, **65** [21] 219901 (2002).
[414]A. Antons, J. B. Neaton, K. M. Rabe, and D. Vanderbilt, "Tunability of the Dielectric Response of Epitaxially Strained $SrTiO_3$ from First Principles," *Phys. Rev. B*, **71** [2] 024102 (2005).
[415]Y. L. Li, S. Choudhury, J. H. Haeni, M. D. Biegalski, A. Vasudevarao, A. Sharan, H. Z. Ma, J. Levy, V. Gopalan, S. Trolier-McKinstry, D. G. Schlom, Q. X. Jia, and L. Q. Chen, "Phase Transitions and Domain Structures in Strained Pseudocubic (100) $SrTiO_3$ Thin Films," *Phys. Rev. B*, **73** [18] 184112 (2006).
[416]A. Vasudevarao, A. Kumar, L. Tian, J. H. Haeni, Y. L. Li, C.-J. Eklund, Q. X. Jia, R. Uecker, P. Reiche, K. M. Rabe, L. Q. Chen, D. G. Schlom, and V. Gopalan, "Mutiferroic Domain Dynamics in Strained Strontium Titanate," *Phys. Rev. Lett*., **97** [25] 257602 (2006).
[417]Y. L. Li, S. Choudhury, J. H. Haeni, M. D. Biegalski, A. Vasudevarao, A. Sharan, H. Z. Ma, J. Levy, V. Gopalan, S. Trolier-McKinstry, D. G. Schlom, Q. X. Jia, and L. Q. Chen, "Phase Transitions and Domain Structures in Strained Pseudocubic (100) $SrTiO_3$ Thin Films," *Phys. Rev. B*, **73** [18] 184112 (2006).
[418]P. Irvin, J. Levy, J. H. Haeni, and D. G. Schlom, "Localized Microwave Resonances in Strained $SrTiO_3$ Thin Films," *Appl. Phys. Lett*., **88** [4] 042902 (2006).
[419]S. Denev, A. Kumar, M. D. Biegalski, H. W. Jang, C. M. Folkman, A. Vasudevarao, Y. Han, I. M. Reaney, S. Trolier-McKinstry, C. B. Eom, D. G. Schlom, and V. Gopalan, "Magnetic Color Symmetry of Lattice Rotations in a Diamagnetic Material," *Phys. Rev. Lett*., **100** [25] 257601 (2008).
[420]H. Z. Ma, J. Levy, M. D. Biegalski, D. G. Schlom, and S. Trolier-McKinstry, "Room-Temperature Electrooptic Properties of Strained $SrTiO_3$ Films Grown on $DyScO_3$," *J. Appl. Phys*., submitted.
[421]A. Vasudevarao, S. Denev, M. D. Biegalski, Y. L. Li, L. Q. Chen, S. Trolier-McKinstry, D. G. Schlom, and V. Gopalan, "Polarization Rotation Transitions in Anisotropically Strained $SrTiO_3$ Thin Films," *Appl. Phys. Lett*., **92** [19] 192902 (2008).
[422]M. D. Biegalski, S. Trolier-McKinstry, D. G. Schlom, S. K. Streiffer, M. Bernhagen, P. Reiche, and R. Uecker, "Asymmetric Dielectric Properties of $SrTiO_3$ Thin Films on $DyScO_3$ Substrates," *J. Appl. Phys*., submitted.
[423]S. Kamba, D. Nuzhnyy, V. Goian, S. Veljko, C. M. Brooks, J. H. Lee, D. G. Schlom, J.-H. Lee, J. Schubert, E. John, T. Katsufuji, and J. Petzelt, "Ferroelectricity in $SrTiO_3$ and $EuTiO_3$ Strained Thin Films: Polar Phonon Properties"; Presented at Fundamental Physics of Ferroelectrics, Williamsburg, Virginia, 2008.
[424]S. K. Streiffer, J. A. Eastman, D. D. Fong, C. Thompson, A. Munkholm, M. V. R. Murty, O. Auciello, G. R. Bai, and G. B. Stephenson, "Observation of Nanoscale 180° Stripe Domains in Ferroelectric $PbTiO_3$ Thin Films," *Phys. Rev. Lett*., **89** [6] 067601 (2002).
[425]E. D. Specht, H.-M. Christen, D. P. Norton, and L. A. Boatner, "X-Ray Diffraction Measurement of the Effect of Layer Thickness on the Ferroelectric Transition in Epitaxial $KTaO_3/KNbO_3$ Multilayers," *Phys. Rev. Lett*., **80** [19] 4317–20 (1998).
[426]H.-M. Christen, L. A. Knauss, and K. S. Harshavardhan, "Field-Dependent Dielectric Permittivity of Paraelectric Superlattice Structures," *Mater. Sci. Eng. B*, **56** [2–3] 200–3 (1998).
[427]H. M. Christen, E. D. Specht, S. S. Silliman, and K. S. Harshavardhan, "Ferroelectric and Antiferroelectric Coupling in Superlattices of Paraelectric Perovskites at Room Temperature," *Phys. Rev. B*, **68** [2] 20101 (2003).
[428]K. Abe, N. Yanase, K. Sano, M. Izuha, N. Fukushima, and T. Kawakubo, "Modification of Ferroelectricity in Heteroepitaxial $(Ba,Sr)TiO_3$ Films for Non-Volatile Memory Applications," *Integr. Ferroelectr*., **21** [1–4] 197–206 (1998).
[429]N. Yanase, K. Abe, N. Fukushima, and T. Kawakubo, "Thickness Dependence of Ferroelectricity in Heteroepitaxial $BaTiO_3$ Thin Film Capacitors," *Jpn. J. Appl. Phys., Part 1*, **38** [9B] 5305–8 (1999).
[430]M. Sepliarsky, S. R. Phillpot, M. G. Stachiotti, and R. L. Migoni, "Ferroelectric Phase Transitions and Dynamical Behavior in $KNbO_3/KTaO_3$ Superlattices by Molecular-Dynamics Simulation," *J. Appl. Phys*., **91** [5] 3165–71 (2002).
[431]V. Gopalan and R. Raj, "Domain Structure–Second Harmonic Generation Correlation in Potassium Niobate Thin Films Deposited on a Strontium Titanate Substrate," *J. Am. Ceram. Soc*., **79** [12] 3289–96 (1996).
[432]V. Gopalan and R. Raj, "Electric Field Induced Domain Rearrangement in Potassium Niobate Thin Films Studied by *in Situ* Second Harmonic Generation Measurements," *J. Appl. Phys*., **81** [2] 865–75 (1997).
[433]Y. Barad, J. Lettieri, C. D. Theis, D. G. Schlom, V. Gopalan, J. C. Jiang, and X. Q. Pan, "Probing Domain Microstructure in Ferroelectric $Bi_4Ti_3O_{12}$ Thin Films by Optical Second Harmonic Generation," *J. Appl. Phys*., **89** [2] 1387–92 (2001).
[434]Y. Barad, J. Lettieri, C. D. Theis, D. G. Schlom, V. Gopalan, J. C. Jiang, and X. Q. Pan, "Erratum: 'Probing Domain Microstructure in Ferroelectric $Bi_4Ti_3O_{12}$ Thin Films by Optical Second Harmonic Generation,' [J. Appl. Phys. **89**, 1387 (2001)]," *J. Appl. Phys*., **89** [9] 5230 (2001).
[435]M. Fiebig, D. Fröhlich, T. Lottermoser, and M. Maat, "Probing of Ferroelectric Surface and Bulk Domains in $RMnO_3$ (R = Y, Ho) by Second Harmonic Generation," *Phys. Rev. B*, **66** [14] 144102 (2002).
[436]K. A. Müller and H. Burkard, "$SrTiO_3$: An Intrinsic Quantum Paraelectric below 4K," *Phys. Rev. B*, **19** [7] 3593–602 (1979).
[437]R. C. Neville, B. Hoeneisen, and C. A. Mead, "Permittivity of Strontium Titanate," *J. Appl. Phys*., **43** [5] 2124–31 (1972).
[438]P. W. Forsbergh Jr., "Effect of a Two-Dimensional Pressure on the Curie Point of Barium Titanate," *Phys. Rev*., **93** [4] 686–92 (1954).
[439]C. J. Fennie and K. M. Rabe, "Magnetic and Electric Phase Control in Epitaxial $EuTiO_3$ from First Principles," *Phys. Rev. Lett*., **97** [26] 267602 (2006).
[440]T. Ando, A. B. Fowler, and F. Stern, "Electronic Properties of Two-Dimensional Systems," *Rev. Mod. Phys*., **54** [2] 437–672 (1982).
[441]A. Tsukazaki, A. Ohtomo, T. Kita, Y. Ohno, H. Ohno, and M. Kawasaki, "Quantum Hall Effect in Polar Oxide Heterostructures," *Science*, **315** [5817] 1388–91 (2007).
[442]H. P. R. Frederikse, W. R. Thurber, and W. R. Hosler, "Electronic Transport in Strontium Titanate," *Phys. Rev*., **134** [2A] A442–5 (1964).
[443]H. P. R. Frederikse and G. A. Candela, "Magnetic Susceptibility of Insulating and Semiconducting Strontium Titanate," *Phys. Rev*., **147** [2] 583–4 (1966).
[444]H. Suzuki, H. Bando, Y. Ootuka, I. H. Inoue, T. Yamamoto, K. Takahashi, and Y. Nishihara, "Superconductivity in Single-Crystalline $Sr_{1-x}La_xTiO_3$," *J. Phys. Soc. Jpn*., **65** [6] 1529–32 (1996).
[445]M. Gurvitch, H. L. Stormer, R. C. Dynes, J. M. Graybeal, and D. C. Jacobson, "Field Effect on Superconducting Surface Layers of $SrTiO_3$;" pp. 47–9, *Extended Abstracts Superconducting Materials*, **Vol. EA–9**, Edited by J. Bevk, and A. I. Braginski. Materials Research Society, Pittsburgh, 1986.
[446]R. Dingle, H. L. Störmer, A. C. Gossard, and W. Wiegmann, "Electron Mobilities in Modulation-Doped Semiconductor Heterojunction Superlattices," *Appl. Phys. Lett*., **33** [7] 665–7 (1978).
[447]R. J. Cava, "Structural Chemistry and the Local Charge Picture of Copper Oxide Superconductors," *Science*, **247** [4943] 656–62 (1990).
[448]J. H. Haeni, "Nanoengineering of Ruddlesden-Popper Phases using Molecular Beam Epitaxy"; Ph.D. Thesis, Pennsylvania State University, 2002. Available on-line at http://etda.libraries.psu.edu/theses/approved/WorldWideIndex/ETD-181/index.html
[449]G. B. Stringfellow (ed), *Phase Equilibria Diagrams*, **Vol. 9**, pp. 126, 130. American Ceramic Society, Westerville, 1992.
[450]T. Ikeda, "A Few Quarternary Systems of Perovskite Type $A^{2+}B^{4+}O_3$ Solid Solutions," *J. Phys. Soc. Jpn*., **14** [10] 1286–94 (1959).
[451]E. M. Levin, C. R. Robbins, and H. F. McMurdie (eds), *Phase Diagrams for Ceramists*, **Vol. 1**, p. 195. American Ceramic Society, Columbus, 1964.
[452]A. K. Gutakovskii, L. I. Fedina, and A. L. Aseev, "High Resolution Electron Microscopy of Semiconductor Interfaces," *Phys. Status Solidi A*, **150** [1] 127–40 (1995).
[453]S. Thoma and H. Cerva, "Comparison of the Information Content in $\langle 110\rangle$- and $\langle 100\rangle$-Projected High-Resolution Transmission Electron Microscope Images for the Quantitative Analysis of AlAs/GaAs Interfaces," *Ultramicroscopy*, **53** [1] 37–51 (1994).
[454]S. Li, J. A. Eastman, J. M. Vetrone, R. E. Newnham, and L. E. Cross, "Dielectric Response in Ferroelectric Superlattices," *Philos. Mag. B*, **76** [1] 47–57 (1997).
[455]N. Sai, B. Meyer, and D. Vanderbilt, "Compositional Inversion Symmetry Breaking in Ferroelectric Perovskites," *Phys. Rev. Lett*., **84** [24] 5636–9 (2000).
[456]J. B. Neaton and K. M. Rabe, "Theory of Polarization Enhancement in Epitaxial $BaTiO_3/SrTiO_3$ Superlattices," *Appl. Phys. Lett*., **82** [10] 1586–8 (2003).
[457]S. M. Nakhmanson, K. M. Rabe, and D. Vanderbilt, "Polarization Enhancement in Two- and Three-Component Ferroelectric Superlattices," *Appl. Phys. Lett*., **87** [10] 102906 (2005).
[458]S. M. Nakhmanson, K. M. Rabe, and D. Vanderbilt, "Predicting Polarization Enhancement in Multicomponent Ferroelectric Superlattices," *Phys. Rev. B*, **73** [6] 060101 (2006).
[459]J. Chaloupka and G. Khaliullin, "Orbital Order and Possible Superconductivity in $LaNiO_3/LaMO_3$ Superlattices," *Phys. Rev. Lett*., **100** [1] 016404 (2008).
[460]T. Shimuta, O. Nakagawara, T. Makino, S. Arai, H. Tabata, and T. Kawai, "Enhancement of Remanent Polarization in Epitaxial $BaTiO_3/SrTiO_3$ Superlattices with 'Asymmetric Structure'," *J. Appl. Phys*., **91** [4] 2290–4 (2002).
[461]M. H. Corbett, R. M. Bowman, J. M. Gregg, and D. T. Foord, "Enhancement of Dielectric Constant and Associated Coupling of Polarization Behavior in Thin Film Relaxor Superlattices," *Appl. Phys. Lett*., **79** [6] 815–7 (2001).
[462]L. Kim, D. Jung, J. Kim, J. S. Kim, and J. Lee, "Strain Manipulation in $BaTiO_3/SrTiO_3$ Artificial Lattice Toward High Dielectric Constant and its Nonlinearity," *Appl. Phys. Lett*., **82** [13] 2118–20 (2003).
[463]D. O'Neill, R. M. Bowman, and J. M. Gregg, "Dielectric Enhancement and Maxwell–Wagner Effects in Ferroelectric Superlattice Structures," *Appl. Phys. Lett*., **77** [10] 1520–2 (2000).
[464]G. Catalan, D. O'Neill, R. M. Bowman, and J. M. Gregg, "Relaxor Features in Ferroelectric Superlattices: A Maxwell–Wagner Approach," *Appl. Phys. Lett*., **77** [19] 3078–80 (2000).
[465]H. Zheng, Q. Zhan, F. Zavaliche, M. Sherburne, F. Straub, M. P. Cruz, L.-Q. Chen, U. Dahmen, and R. Ramesh, "Controlling Self-Assembled Perovskite-Spinel Nanostructures," *Nano Lett*., **6** [7] 1401–7 (2006).
[466]S. Ríos, A. Ruediger, A. Q. Jiang, J. F. Scott, H. Lu, and Z. Chen, "Orthorhombic Strontium Titanate in $BaTiO_3$–$SrTiO_3$ Superlattices," *J. Phys. Cond. Matter*, **15** [21] L305–9 (2003).
[467]K. Johnston, X. Y. Huang, J. B. Neaton, and K. M. Rabe, "First-Principles Study of Symmetry Lowering and Polarization in $BaTiO_3/SrTiO_3$ Superlattices with in-Plane Expansion," *Phys. Rev. B*, **71** [10] 100103(R) (2005).
[468]Y. L. Li, S. Y. Hu, D. Tenne, A. Soukiassian, D. G. Schlom, L. Q. Chen, X. X. Xi, K. J. Choi, C. B. Eom, A. Saxena, T. Lookman, and Q. X. Jia, "Interfacial

Coherency and Ferroelectricity of $BaTiO_3/SrTiO_3$ Superlattice Films," *Appl. Phys. Lett.*, **91** [25] 252904 (2007).
[469]Y. L. Li, S. Y. Hu, D. Tenne, A. Soukiassian, D. G. Schlom, X. X. Xi, K. J. Choi, C. B. Eom, A. Saxena, T. Lookman, Q. X. Jia, and L. Q. Chen, "Prediction of Ferroelectricity in $BaTiO_3/SrTiO_3$ Superlattices with Domains," *Appl. Phys. Lett.*, **91** [11] 112914 (2007).
[470]C. Ederer and N. A. Spaldin, "Effect of Epitaxial Strain on the Spontaneous Polarization of Thin Film Ferroelectrics," *Phys. Rev. Lett.*, **95** [25] 257601 (2005).
[471]K. M. Rabe, "Theoretical Investigations of Epitaxial Strain Effects in Ferroelectric Oxide Thin Films and Superlattices," *Curr. Opin. Solid State Mater. Sci.*, **9** [3] 122–7 (2006).
[472]C. Ederer and N. A. Spaldin, "Recent Progress in First-Principles Studies of Magnetoelectric Multiferroics," *Curr. Opin. Solid State Mater. Sci.*, **9** [3] 128–39 (2006).
[473]J. B. Neaton, C. Ederer, U. V. Waghmare, N. A. Spaldin, and K. M. Rabe, "First-Principles Study of Spontaneous Polarization in Multiferroic $BiFeO_3$," *Phys. Rev. B*, **71** [1] 014113 (2005).
[474]O. Dieguez, K. M. Rabe, and D. H. Vanderbilt, "First-Principles Study of Epitaxial Strain in Perovskites," *Phys. Rev. B*, **72** [14] 144101 (2005).
[475]M. Dawber, K. M. Rabe, and J. F. Scott, "Physics of Thin-Film Ferroelectric Oxides," *Rev. Mod. Phys.*, **77** [4] 1083–130 (2005).
[476]H. W. Jang, S. H. Beak, D. Ortiz, C. M. Folkman, R. R. Das, Y. H. Chu, P. Shafer, J. X. Zhang, S. Choudhury, V. Vaithyanathan, Y. B. Chen, X. Q. Pan, D. G. Schlom, L. Q. Chen, R. Ramesh, and C. B. Eom, "Strain-Induced Polarization Rotation in Epitaxial (001) $BiFeO_3$ Thin Films," *Phys. Rev. Lett.*, in press.

Long-Qing Chen is Professor of Materials Science and Engineering at Penn State University. He received a B.S. degree from Zhejiang University in China, a M.S. degree from State University of New York at Stony Brook, and a Ph.D. degree from MIT. After a 2-year post-doc appointment at Rutgers University, he joined the faculty at Penn State in 1992. His main research interest is in developing computational models for predicting mesoscale microstructure evolution in advanced materials. Prof. Chen is the author or co-author of more than 200 papers and has delivered more than 150 invited presentations. He received numerous awards including an ONR Young Investigator Award, a NSF special research creativity award, a Wilson Award for Excellence in Research from his college, a University Faculty Scholar Medal in Engineering at Penn State, a Outstanding Overseas Young Scholar by the Chinese Natural Science Foundation, a Changjiang Chair Professorship by the Chinese Ministry of Education, a Guggenheim Fellowship, a Royal Society Kan Tong Po Fellowship, and the 2006 ASM Materials Research Silver Medal.

Xiaoqing Pan is a Professor in the Department of Materials Science and Engineering at the University of Michigan, Ann Arbor. He received B.S. and M.S. degrees in condensed matter physics from Nanjing University in China and a Ph.D. degree from Universität des Saarlandes in Germany. After a post-doc at the Max-Planck Institute für Metallforschung in Stuttgart, he joined the faculty at the University of Michigan. His research interests involve the epitaxial growth and structural characterization of functional materials including catalysts, oxide semiconductors, dielectric, and ferroelectric oxides. He is particularly interested in the structure–property relationships of interfaces and defects at the atomic scale. He is best known for his atomic scale characterization of oxide materials using high-resolution transmission electron microscopy. He has published over 200 papers. He has received the National Science Foundation's CAREER Award and the Chinese Natural Science Foundation's Outstanding Young Investigator Award.

Darrell Schlom is a Professor in the Department of Materials Science and Engineering at Cornell University. He received a B.S. degree from Caltech, and M.S. and Ph.D. degrees from Stanford University. After a post-doc at IBM's research lab in Zurich, Switzerland, he joined the faculty at Penn State University where the work described in this paper was performed. His research interests involve the heteroepitaxial growth and characterization of oxide thin films, especially those with functional properties (ferroelectric, piezoelectric, ferromagnetic, or a combination of these properties), including their epitaxial integration with semiconductors. He is particularly interested in the preparation of high quality oxide heterostructures with electronic applications (e.g., superlattices and metastable phases of dielectric and ferroelectric oxides) by MBE. He has published over 300 papers and has seven patents. He has been awarded invention achievement awards by IBM and SRC; young investigator awards by ONR, NSF, and the American Association for Crystal Growth; an Alexander von Humboldt Research Fellowship, and the ASM International Bradley Stoughton Award for Young Teachers. He is a Fellow of the American Physical Society.

Andreas Schmehl is a researcher in the group of Prof. Jochen Mannhart at the Center for Electronic Correlations and Magnetism at the University of Augsburg, Germany. He received a physics diploma and a Ph.D. degree in physics from the University of Augsburg. As part of a Feodor Lynen research scholarship, awarded by the Alexander von Humboldt foundation, he spent 2 years as post-doc in the group of Prof. Darrell G. Schlom at Penn State University. His research interests involve the electronic properties of interfaces in materials with strong electronic correlations, electronics based on oxide thin films, and semiconductor-based spin electronics. His main focus is the preparation of high-quality metal-oxide thin films (spin polarized semiconductors, superconductors, ferromagnets) and their utilization for novel device concepts as well as for basic research. He has published over 30 papers and owns four patents. He is currently working on his habilitation.

Mark Zurbuchen is a senior member of the technical staff in the Microelectronics Technology Department at The Aerospace Corporation. He received a B.S. degree from U. Missouri, an M.S. from Rensselaer, and a Ph.D. from Penn State. He worked in R&D at a small tech firm and as a post-doc at Argonne. He was at NIST prior to joining the staff at Aerospace, and is owner of TAECO LLC (www.taecompany.com). His interest centers on synthesis and characterization of heteroepitaxial systems, particularly for the integration of heterogeneous materials and the formation of new compounds for microelectronic applications. His current work focuses on formation dynamics of epitaxial systems having differing anion chemistries (e.g., oxides, nitrides, fluorides, and sulfides), and on 3D analysis of nanoscale structures by TEM tomography. His main expertise are in TEM and X-ray diffraction methods, and film growth by pulsed-laser deposition. He has published 27 papers and has 10 patents awarded or pending. He has been awarded invention achievement awards by Aerospac e Corp., and an NRC Postdoctoral Fellowship award. □